

3
2008

This is to certify that the
dissertation entitled

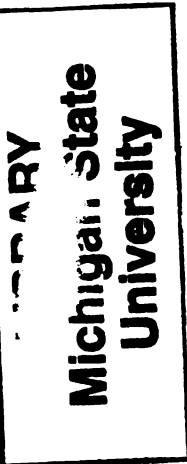
**DEVELOPMENT OF STRUCTURE-PROPERTY
RELATIONSHIPS FOR HYDRATED CEMENT PASTE,
MORTAR AND CONCRETE**

presented by

TEWODROS TEKESTE GHEBRAB

has been accepted towards fulfillment
of the requirements for the

Ph.D. degree in Civil and Environmental
Engineering



Major Professor's Signature

4/22/08

Date

PLACE IN RETURN BOX to remove this checkout from your record.
TO AVOID FINES return on or before date due.
MAY BE RECALLED with earlier due date if requested.

DATE DUE	DATE DUE	DATE DUE

**DEVELOPMENT OF STRUCTURE-PROPERTY RELATIONSHIPS FOR
HYDRATED CEMENT PASTE, MORTAR AND CONCRETE**

By

Tewodros Tekeste Ghebrab

A DISSERTATION

**Submitted to
Michigan State University
in partial fulfillment of the requirements
for the degree of**

DOCTOR OF PHILOSOPHY

Department of Civil & Environmental Engineering

2008

ABSTRACT

DEVELOPMENT OF STRUCTURE-PROPERTY RELATIONSHIPS FOR HYDRATED CEMENT PASTE, MORTAR AND CONCRETE

By

Tewodros Tekeste Ghebrab

A mechanistic approach was adopted to develop models for the mechanical properties of hydrated cement paste, mortar and concrete. These models reflect the fundamental structure of concrete, and represent a departure from the predominantly empirical models available for cement-based materials. The intrinsic elastic modulus and fracture toughness of hydrated cement paste were determined based on the interatomic interactions between calcium silicate hydrate (C-S-H) particles, which are the primary binder among the hydration products of cement. The elastic modulus model of hydrated cement paste was developed by introducing the effect of elliptical capillary pores into the corresponding intrinsic model. The fracture toughness model of hydrated cement paste was also developed by introducing the energy dissipation associated with the C-S-H/C-S-H debonding and the phononic frictional pullout of calcium hydroxide (CH) crystals, with the latter phenomenon found to be the major contributor. The strength of hydrated cement paste was determined using the elastic fracture mechanics principles. Experimental results and available empirical models were used to validate the models. Mechanical models for cement mortar were developed by introducing the effects of fine

aggregate on hydrated cement paste. The elastic modulus model of cement mortar accounts for the positive effects of the high elastic modulus fine aggregates, and the negative effects of the interfacial transition zone. The fracture toughness model of cement mortar was developed by introducing the energy dissipation associated with the pull-out of fine aggregates into the fracture toughness model of hydrated cement paste. The strength model of cement mortar was developed using the elastic modulus and fracture toughness models based on fracture mechanics concepts, with due consideration given to the effects of fine aggregates in restrained shrinkage microcracking of cement mortar. Experimental results and empirical models were used to verify the mechanistic models of cement mortar. The mechanistic models of concrete were developed based on the corresponding models of cement mortar by introducing various effects of coarse aggregates. The fracture toughness model of concrete accounted for the energy dissipation associated with pullout of coarse aggregates from cement mortar. The approach to development of elastic modulus and strength models was similar to that used for development of the corresponding models of cement mortar. The predictions of the mechanistic models of concrete compared favorably with experimental results. The mechanistic models of concrete were tailored for application to high-volume fly ash concrete, and were used to determine the effects of high-volume replacement of cement with coal fly ash on the mechanical properties of concrete. Some comparisons were also made between the predictions of the mechanistic models and the test data available for high-volume fly ash concrete.

DEDICATION

**This dissertation is fondly dedicated to my dear wife, children, father, mother, sisters, brothers, and the Baha'i Community of East Lansing for their support and prayers.
Many Thanks be to The Almighty God!**

ACKNOWLEDGEMENT

The work of this research was supported partly by IIE, Fulbright, and Washtenaw County Road Commission. The author thanks the research guidance committee for their comments and contributions. Special thanks goes to my advisor, Professor Parviz Soroushian, for his understanding and support.

TABLE OF CONTENTS

LIST OF TABLES.....	ix
LIST OF FIGURES.....	xi
KEY TO SYMBOLS OR ABBREVIATIONS.....	xvii
INTRODUCTION.....	1
CHAPTER 1	
LITERATURE REVIEW	6
1.1 Chemistry of Hydration of Cement.....	6
1.1.1 Introduction.....	6
1.1.2 Hydration of Tricalcium Silicate (C_3S) and Dicalcium Silicate (C_2S).....	7
1.2 Capillary Pores.....	14
1.3 Structure-Property Relationship of Cementitious Materials.....	19
1.4 Fly Ash.....	23
1.4.1 Type and Trends in Quality of Fly Ash.....	23
1.4.2 Effect of Fly Ash on Chemistry of Cement Hydration and Cement Hydration Products.....	24
1.4.3 Effect of Fly Ash on Capillary Pore System.....	27
1.4.4 Air-Entrainment of Concrete with Fly Ash.....	30
1.4.5 Effect of High Fly Ash Volumes on Engineering Properties of Concrete.....	32
1.4.6 Effect of High Fly Ash Volumes on Hydration of Cement.....	32
1.4.7 Effect of High Fly Ash Volumes on Strength of Concrete.....	35
CHAPTER 2	
MECHANICAL MODELS OF HYDRATED CEMENT PASTE	38
2.1 Introduction.....	38
2.2 Hydrated Cement Paste Free From Capillary Pores and Microcracks (Compact Hydrated Cement Paste).....	39
2.2.1 Molecular Interactions Between C-S-H Particles.....	39
2.2.2 Modulus of Elasticity of Compact Hydrated Cement Paste (E_o)..	42
2.2.3 Fracture Toughness of Compact Hydrated Cement Paste (G_o)....	48
2.2.3.1 Fracture Toughness Due to Debonding Between C-S-H Globules (G_d).....	48
2.2.3.2 Fracture Toughness Due to CH Crystal Pull-out (G_p).....	51

2.2.4 Intrinsic Tensile Strength of Compact Hydrated Cement Paste (σ_{to}).....	60
2.3 Hydrated Cement Paste.....	61
2.3.1 Introduction.....	61
2.3.2 Elastic Modulus of Hydrated Cement Paste.....	61
2.3.3 Fracture Toughness of Hydrated Cement Paste.....	66
2.3.4 Tensile Strength of Hydrated Cement Paste.....	66
2.3.4.1 Shrinkage Microcracks.....	67
2.3.4.2 Tensile Strength of Hydrated Cement Paste.....	70
2.3.4.3 Parametric Study of the Effects of Various Parameters on the Tensile Strength of Hydrated Cement Paste.....	71
2.3.4.4 Comparing the Predictions of the Mechanistic Tensile Strength Model of Hydrated Cement Past with those of Empirical Models	89
2.3.5 Compressive Strength Model of Hydrated Cement Paste.....	91
CHAPTER 3	
MODELING THE MECHANICAL PROPERTIES OF MORTAR BASED ON MECHANISTIC APPROACH.....	94
3.1 Introduction.....	94
3.2 Modeling.....	95
3.2.1 Modulus of Elasticity of Cement Mortar.....	95
3.2.2 Parametric Study of the Effect of the Fine Aggregate Elastic Modulus on the Modulus of Elasticity of Cement Mortar.....	106
3.2.3 Comparing the Predictions of Mechanistic Model of the Elastic Modulus of Cement Mortar with those of Empirical Models.....	116
3.2.4 Mechanistic Model for the Fracture Toughness of Cement Mortar.....	117
3.2.4.1 Energy Released During Debonding of Sand Particles from Hydrated Cement Paste.....	120
3.2.4.2 Energy Released During Pull-out of Sand Particles from Hydrated Cement Paste.....	122
3.2.5 Tensile Strength Model of Cement Mortar.....	130
CHAPTER 4	
MODELING THE MECHANICAL PROPERTIES OF CONCRETE BASED ON MECHANISTIC APPROACH.....	135
4.1 Introduction.....	135
4.2 Modeling.....	137
4.2.1 Modulus of Elasticity of Concrete.....	138
4.2.1.1 Parametric Study on the Influence of the Modulus of Elasticity of Coarse Aggregates on the Concrete Elastic Modulus.....	148
4.2.1.2 Comparing the Predictions of the Mechanistic Model of Concrete Elastic Modulus with those of Empirical Models.....	156

4.2.2 Mechanistic Model for the Fracture Toughness of Concrete.....	158
4.2.2.1 Energy Released During Debonding of Coarse Aggregates from Hydrated Cement Paste in the Interfacial Transition Zone of Concrete.....	162
4.2.2.2 Energy Released During Pull-out of Coarse Aggregates from Cement Mortar in the Interfacial Transition Zone of Concrete.....	163
4.2.3 Mechanistic Model for the Tensile Strength of Concrete.....	168
4.2.4 Compressive Strength Model of Concrete.....	174
4.2.5 Comparing the Predictions of the Compressive Strength Model of Concrete with those of Empirical Models	179
CHAPTER 5	
MECHANICAL MODELS OF HIGH-VOLUME FLY ASH CONCRETE.....	181
5.1 Introduction.....	181
5.2 Development of a Strength Model for High-Volume Fly Ash Concrete....	182
5.3 Concrete Containing 50% Replacement of Cement with Fly Ash.....	183
5.3.1 Fracture Toughness of Concrete Containing 50% Fly Ash as Replacement for Cement.....	185
5.3.2 Modulus of Elasticity of Concrete Containing 50% Fly Ash As Replacement for Cement	193
5.3.3. Tensile Strength of Concrete Containing 50% Fly Ash.....	198
5.3.4 Compressive Strength of Concrete Containing 50% Fly Ash.....	202
5.3.5 Comparing the Predictions of the Mechanistic Model of the Strength of Concrete Containing 50% Fly Ash Cement with Experimental Results	206
SUMMARY	209
REFERENCES.....	218

LIST OF TABLES

- Table 1.1 - Calculated porosities based on the Powers-Brownyard model
- Table 1.2 - Degree of reaction of fly ash in fly ash concrete pastes
- Table 2.1 - Effects of the distance between C-S-H globules on bond strength and modulus of elasticity of compact hydrated cement paste free from capillary pores and microcracks
- Table 2.2 - Calculation of the fracture toughness (due to debonding of C-S-H globules) of compact hydrated cement paste free from capillary pores and microcracks
- Table 2.3 - Summary of the variations of the fracture toughness due to C-S-H/C-S-H debonding, (G_d) in J/m^2 , with radius of globules, R_g , and F_{dvw}
- Table 2.4 - Significance of CH diameter and thickness on fracture toughness due to CH pull-out (G_p)
- Table 3.1 - Volume fractions of the interfacial transition zone and the hydrated cement paste for different aggregate sizes (at constant aggregate volume) in cement mortar
- Table 3.3 - The E_h and E_i values calculated for different values of capillary porosity in hydrated cement paste
- Table 3.4 - The bulk and shear moduli of fine aggregate (sand) in mortar
- Table 3.5 - The upper and lower bounds of bulk modulus and shear modulus of cement mortar with fine aggregate having modulus of elasticity of 70 GPa
- Table 3.6 - The upper and lower bounds of bulk modulus and shear modulus of cement mortar with fine aggregate having modulus of elasticity of 80 GPa
- Table 3.7 - The upper and lower bounds of bulk modulus and shear modulus of cement mortar with fine aggregate having modulus of elasticity of 90 GPa
- Table 3.8 - The upper and lower bounds of the elastic moduli of three cement mortars each containing a fine aggregate with a specific modulus of elasticity

- Table 4.1 - Volume fractions of the interfacial transition zone and the cement mortar for different sizes of coarse aggregates in concrete
- Table 4.2 - E_m and E_{ic} values calculated for different values of hydrated cement paste capillary porosity
- Table 4.3 - Bulk and shear moduli of coarse aggregates in concrete.
- Table 4.4 - Upper and lower bounds of the bulk and shear moduli of concrete for different sizes of coarse aggregates having an elastic modulus of 70 GPa
- Table 4.5 - Upper and lower bounds of the bulk shear moduli of concrete with coarse aggregates of different size having elastic modulus of 80 GPa
- Table 4.6 - Upper and lower bounds of the bulk and shear moduli of concrete with coarse aggregates of different size having elastic modulus of 90 GPa
- Table 4.7 - Upper and lower bounds of the modulus of elasticity of three concretes with coarse aggregates of different elastic moduli
- Table 4.8 - Tensile strength of concrete with different maximum aggregate sizes
- Table 4.9 - Compressive strength of concrete with different maximum aggregate sizes
- Table 5.1 - Reduction of CH and fly ash from hcp during pozzolanic activity
- Table 5.2 - Effect of unreacted fly ash and cement particles on fracture toughness of hydrated cement paste
- Table 5.3 - Modulus of elasticity of hcp, mortar and concrete and fracture toughness and tensile strength of concrete, containing 50% fly ash, in 28-days
- Table 5.4 - Modulus of elasticity of hcp, mortar and concrete and fracture toughness and tensile strength of concrete, containing 50% fly ash, in 90-days
- Table 5.5 - Modulus of elasticity of hcp, mortar and concrete and fracture toughness and tensile strength of concrete, containing 50% fly ash, in 180-days
- Table 5.6 - Modulus of elasticity of hcp, mortar and concrete and fracture toughness and compressive strength of concrete, containing 50% fly ash, in 28-days
- Table 5.7 - Modulus of elasticity of hcp, mortar and concrete and fracture toughness and compressive strength of concrete, containing 50% fly ash, in 90-days
- Table 5.8 - Modulus of elasticity of hcp, mortar and concrete and fracture toughness and compressive strength of concrete, containing 50% fly ash, in 180-days

LIST OF FIGURES

- Fig. 1.1 - Microstructure of a hydrated cement paste. It shows that the structure is not homogenous; some areas are dense and the others are porous. Massive crystals of calcium hydroxide, long and slender needles of ettringite, and aggregation of small fibrous crystals of calcium silicate hydrate can be observed by magnifying the porous areas
- Fig. 1.2 - Model of a well-hydrated Portland cement paste 'A' represents aggregation of poorly crystalline C-S-H particles. 'H' represents hexagonal crystalline products such as CH, C_4ASH_{18} , C_4AH_{19} . 'C' represents capillary pores
- Fig. 1.3 - Schematic representation of the internal structure of a cement paste in various phases of hydration (not to scale) (a) Dormant period (b) and (c) Setting (d) Hardening; Black mass: unhydrated cement; Fibers: hydration products. White mass: pores
- Fig. 1.4 - Degree of hydration of the constituents in a type I cement as a function of time
- Fig. 1.5 - (A,B) Types I and II C-S-H, respectively (SEM of fracture surfaces, courtesy K.L. Scrivener). (C,D) SEM/STEM pair of ion beam thinned section, showing Type III C-S-H and Type IV C-S-H. (A) is of an ordinary Portland cement paste, $w/c = 0.5$, aged 10 h. (B) is of a paste of an oil well cement, $w/c = 0.44$, with 2.4% of $CaCl_2$ on the weight of cement, aged 1 day. (C) and (D) are of a C_3S paste, $w/c = 0.47$, aged 330 days.
- Fig. 1.6 - Pore size distribution in fresh cement paste (C indicates capillary pores; the black spots are gels; and the spaces between them are gel pores).
- Fig. 1.7 - Relations between compressive strength (log scale) and porosity; data from various sources for Portland cement pastes cured at ordinary temperatures (open circles), hot pressed Portland cement paste (filled circle), autoclaved pastes of Portland cement, sometimes with added sulfur (filled square) and autoclaved pastes of Portland cement with 50% (open squares) or 30% (cross) of added fly ash.
- Fig. 1.8 - Typical Class F fly ash: (a) spherical and glassy particles; (b) a Plerospher
- Fig. 1.9 - Cement Particles

- Fig. 1.10 - Diagrammatic representation of well-hydrated cement pastes made with a Portland pozzolana cement. As compared to Fig. 1.2, the capillary voids are either eliminated or reduced due to the pozzolanic reaction.
- Fig. 1.11 - Change in pore size distribution (determined by mercury porosimetry) in cement paste containing 30% of Class F fly ash by mass of total cementitious material
- Fig. 1.12 - $\text{Ca}(\text{OH})_2$ content relative to the cement content in PC and FC pastes (based on ignited weight). (a) $w/b = 0.3$, and (b) $w/b = 0.5$
- Fig. 2.1 - C-S-H morphology and geometric arrangement
- Fig. 2.2 - (a) Bonding energy as a function of the distance of separation; (b) force-displacement curve
- Fig. 2.3 - Stress-strain curve approximated as a half sine wave
- Fig. 2.4 - Hexagonal CH crystal
- Fig. 2.5 - CH orientation with flat surface parallel to the direction of loading (a) side view (b) front view
- Fig. 2.6 - Schematic model of CH pull-out
- Fig. 2.7 - Schematics of the effective contact area between CH crystal and C-S-H globules
- Fig. 2.8 - Capillary pore shape and interactions, and the resulting stress concentration
- Fig. 2.9 - Modulus of elasticity-porosity relationships
- Fig. 2.10 - Schematic presentation of the formation of microcracks in otherwise compact hydrated cement paste
- Fig. 2.11 - Influence of CH thickness on the strength-porosity relationship of hcp for spherical capillary pores, C-S-H globule diameter of 6 nm, distance between C-S-H globules of 0.18 nm, and CH crystal diameter of: (a) 1000 nm; (b) 10,000 nm
- Fig. 2.12 - Influence of CH thickness on the strength-porosity relationship of hcp for spherical capillary pores, C-S-H globule diameter of 6 nm, distance between C-S-H globules of 0.32 nm, and CH crystal diameter of: (a) 1000 nm; (b) 10,000 nm
- Fig. 2.13 - Influence of CH thickness on strength-porosity relationship of hcp for spherical capillary pores, C-S-H globule diameter of 8 nm, distance between

C-S-H globules of 0.18 nm, and CH crystal diameter of: (a) 1000 nm; (b) 10,000 nm

Fig. 2.14 - Influence of CH thickness on strength-porosity relationship of hcp for spherical capillary pores, C-S-H globule diameter of 8 nm, distance between C-S-H globules of 0.32 nm, and CH crystal diameter of: (a) 1000 nm; (b) 10,000 nm

Fig. 2.15 - Influence of CH thickness on strength-porosity relationship of hcp for ellipsoidal capillary pores, C-S-H globule diameter of 6 nm, distance between C-S-H globules of 0.18 nm, and CH crystal diameter of: (a) 1000 nm; (b) 10,000 nm

Fig. 2.16 - Influence of CH thickness on strength-porosity relationship of hcp for ellipsoidal capillary pores, C-S-H globule diameter of 6 nm, distance between C-S-H globules of 0.32 nm, and CH crystal diameter of: (a) 1000 nm; (b) 10,000 nm

Fig. 2.17 - Influence of CH thickness on strength-porosity relationship of hcp for ellipsoidal capillary pores, C-S-H globule diameter of 8 nm, distance between C-S-H globules of 0.18 nm, and CH crystal diameter of: (a) 1000 nm; (b) 10,000 nm

Fig. 2.18 - Influence of CH thickness on strength-porosity relationship of hcp for ellipsoidal capillary pores, C-S-H globule diameter of 8 nm, distance between C-S-H globules of 0.32 nm, and CH crystal diameter of: (a) 1000 nm; (b) 10,000 nm

Fig. 2.19 - Influence of the C-S-H globule diameter on the strength-porosity relationships of hcp for spherical capillary pores, distance between C-S-H globules of 0.18 nm, and CH crystal diameter of: (a) 1000 nm; (b) 10,000 nm

Fig. 2.20 - Influence of the C-S-H globule diameter on the strength-porosity relationships of hcp for spherical capillary pores, distance between C-S-H globules of 0.32 nm, and CH crystal diameter of: (a) 1000 nm; (b) 10,000 nm

Fig. 2.21 - Influence of the C-S-H globule diameter on the strength-porosity relationships of hcp for ellipsoidal capillary pores, distance between C-S-H globules of 0.18 nm, and CH crystal diameter of: (a) 1000 nm; (b) 10,000 nm

Fig. 2.22 - Influence of the C-S-H globule diameter on the strength-porosity relationships of hcp for ellipsoidal capillary pores, distance between C-S-H globules of 0.32 nm, and CH crystal diameter of: (a) 1000 nm; (b) 10,000 nm

- Fig. 2.23 - Influence of the distance between C-S-H globules on the strength-porosity relationships of hcp for spherical capillary pores with CH diameter of: (a) 1000 nm; (b) 10,000 nm**
- Fig. 2.24 - Influence of the distance between C-S-H globules on the strength-porosity relationships of hcp for ellipsoid capillary pores with CH diameter of: (a) 1000 nm; (b) 10,000 nm**
- Fig. 2.25 - Comparing the predictions of the mechanistic and empirical tensile strength models of hcp**
- Fig. 2.26 - Crack formation due to compressive in hydrated cement paste specimen**
- Fig. 2.27 - Predications of the compressive strength model of hcp versus those of empirical models derived based on experimental results**
- Fig. 3.1 - Variation of the interfacial transition zone thickness with aggregate size**
- Fig 3.2 - Schematic presentation of the geometric model of a sand particle**
- Fig. 3.3 - The relationship between the moduli of elasticity of the hydrated cement paste and the interfacial transition zone in cement mortar**
- Fig. 3.4 - The upper and lower bounds of the elastic moduli of three cement mortars each containing fine aggregates with different elastic moduli**
- Fig. 3.5 - Comparing the predictions of theoretical model for the elastic modulus of cement mortar with those of empirical model based on substantial test data**
- Fig. 3.6 - Surface roughness of fine aggregate, and interaction of the hydrated cement paste (hcp) at the interfacial transition zone**
- Fig 3.7 - The cracking pattern of the hydrated cement paste dendrite due to force P generated by sand pull-out**
- Fig. 3.8 - Surface of sand particle subjected to frictional pull-out**
- Fig. 3.9 - Fracture toughness of mortar as a function of the capillary porosity of hydrated cement paste**
- Fig. 3.10 - Fracture toughness of mortar as a function of the volume fraction of sand for a capillary porosity of 0.3**
- Fig. 3.11 - Fracture toughness of mortar as a function of the volume fraction of sand for a capillary porosity of 0.05**

- Fig. 3.12 - Fracture toughness of mortar as a function of the volume fraction of sand for a capillary porosity of 0**
- Fig. 3.13 - The critical shrinkage crack in cement mortar bridging between two adjacent sand particles**
- Fig. 3.14 - Tensile strength of cement mortar as a function of the capillary porosity of hydrated cement paste**
- Fig. 3.15 - Tensile strength of mortar as a function of the volume fraction of sand for a capillary porosity of 0.3**
- Fig 4.1 - The coarse aggregate shape model**
- Fig. 4.2 - Relationship between the elastic moduli of cement mortar and interfacial transition zone in concrete**
- Fig. 4.3 - Upper and lower bounds of the modulus of elasticity of three concretes with coarse aggregates of different elastic moduli**
- Fig. 4.4 - Comparing the predictions of theoretical model for the elastic modulus of concrete with those of empirical model based on substantial test data**
- Fig. 4.5 - Surface roughness of the coarse aggregate, and bonding of cement mortar at the interfacial transition zone**
- Fig 4.6 - The cracking pattern of the cement mortar dendrite due to the force P associated with the coarse aggregate pull-out stress**
- Fig. 4.7 - Average surface area of the aggregate particle subjected to frictional pull-out**
- Fig. 4.8 - Fracture toughness of concrete as a function capillary porosity**
- Fig. 4.9 - Inherent shrinkage crack in cement mortar bridging between two sand particles**
- Fig. 4.10 - Tensile strength-capillary porosity relationship for concrete with different maximum aggregates sizes**
- Fig. 4.11 - Schematic of conical wedges forming above and below coarse aggregates as concrete fails**
- Fig. 4.12 - Compressive strength-capillary porosity relationship for concrete with different maximum aggregates sizes**
- Fig. 4.13 - Validation of the prediction of compressive strength model of concrete by experiment based empirical models and results**

Fig. 5.1 - Schematic presentation of approximate surface area of fly ash particle subjected to pull-out as hcp cracks

Fig. 5.2 - Effect of age on fracture toughness of high-volume fly ash hcp

Fig. 5.3 - Tensile strength of high-volume fly ash concrete at different ages

Fig. 5.4 - Compressive strength of high-volume fly ash concrete at different ages

Fig. 5.5 - Validation of the 28-day compressive strength model of concrete containing 50% fly ash

Fig. 5.6 - Validation of the 90-day compressive strength model of concrete containing 50% fly ash

KEY TO SYMBOLS OR ABBREVIATIONS

- A = empirical coefficient
 A_c = effective projected contact area of C-S-H globule
 A_{cad} = surface area of a coarse aggregate subjected to debonding and pull-out stresses
 A'_{cad} = effective surface area of a coarse aggregate subjected to debonding stresses
 A'_{cap} = effective surface area of a coarse aggregate subjected to pull-out friction
 A'_{capm} = total surface area of the cement mortar subjected to shear stress during pull-out of coarse aggregate
 A_{ECH} = effective are of CH subjected to pull-out friction
 A_{fa} = projected plane area of the fly ash surface are subjected to pull-out
 A_g = total projected area of C-S-H globule
 A_s = surface area of CH subjected to pull-out friction
 A_{sd} = interfacial surface are of sand subjected to debonding stress
 A'_{sd} = effective interfacial surface area of sand subjected to debonding stress
 A'_{sp} = effective interfacial surface area of sand subjected to pull-out friction
 A'_{sph} = total surface area of hcp subjected to frictional stress during sand pull-out
 A_{sk} = surface area of CH subjected to skin friction
 a = half of major axis length of elliptical capillary pore
 $\alpha_{t=28}$ = degree of hydration at the age of 28-days
 b_0 = equilibrium atomic spacing (minimum energy)
 b = half of minor axis length of elliptical capillary pore
 β = empirical coefficient
 C = empirical coefficient
 CH = calcium hydroxide
 CH_p = CH produced during hydration
 CH_r = CH reacted during pozolanic activity
 $C-S-H$ = calcium silicate hydrate
 D_{CH} = diameter of CH crystal
 d = clear distance between two globules
 d_c = clear distance between capillary pores
 d_g = diameter of C-S-H globule
 E = modulus of elasticity
 E_i = modulus of elasticity of interfacial transition zone
 E_{fl} = energy dissipated during pull-out of a single CH crystal
 E_{im} = modulus of elasticity of interfacial transition zone in mortar

E_h = modulus of elasticity of hcp
 E_{m-} = lower bound modulus of elasticity of cement mortar
 E_{m+} = upper bound modulus of elasticity of cement mortar
 E_o = modulus of elasticity at zero porosity
 E_s = modulus of elasticity of sand (fine aggregate)
 E_c = modulus of elasticity of concrete
 E_{ca} = modulus of elasticity of coarse aggregate
 E_{ccf} = modulus of elasticity of high-volume fly ash concrete under compression
 E_{ctf} = modulus of elasticity of high-volume fly ash concrete under tension
 E_{hf} = modulus of elasticity of high-volume fly ash cement paste
 E_{ic} = modulus of elasticity of interfacial transition zone in concrete
 E_{mf} = modulus of elasticity of high-volume fly ash mortar
 ε = strain
 ε_{sh} = shrinkage strain
 F_f = phononic friction force
 F_g = force required to break the bond strength between two C-S-H globules
 F_{vdw} = van der waals force per unit area
 G_{add} = additional fracture toughness due to the wedging action of mortar cones forming on top of coarse aggregates in concrete under compression
 G_c = fracture toughness of concrete under tension
 G_{cad} = fracture toughness of concrete due to debonding of coarse aggregates from mortar
 G_{cc} = fracture toughness of concrete under compression
 G_{chsp} = energy released per unit fractured area of interfacial transition zone in mortar
 G_d = fracture toughness of hcp due to debonding of C-S-H globules
 G_{fa} = the contribution to fracture toughness of a single fly ash particle
 G_{ic} = total energy release rate per unit fractured area of the interfacial transition zone in concrete
 G_h = fracture toughness of hcp
 G_{hf} = fracture toughness of high-volume fly ash concrete
 G_{im} = total energy released per unit fractured area of interfacial transition zone in mortar
 G_m = fracture toughness of cement mortar
 G' = shear modulus
 G'_i = shear modulus of interfacial transition zone
 G'_h = shear modulus of hcp
 G'_{m-} = lower bound shear modulus of cement mortar
 G'_{m+} = upper bound shear modulus of cement mortar
 G'_c = shear modulus of concrete
 G'_{ca} = shear modulus of coarse aggregate

G'_{ic} = shear modulus of interfacial transition zone in concrete
 G'_{c-} = lower bound shear modulus of concrete
 G'_{c+} = upper bound shear modulus of concrete
 G_o = intrinsic fracture toughness of hcp
 G_{of} = intrinsic fracture toughness of high-volume fly ash concrete
 G_p = fracture toughness of hcp due to CH pull-out
 G_{sd} = fracture toughness during debonding of sand from interfacial transition zone
 γ_s = surface energy
 hcp = hydrated cement paste
 h_w = dielectric constant
 K' = bulk modulus
 K_1 = stress concentration amplification factor for a single capillary pore
 K_2 = stress concentration amplification factor for two capillary pores
 K'_h = bulk modulus of hcp
 K'_i = bulk modulus of interfacial transition zone
 K'_{m-} = lower bound bulk modulus of cement mortar
 K'_{m+} = upper bound bulk modulus of cement mortar
 K'_s = bulk modulus of sand (fine aggregate)
 K'_c = bulk modulus of concrete
 K'_{ca} = bulk modulus of coarse aggregate
 K'_{ic} = bulk modulus of interfacial transition zone in concrete
 K'_{c-} = lower bound bulk modulus of concrete
 K'_{c+} = upper bound bulk modulus of concrete
 l = crack length
 l_c = critical crack length
 N_{CHP} = number of CH crystals per plane section
 N_{CHV} = number of CH crystals per unit cubic cell volume
 N_{ca} = number of coarse aggregates per unit volume of concrete
 N_s = number of sand particles per unit volume of cement mortar
 P = porosity
 P_h = capillary porosity
 P_i = porosity of interfacial transition zone
 P_m = porosity of mortar
 P_c = porosity of concrete
 P_{CR} = zero-strength porosity

P_{CH} = perimeter of CH crystal
 R = radius of CH crystal
 R_{FA} = percent reduction of fly ash after t day of hydration
 R_g = radius of C-S-H globules
 r_c = radius of the effective projected contact area of C-S-H globule
 r_{fa} = is the radius of the fly ash particle
 S_c = surface area of one of the mortar conical wedges covering the coarse aggregate
 S_{fa} = pulled-out surface area of fly ash
 SG_F = specific gravity of fly ash particles
 SG_{PC} = specific gravity of unhydrated cement grains
 t_s = radius of a sphere equivalent to fine aggregate
 σ = strength or stress
 σ_{cc} = compressive strength of concrete
 σ_{ct} = tensile strength of concrete
 σ_{ccf} = compressive strength of high-volume fly ash concrete
 σ_{ctf} = tensile strength of high-volume fly ash concrete
 σ_o = strength at zero porosity
 σ_{max} = maximum stress to break the bond between C-S-H globules
 σ_{hc} = compressive strength of hcp
 σ_{ht} = tensile strength of hcp
 t_{CH} = thickness of CH crystal
 t_i = thickness of interfacial transition zone
 t_r = ratio of the thickness of the interfacial transition zone to a radius of a sphere equivalent to fine aggregate
 t_{rc} = ratio of interfacial thickness to a radius of a sphere equivalent to coarse aggregate
 t_{ic} = thickness of interfacial transition zone in concrete
 r_{ca} = radius of radius of a sphere equivalent to coarse aggregate
 τ_f = phononic friction stress
 U_{cad} = energy released due to debonding of coarse aggregate from mortar
 U_{CG} = unhydrated cement grains
 U_{CH} = unreacted calcium hydroxide crystals
 U_{chcap1} = energy released due to CH pull-out when A'_{capm} fractures
 U_{chcap2} = energy released due to CH pull-out at the bottom surface of the aggregate particle
 U_{chcap} = total energy released due to CH pull-out during the pull-out of the aggregate particle from the cement mortar
 U_{chsp1} = energy released due to CH pull-out upon fracture over A'_{sph}
 U_{chsp2} = energy released due to CH pull-out at the bottom surface of sand particle
 U_{chsp} = total energy released due to CH pull-out during the pull-out of sand from hydrated cement paste in mortar

U_e = strain energy released during cracking
 U_i = energy released during cracking
 U_{sd} = energy released during debonding of sand from interfacial transition zone
 V_{CH} = volume of CH crystal
 V'_{fa} = volume fraction of fly ash in hcp
 V'_h = volume fraction of hcp
 V_h = volume of hcp
 V_i = volume of interfacial transition zone
 V_m = volume of cement mortar
 V_{pm} = pore volume of mortar
 V_{ph} = pore volume of hcp
 V_{pi} = pore volume of interfacial transition zone
 V_s = volume of sand
 V_{li} = volume of interfacial transition zone surrounding a single aggregate
 V_{pm} = pore volume of mortar
 V_{pic} = pore volume of interfacial transition zone in concrete
 V_c = volume of concrete
 V_{ca} = volume of coarse aggregate
 V_{ic} = volume of interfacial transition zone in concrete
 V_{lic} = volume of interfacial transition zone surrounding a single coarse aggregate
 V_{lca} = volume of a single coarse aggregate
 V'_s = volume fraction of sand
 V'_m = volume fraction of mortar
 V'_{ca} = volume fraction of coarse aggregate
 V'_{ic} = volume fraction of interfacial transition zone in concrete
 ν = poisons ratio
 w/b = water-to-binder ratio
 y = crack width at the periphery of CH crystal
 Z = distance from the geometric center of CH crystal to the line marking the exposed part of the crystal from the adhering C-S-H globules during pull-out

INTRODUCTION

Portland cement concrete, henceforth referred to as concrete, is a composite material widely used in the construction industry. It is composed of aggregates and cement binder. Concrete technology was put into practice by ancient Romans in about 2000 B.C.,¹ using natural pozzolans as binder. Intensive use of concrete as construction material started during the 19th century.² Nowadays, concrete is widely used all over the world. Worldwide, about six billion tons of concrete are produced annually. Production of concrete is a \$100 billion industry, which provides job opportunities for over two million individuals.³

Concrete has some drawbacks which limit its effective use. Large weight-to-strength ratio, sensitivity to environmental attack and brittleness are some of the disadvantages of concrete. The two main advantages of concrete are its strength and durability. Its low tensile-to-compressive strength ratio requires generally necessitates the use of reinforcing materials, which add to the cost of concrete structures. Further, concrete (in spite of desirable durability characteristics) eventually deteriorates under environmental effects. The growing emphasis on energy and environmental issues also demand close consideration of the energy consumption and polluting effects of cement production. The addition of pozzolans (e.g., coal fly ash) can help improve the durability of concrete and

reduce the overall energy consumption and polluting effects associated with production of concrete.

Most models developed for the mechanical properties of cementitious materials are empirical, and derived based on experimental results. Empirical models are helpful, but may not provide comprehensive solutions that are generally applicable.

Given the porous nature of concrete, strength-porosity relationships have been emphasized in modeling of concrete performance. The Balshin model (Eqn. 1.2) is among the strength-porosity relationships commonly applied to concrete.⁴

$$\sigma = \sigma_0(1 - P)^A \quad (1.2)$$

where, σ_0 is compressive strength at zero porosity; P is porosity, and A is an empirical coefficient.

Ryshkewitch conducted experimental investigations to study the influence of porosity on ceramic materials, and developed another empirical strength-porosity relationship (Eqn. 1.3).⁵ The Ryshkewitch model fits well to strength at high porosity levels, but tends to overestimate strength at relatively low porosities.⁶

$$\sigma = \sigma_0 e^{-\beta P} \quad (1.3)$$

where, σ_0 is compressive strength at zero porosity; and β is an empirical coefficient.

Another empirical strength-porosity relationship developed by Schiller (Eqn. 1.4) produces results comparable to those obtained with the Ryshkewitch model except for the extremes of porosity.⁷

$$\sigma = C \ln \frac{P_{CR}}{P} \quad (1.4)$$

where, P is porosity; P_{CR} is zero-strength porosity; and C is an empirical coefficient.

The purpose of this research was to develop models for the mechanical properties of concrete which are based on structure-property relationships and account for the molecular interactions of the phases present in the concrete structure. Hydrated cement paste (the binder in concrete) is a complex assembly of nano-scale semi-crystalline and micro-scale crystalline solids bound together by physical interactions, and a host of nano- to micro-scale defects (pores, cracks). The introduction of aggregate further complicate the structure of concrete. In spite of these complexities, concrete cannot defy the laws of physics and mechanics; it should thus be possible to model concrete starting from intermolecular interactions, with mechanics laws employed to incorporate various complexities into the basic model. A sequential approach is adopted in this research to develop first intrinsic models (neglecting defects) for hydrated cement paste (hcp), followed by modeling of hcp with defects (capillary pores and microcracks);

subsequently, the effects of fine and then coarse aggregates on the structure, defects and failure mechanisms of the hcp binder are introduced in order to develop the cement mortar and concrete models. The hydrated cement paste is modeled as an assembly of nanostructured calcium silicate hydrate globules and micro-scale crystalline products (predominantly calcium hydroxide). The hcp models provides the basis for development of cement mortar and concrete models. Cement mortar and concrete are modeled as three-phase materials comprising hydrated cement paste, aggregates, and the interfacial transition zone. The models developed in this research are also tailored to evaluate the mechanical properties of high-volume fly ash concrete.

The theoretical predictions of the fundamental models developed in this research compare favorably with experimental results, confirming that the complexity of the concrete structure is not an unsurmountable obstacle against development of structure-property relationships based on fundamental laws of physics and mechanics.

This research represents an effort to develop models for concrete which start with interatomic interactions and the nano- and micro-structure of cement hydration products, and then incorporate such micro-structural features as the capillary pore system and microcracks, and finally consider the micro- and macro-structural implications of introducing fine and coarse aggregates. The key inspiration for development of these models was to depart from the empiricism which has governed past efforts to model the behavior of concrete under load. The models developed here represent structure-property relationships which highlight the need to further explore some key structural features of

concrete, particularly those at nano- and micro-scales. The models can be used to guide new developments towards improvement of concrete properties through refinement of its structure.

The mechanistic models developed in this project can be used to provide preliminary guides in development of new concrete materials (e.g., additives) which refine the structure and thus properties of concrete. Knowledge of the mechanisms of action of these materials (additives) in concrete can be used to predict any changes in the concrete structure (at nano-, micro- and/or macro-scales) resulting from their introduction. The mechanistic models can then be used to predict the effects of such changes in concrete structure on its material properties. This would guide the selection of additive types and dosages, and reduce the extent of trial-and-adjustment experimental work.

CHAPTER 1

LITERATURE REVIEW

1.1 Chemistry of Hydration of Cement

1.1.1 Introduction

Cement is a complex material composed of different phases which are Tricalcium Silicate (C_3S), Dicalcium Silicate β -(C_2S), Tricalcium Aluminate (C_3A) and Tetracalcium Aluminoferrite (C_4AF). Hydration of cement, as the name implies, is a mere combination of anhydrate cement phases with water to form hydrate phases.⁹ The cement particles disperse in water and form a plastic type material called paste.¹⁰ Therefore, hydration of cement implies the hydration of its constituent phases, which is a very complex chemical reaction that takes place between water and cement grains to produce hydrates.⁹ The amount of water needed to hydrate a certain amount of cement has to be proportioned for it affects the property of concrete both as fresh as well as hardened paste.¹⁰ As the volume of the hydration products increases in a paste, it creates an interlock mechanism and as a result the porosity of the paste reduces and leads to setting and hardening.¹⁰

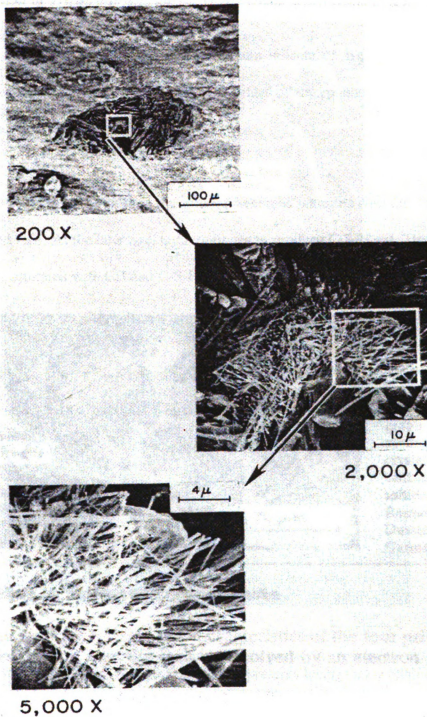


Fig. 1.1 - Microstructure of a hydrated cement paste. It shows that the structure is not homogenous; some areas are dense and the others are porous. Massive crystals of calcium hydroxide, long and slender needles of ettringite, and aggregation of small fibrous crystals of calcium silicate hydrate can be observed by magnifying the porous areas.¹¹

1.1.2 Hydration of Tricalcium Silicate (C_3S) and Dicalcium Silicate (C_2S)

Tricalcium silicate or Alite (C_3S) and Dicalcium silicate or Belite β -(C_2S) produce calcium hydroxide (CH) and calcium silicate hydrates of amorphous or poorly crystalline and porous gel(C-S-H) (Fig. 1.1).⁹

During the early stage of hydration, the solution becomes saturated with the CH produced from C_3S and C_3A . At the later age, C_3S continues to produce C-S-H gel. The solution at this period is saturated with CH and C-S-H (Fig. 1.2).¹⁰

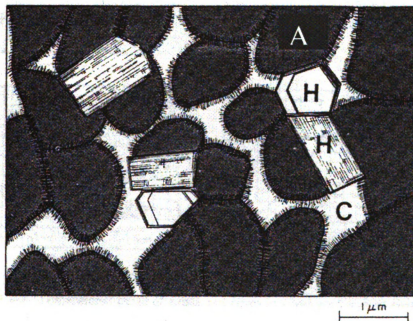


Fig. 1.2 - Model of a well-hydrated Portland cement paste. 'A' represents aggregation of poorly crystalline C-S-H particles. 'H' represents hexagonal crystalline products such as CH, C_4ASH_{18} , C_4AH_{19} . 'C' represents capillary pores.¹¹

C_3S has a more predominant effect on the setting process of cement paste than C_3A , for a large amount of C-S-H gels were observed to form and interlock at the initial set, which grows into an interlocking mass at the final set (Fig. 1.3).¹²

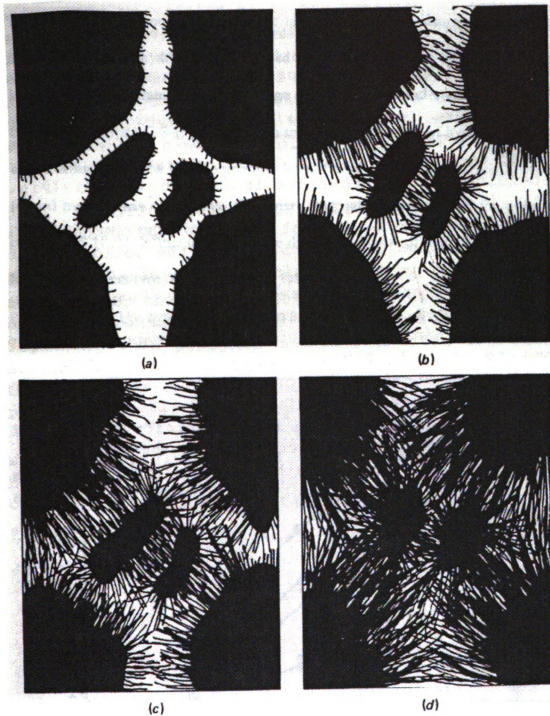


Fig. 1.3 - Schematic representation of the internal structure of a cement paste in various phases of hydration (not to scale). (a) Dormant period. (b) and (c) Setting. (d) Hardening. Black mass: unhydrated cement. Fibers: hydration products. White mass: pores.¹⁰

There are two fundamental stages in the rate of hydration of cement. The first stage is that at early stage, hydration is controlled by chemical reaction and thus each particle hydrates at its own rate. The second stage occurs when the outer surfaces of grains are coated with hydrate C-S-H gels, and as a result the mechanism of hydration is governed by the diffusion of new hydrate products from the anhydrate grain surface. These newly formed hydrate gels diffuse into the water-filled outer space through the pores of the coating C-S-H gel. In this later stage, the difference in rate of hydration becomes small for a given cement type, as shown in Fig. 1.4.¹³

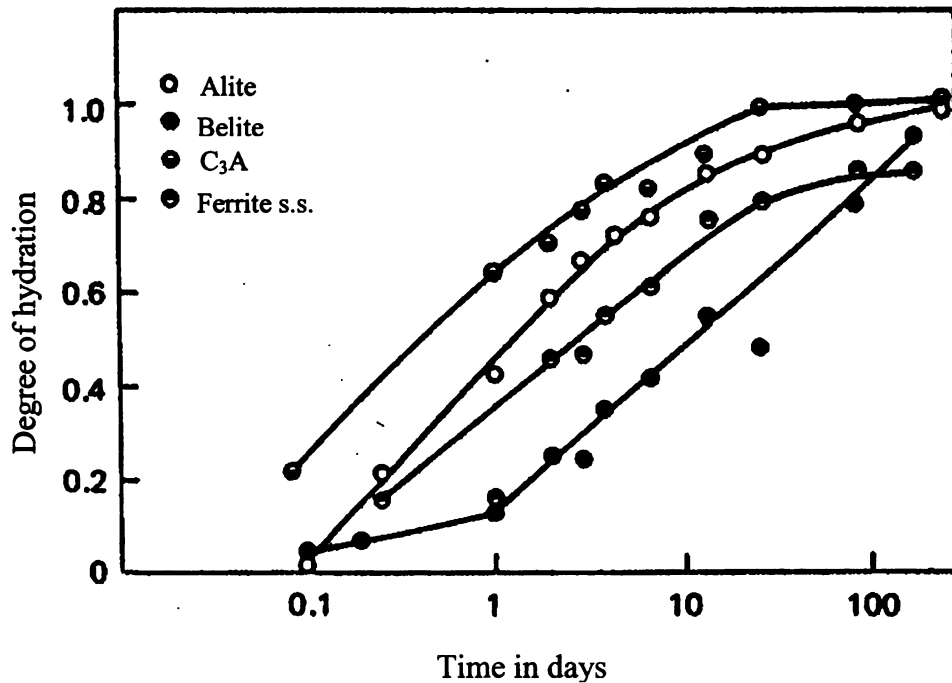


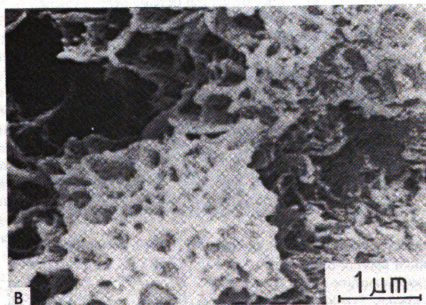
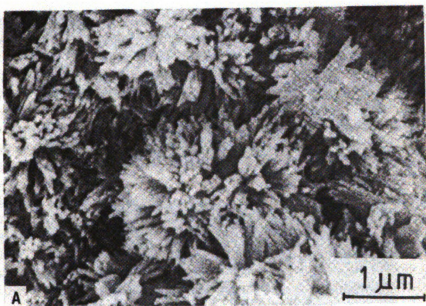
Fig. 1.4 - Degree of hydration of the constituents in a type I cement as a function of time¹²

Various studies have been made on C_3S and $\beta-C_2S$ to determine their composition in terms of Ca/Si ratio. Ca/Si ratio of C-S-H can be determined from the amount of CH and CO_2 present in a fully hydrated paste, using TG (Thermogravimetry) and DTA (Differential Thermal Analysis).¹⁴

C-S-H gel or cement paste has a layered structure, which acquires rigidity upon the occurrence of pore solutions that make interlayer spaces. In a saturated condition, where the pores are filled with water, C-S-H can be hydrated to a higher degree. C-S-H formation in cement paste is highly dependent on the availability of space to enable the anhydrate grains produce hydrate gels from their internal and outer layers. Thus to achieve almost a complete hydration and get ample pore space, an optimum amount of water (42-44% by weight of cement) should be added.⁹ Different researchers came up with almost similar composition of C-S-H: $1.7CaO.SiO_2.2.1H_2O$,¹⁵ $1.64CaO.SiO_2.1.96H_2O$.¹⁶ Based on D-drying procedure, the water content for a fully saturated C_3S is about 20.4-22% corresponding to C-H-S of $1.7CaO.SiO_2.1.3-1.5H_2O$.¹⁷

During hydration, some microscopic investigations have revealed that CH was observed to accumulate as an isolated mass of small size at more concentration with C_3S than with C_2S . Further, a gel forms around the anhydrate grains and moves towards the water space as a hydrate. The hydrates of calcium silicates were found to be of two types; those that are hydrates of the inner part of the grains, which are large and amorphous in structures, and those products of the outer part of the grain which forms in the water-filled space,

which have a column or fiber like structure.⁹ C-S-H gel have four morphological types that develop with age of the cement or calcium silicate paste (Fig. 1.5).¹⁸ Type I is fibrous and Type II is honeycomb like, and both occur at early age. Type III has a tightly packed grains and Type IV is a featureless which occurs at older age as Type III.



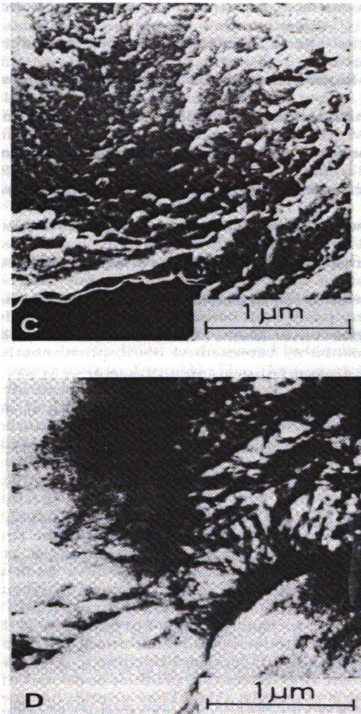


Fig. 1.5 - (A,B) Types I and II C-S-H, respectively (SEM of fracture surfaces, courtesy K.L. Scrivener). (C,D) SEM/STEM pair of ion beam thinned section, showing Type III C-S-H and Type IV C-S-H. (A) is of an ordinary Portland cement paste, $w/c = 0.5$, aged 10 h. (B) is of a paste of an oil well cement, $w/c = 0.44$, with 2.4% of CaCl_2 on the weight of cement, aged 1 day. (C) and (D) are of a C_3S paste, $w/c = 0.47$, aged 330 days.¹⁸

1.2 Capillary Pores

Fresh cement paste is mainly composed of hydration products of different phases, unhydrated cement grains, free water, capillary pores, gel pores and some other minor components. Capillary pores, the water-filled spaces in fresh cement paste, are the main suppliers of water for hydration. During hydration, most of the water added to dry cement is temporarily stored in the capillary pores until it reacts with cement grains. Capillary pores are part of the gross volume of concrete that has not been replaced by hydration products. The size of capillary pores in cement paste varies with water/cement ratio and degree of hydration.¹⁹ The size and distribution of these pores, in addition to interfacial cracks, constitute the microstructure of concrete or cement mortar, which determines concrete permeability as well as strength.²⁰ Capillary pores of highly saturated cement paste form an interconnected piping system distributed throughout the paste. This system makes the cement paste more permeable and thus more susceptible to deterioration under freezing and thawing cycles, and chemical attacks.²¹ Under prolonged curing, the degree of hydration increases with time and the hydration products continue to precipitate into the capillary space. As the newly formed hydration products grow in mass, they start to block the capillary piping system and finally reduce it to the capillary pore system.¹⁹ Further, the newly formed gels suck up the water from the capillary system. This suction of water reduces the capillary pores size.⁹ This indicates that strength and durability of cementitious materials can be reduced by further progress in cement hydration.

The unhydrated cement grains react with the water in the capillary pores to produce porous hydrate gels, having interstitial spaces called *gel pores*. Gel pores are filled with water sucked from the capillary pores. Gel pores are relatively smaller in size than capillary pores (Fig. 1.6). The water in gel pores is referred as *gel water*.¹⁹ The formation of hydrate gels depends on the availability of sufficient water for chemical reactions and for filling the gel pores that form after reactions. If the water is insufficient, gels form until the capillary pores dry up.¹⁹

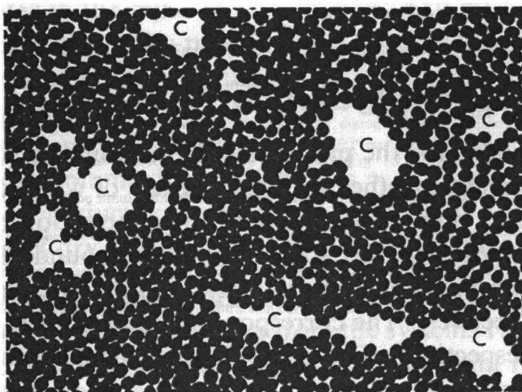


Fig. 1.6 - Pore size distribution in fresh cement paste. (C indicates capillary pores; the black spots are gels; and the spaces between them are gel pores).²²

Under sufficient water/cement ratio, a unit volume of cement produces about double of its size hydration products. At critical water/cement ratio, which is 1.2 by volume (0.4 by

weight), the hydration products fill up all the available space and no further reaction takes place. On the other hand, if sufficient water is added, a capillary pore space is created to keep the extra water.²³

Hydration gels have a limiting minimum size beyond which new particles are, due to insufficient space, unable to hydrate. If the water/cement ratio is low and no water movement is allowed during hydration, the gel pores do not get sufficient water and the capillary pores become empty. This is a phenomenon called self desiccation, where the hydration becomes very slow under the resulting low relative humidity, even though there is enough space available. Emptying the capillary pores can result in permanent change of the pore structure, which can affect the strength of the hardened paste. This demonstrates the necessity of providing sufficient water during curing.⁹ Compressive strength of concrete is adversely affected by its porosity (Fig. 1.7).²⁴ The weakening effect of pores can be simulated to that of tension cracks. These pores minimize the bond area between hydration products formed by interlocking. Further, for a given porosity, saturated cement pastes are weaker than dry ones. This is attributed to the fact that water molecules in pores weaken the forces of attraction between particles.⁹

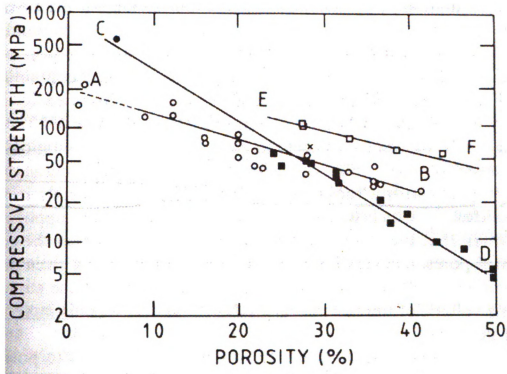


Fig. 1.7 - Relations between compressive strength (log scale) and porosity; data from various sources for Portland cement pastes cured at ordinary temperatures (open circles), hot pressed Portland cement paste (filled circle), autoclaved pastes of Portland cement, sometimes with added sulfur (filled square) and autoclaved pastes of Portland cement with 50% (open squares) or 30% (cross) of added fly ash.²⁴

Taking the total water porosity as the sum of capillary porosity and gel porosity, Powers and Brownyard have demonstrated (Table 1.1) that capillary and total water porosities decrease while gel porosity increases as hydration proceeds.²⁵

Table 1.1 - Calculated porosities based on the Powers-Brownyard model

w/c Ratio	Fraction of cement hydrated (α)	Capillary porosity	Gel porosity	Total water porosity
0.3	0.00	0.49	0.00	0.49
0.3	0.79	0.00	0.27	0.27
0.4	0.00	0.56	0.00	0.56
0.4	1.00	0.03	0.29	0.32
0.5	0.00	0.61	0.00	0.61
0.5	1.00	0.15	0.26	0.41
0.6	0.00	0.65	0.00	0.65
0.6	1.00	0.24	0.23	0.47

Capillary porosity affects the mechanical properties of cementitious products. The strength and modulus of elasticity of cement paste, for example, is inversely proportional to capillary porosity; they are related by the following formula:²⁶

$$E = E_o (1 - P_h)^3 \quad (1.1)$$

where, E = Elastic modulus; $E_o = E$ at zero porosity; and P_h = capillary porosity.

Unlike strength, modulus of elasticity is larger in saturated pastes than in dry ones. This is because the water infilling capillary pores cause an increase in stiffness.²⁷

1.3 Structure-Property Relationships of Cementitious Materials

Though concrete has many properties that need to be addressed during quality assurance, strength is the most common property used in the evaluation of concrete. The reason could be that strength can be measured conveniently, and most parameters which affect concrete strength also influence other major properties of concrete such as permeability and durability. Thus, concrete is generally formulated and produced to meet targeted strength requirements.

Concrete comprises different phases at various scales. These phases include hydrated cement paste and aggregates at macro-scale, interfacial transition zone, microcracks and capillary pores at micro-scale, and hydration products such as calcium silicate hydrate (C-S-H) at nano-scale. This complex composition of concrete makes the theoretical prediction of its mechanical and physical properties very complicated. Concrete is a quasi-brittle material and most of the theories applied in predicting the mechanical properties of brittle ceramics do not directly apply to concrete. The theories developed based on the nano-scale structure of concrete will have to be refined for application at micro- or macro-scales.

Lack of proper understanding of the concrete behavior under stress has led to predominantly empirical approaches to modeling of concrete. Empirical models are helpful, but may not provide comprehensive solutions that are generally applicable.

Given the porous nature of concrete, strength-porosity relationships have been emphasized in modeling of concrete performance. The Balshin model (Eqn. 1.2) is among the strength-porosity relationships commonly applied to concrete.⁴

$$\sigma = \sigma_0(1 - P)^A \quad (1.2)$$

where, σ_0 is compressive strength at zero porosity; and A is an empirical coefficient.

Ryshkewitch had conducted experimental investigations to study the influence of porosity on ceramic materials, and developed another empirical strength-porosity relationship (Eqn. 1.3).⁵ The Ryshkewitch model fits well to strength at high porosity, but tends to overestimate strength at relatively low porosities.⁶

$$\sigma = \sigma_0 e^{-\beta P} \quad (1.3)$$

where, σ_0 is compressive strength at zero porosity; and β is an empirical coefficient.

Another empirical strength-porosity relationship developed by Schiller (Eqn. 1.4) produces results comparable to those obtained with the Ryshkewitch model except for the extremes of porosity.⁷

$$\sigma = C \ln \frac{P_{CR}}{P} \quad (1.4)$$

where, P is porosity; P_{CR} is zero-strength porosity; and C is an empirical coefficient.

All above models have empirical parameters which depend on material properties. This makes the models material-specific, and experiments are required to determine those parameters for every new material. This limits the range of applicability of such models, and does not make them useful in exploratory development of new concrete materials. In the strength models of concrete, porosity is considered as a sole parameter affecting the property of concrete. New concrete materials, including those incorporating large volumes of coal fly ash, could refine the size distribution of capillary pores, thereby altering concrete strength while minimally changing its total porosity. A more fundamental approach to modeling of concrete is needed, which accounts for the interatomic interactions at nano-scale, capillary porosity and microcracks at micro-scale, and the effects of the interfacial transition zone at macro-scale.

With a more comprehensive understanding of concrete structure emerging, several theoretical models have been developed to predict the mechanical properties of concrete. However, most of these models account for micro- or macro-scale structure of concrete, but neglect the fundamental nano-scale features of the concrete structure. Some of the methods and theories applied in developing these models are described below.

Ortiz and Popov modeled concrete as a two phase composite material, composed of cement mortar and aggregates, by postulating the energy balance equation.⁸ First they modeled the performance of the two phases separately, and then combined them using the

mixture theory to get one model for the mechanical performance of concrete. Ortize accounted for the inelasticity of concrete in his model by applying the rate-independent model of distributed damage for mortar, and then the mixture theory to account for the composite nature of concrete.²⁸ Rezende has also used damage mechanics concepts to propose a rate-independent constitutive theory for the inelastic behavior of concrete, considering shear and hydrostatic tension damages as the basic damage mechanisms.²⁹ Nerma et. al. has developed a model for the behavior of concrete under load based on micromechanics. They modeled concrete at macro-scale, where it was considered as a two-phase composite material composed of cement mortar and aggregates.³⁰

Past efforts to model the properties of concrete and other cementitious materials have been largely empirical. There are, however, some efforts reported to develop models which predict concrete properties based on its basic structure. Mattei et. Al. developed a multi-scale model for the mechanical properties of concrete based on physical interactions between various phases present in concrete structure. Concrete is modeled here as a two-phase material comprising mortar and coarse aggregate, with mortar comprising, in turn, of cement paste (with microcracks and pores) and fine aggregates. This model is oriented toward prediction of the constitutive (stress-strain) behavior of concrete, and considers the loss of stiffness resulting from crack propagation in concrete. The cracks are assumed to occur at aggregate interfaces prior to loading, and to propagate first at the interface and then into the mortar phase under load. Fine aspects of the concrete structure, including the micro-structure of capillary pore system, and the nano-

and micro-structures of hydration products (calcium silicate hydrate, calcium hydroxide, etc.) are not considered in this model.

1.4 Fly Ash

1.4.1 Types and Trends in Quality of Fly Ash

Pozzolana refers to naturally occurring or artificially produced materials which contains highly reactive silica. These materials are not cementitious, but they have compounds which produce cementitious products upon reaction with other compounds from different sources. To get a stable cementitious compound, the pozzolana has to be divided finely and reacted in the presence of water. The reactivity of pozzolanas depends partly on the shape and fineness of its particles. Pozzolanas of amorphous (glassy) silica react more readily than those of crystalline ones.¹⁹

Fly Ash, the pulverized-fuel ash, is the most common artificial pozzolana obtained from the coal used in power stations at combustion temperatures of about 1000 °C.³¹ Fly ash is different from the ash that collects at the bottom of furnace (bottom ash). Due to their spherical shape and fineness, fly ash particles have large surface areas which allow them to react readily.¹⁹ The chemical properties of fly ash depend on the mineral content of coal and the burning condition in power station.⁹ According to ASTM C 618-94a, fly ash is classified based on the type and source of coal. Class F fly ash, the most commonly available which is mainly siliceous, originates from bituminous coal and anthracite. The

other type, Class C fly ash, has high lime content and originates from sub-bituminous coal and lignite. The latter has more CaO content than the former, and is hydraulic.¹⁹

The cementitious property of Class C fly ash increases with the rise in CaO content. With 10% to 20% of CaO content, Class C fly ash acts as cementitious and pozzolanic materials, respectively; more than 20% of CaO content makes the ash more cementitious.³² The reason for Class C fly ash, at high lime content, to become cementitious is that lime can react with the silica and alumina constituents of ash in the presence of water. Class C fly ash has lower carbon content than Class F, and its fineness is higher. Class C fly ash is not as popular as Class F in the construction industry. The reason could be that the lime and sulfur constituents of ash might have a detrimental effect in concrete.³³

1.4.2 Effect of Fly Ash on Chemistry of Cement Hydration and Cement Hydration Products

Fly ash, as mentioned above, is not cementitious as such; it can be classified under latent hydraulic materials, and is always used in conjunction with Portland cement. During cement hydration, the silica portion of fly ash readily reacts with the calcium hydroxide (CH), precipitating from the hydration process, to produce a cementitious material (calcium silicate hydrate). Fly ash can be blended with Portland cement or added to it even during mixing of concrete.¹⁹

Fly ash, particularly Class F, is relatively slow to react during early stages of reaction. It starts to react more intensely almost a week after the initial mixing. This has been explained by the observation that fly ash becomes stimulated to react when the alkalinity of pore solution increases.³⁴ The rise in alkalinity is achieved by the concentration of alkaline products of Portland cement hydration. Therefore, fly ash has to wait until this favorable condition is created.¹⁹ When the alkalinity of pore solution reaches its required level, fly ash particles start to react with the calcium hydroxide produced from hydration of Portland cement. This reaction takes place on the surface of fly ash particles which retain their original spherical shape for some time.

Pozzolanic cements, mostly Class F fly ash, have generally low early strength. They are low heat cements, and resist sulfate and weak acid attacks on concrete. Fly ash reacts with the calcium hydroxide produced from hydration of Portland cement. This process reduces the level of calcium hydroxide, and there will remain limited calcium hydroxide to react with sulfate to produce ettringite, which is the cause for sulfate attack.¹⁹

Fly ash concrete absorbs more water, proportional to the fly ash content, than ordinary Portland cement concrete. This is due to the slow reaction resulting from its pozzolanic property. Therefore, to achieve the desired effect of fly ash, sufficient curing is necessary.¹⁹

Fly ash concrete demonstrates good workability as compared to Portland cement concrete. This is attributed to the spherical shape of fly ash particles which reduce

viscosity (Fig. 1.8). In Portland cement, under low water/cement ratio and with the precipitation of new hydration products, the cement past becomes stiff and cement particles get packed. This may increase the viscosity of the paste because of increased surface friction, and particle interlocking resulting from the irregular shape of the cement particles (Fig. 1.9). Unlike Portland cement particles, fly ash particles have spherical shape which renders less problem of particle interlocking and surface friction. This property of fly ash helps in increasing the workability of concrete at low water/cement ratio. The amount of fly ash required to deal with such problems is only about 20% by mass.¹⁹

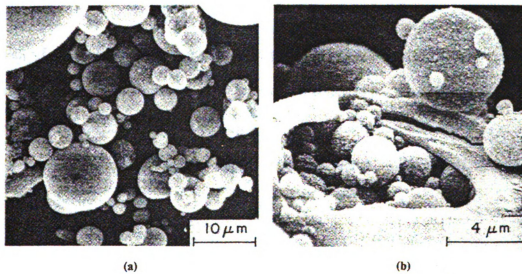


Fig. 1.8 - Typical Class F fly ash: (a) spherical and glassy particles; (b) a Plerospher³⁵



Fig. 1.9 - Cement Particles³⁶

Fly ash, of a definite amount, contributes to the later age strength of concrete. Some of the main factors which contribute to the strength of concrete are the stiffness of the paste and the paste-aggregate bond. For a given water/cement ratio, the stiffness of the past can increase when more hydration products, from pozzolanic reaction, diffuse into and minimize capillary pores.³⁷

1.4.3 Effect of Fly Ash on Capillary Pore System

The pozzolanic activity of fly ash starts when the pore water alkalinity is increased. This level of alkalinity is reached through the accumulation of calcium hydroxide, produced from hydration of cement, in the pore water. This level triggers the reaction of calcium hydroxide with the silica part of the fly ash to give off new hydration products. Over

time, the accumulated reaction products diffuse into the capillary pores and result in narrowing of the capillary system (Figs. 1.10 and 1.11).³⁴

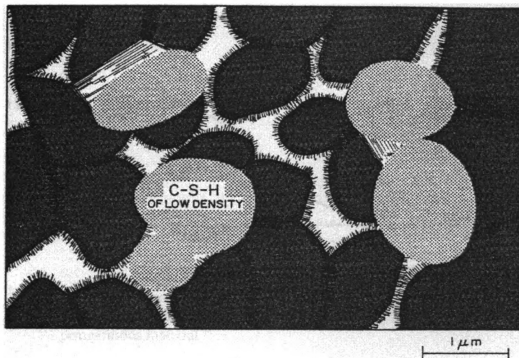


Fig. 1.10 - Diagrammatic representation of well-hydrated cement pastes made with a Portland pozzolana cement. As compared to Fig. 1.2, the capillary voids are either eliminated or reduced due to the pozzolanic reaction³⁵

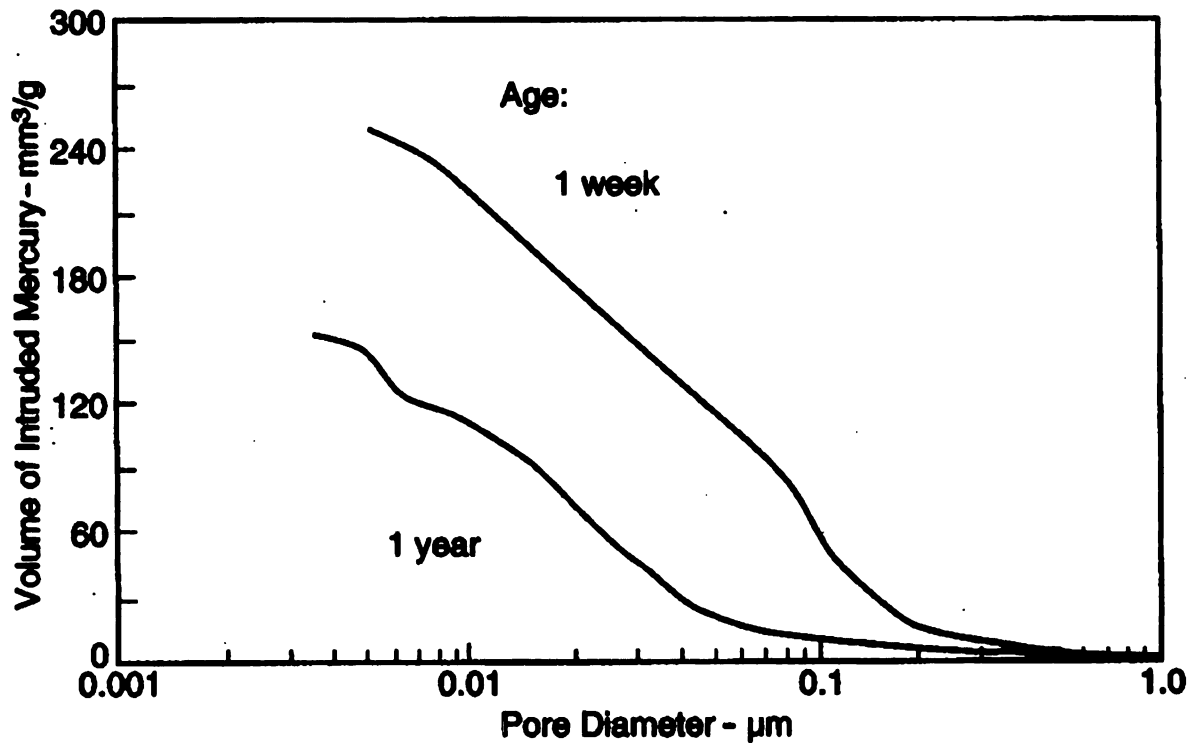


Fig. 1.11 - Change in pore size distribution (determined by mercury porosimetry) in cement paste containing 30% of Class F fly ash by mass of total cementitious material ³⁴

Portland cement concrete with high water/cement ratio has a network of capillary pore water. These interconnected pipes act as open channel for bleeding of concrete and upon setting they retain a tube like structure which increases the permeability of concrete. This phenomenon is considerably reduces in the presence of fly ash. The newly formed C-S-H, from the pozzolanic activity, start to fill up the capillary pores and even block the channel; the capillary piping system becomes discrete and small pores.³⁸ The concrete then gains impermeability and strength as a result of this pozzolanic activity.³⁹

1.4.4 Air-Entrainment of Concrete with Fly Ash

Freezing and thawing are the weather-induced problems which adversely affect the performance of concrete, especially when it is saturated, unless concrete is properly designed to account for such deteriorating effects. The performance of concrete against frost action can be improved when the following conditions are fulfilled: (1) the presence of uniformly distributed entrained air; (2) use of coarse aggregates which are sound; and (3) protecting concrete against frost until it acquires certain strength.⁴⁰

Air-entrainment of concrete is done during mixing by adding a certain amount of an air-entraining admixture required to give the desired volume, size and distribution of air bubbles, with the dispersion of air bubbles remaining unaffected by the process of transportation, placement and upon hardening of concrete.⁴⁰

The range of adsorption of air-entraining admixtures depends on the carbon content, organic matter content and loss-on-ignition of fly ash. Concrete containing Class C fly ash requires less air-entraining admixture, and loses less entrained air when compared with concrete containing Class F fly ash. This could be attributed to Class C fly ash having low carbon and high lime contents. The higher the alkaline content, the lower would be air-entraining admixture requirement. Concrete containing Class F fly ash loses about 59% of the total entrained air in about 90 minutes after mix preparation. Therefore, the loss of entrained air is proportional to the demand for air-entraining

admixtures.⁴¹ The excessive demand for air-entraining admixtures can be minimized by deactivating the carbon content by exposing fly ash to certain chemicals such as chlorine gas, calcium hypochlorite and surfactants.⁴²

The amount of air-entraining admixtures required in fly ash concrete is higher when compared with normal cement concrete. This is attributed to the carbon present in fly ash, which adsorbs the air-entraining agent. The degree of adsorption by carbon depends on its surface area, type, and polarity. High-carbon-content fly ash disrupts the air entrainment process by adsorbing some air-entraining agents within porous carbon particles.¹⁹ The performance of air-entrained concrete against freezing and thawing has a direct relation with the amount of fly ash present in concrete. Concrete comprising up to 20% Class C fly ash as replacement for cement demonstrates acceptable performance against freezing and thawing, as far as the desired size and distribution of air bubbles are entrained after satisfying the demand of the fly ash carbon. As the fly ash content increases, the durability of concrete, with respect to frost action, reduces. Concrete with 50% Class C fly ash replacement demonstrated scaling problems after 400 cycles of freezing and thawing.⁴³ Further, Virtanen has concluded that the addition of fly ash, to a certain extent, has no considerable effect on the performance of concrete against freezing and thawing, as far as the strength and the air content are maintained.⁴⁴ However, Brown et al. suggested that, owing to the later age strength development, the performance of blended cement concrete has to be evaluated after a prolonged curing period. Blended cements have demonstrated higher resistance against freezing and thawing than ordinary

cement concrete. This is attributed to the higher strength gained at later age due to pozzolanic action.⁴⁵

1.4.5 Effects of High Fly Ash Volumes on Engineering Properties of Concrete

Fly ash, as discussed in the preceding chapters, has many advantages when used as a cement replacement. It improves the workability and strength of concrete. Due to its spherical shape, fly ash reduces the water demand of fresh concrete for improved workability, which results in changed structure and properties of concrete. This occurs because the products of the pozzolanic reaction diffuse into the capillary pores.¹⁹ The effect of fly ash on concrete properties depend on the amount of fly ash utilized. The optimum fly ash content depends on the particular performance gains desired.

1.4.6 Effect of High Fly Ash Volumes on Hydration of Cement

Generally, fly ash does not react with water as such. It reacts, after 3 to 7 days of hydration, with calcium hydroxide, which precipitates from the hydration of Portland cement. Theoretically, high-volume fly ash concrete needs prolonged curing periods to fully complete the hydration process. However, after about 91 days, still unreacted calcium hydroxide and fly ash exist in the hardened cement paste.⁴⁶ One may thus consider high-volume fly ash cement paste as a composite material with unreacted ash particles behaving as reactive micro-aggregates.⁴⁷ Table 1.2 shows the degree of reaction of fly ash at various volumes with different water/binder ratios of different curing periods. At the age of 7 days, about 5% of fly ash has started to react.⁴⁸ This is attributed

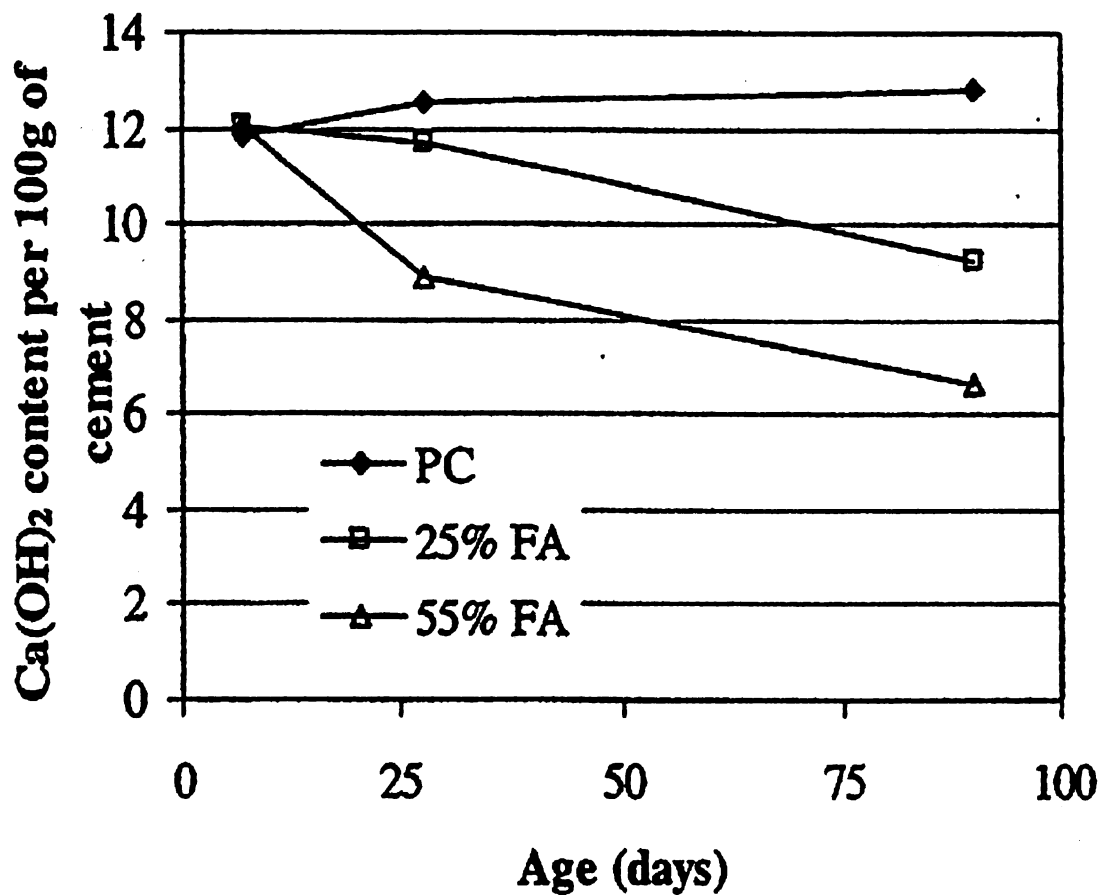
to either the initial reaction of fly ash, or to the reason that at early age fly ash particles are involved in the formation of ettringite.⁴⁹

Table 1.2 - Degree of reaction of fly ash in fly ash concrete pastes⁴⁸

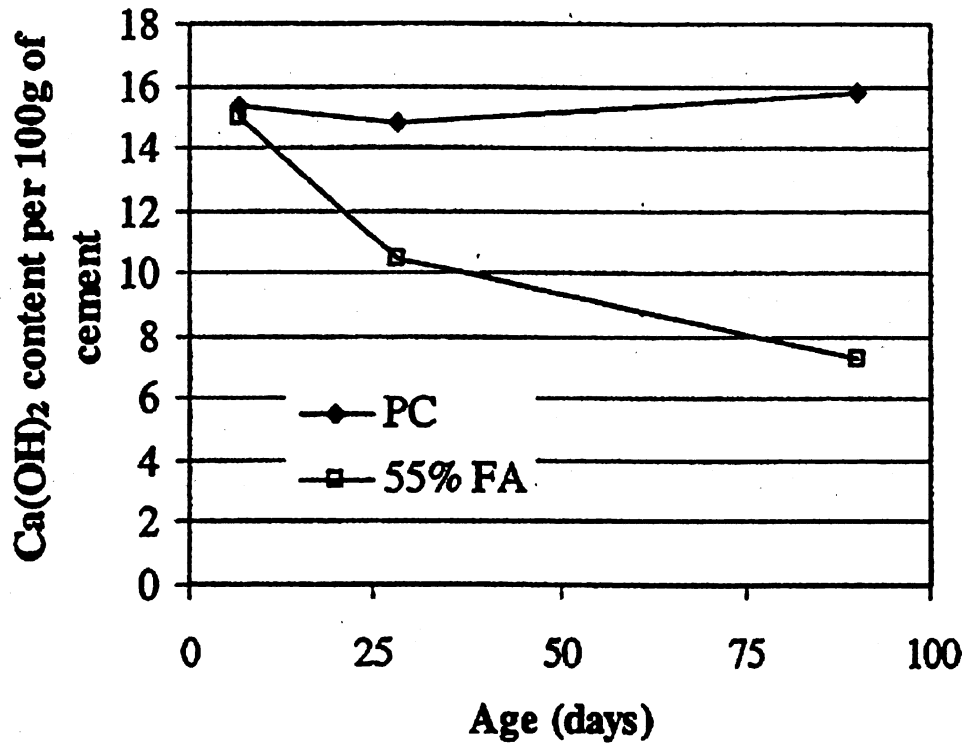
w/b	Fly ash replacement (%)	Degree of reaction (%)		
		7 days	28 days	90 days
0.19	25	5.09	13.71	17.54
	45	4.85	10.84	14.8
0.24	25	5.65	13.94	22.56
	45	5.28	12.81	16.45
0.30	25	6.67	14.41	24.58
	55	4.98	11.21	17.03
0.50	25	6.40	12.23	29.52
	55	5.26	9.82	19.41

The reduction in degree of reaction with high-volume fly ash replacement of cement, as in Table 1.2, is attributed to the low calcium ion concentration in pore water, resulting from the high replacement of cement with fly ash. Another factor could also be that the high water/binder ratio dilutes the calcium ion concentration in pore water and reduces the contact between particles. Therefore, high-volume fly ash concrete needs prolonged curing to overcome all these problems at a later age and provide the required strength.⁵⁰

The degree of hydration of Portland cement can be known from the amount of calcium hydroxide precipitated. The same approach can not be applied in the case of cement partially replaced by with fly ash. The reason is that calcium hydroxide also reacts with fly ash. However, from the level of calcium hydroxide in cement paste, the rate of hydration of fly ash can be estimated. During the period from 7 to 28 days of age, about 14 % of fly ash particles react with calcium hydroxide.⁴⁹ Fig. 1.12 demonstrates that the rate of reaction of fly ash cement can be obtained from the reduction in calcium hydroxide concentration of paste.⁵⁰



(a)



(b)

Fig. 1.12 - Ca(OH)₂ content relative to the cement content in PC and FC pastes (based on ignited weight). (a) w/b = 0.3, and (b) w/b = 0.5⁴⁹

1.4.7 Effect of High Fly Ash Volumes on Strength of Concrete

High-volume fly ash concrete is an ideal construction material from the economic point of view. It replaces large amounts of cement which consumes substantial amounts of energy for its manufacturing. When used in high strength concrete, fly ash reduces the demand for admixtures. However, there may be limits on the volume of fly ash replacing cement if certain combinations of properties are to be provided. As mentioned above, reaction of fly ash depends on the presence of calcium hydroxide. If the cement

replacement is too much, there will not be enough cement left to produce calcium hydroxide for fly ash to react. The strength of fly ash concrete, at a given age, depends on the degree of hydration. The degree of hydration also depends on other factors including gel/space ratio.⁵¹ The low early strength of high-volume fly ash cement is partly due to the rise in net water/cement ratio resulting from the high-volume replacement of cement with fly ash.⁵² At the later stages of hydration, when hydration products precipitate on the surface of fly ash particles, the pozzolanic activity of fly ash increases the bond strength between fly ash and cement particles. This makes the paste more homogenous, and increases the stiffness of paste, which contributes to the increment in concrete strength.⁵⁰ For strength gain, more hydration should take place. If there is limited pore space, the hydration process slows down because when the pore spaces are filled with gel.²³ The other advantage of high-volume fly ash is that it increases the strength of the bond between particles and reduces the negative side effects of calcium hydroxide by consuming it.⁵¹

High-volume replacement of with fly ash (e.g. 50% replacement) has yielded desirable fresh mix workability providing relatively good strength increment at 28 days.⁵³ Water/binder ratio affects the impact of high-volume fly ash replacement on concrete strength. The early strength of high-volume fly ash concrete is less adversely affected by lower water/binder ratio than by higher water/binder ratio.⁴⁸

The effect of high-volume fly ash replacement of cement on the compressive strength of cement mortar is different than for concrete. Generally, higher strengths are achieved in

concrete than in mortar. This is attributed to the effect of fly ash on improving the interfacial bond between the cement matrix and aggregates.⁴⁸

Class C fly ash, despite its high lime and sulfate contents which can adversely influence concrete properties, increases the early strength of concrete. It yields desirable levels of strength when used as cement replacement (30%) and also as aggregate (50% by weight of cement). However, the ettringite formation problem has to be studied.³⁶

CHAPTER 2

MECHANICAL MODELS OF HYDRATED CEMENT PASTE

2.1 Introduction

Hydrated cement paste is a complex composite material with multiple phases at micro- and nano-scales. These features complicate development of structure-property relationships for hydrated cement paste. Several empirical structure-property relationships have been developed for hydrated cement paste based on laboratory experiments.^{4, 5} Computational tools are also used toward modeling of hydrated cement paste.

The multi-phase nature of hydrated cement paste at different scales distinguishes it from technical ceramics. Unlike most ceramics, hydrated cement paste does not fracture in a brittle mode. It is heterogeneous at micro-scale, where capillary pores, large CH crystals and shrinkage microcracks are distributed randomly. The presence of these capillary pores and microcracks produces stress concentrations which weaken the strength and stiffness of material, but also contributes to the fracture toughness of hydrated cement paste through arrest and deflection of microcracks, formation of microcrack processing zone, and frictional energy dissipation during pull-out of calcium hydroxide crystals.

These phenomena render hydrated cement paste semi-brittle with some level of ductility and energy absorption capacity.

This paper presents analytical models for the mechanical performance of hydrated cement paste. The models incorporate intermolecular interactions between nano-scale C-S-H particles, effects of capillary pores and microcracks, and frictional pull-out of calcium hydroxide micro-scale platelets.

The models for hydrated cement paste are developed in two steps. The first step focuses on compact hydrated cement paste free from capillary pores and microcracks (henceforth referred as “compact hydrated cement paste”), and the second step incorporates the effects of capillary pores and microcracks into the models developed for compact hydrated cement paste.

2.2 Hydrated Cement Paste Free from Capillary Pores and Microcracks (Compact Hydrated Cement Paste)

2.2.1 Molecular Interactions between C-S-H Particles

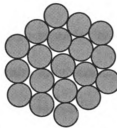
Mechanical models for compact hydrated cement paste were first developed based on phase interactions at molecular level. These models were later modified by introducing the effects of capillary pores and microcracks for application to hydrated cement paste with these micro-defects. This section focuses on compact hydrated cement paste.

The interactions between nano-scale calcium silicate hydrate (C-S-H) particles play key roles in determining the mechanical properties of hydrated cement paste.⁵⁴ C-S-H particles are non-crystalline hydration products with large surface areas which enhance their bonding to each other and to other particles within their reach through van der Waals interactions. Therefore, C-S-H plays a predominant role in rendering hydrated cement paste its cementitious properties.⁵⁵

Given the significant binding role of C-S-H particles, the first step in theoretical modeling focused on the morphology and structural arrangement of C-S-H particles in order to determine the bond strength between them. Research toward determination of the detailed morphology of C-S-H is still in progress. C-S-H has been likened by several researchers to Tobermorite mineral because of their similar compositions.⁵⁶ Although C-S-H particles grow to have a size of approximately $60 \times 30 \times 5 \text{ nm}^3$, they have been modeled as an agglomeration of unit particles making a spherical globule.⁵⁷ This geometrical modeling was adopted in the research repeated herein. An agglomeration of basic C-S-H units is assumed to make a spherical C-S-H particles (globule) with diameter ranging from 6 to 8 nm (Fig. 2.1).⁵⁸ Due to the availability of water and space, the C-S-H particles which form at the outer part of hydrating cement grain have lower density than the ones which form at the inner part. A low density C-S-H is assumed to be an agglomeration of globules bonding to each other and having a gel porosity of about 28% (of the globule volume).⁵⁷



(a) Single C-S-H globule



(b) Agglomeration of globules

Fig. 2.1 - C-S-H morphology and geometric arrangement

The bonding between C-S-H globules involves van der waals interactions caused by weak physical electrostatic attractions between molecules in neighboring globules. The van der waals force per unit area (F_{vdw}) between two flat surfaces separated by a distance d can be expressed as follows:⁵⁹

$$F_{vdw} = \frac{3 h_w}{16 \pi^2 d^3} \quad (2.1)$$

where, h_w is the dielectric constant, approximately 10eV or 1.6022×10^{-18} J for C-S-H,⁵⁹ d is the clear distance between two C-S-H globules.

This equation can be applied to C-S-H globules as far as an effective (circular) area is used with d taken as the minimum distance between two C-S-H globules (0.18 to 0.32 nm).⁵⁵

Substituting the above values into Eqn. 2.1 gives a van der waals bond strength between two adjacent C-S-H globules of 0.93 to 5.22 GPa, depending upon the size and spacing of globules. The effective area of adjacent globules over which this stress operates will be presented later in discussions on fracture toughness.

2.2.2 Modulus of Elasticity of Compact Hydrated Cement Paste (E_c)

The modulus of elasticity of compact hydrated cement paste was determined by considering the effect of relative movement of neighboring C-S-H globules against the resistance of the bond strength between them. The relationship between the theoretical cohesive stress (σ_{\max}) required to debond two C-S-H globules at a distance d from each other, the corresponding modulus of elasticity (E) and the minimum surface energy (γ_s), developed by Mindess et al.²⁰ was applied to approximate the modulus of elasticity of compact hydrated cement paste (Eqn. 2.2).

A typical curve representing the energy interaction between two C-S-H globules as a function of their separation is shown in Fig. 2.2(a).⁶⁰ The minimum energy state is obtained at the equilibrium distance between two particles (b_0). The minimum energy required to separate two physically bonded surfaces is twice the surface energy, γ_s . The

force-displacement curve shown in Fig. 2.2(b) is obtained by differentiating the curve in Fig. 2.2(a). The modulus of elasticity of the two bonded C-S-H globules can be estimated from the initial curve in Fig. 2.2(b). The force-displacement curve can be transformed into the stress-strain curve as shown in Fig. 2.3.⁶⁰ Approximating the stress-strain curve by a half sine curve, the total energy required to separate two surfaces, $2\gamma_s$, can be calculated as the area under the curve, and the initial slope is modulus of elasticity, E_o . According to Mindess et al.,⁶⁰ the relationship between maximum tensile strength, σ_{max} and modulus of elasticity, E_o , can be approximated based on the energy interactions stated above.

Stress, varying as a sine function of x , can be expressed as:

$$\sigma = \sigma_{\max} \sin \frac{2\pi x}{\lambda} \quad (2.2)$$

The energy required to cause fracture can be calculated as:

$$2\gamma_s = \int_0^{\lambda/2} \sigma_{\max} \sin \frac{2\pi x}{\lambda} dx = \frac{\lambda \sigma_{\max}}{\pi} \quad (2.3)$$

Applying Hook's law for small displacements,

$$\sigma = E \varepsilon = E \frac{x}{b_0} \quad (2.4)$$

Taking $\sin x \approx x$ for small angles, and substituting Eqns. 2.2 into 2.4 yields:

$$\sigma_{\max} = \frac{\lambda E}{2 \pi b_0} \quad (2.5)$$

Equating Eqns. 2.3 and 2.5 yields:

$$\sigma_{\max} = \left(\frac{E \gamma_s}{b_0} \right)^{1/2} \quad (2.6)$$

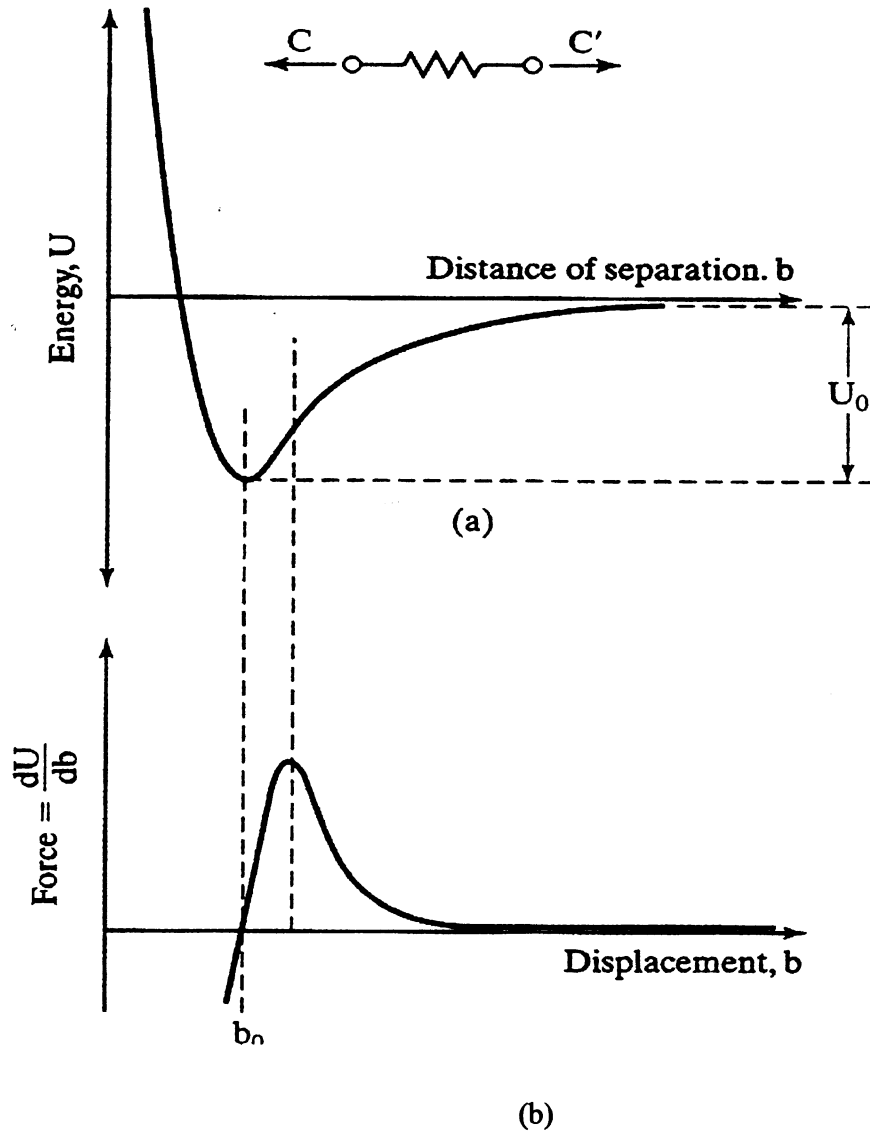


Fig. 2.2 - (a) Bonding energy as a function of the distance of separation; (b) force-displacement curve⁶⁰

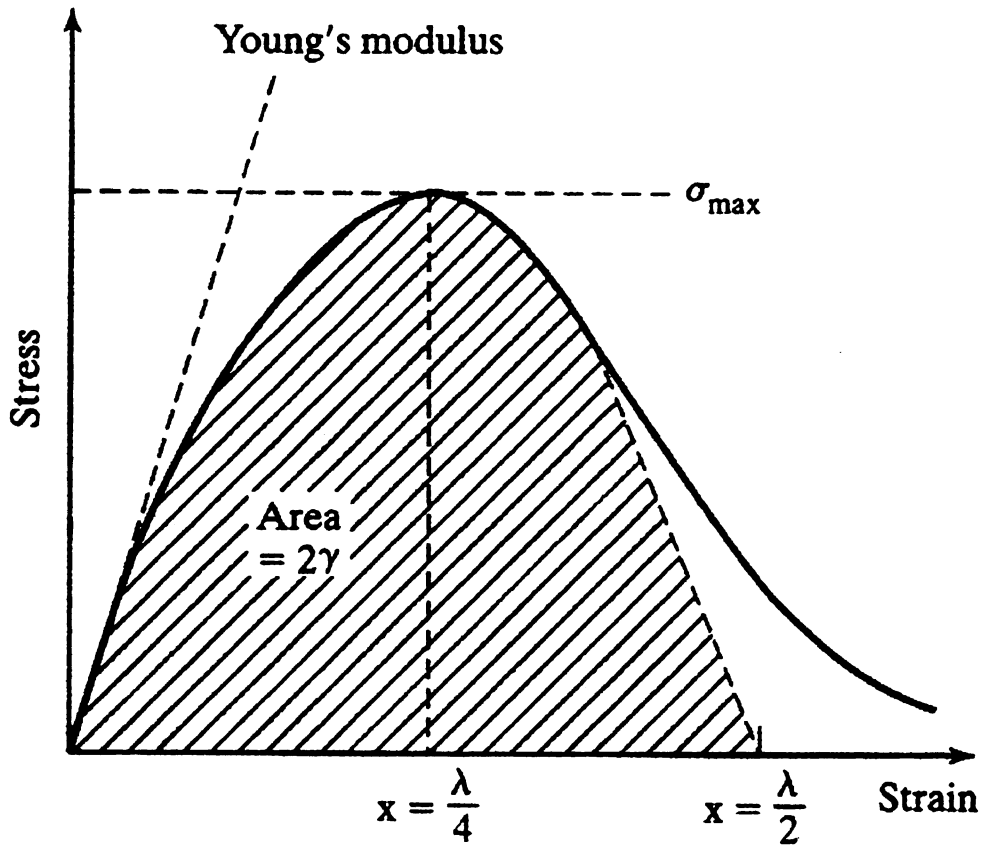


Fig. 2.3 - Stress-strain curve approximated as a half sine wave ⁶⁰

The elastic modulus can thus be determined from the stress-strain relationship between C-S-H globules, as shown above. This relationship can be reasonably approximated to be about $E_o/10$ for cohesive solids.⁶¹ Therefore, the relationship between bond strength and the intrinsic modulus of elasticity was approximated as follows:

$$E_o \approx 10 \sigma_{\max} \tag{2.7}$$

where, σ_{\max} is the bond strength between particles under consideration, that is F_{vdw} (the van der Waals force per unit area); the relationship thus becomes:

$$E_o \approx 10 F_{vdw} \quad (2.8)$$

Substituting the values of F_{vdw} derived earlier into Eqn. 2.8 yields the values of E_o , which range from 9.3 to 52.2 GPa, depending upon the size and spacing of C-S-H globules (Table 2.1). The bond strength and modulus of elasticity of compact hydrated cement paste are influenced strongly by the distance between the C-S-H globules, irrespective of their sizes, as shown in Table 2.1.

Table 2.1 - Effects of the distance between C-S-H globules on bond strength and modulus of elasticity of compact hydrated cement paste free from capillary pores and microcracks.

Diameter of C-S-H globules dg (m)	Distance between C-S-H globules d (m)	Bond stress between globules F_{vdw} (Pa)	Modulus of Elasticity E_o (Pa)
6.00E-09	1.80E-10	5.22E+09	5.22E+10
	2.00E-10	3.80E+09	3.80E+10
	3.20E-10	9.29E+08	9.29E+09
8.00E-09	1.80E-10	5.22E+09	5.22E+10
	2.00E-10	3.80E+09	3.80E+10
	3.20E-10	9.29E+08	9.29E+09

Fr

un

CF

(se

to

nar

ene

the

2.2

The

H g

Wa

2.2.3 Fracture Toughness of Compact Hydrated Cement Paste (G_o)

Fracture toughness of compact hydrated cement paste is defined here as the energy per unit crack area dissipated in the process of breaking C-S-H/C-S-H bonds and pull-out of CH crystals. The latter was found to be the major contributor to the fracture toughness (see the following sections). The energy dissipation mechanism in CH pull-out is related to friction at nano-level. The frictional stress was thus treated as phononic friction at nano-scale.⁵⁹ The total intrinsic fracture toughness (G_o) was taken as the sum of the energy dissipated due to C-S-H/C-S-H debonding and frictional CH pull-out; however, the contribution from the former is relatively insignificant.

2.2.3.1 Fracture Toughness Due to Debonding Between C-S-H Globules (G_d)

The fracture toughness contributed by the rupture of interatomic bonds between two C-S-H globules was determined using an equation which relates fracture toughness to van der Waals strength as shown below.⁵⁹

$$F_{vdw} = \left(\frac{3G_d}{2\pi^2 k^2 R_g} \right)^{\frac{1}{3}} \quad (2.9)$$

where, R_g is the radius of C-S-H globule (ranges between 3 and 4 nm); F_{vdw} was found earlier to range from 0.93 to 5.22 GPa (Table 2.1); and

$$k = \frac{1.5(1 - \nu^2)}{E_o} \quad (2.10)$$

where, E_o is intrinsic modulus of elasticity; and ν is Poisson's ratio (~ 0.2) of compact hydrated cement paste.

In the above model, R_g and F_{vdw} are independent variables which can vary over a range; a parametric study was conducted in order to assess the significance of their effects on the fracture toughness model. The parameters calculated for arriving at the G_d value (fracture toughness due to C-S-H/C-S-H debonding) are presented in Table 2.2. The variations of G_d with the radius of C-S-H globule (R_g) and the bond strength (F_{vdw}) for compact hydrated cement paste is summarized in Table 2.3.

Table 2.2 - Calculation of the fracture toughness (due to debonding of C-S-H globules) of compact hydrated cement paste free from capillary pores and microcracks.

d_g (m)	d (m)	F_{vdw} (Pa)	E_o (Pa)	k	G_d (J/m ²)
6.00E-09	1.80E-10	5.22E+09	5.22E+10	2.76E-11	2.14
	2.50E-10	1.95E+09	1.95E+10	7.39E-11	0.80
	3.20E-10	9.29E+08	9.29E+09	1.55E-10	0.38
8.00E-09	1.80E-10	5.22E+09	5.22E+10	2.76E-11	2.85
	2.00E-10	3.80E+09	3.80E+10	3.78E-11	2.08
	3.20E-10	9.29E+08	9.29E+09	1.55E-10	0.51

Table 2.3 - Summary of the variations of the fracture toughness due to C-S-H/C-S-H debonding, (G_d) in J/m², with radius of globules, R_g , and F_{vdw} .

		F_{vdw} (GPa)						
		0.93	1.0	2.0	3.0	4.0	5.0	5.22
Radius of globule, R_g (nm)	3.0	0.38	0.41	0.82	1.23	1.64	2.05	2.14
	3.2	0.41	0.44	0.87	1.31	1.75	2.18	2.28
	3.4	0.43	0.46	0.93	1.39	1.86	2.32	2.42
	3.6	0.46	0.49	0.98	1.47	1.96	2.46	2.56
	3.8	0.48	0.52	1.04	1.56	2.07	2.59	2.71
	4.0	0.51	0.55	1.09	1.64	2.18	2.73	2.85

It can be observed from Table 2.3 that the maximum contribution of C-S-H/C-S-H debonding to the fracture toughness of compact hydrated cement paste is 2.85 J/m²,

which is quite small when compared with the contribution of CH pull-out (see next section). Hence, the variations in the C-S-H/C-S-H debonding contributions (resulting from changes in different parameters) to fracture toughness are not practically significant.

2.2.3.2. Fracture Toughness Due to CH Crystal Pull-Out (G_p)

CH crystals make about 20-25 % by volume of the hydration product in hydrated cement paste;⁶² they are generally hexagonal in shape (Fig. 2.4).⁶³ The width of CH crystals in hydrated cement paste ranges from 1000 to 10,000 nm, and their thickness from 220 to 260 nm.^{64, 65} Frictional pull-out of CH plates from hydrated cement paste is another factor contributing to the fracture toughness of hydrated cement paste. For ease of computation, CH plates were assumed to be circular (instead of hexagonal). The contribution of CH pull-out to fracture toughness represents the energy dissipated in the form of heat due to phononic friction (associated with atomic vibration) between the surfaces of CH crystals and the C-S-H nanoparticles.⁶⁶ This frictional energy dissipation during pull-out of CH crystals depends on the orientation of the CH crystals relative to the direction of loading. The maximum and minimum energy dissipations occur when the flat surface of CH crystal is at an angle with and perpendicular to the direction of loading, respectively. Therefore, a vertical CH orientation, with its flat surface parallel to the direction of loading (Fig. 2.5), is assumed to account for the random orientation of CH crystals in hydrated cement paste.

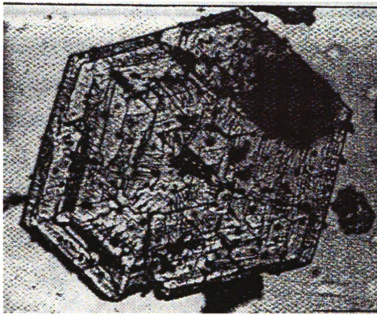


Fig. 2.4 - Hexagonal CH crystal ⁶³

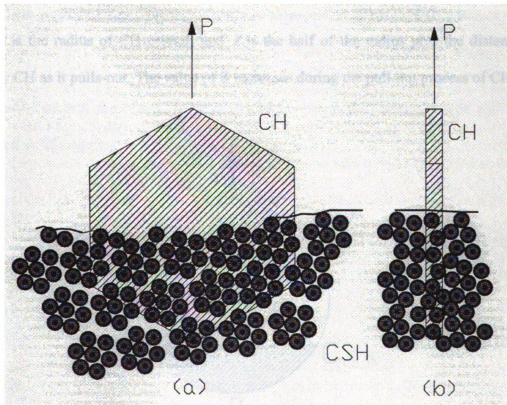


Fig. 2.5 - CH orientation with flat surface parallel to the direction of loading
(a) side view (b) front view

The portion of the width (diameter) of a single CH crystal which could be subjected to phononic friction as the CH pulls out from a cluster of C-S-H globules ranges between 0 and 0.5 (of the width). Therefore, a quarter of the diameter of CH crystals was assumed to be subject to phononic friction for the purpose of estimating an average CH pull-out length. The part of CH crystal cross-section subjected to frictional pull-out is a segment bound by a chord 0.5R away from the center of the circle as shown in Fig. 2.6. The area of this segment (A_s) can be obtained as the difference between the OABC and the OAC areas.

$$A_s = 2R^2 \cos^{-1}\left(\frac{Z}{R}\right) - Z\sqrt{R^2 - Z^2} \quad (2.11)$$

where, R is the radius of CH crystal; and Z is the half of the radius plus the distance moved by CH as it pulls-out. The value of Z increases during the pull-out process of CH.

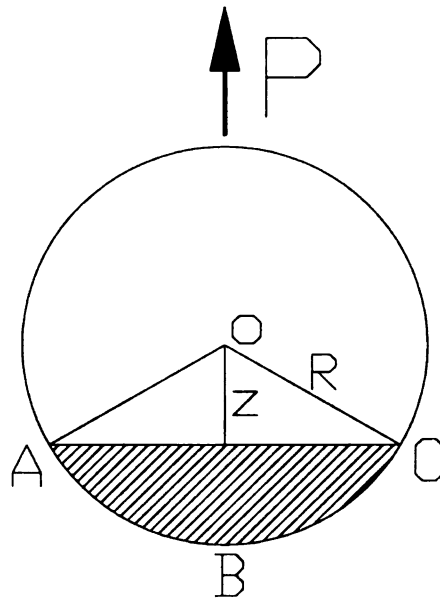


Fig. 2.6 - Schematic model of CH pull-out

The actual contact area between spherical C-S-H globules and the flat surface of circular CH crystal in compact hydrated cement paste was determined based on the assumed morphology and structural arrangement of C-S-H globules (Fig. 2.7).

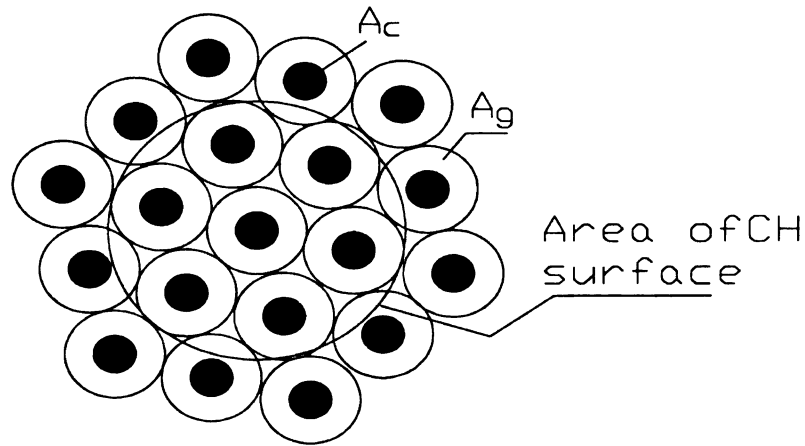


Fig. 2.7 - Schematics of the effective contact area between CH crystal and C-S-H globules

The effective contact area (A_c) subjected to bond energy (G_d) per unit area can be determined as follows:⁵⁹

$$A_c = \pi r_c^2 \quad (2.12)$$

$$r_c = \left(1.5\pi k R_g^2 G_d\right)^{1/3} \quad (2.13)$$

where, R_g is the radius of the C-S-H globule.

The values of r_c and A_c range from 1.4 to 1.8 nm and 5.8 to 10 nm², respectively. The total effective contact area of all C-S-H globules contacting both faces of a single CH crystal can thus be calculated as follows:

$$A_{ECH} = 0.8 \frac{A_c}{A_g} A_s \quad (2.14)$$

where, A_g is the projected area of a C-S-H globule.

The value of A_{ECH} calculated above ranges from 5.15 to 0.00515 nm², as shown in Table 2.4. Eqn. 2.14 is multiplied by 0.8 to account for gel porosity.

The next step was to determine the frictional force acting on the CH surface as it pulls out. For the atomically sharp surfaces of CH crystals, nano-scale phononic friction dominates, where collision of vibrating molecules as two flat surfaces slide against each other dissipate energy in the form of heat. The phononic frictional stress (τ_f) associated with CH pull-out can be estimated at about 1 GPa.⁶⁷

The frictional force (F_f , newtons) due to phononic friction can be computed as the effective area of CH subjected to frictional pull-out (A_{ECH} , m²) times the phononic friction stress acting on it:

$$F_f = \tau_f A_{ECH} = 1 \times 10^9 \times A_{ECH} \quad (2.15)$$

The energy dissipated by pull-out of a single CH crystal, E_{f1} , is computed as the work done by F_f during pull-out of CH crystal over a distance equal to half its radius:

$$E_{f1} = \int_{R/2}^R F_f dz = \int_{R/2}^R 10^9 \tau_f A_{ECH} dz \quad (2.16)$$

The next task was to approximate the possible number of CH crystals per unit area of hydrated cement paste in order to calculate the amount of energy dissipated per unit cracked area. The number of CH crystals in a unit cubic cell can be estimated by assuming a uniform distribution of vertically oriented CH crystals. The amount of CH in mature Portland cement paste ranges from 20 to 25 percent of the solid volume (estimated at 22% on average).⁶⁴ The volume of a single CH crystal (V_{CH}) can be calculated as:

$$V_{CH} = \pi R^2 t_{CH} \quad (2.17)$$

The number of CH crystals per unit cubic cell volume (N_{CHV}) can be obtained as:

$$N_{CHV} = \frac{0.22 * 1}{V_{CH}} \quad (2.18)$$

The number of CH crystals in a plane parallel to any side of the unit cubic cell, N_{CHP} , is:

$$N_{CHP} = (N_{CHV})^{2/3} \quad (2.19)$$

The total energy per unit area (G_p) due to pull-out of CH crystals can thus be calculated as follows:

$$G_p = E_{f1} N_{CHP} \quad (2.20)$$

The values of G_p calculated using the above approach range between 5.42 and 281 J/m² (See Table 2.4).

Therefore, the total intrinsic fracture toughness of compact hydrated cement paste (G_o) can be determined as the sum total of energy dissipation by CH pull-out (G_p) and debonding of C-S-H nanoparticles (G_d):

$$G_o = G_d + G_p \quad (2.21)$$

The values of G_o calculated using the above equation range between 5.82 and 283 J/m² (Table 2.4), compared to measured values which range from about 16.9 to 41.0 J/m² for fracture toughness (G_{IC}) of compact cement pastes.⁶⁸ Table 2.4 summarizes the sensitivity

of the calculated value of the fracture toughness due to CH pull-out (G_p) and the total fracture toughness (G_o) to variations in the parameters of model. It can be observed from the table that variations in the size of C-S-H globules (d_g), the distance between C-S-H globules (d), and the thickness of CH crystals (t_{CH}) do not significantly affect the calculated values of G_d and G_o . Major variations in the calculated values of fracture toughness were observed with changes in the width of CH crystals (D_{CH}). An average size of CH crystals, obtained from a reasonable CH size distribution in hydrated cement paste, was used in this research.

Table 2.4 - Significance of CH diameter and thickness on fracture toughness due to CH pull-out (Gp)

dg (m) 10^{-9}	d (m) 10^{-10}	F_{ov} (Pa) 10^9	E_0 (Pa) 10^9	k 10^{-11}	G_{CHS} (J/m ²)	r_c (m) 10^{-9}	A_p (m ²) 10^{-18}	D_{CH} (m) 10^{-6}	t_{CH} (m) 10^{-7}	A_S (m ²) 10^{-19}	A_{ECH} (m ²) 10^{-20}	E_I (J/m ²) 10^{-11}	V_{CH} (m ³) 10^{-18}	G_p (J/m ²)	G_o (J/m ²)	
6	1.8	5.22	52.2	2.76	2.14	1.4	6	10	2.2	0.315	0.515	0.515	0.173	6.05	8.19	
									2.6	0.315	0.515	0.515	0.204	5.42	7.55	
									2.4	0.315	0.515	0.515	0.188	5.71	7.85	
	3.2	9.29	9.29	1.55	0.38	1.4	6	10	2.2	0.315	0.515	0.515	0.173	6.05	6.43	
									2.6	0.315	0.515	0.515	0.204	5.42	5.80	
									2.4	0.315	0.515	0.515	0.188	5.71	6.09	
8	1.8	5.22	52.2	2.76	2.85	1.8	10	10	2.2	0.315	0.515	0.515	0.173	281.00	283.84	
									2.6	0.315	0.515	0.515	0.204	251.38	254.23	
									2.4	0.315	0.515	0.515	0.188	265.16	268.01	
	3.2	9.29	9.29	1.55	0.51	1.8	10	10	10	2.2	0.315	0.515	0.515	0.173	6.05	6.56
										2.6	0.315	0.515	0.515	0.204	5.42	5.92
										2.4	0.315	0.515	0.515	0.188	5.71	6.22

2.2.4 Intrinsic Tensile Strength of Compact Hydrated Cement Paste (σ_o)

The tensile strength of compact hydrated cement paste was determined from the force required to break the bond between two basic C-S-H globules. The total force required to separate two surfaces of physically bonded C-S-H globules was determined as the sum of the forces required to break each bonded C-S-H globule divided by the total debonded surface area.

The tensile force required to break the bond between two basic C-S-H globules (F_g) can be determined as:

$$F_g = A_c F_{vdw} \quad (2.22)$$

The intrinsic tensile strength (σ_o) can be determined, assuming 20% gel porosity, as follows:

$$\sigma_o = 0.8 \frac{F_g}{A_g} \quad (2.23)$$

The values of σ_o calculated using the above equations range between 152 and 854 MPa, compared with the measured value of about 930 MPa for the tensile strength of compact hydrated cement paste.⁵⁵

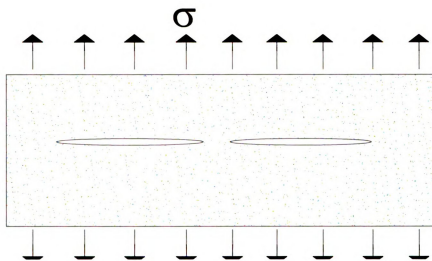
2.3. Hydrated Cement Paste

2.3.1. Introduction

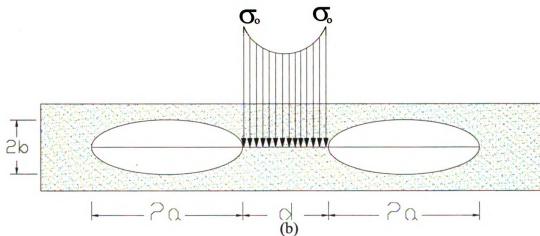
The term “hydrated cement paste” is used here to refer to a conventional hydrated cement paste which incorporates capillary pores and microcracks in its microstructure. The mechanical and physical properties of hydrated cement paste are affected by the presence of these micro defects, which should be accounted for in calculation of their strength, modulus of elasticity and fracture toughness. Capillary pores and microcracks affect the modulus of elasticity of hydrated cement paste by reducing the effective contact area and generating stress concentration. The shape and size distribution of the capillary pores significantly affect the modulus of elasticity of hydrated cement paste. Capillary pores are assumed hence to have an elliptical shape with the ratio of the major-to-minor axis about 2.⁶⁹

2.3.2. Elastic Modulus of Hydrated Cement Paste

In modeling the elastic modulus of hydrated cement paste, the first step involves determining the relationship between capillary porosity and pore size. Uniform size capillary pores distributed uniformly in space were assumed for ease of computations (Fig. 2.8).



(a) Adjacent capillary pores



(b) Effect of adjacent capillary pores on stress concentration

Fig. 2.8 - Capillary pore shape and interactions, and the resulting stress concentration

If a unit volume of hydrated cement paste, enclosing a single pore, is considered to have $2a+d_c$ width, $2b$ thickness and a unit length (see Fig. 2.8b for notation), then porosity can be approximated as:

$$p = \frac{\pi a}{4a + 2d_c} \quad (2.24)$$

$$\frac{d_c}{a} = \frac{(\pi - 4p)}{2p} \quad (2.25)$$

The effect of interactions between two adjacent capillary pores, separated by a distance d_c , on stress concentration in hydrated cement paste can be determined using the relationship between d_c and the amplification factor (K_2) with the stress concentration due to a single elliptical capillary pore (K_1).⁷⁰

$$K_2 = K_1 \left(\frac{d_c}{a} \right)^{-0.37} \quad (2.26)$$

where, K_1 is the stress concentration factor due to a single ellipse; and K_2 is the stress concentration amplification factor due to the interaction of adjacent capillary pores. The following expression can be used to calculate K_1 :

$$K_1 = 1 + 2 \frac{a}{b} \quad (2.27)$$

From Fig. 2.8, it can be observed that $\sigma_o = K_2\sigma$, and since for constant strain in the linear elastic range, E/E_o is equal to σ/σ_o , one concludes that $E/E_o = 1/K_2$.

$$\frac{E}{E_o} = \frac{\sigma}{\sigma_o} = \frac{1}{K_2} = \frac{1}{K_1} \left(\frac{d_c}{a} \right)^{0.37} \quad (2.28)$$

Substituting Eqn. 2.25 and K_1 into Eqn. 2.28, and simplifying the resulting equation, gives the model for the modulus of elasticity of hydrated cement paste,

$$E_h = 0.77E_o \frac{(1 - p_h)(\pi - 4p_h)^{0.37}}{\left(1 + 2 \frac{a}{b} \right) p_h^{0.37}} \quad (2.29)$$

The analytical model is plotted as a function of porosity and compared with empirical models in Fig. 2.9. The analytical model is observed to compare reasonably well with empirical models which reflect the trends observed in experiments.

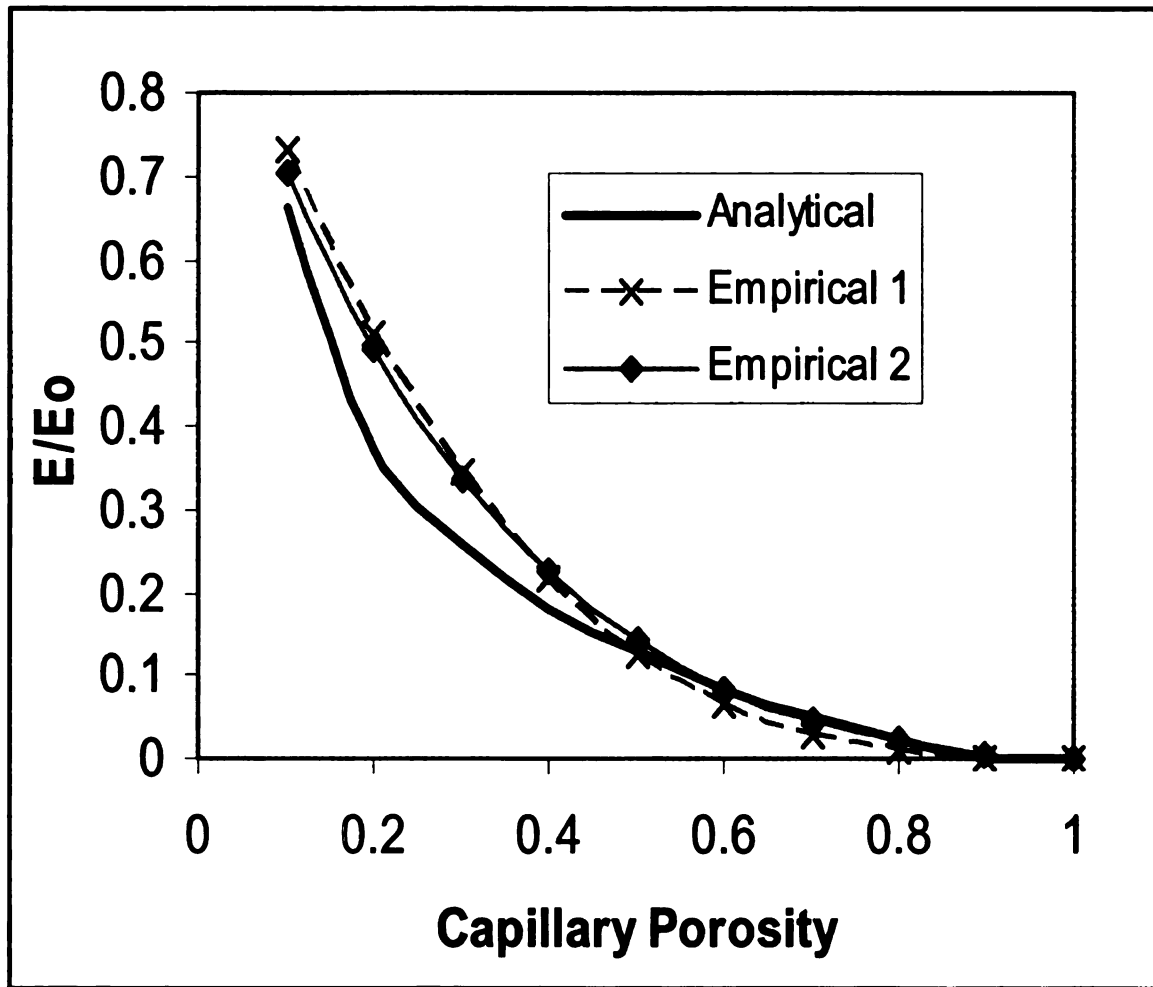


Fig. 2.9 - Modulus of elasticity-porosity relationships

Cement-based materials incorporate entrapped air voids which reflect imperfect compaction of these materials. Entrapped air voids in concrete are comparable in size to the largest microcracks considered in our models. When compared with microcracks, however, the entrapped air voids have relatively large radii of curvature, which makes them less critical than microcracks with sharp tips in terms of stress concentration. Hence, tensile strength would still be governed by the largest microcracks in lieu of entrapped air voids. The infrequent occurrence of entrapped air voids in concrete as well

as the relatively small stress concentrations associated with them indicates that their effects on mechanical properties of concrete are relatively small.

2.3.3. Fracture Toughness of Hydrated Cement Paste (G)

The fracture surface of hydrated cement paste is not highly tortuous, and thus the fracture toughness of hydrated cement paste (G_h) can be assumed to vary linearly with porosity as shown in Eqn. 2.30.

$$G_h = G_o(1 - p_h) \quad (2.30)$$

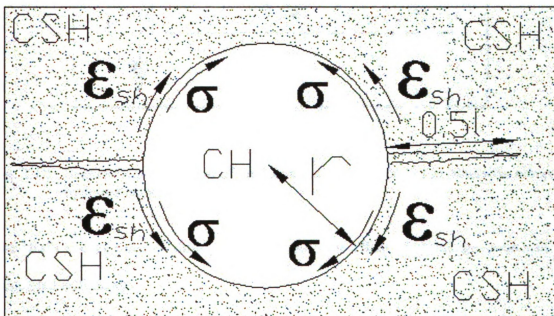
where, G_o is the fracture toughness of compact hydrated cement paste; and p_h is capillary porosity.

2.3.4. Tensile Strength of Hydrated Cement Paste

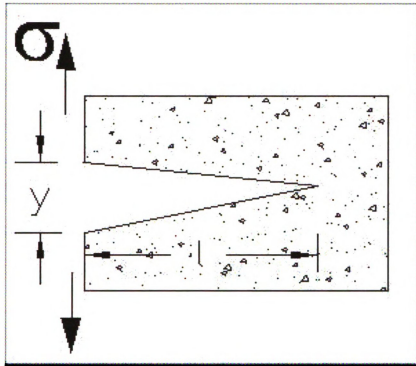
The Griffith's equation for linear elastic fracture mechanics (LEFM) is used to predict the tensile strength of hydrated cement paste in order to use this model, one needs to determine the critical crack length for hydrated cement paste. Microcracks develop in cementitious materials even before the application of loads. These microcracks result from the restraint of thermal and drying shrinkage of hydrated cement paste at early age. Calculation of the critical crack length in hydrated cement paste is presented below.

2.3.4.1. Shrinkage Microcracks

The formation of microcracks in hydrated cement paste is due to the differential shrinkage that exists between the relatively stiff CH crystal and the softer C-S-H gel. Restraint of the shrinkage strains in C-S-H gel by CH crystals lead to microcracking of the young hydrated cement paste. Restrained shear stresses cause debonding of C-S-H from the CH surface and subsequent cracking of hydrated cement paste (Fig. 2.10).



(a) Shrinkage cracking around CH crystal



(b) Simplified crack model

Fig. 2.10 - Schematic presentation of the formation of microcracks in otherwise compact hydrated cement paste

The strain energy released during cracking under the effect of shrinkage strain can be calculated as follows:

$$U_e = \varepsilon_{sh} E_o A_{sk} y \quad (2.31)$$

where, U_e = strain energy released during cracking; ε_{sh} = shrinkage strain; E = modulus of elasticity of C-S-H; A_{sk} (surface area of CH subjected to skin friction) = $(P_{CH})(t_{CH})$; y (crack width at the periphery of CH crystal) = $\varepsilon_{sh} P_{CH}$; and P_{CH} and t_{CH} are the perimeter and thickness of CH crystal, respectively.

Substituting the above expressions into Eqn. 2.31 yields:

$$U_e = (\varepsilon_{sh} P_{CH})^2 E_o t_{CH} \quad (2.32)$$

The energy dissipated upon cracking (U_i) can be calculated as follows:

$$U_i = G_d l t_{CH} \quad (2.33)$$

where, G_d is the fracture toughness due to C-S-H debonding; and l is crack length.

Equating U_e (Eqn. 2.32) and U_i (Eqn. 2.33) yields the following expression for crack length, l :

$$l = \frac{(\varepsilon_{sh} P_{CH})^2 E_o}{G_d} \quad (2.34)$$

Due to the unavailability of sufficient information on the relationship between capillary porosity (p) and shrinkage strain (ε_{sh}), an empirical relationship was determined using experimental results⁷¹ as follows:

$$\varepsilon_{sh} = 0.0148 p_h - 8.8 \times 10^{-4} \quad (2.35)$$

After substituting Eqn. 2.35 into Eqn. 2.34 and simplifying it, the following expression can be derived for crack length:

$$l = \frac{39.8 E_o r_{CH}^2 (0.0148 p_h - 8.8 \times 10^{-4})^2}{G_d} \quad (2.36)$$

where, r_{CH} is the radius of the largest possible CH crystal; a 100 μm diameter CH was considered.⁶⁴ The critical crack length l' is half of l plus the diameter of CH:

$$l_c = 0.5(l + 2r_{CH}) \quad (2.37)$$

2.3.4.2 Tensile Strength of Hydrated Cement Paste

The Griffith equation defines the relationship between tensile strength (σ_t) and critical crack length (l'):

$$\sigma_{ht} = \sqrt{\frac{E_h G_h}{\pi l_c}} \quad (2.38)$$

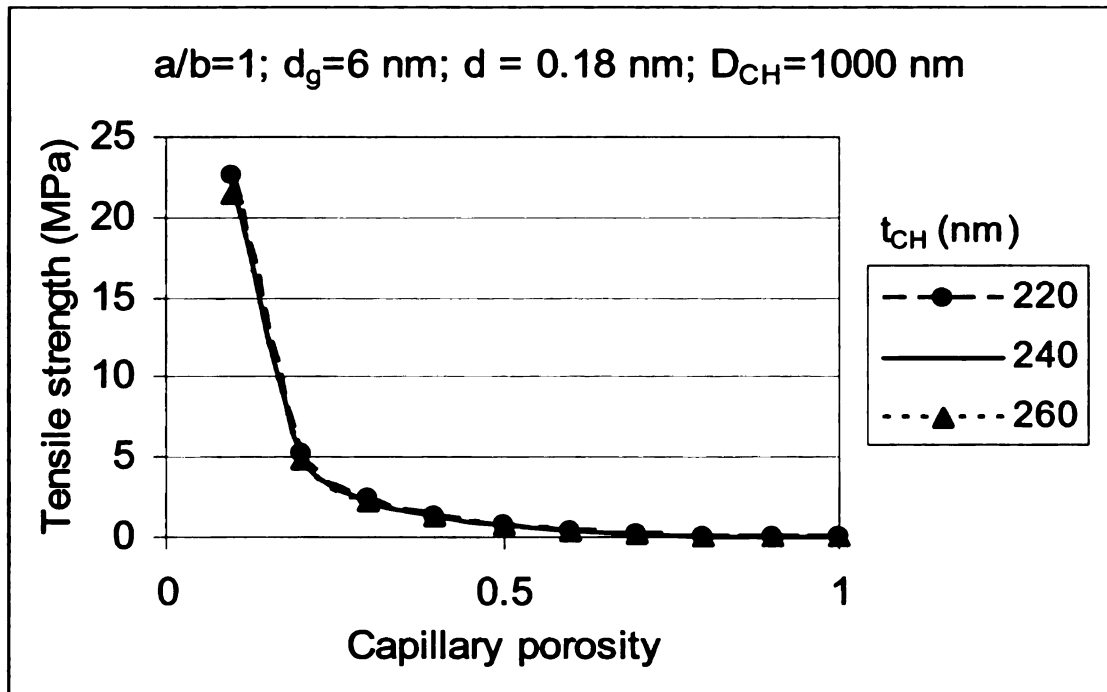
Substituting Eqns. 2.29 for E, 2.30 for G and 2.37 for l' into Eqn. 2.38 yields:

$$\sigma_{ht} = \sqrt{\frac{0.77 E_o G_o (1 - p_h)^2 (\pi - 4 p_h)^{0.37}}{\pi l_c \left(1 + 2 \frac{a}{b}\right) p_h^{0.37}}} \quad (2.39)$$

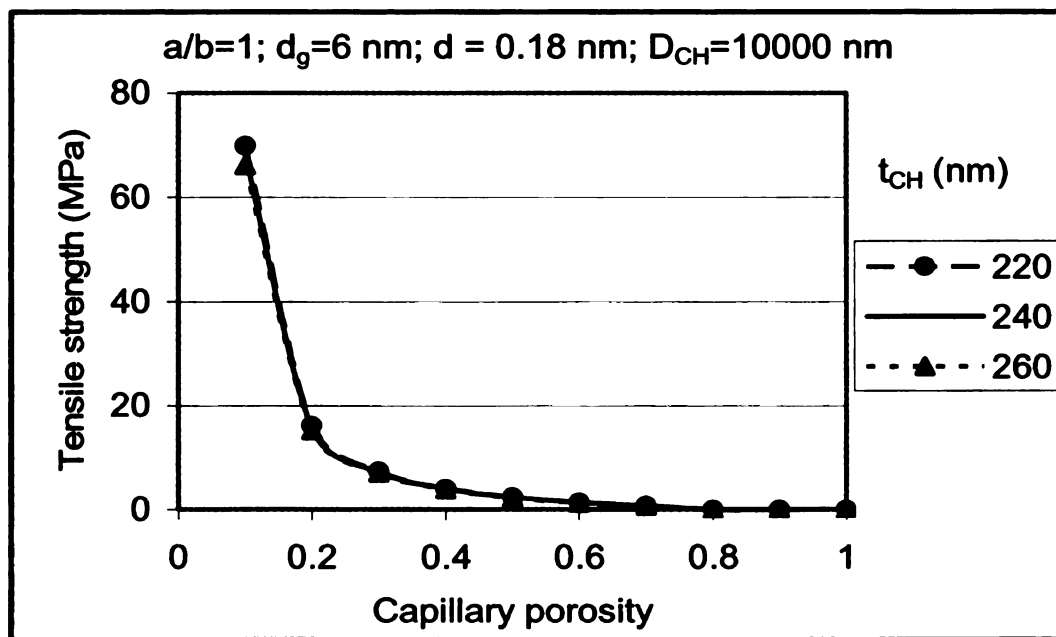
2.3.4.3 Parametric Study of the Effects of Various Parameters on the Tensile Strength of Hydrated Cement Paste

An extensive parametric study was conducted to identify parameters defining the characteristics of C-S-H, CH and capillary pores which significantly influence the strength of hydrated cement past. The effects of CH thickness and diameter are shown in Figs. 2.11 through 2.18. It can be observed from these figures that (for constant capillary pore size, distance between C-S-H globules and diameter of C-S-H globule and CH crystal) the variation of CH thickness (within a reasonable range) only minimally affect the strength. The capillary pore aspect ratio (a/b) and the CH crystal diameter, on the other hand, have important effects on strength. The effect of capillary pore aspect ratio can be observed by comparing the graphs in Figs. 2.11(a) and 2.15(a). The strength values of the former are almost twice those of the latter. This could be attributed to the higher stress concentrations that occur when capillary pores are modeled as ellipsoids rather than spheres. The effect of CH crystal diameter on strength-porosity relationship can be assessed by comparing graphs (a) and (b) in any one of these figures. For example, in Fig. 2.11, the strength of hydrated cement paste with 10,000 nm CH diameter is about three times that of hydrated cement paste with 1000 nm CH diameter. This significant

effect could be attributed to the effect of CH size on the fracture toughness of hydrated cement paste. The larger the diameter of CH crystal, the higher is the fracture toughness due to the high contact surface for phononic friction as the CH crystal pulls out. However, in real sense, not all the CH crystals have such a large size. CH crystals grow in size only when there is adequate free space. From this perspective, it is unlikely that the majority of CH crystals will reach the larger size.

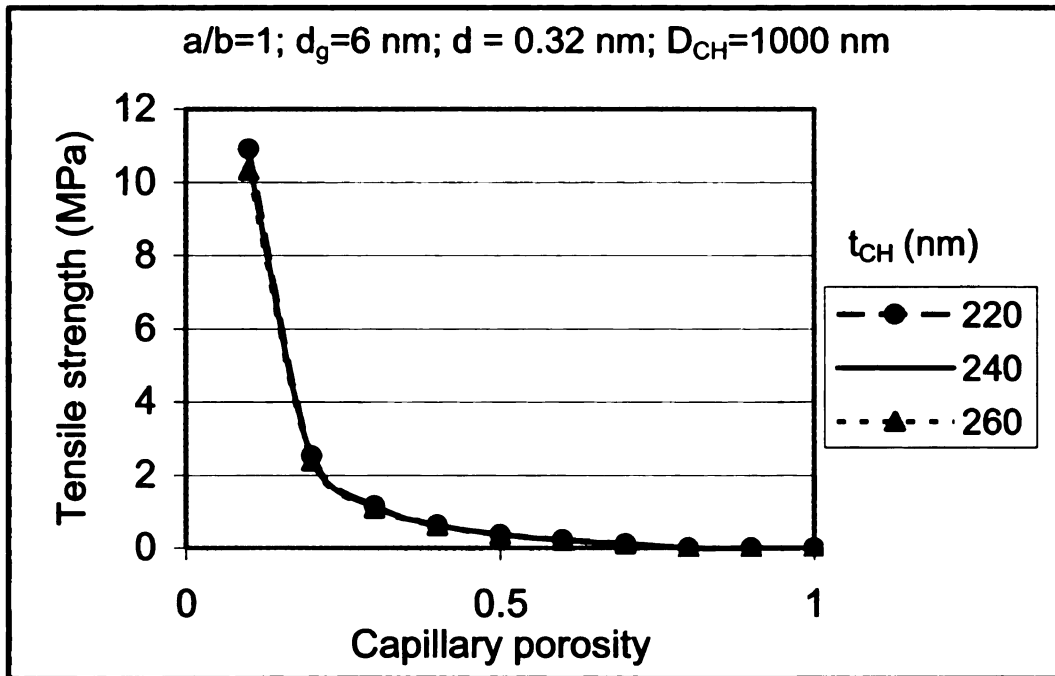


(a)

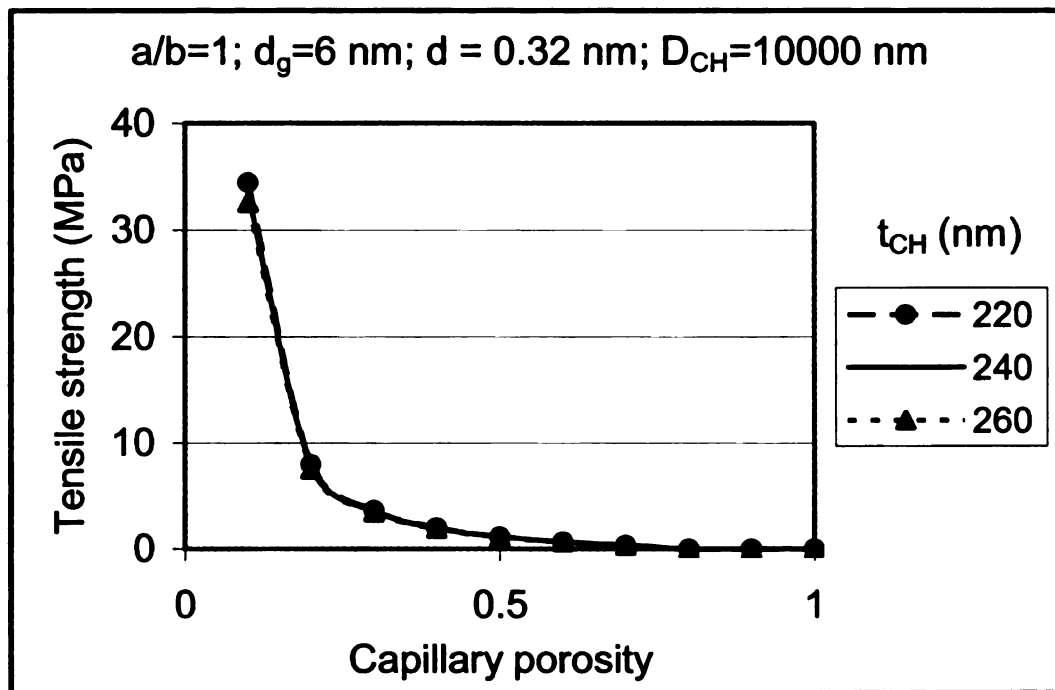


(b)

Fig. 2.11 - Influence of CH thickness on the strength-porosity relationship of hcp for spherical capillary pores, C-S-H globule diameter of 6 nm, distance between C-S-H globules of 0.18 nm, and CH crystal diameter of: (a) 1000 nm; (b) 10,000 nm

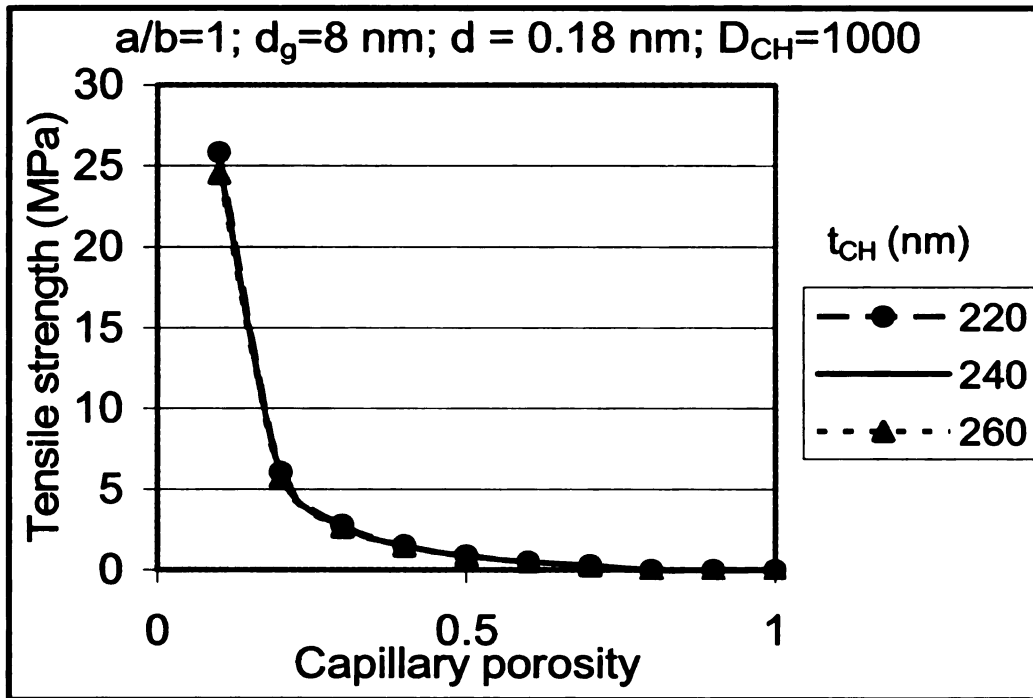


(a)

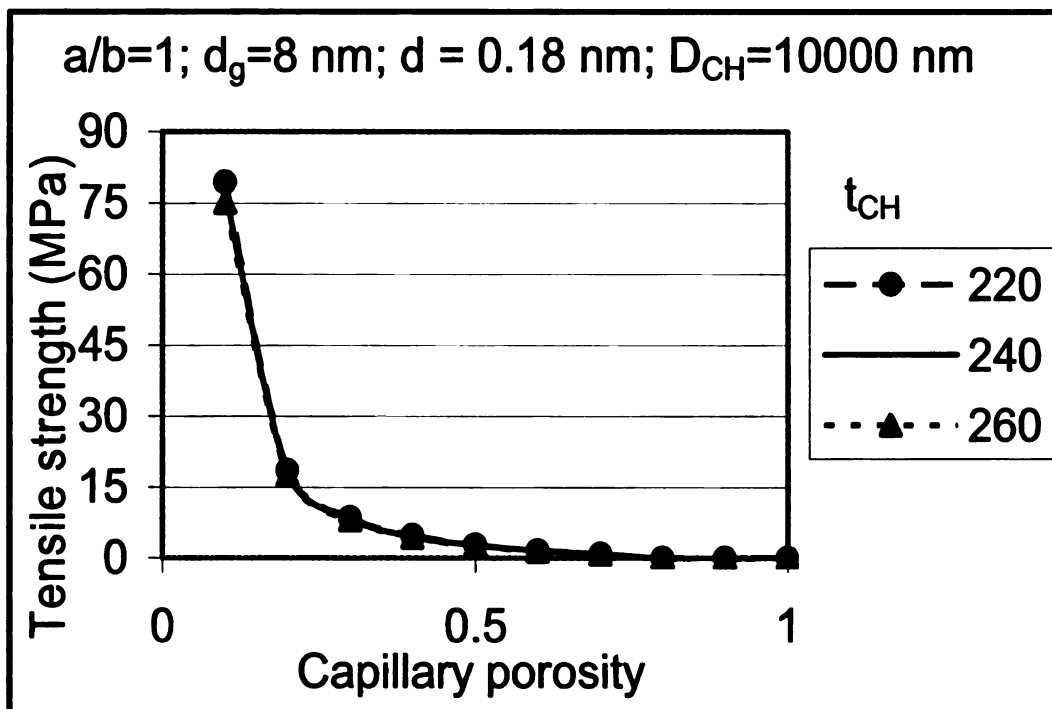


(b)

Fig. 2.12 - Influence of CH thickness on the strength-porosity relationship of hcp for spherical capillary pores, C-S-H globule diameter of 6 nm, distance between C-S-H globules of 0.32 nm, and CH crystal diameter of: (a) 1000 nm; (b) 10,000 nm

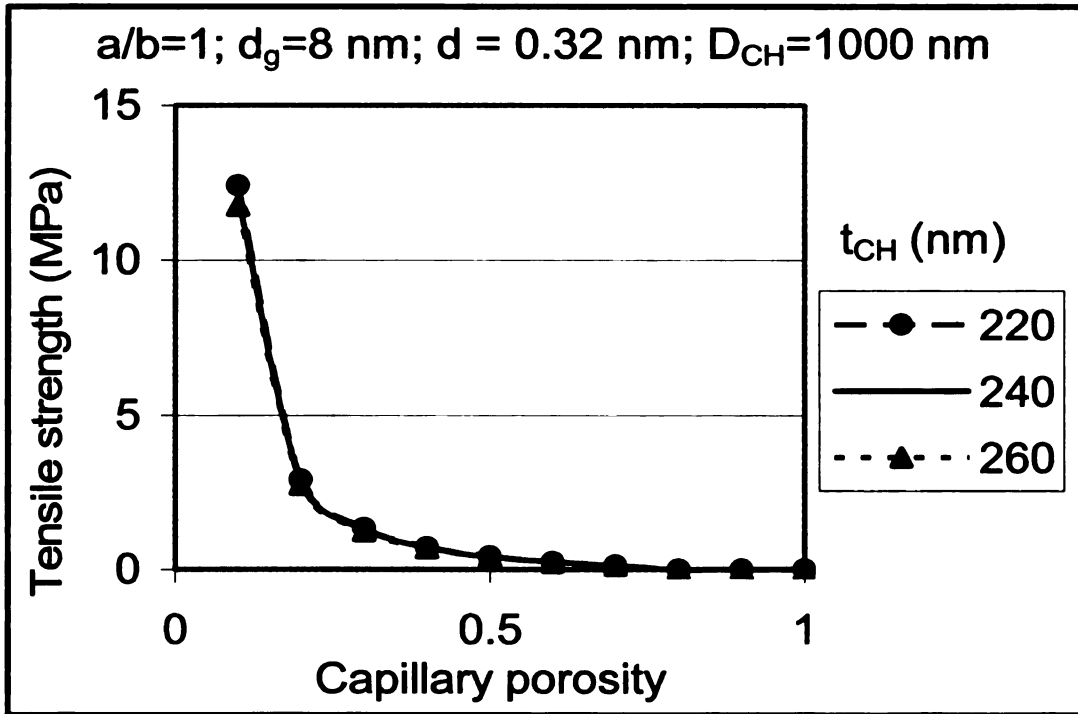


(a)

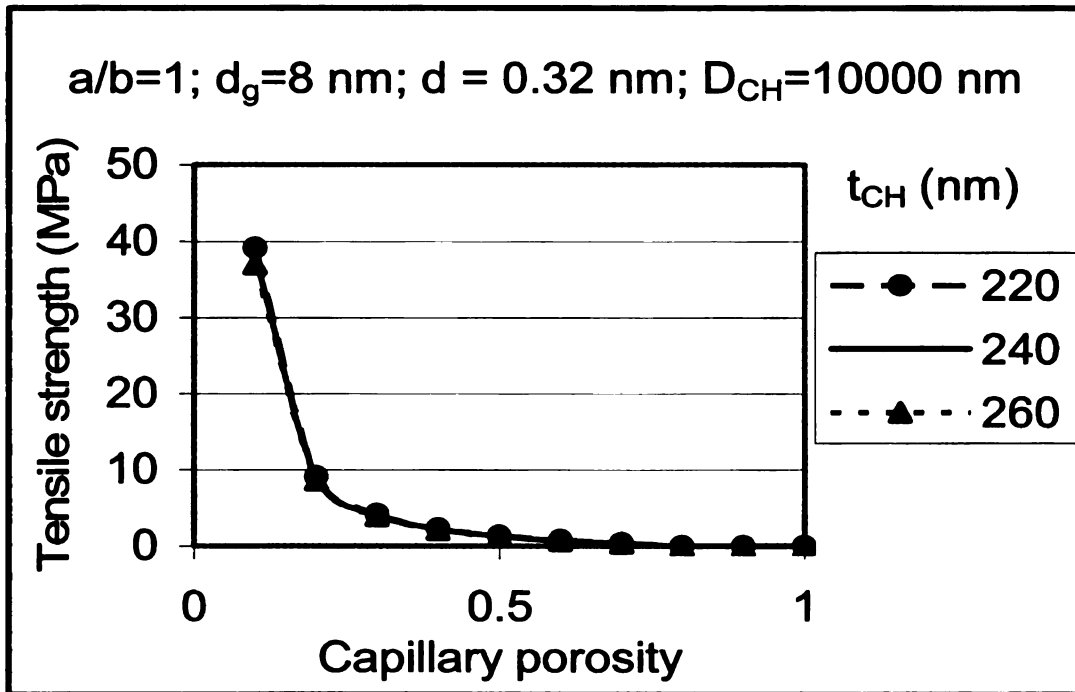


(b)

Fig. 2.13 - Influence of CH thickness on strength-porosity relationship of hcp for spherical capillary pores, C-S-H globule diameter of 8 nm, distance between C-S-H globules of 0.18 nm, and CH crystal diameter of: (a) 1000 nm; (b) 10,000 nm

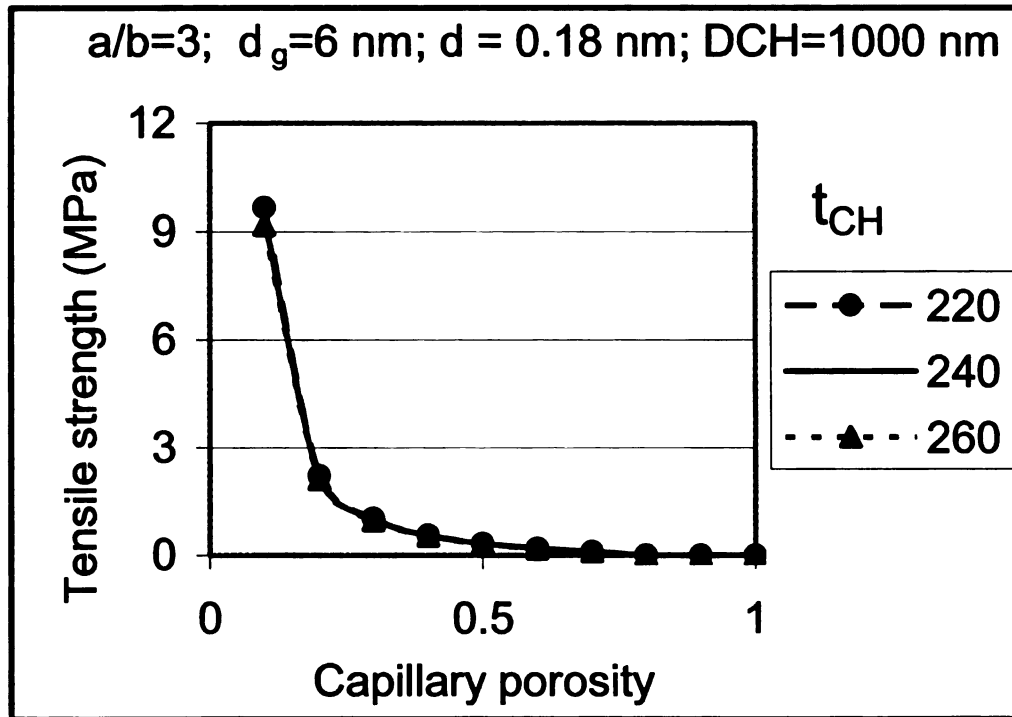


(a)

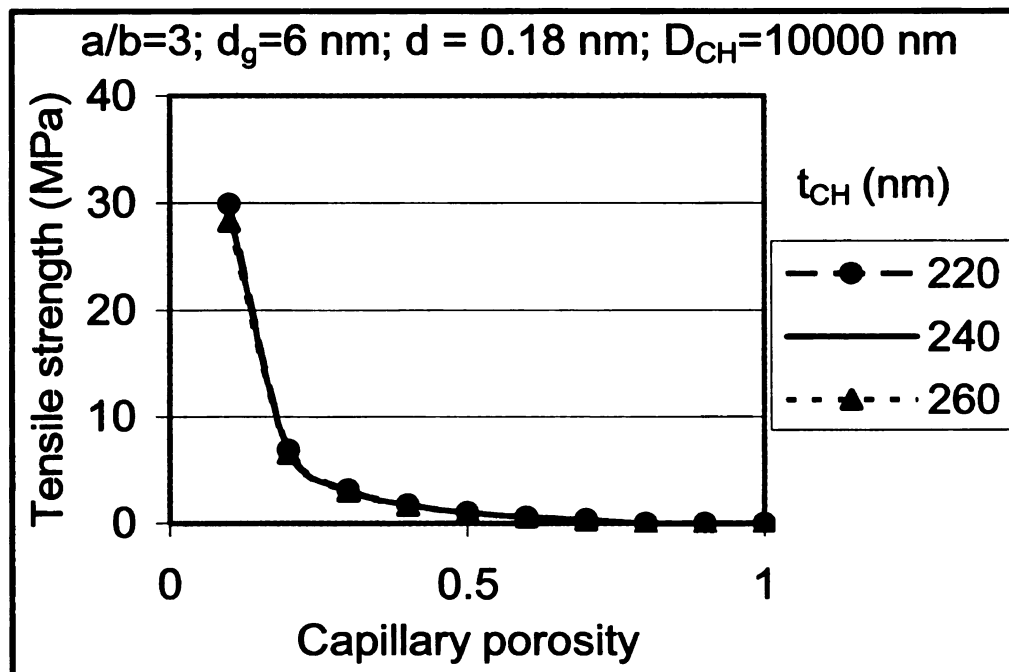


(b)

Fig. 2.14 - Influence of CH thickness on strength-porosity relationship of hcp for spherical capillary pores, C-S-H globule diameter of 8 nm, distance between C-S-H globules of 0.32 nm, and CH crystal diameter of: (a) 1000 nm; (b) 10,000 nm

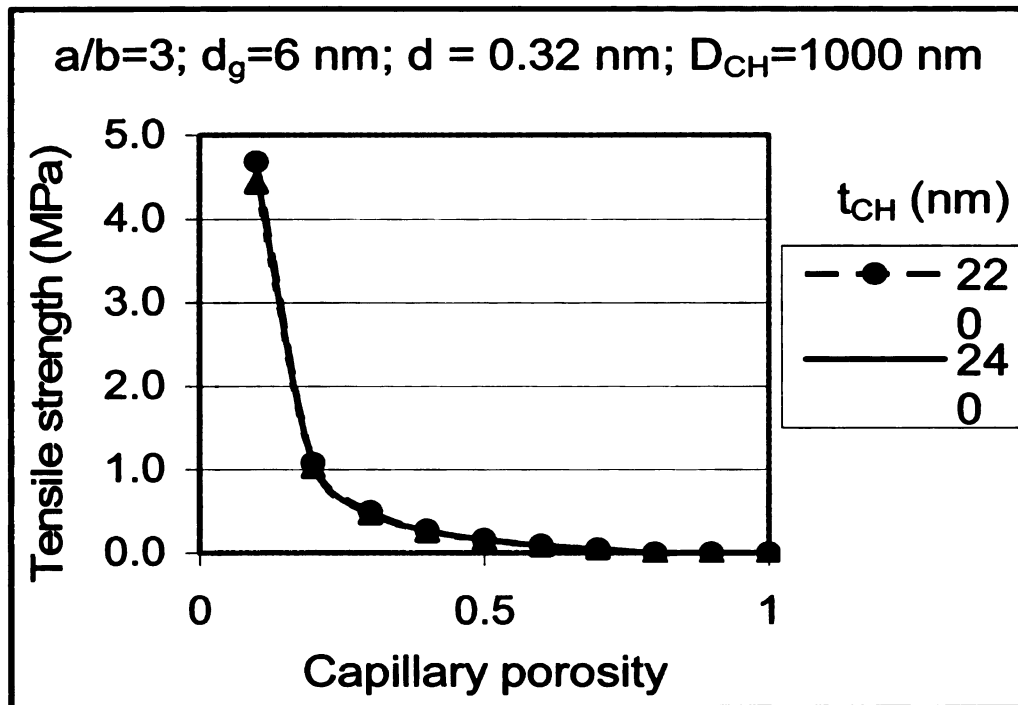


(a)

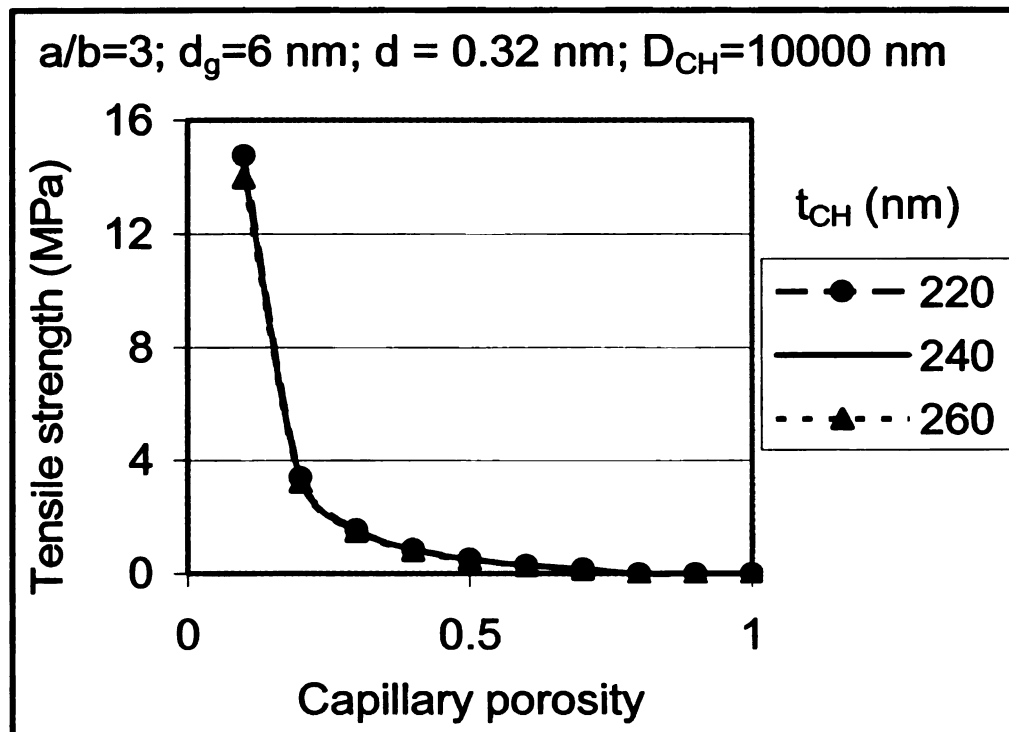


(b)

Fig. 2.15 - Influence of CH thickness on strength-porosity relationship of hcp for ellipsoidal capillary pores, C-S-H globule diameter of 6 nm, distance between C-S-H globules of 0.18 nm, and CH crystal diameter of: (a) 1000 nm; (b) 10,000 nm

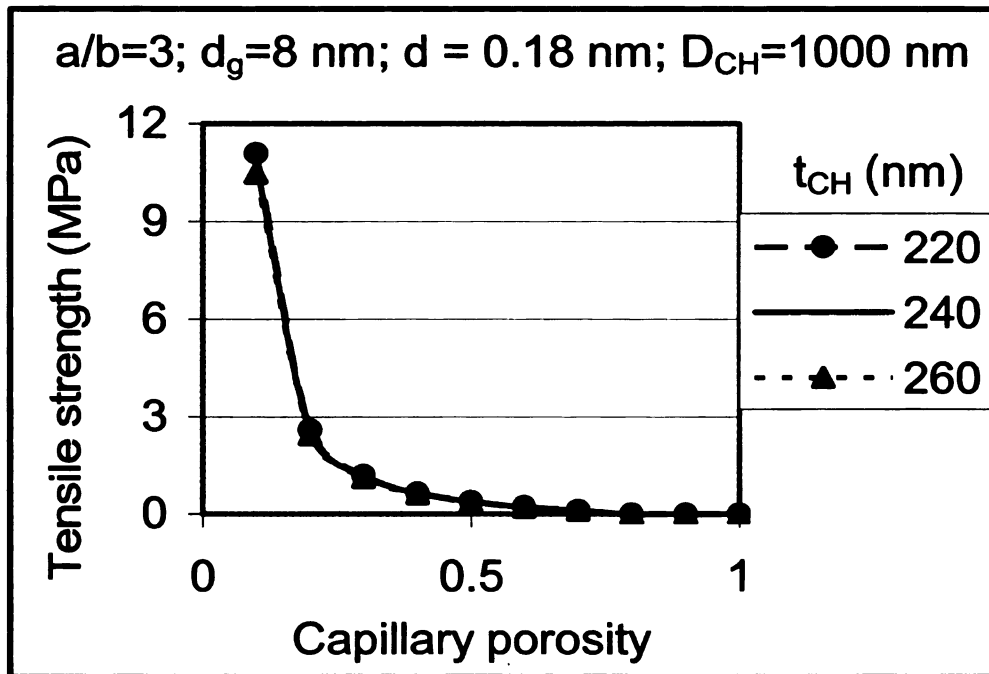


(a)

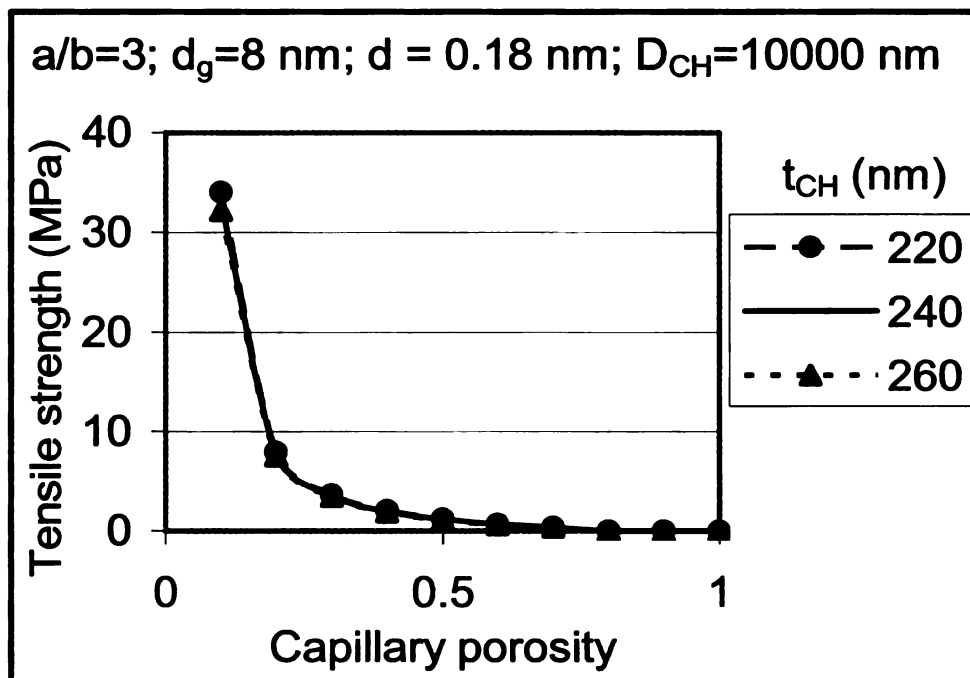


(b)

Fig. 2.16 - Influence of CH thickness on strength-porosity relationship of hcp for ellipsoidal capillary pores, C-S-H globule diameter of 6 nm, distance between C-S-H globules of 0.32 nm, and CH crystal diameter of: (a) 1000 nm; (b) 10,000 nm

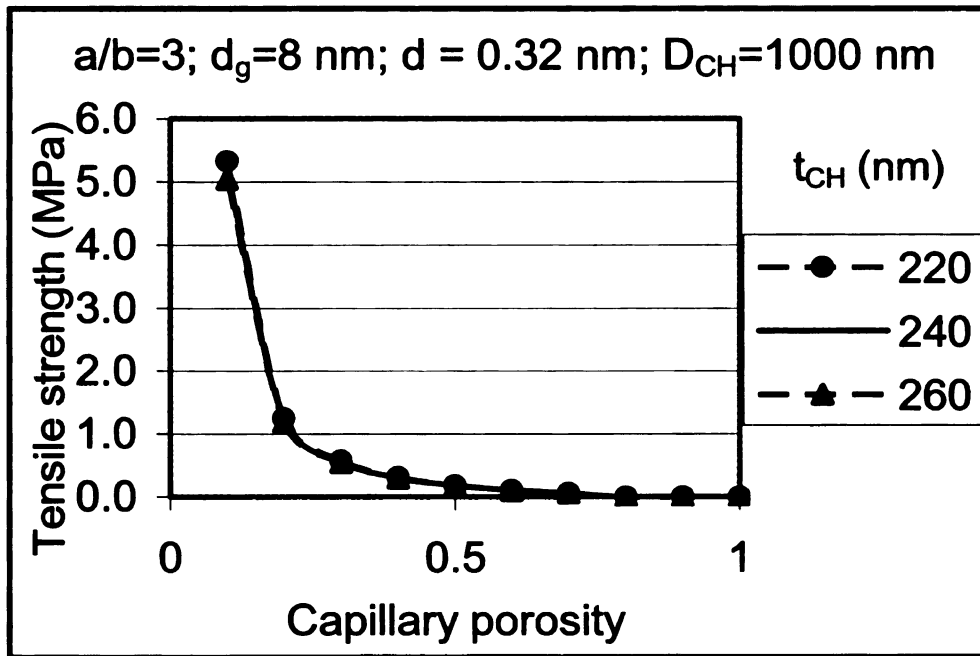


(a)

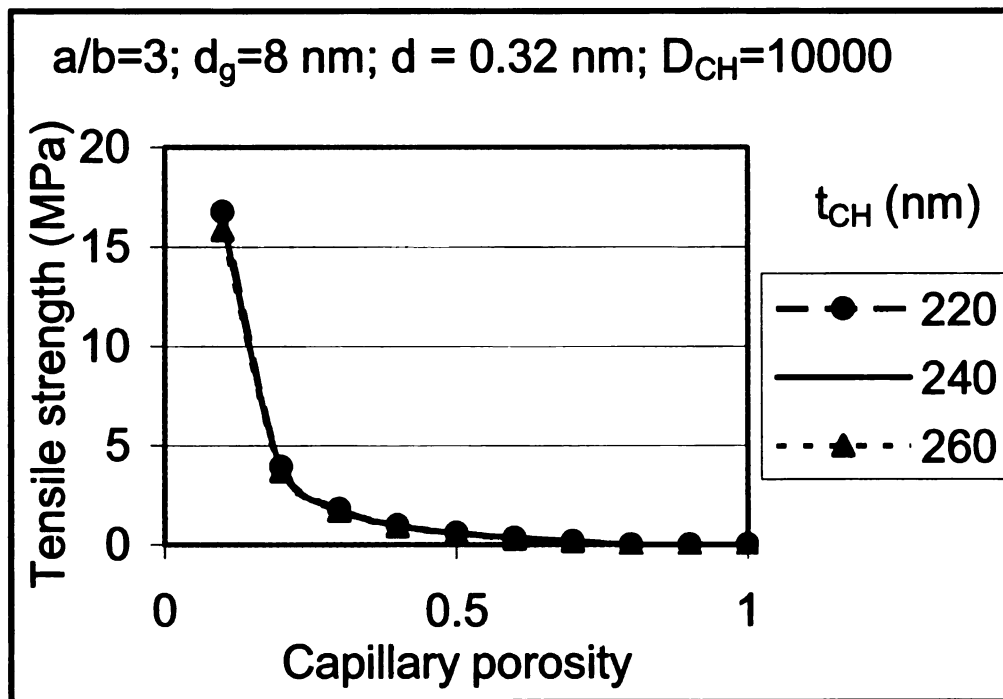


(b)

Fig. 2.17 - Influence of CH thickness on strength-porosity relationship of hcp for ellipsoidal capillary pores, C-S-H globule diameter of 8 nm, distance between C-S-H globules of 0.18 nm, and CH crystal diameter of: (a) 1000 nm; (b) 10,000 nm



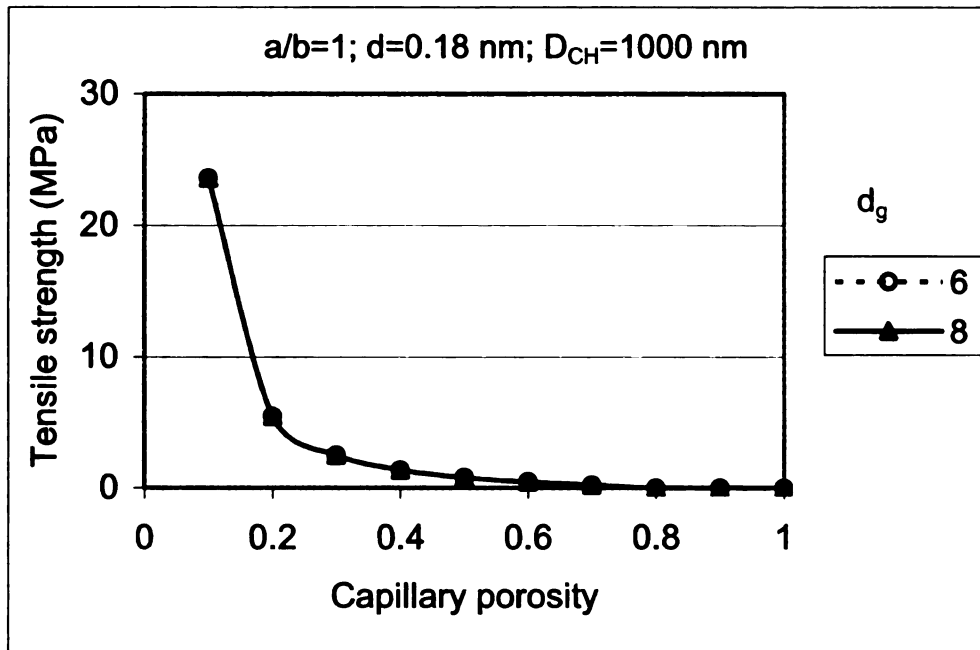
(a)



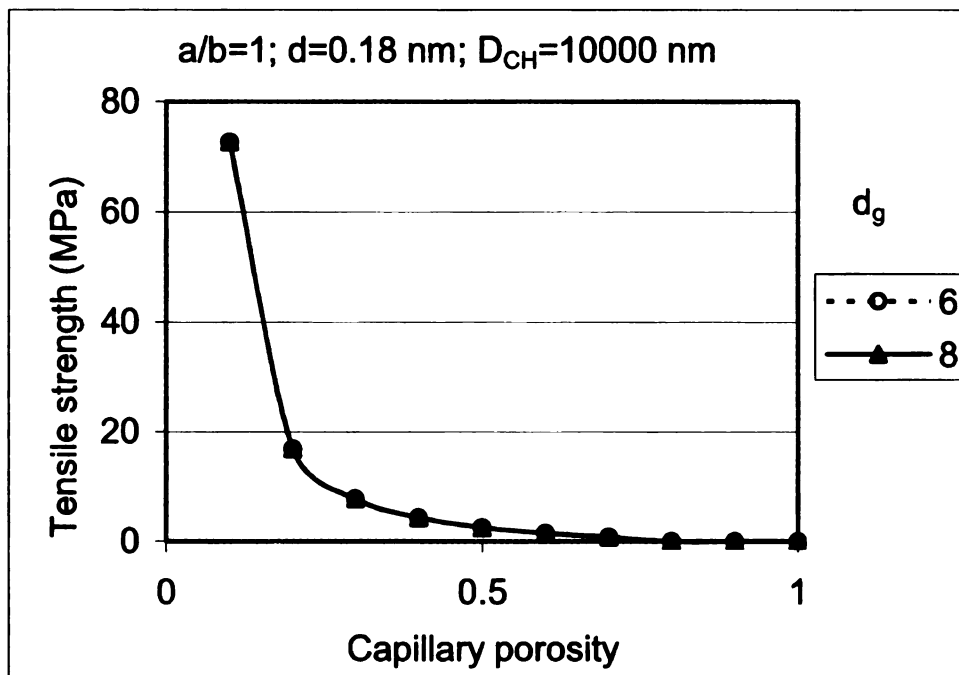
(b)

Fig. 2.18 - Influence of CH thickness on strength-porosity relationship of hcp for ellipsoidal capillary pores, C-S-H globule diameter of 8 nm, distance between C-S-H globules of 0.32 nm, and CH crystal diameter of: (a) 1000 nm; (b) 10,000 nm

A study on the effect of C-S-H globules diameter (d_g) on the strength-porosity relationship in hydrated cement paste was conducted using an average CH thickness of 240 nm. The results are summarized in Fig. 2.19 through Fig. 2.22. It is obvious that the influence of the range of d_g is not significant. Therefore, an average value of 7 nm was safely considered in developing the mechanical model of hydrated cement paste.

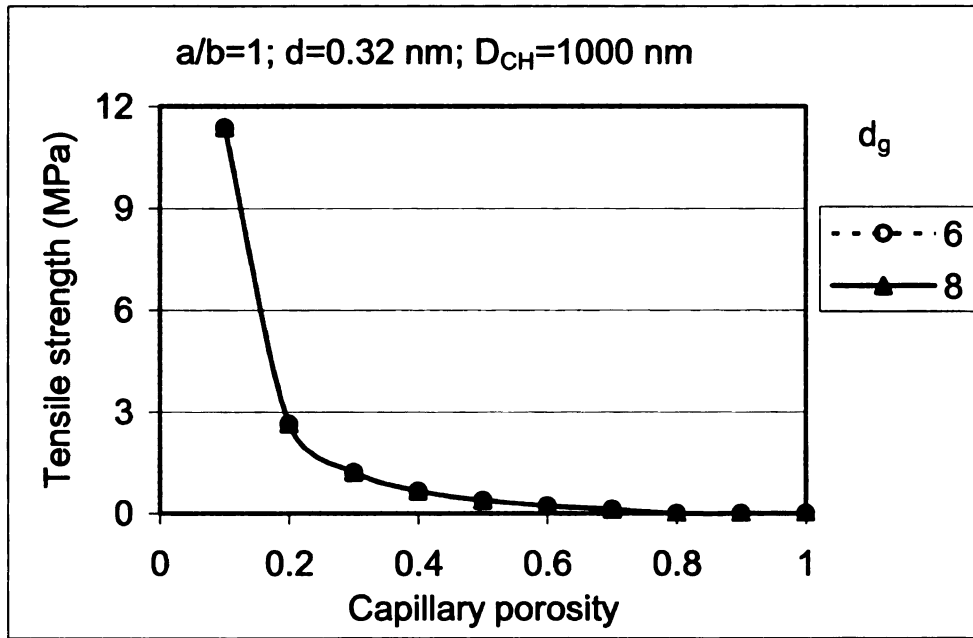


(a)

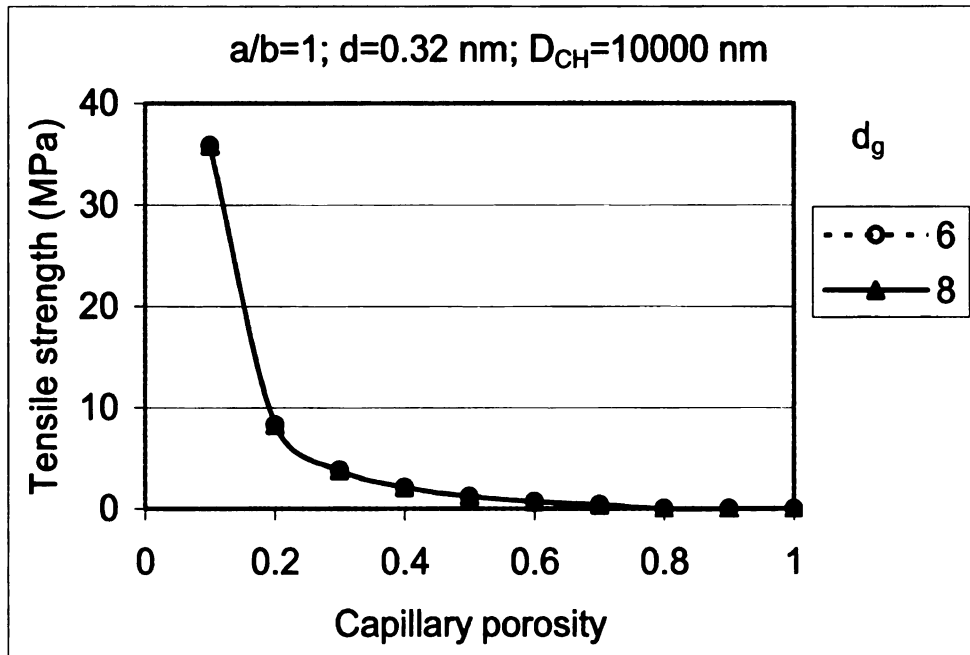


(b)

Fig. 2.19 - Influence of the C-S-H globule diameter on the strength-porosity relationships of hcp for spherical capillary pores, distance between C-S-H globules of 0.18 nm, and CH crystal diameter of: (a) 1000 nm; (b) 10,000 nm

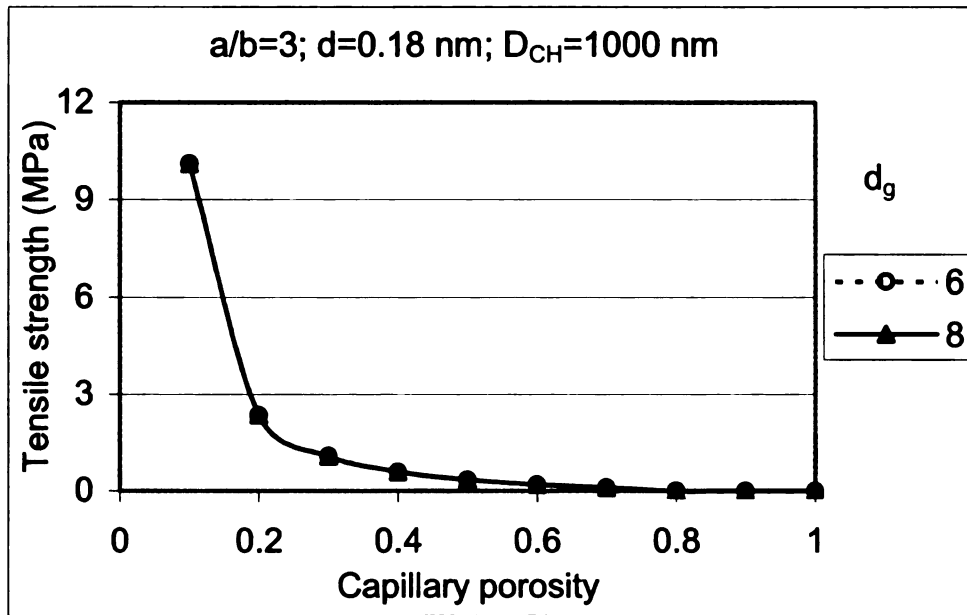


(a)

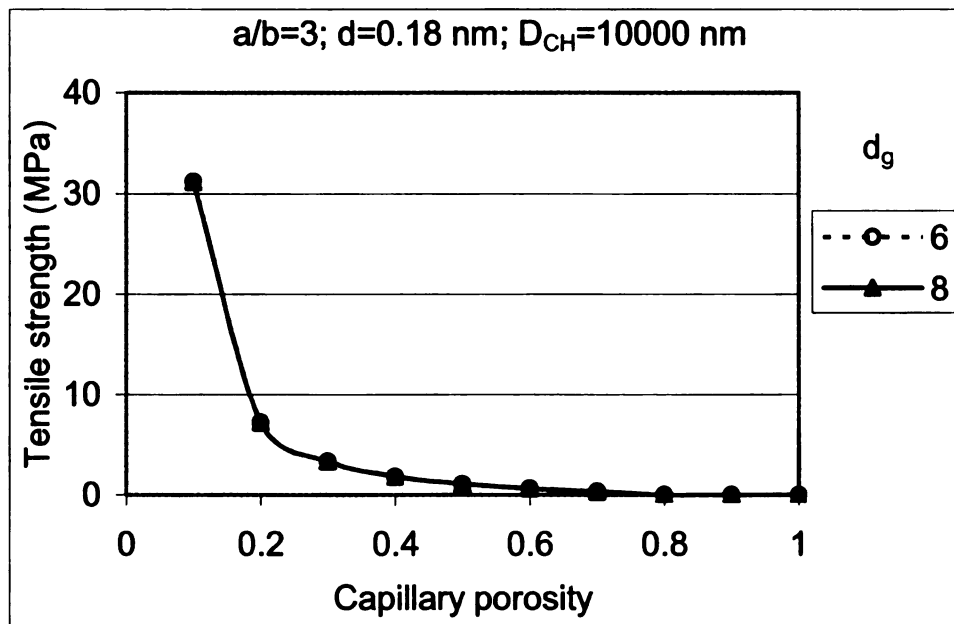


(b)

Fig. 2.20 - Influence of the C-S-H globule diameter on the strength-porosity relationships of hcp for spherical capillary pores, distance between C-S-H globules of 0.32 nm, and CH crystal diameter of: (a) 1000 nm; (b) 10,000 nm

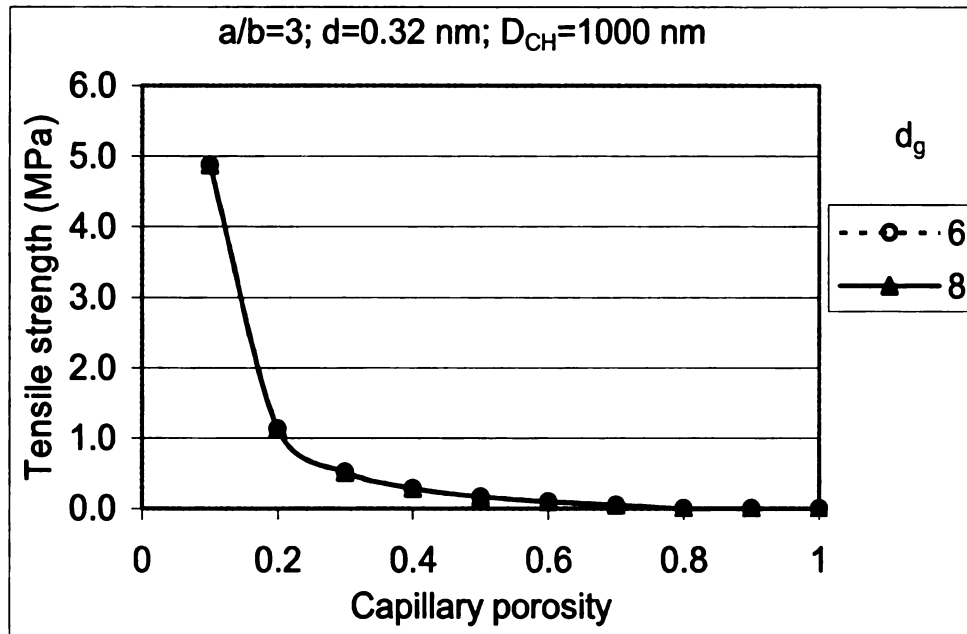


(a)

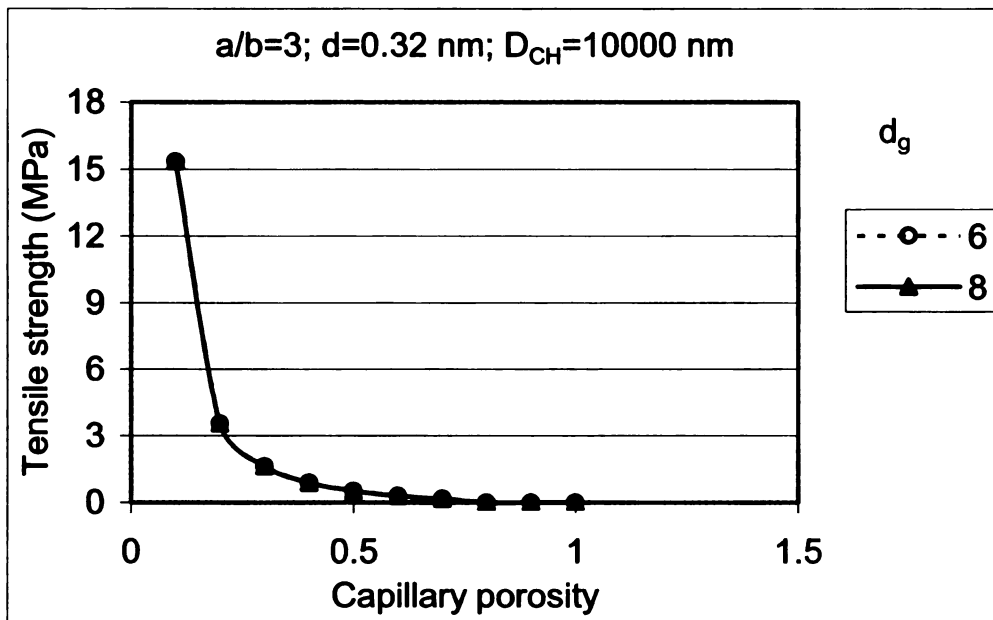


(b)

Fig. 2.21 - Influence of the C-S-H globule diameter on the strength-porosity relationships of hcp for ellipsoidal capillary pores, distance between C-S-H globules of 0.18 nm, and CH crystal diameter of: (a) 1000 nm; (b) 10,000 nm



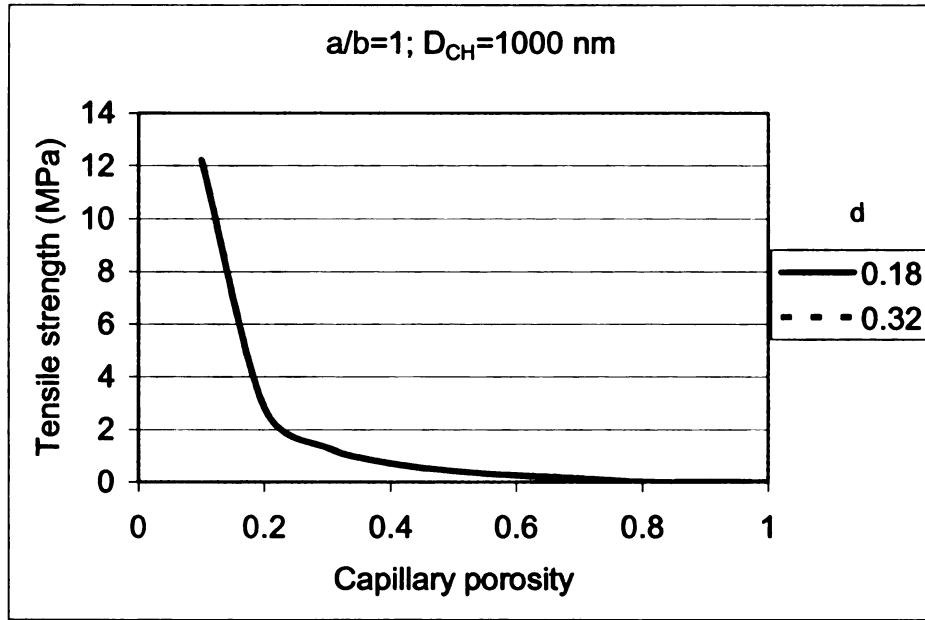
(a)



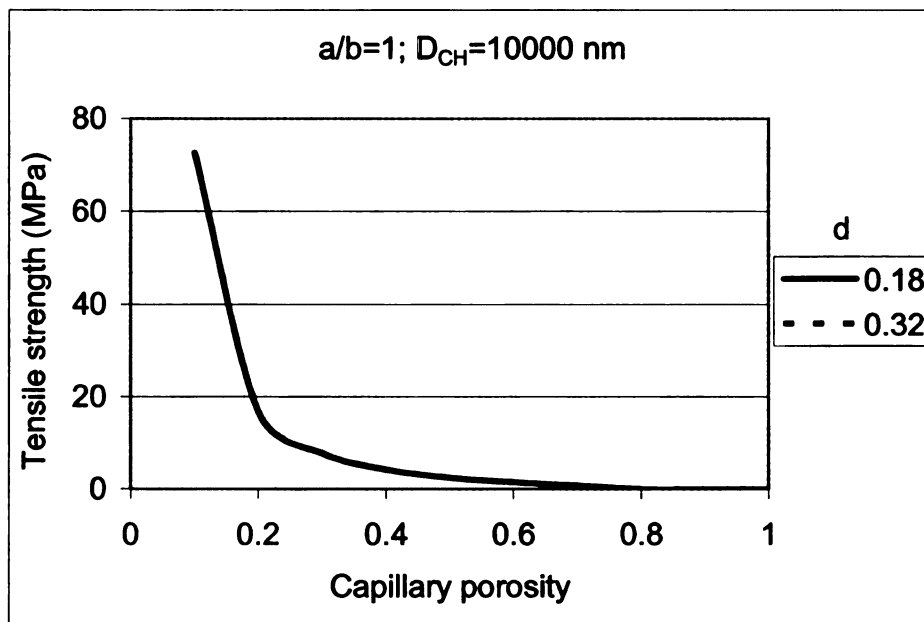
(b)

Fig. 2.22 - Influence of the C-S-H globule diameter on the strength-porosity relationships of hcp for ellipsoidal capillary pores, distance between C-S-H globules of 0.32 nm, and CH crystal diameter of: (a) 1000 nm; (b) 10,000 nm

The next step in the parametric study was to investigate the influence of the distance between C-S-H globules (d) on the strength of hydrated cement paste. In this investigation, the number of independent parameters is reduced by taking C-S-H diameter and CH thickness to be 7 nm and 240 nm, respectively. The resulting strength-porosity relationships are summarized in Figs. 2.23 and 2.24. The results suggest that the influence of the variation of d within the specified range on the strength-porosity relationship is highly pronounced at lower porosities. An average value of 0.2 nm was adopted for d in the model based on the recommendations in the literature.⁵⁷

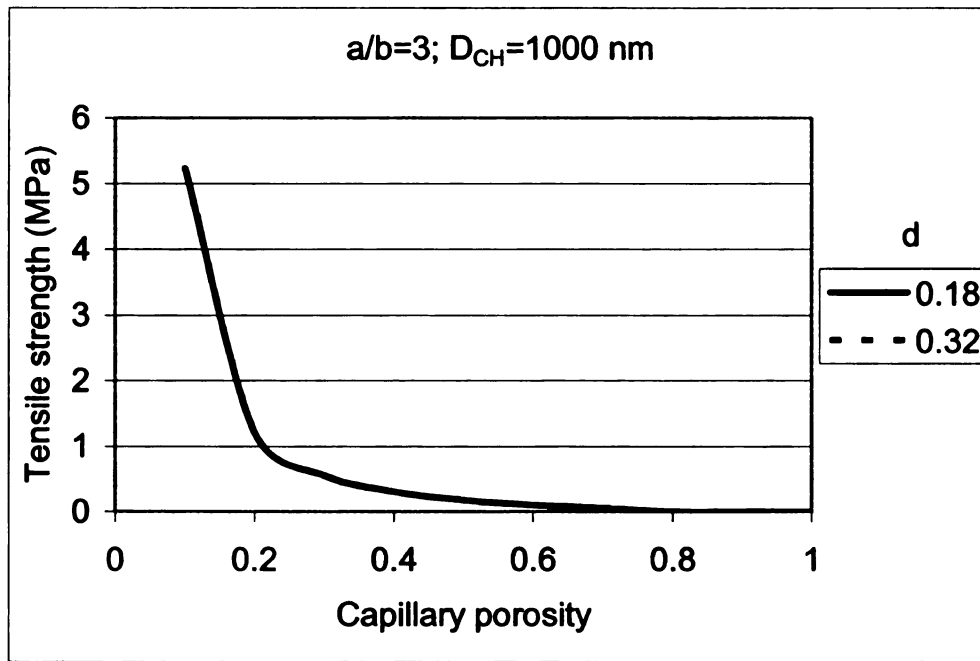


(a)

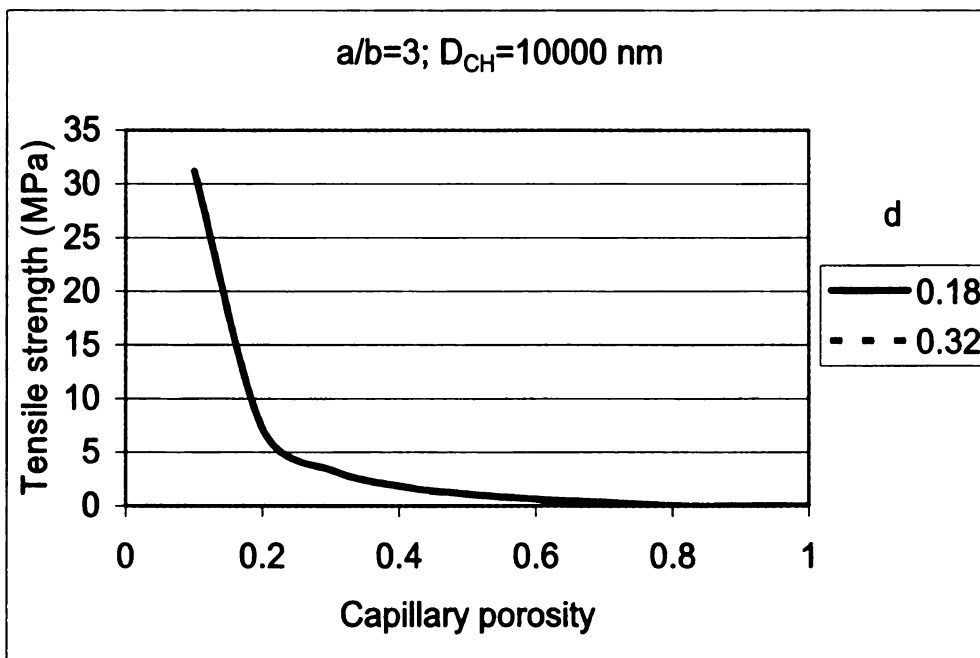


(b)

Fig. 2.23 - Influence of the distance between C-S-H globules on the strength-porosity relationships of hcp for spherical capillary pores with CH diameter of: (a) 1000 nm; (b) 10,000 nm



(a)



(b)

Fig. 2.24 - Influence of the distance between C-S-H globules on the strength-porosity relationships of hcp for ellipsoid capillary pores with CH diameter of: (a) 1000 nm; (b) 10,000 nm

2.3.4.4 Comparing the Predictions of the Mechanistic Tensile Strength Model of Hydrated Cement Past with those of Empirical Models

The values of different parameters governing the tensile strength of hcp were determined using the ranges suggested in the literature (presented earlier), with parametric studies conducted to assess the significance of various parameters in order to assist with final selection of values within the suggested ranges. The final selections were as follows: r_{CH} (radius of largest possible CH crystal) = 50,000 nm; $E_o = 38$ Gpa; $G_d = 1.56$ J/m²; and the ratio of the major-to-minor axis of capillary pores was 2.⁶⁹ E_o and G_d were calculated by considering the average values of d (the distance between two C-S-H globules) and R_b (the radius of C-S-H globule)⁵⁷ to be 0.2 nm and 3.5 nm, respectively. Average thickness and diameter of CH crystal were assumed to be 240 nm and 2500 nm, respectively, where the later is close to mean value of CH size distribution. Substituting the above values into Eqn. 2.37 yields:

$$\sigma_{ht} = 6.73(1 - p_h) \sqrt{\frac{(\pi - 4p_h)^{0.37}}{p_h^{0.37} (10^6 (0.0148p_h - 8.8 \times 10^{-4})^2 + 0.041)}} \quad (2.40)$$

where, σ_{ht} = is the tensile strength of hcp in MPa.

The above equation is observed in Fig. 2.25 to compare favorably with an empirical model which reflects experimental result. The empirical models developed by Balshin⁵¹

(Eqn. 2.41) and Ryshkevitch⁵² (Eqn. 2.42) were used for evaluating the prediction of the theoretical model for the tensile strength of hydrated cement paste.

$$\sigma_{ht} = 46 (1 - p)^{9.97} \quad (2.41)$$

$$\sigma_{ht} = 52 e^{-14.47 p} \quad (2.42)$$

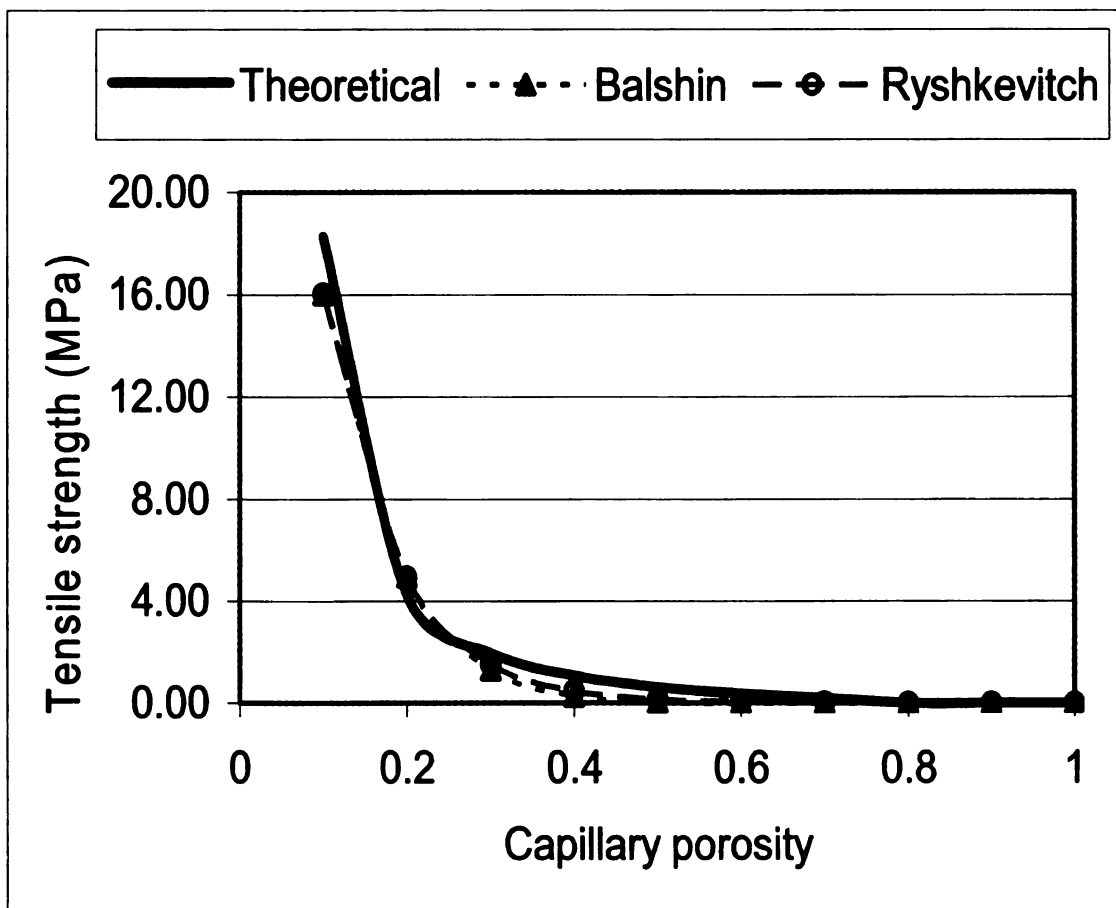


Fig. 2.25 - Comparing the predictions of the mechanistic and empirical tensile strength models of hcp

2.3.5 Compressive Strength Model of Hydrated Cement Paste

Several experimental studies have demonstrated that the mechanism of failure of hydrated cement paste subjected to compressive stress is by forming bundles of cracks parallel to the direction of loading. The crack lines are nearly straight and do not have pronounced tortuosity. Based on this observation, one can conclude that the compressive failure is due to the lateral tensile stresses caused by the poisson's effect (Fig. 2.26).

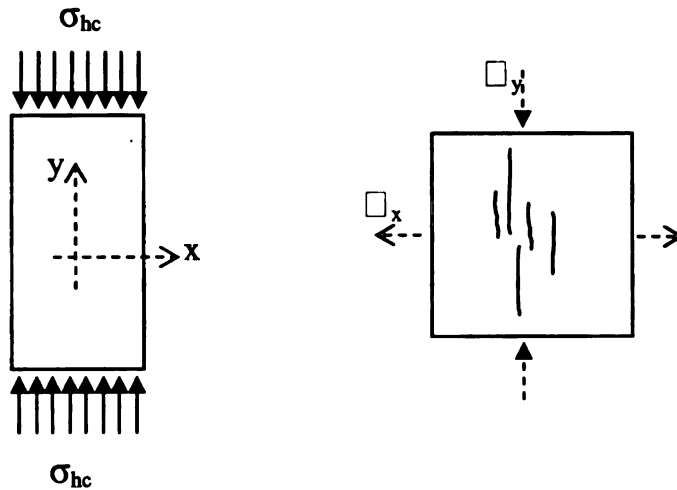


Fig. 2.26 - Crack formation due to compressive in hydrated cement paste specimen

The Poisson's effect under compression can be expressed as follows,

$$\varepsilon_x = -\nu\varepsilon_y = -\nu \frac{\sigma_{hc}}{E_h} \quad (2.43)$$

and

$$\varepsilon_x = \frac{\sigma_{ht}}{E_h} \quad (2.44)$$

Substituting Eqn. 2.42 into Eqn. 2.41 yields,

$$\sigma_{hc} = -\frac{\sigma_{ht}}{\nu} \quad (2.45)$$

Substituting Eqn. 2.40 into Eqn. 2.45 and taking the value of ν to be 0.2 gives the following compressive strength model of hydrated cement paste:

$$\sigma_{hc} = 33.63(1 - p_h) \sqrt{\frac{(\pi - 4p_h)^{0.37}}{p_h^{0.37} (10^6 (0.0148p - 8.8 \times 10^{-4})^2 + 0.041)}} \quad (2.46)$$

where, σ_{hc} is the compressive strength of hcp in MPa.

The predictions of the above model are evaluated by comparing them with those of empirical models developed based on experimental results (Fig. 2.27). The empirical models developed by Balshin⁵¹ (Eqn. 2.47) and Ryshkevitch⁵² (Eqn. 2.48) were used for evaluating the predictions of the theoretical model for the compressive strength of hydrated cement paste.

$$\sigma_{hc} = 540(1 - p)^{14.47} \quad (2.47)$$

$$\sigma_{hc} = 636 e^{-17.04 p} \quad (2.48)$$

It can be observed in Fig. 2.27 that there is no significant difference between the theoretical and empirical models except at smaller porosities, where even the empirical models are also considered to be less accurate.

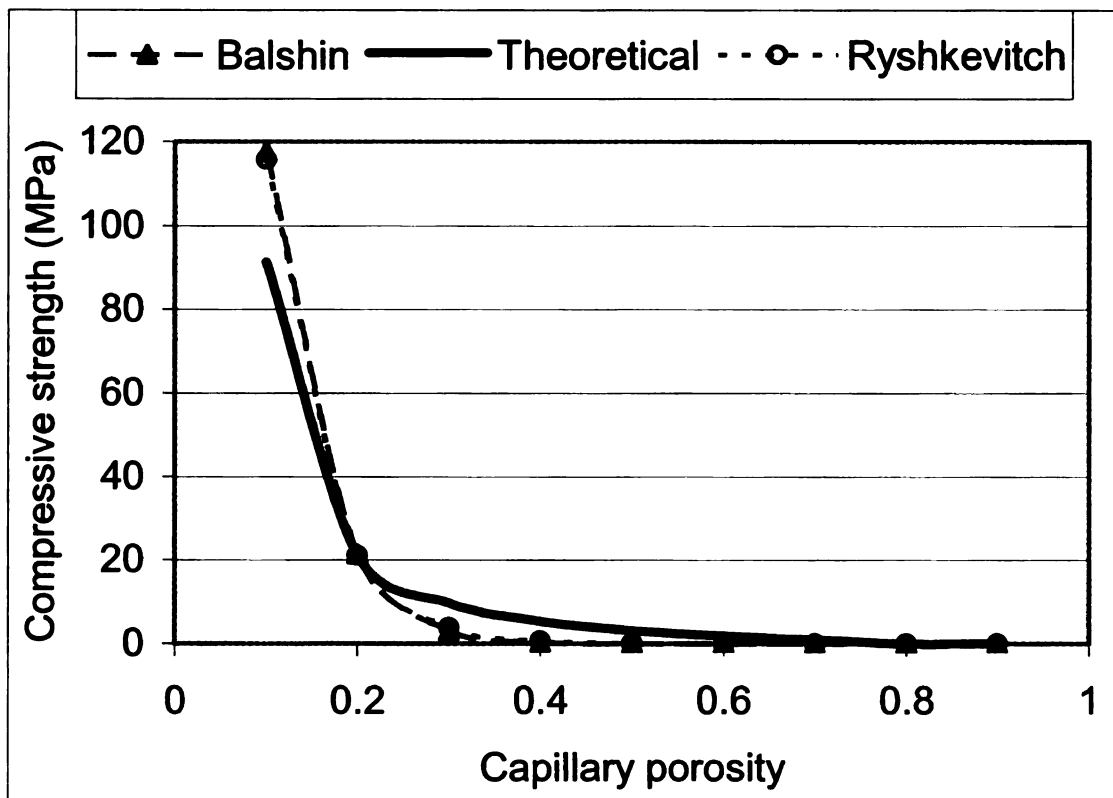


Fig. 2.27 - Predications of the compressive strength model of hcp versus those of empirical models derived based on experimental results.

CHAPTER 3

MODELING THE MECHANICAL PROPERTIES OF MORTAR BASED ON MECHANISTIC APPROACH

3.1 Introduction

Mortar is a composite material with general properties that are affected by the arrangement, characteristics and proportions of the constituent materials. These factors also influence the characteristics and arrangement of the three phases at micro-level. These phases are the hydrated cement paste, fine aggregate (sand), and interfacial transition zone. The interfacial transition zone is usually expressed as a region having a thickness of 30-50 μm , in which the cement paste composition differs significantly from that of the bulk cement paste.⁷² The interfacial transition zone has much higher porosity and CH volume fraction, and lower contents of C-S-H gel and unhydrated cement paste, than the bulk cement paste. This is attributed, to some extent, to the low packing of C-S-H gels near the surface of the aggregate particle.^{72,73} This phenomenon renders interfacial transition zone the weakest zone in mortar or concrete.⁷⁴ Therefore, the presence of the interfacial zone adds to the complexity of mortar or concrete. From the component materials point of view, the major factors affecting the bond strength of mortar include the water/cement ratio of the hydrated cement paste, the mineralogical nature and origin of fine aggregates, the surface roughness of aggregates, the age of the cement paste, and the aggregate size.⁷⁵

In this chapter, an attempt has been made to develop mechanical models of cement mortar based on mechanistic (theoretical) approach.

3.2 Modeling

The mechanical models of cement mortar were developed by expanding upon the models of hydrated cement paste. The addition of fine aggregates to hydrated cement paste changes the paste into a composite material. In this process, mortar is considered as a composite material composed of the hydrated cement paste matrix and fine-aggregate fillers. At micro-scale, another third phase is considered - the interfacial transition zone. The interfacial transition zone in mortar is a thin porous zone at the interface between hydrated cement paste and the surface of fine aggregate. The inclusion of aggregates into cement, unlike any other ceramics, does not improve the strength of the hydrated cement paste; rather, it reduces the strength considerably. This strength loss could be attributed to the influence of the interfacial transition zones, which are called the zones of weakness in cementitious materials where the porosity and the CH concentration are relatively high.

3.2.1 Modulus of Elasticity of Cement Mortar

Cracks propagate in cement mortar mostly through the hydrated cement paste and along the interfaces between hydrated cement paste and fine aggregate surfaces. This indicates

that the interfacial transition zone influences the mechanical properties of cement mortar. In modeling the modulus of elasticity of cement mortar, the effect of interfacial transition zone was considered. Cement mortar was modeled as a composite material composed of three phases: the hydrated cement paste, fine aggregates, and the interfacial transition zone.

In order to develop the modulus of elasticity model of cement mortar, it was necessary to determine the modulus of elasticity and shear modulus of every constituent phase of the composite material. For hydrated cement paste, the modulus of elasticity model developed in the preceding chapter (Eqn. 2.29) was used. The modulus of elasticity of the interfacial transition zone of cement mortar (E_{im}) was derived using the modulus of elasticity of hydrated cement paste with some modification. The porosity of the interfacial transition zone was considered to be about twice that of the hydrated cement paste.⁷⁶ This variation in porosity was accounted for in developing the modulus of elasticity of the interfacial transition zone (E_{im}) based on that of the hydrated cement paste (E_h). The modulus of elasticity of fine aggregates (E_s) ranges from 70 GPa to 90 GPa, depending on the aggregate type.⁷⁷ A parametric study was conducted to evaluate the significance of this range in determining the modulus of elasticity of cement mortar.

The upper and lower bounds of the modulus of elasticity of cement mortar were calculated from an equation relating the modulus of elasticity of a composite material to its shear modulus (G'_m) and bulk modulus (K'_m) (Eqn. 3.1).⁷⁸ The upper and lower bounds of the shear modulus and bulk modulus were calculated using the Hashin's modulus of

elasticity model for three-phase composite materials (Eqns. 3.2 – 3.5).⁷⁸ The steps followed in the computation of the upper and lower bounds for the modulus of elasticity of cement mortar are presented below.

The upper and lower bounds of the modulus of elasticity of mortar, E_m , were approximated as follows:⁷⁸

$$\frac{9K'_{m-}G'_{m-}}{3K'_{m-} + G'_{m-}} \leq E_m \leq \frac{9K'_{m+}G'_{m+}}{3K'_{m+} + G'_{m+}} \quad (3.1)$$

Where K'_{m+} and K'_{m-} are the upper and lower bounds of the bulk modulus of cement mortar, respectively; and G'_{m+} and G'_{m-} are the upper and lower bounds of the shear modulus of cement mortar, respectively.⁷⁸ These parameters were calculated as follows:

Lower bound of the bulk modulus of cement mortar, K'_{m-} ,⁷⁸

$$\frac{1}{K'_{m-}} = \frac{V'_h}{K'_h} + \frac{V'_s}{K'_s} + \frac{3V'_t t_r}{K'_i + 1.33G'_i} \quad (3.2)$$

Upper bound of the bulk modulus of cement mortar, K'_{m+} ,⁷⁸

$$K'_{m+} = V'_h K'_h + \frac{V'_s K'_s}{1 + \frac{3K'_s t_r}{K'_i + 1.33 G'_i}} \quad (3.3)$$

Lower bound of the shear modulus of cement mortar, G'_{m-} ,⁷⁸

$$\frac{1}{G'_{m-}} = \frac{V'_h}{G'_h} + \frac{V'_s}{G'_s} + 0.4V'_s t_r \left(\frac{2}{K'_i + 1.33 G'_i} + \frac{6}{G'_i} \right) \quad (3.4)$$

Upper bound of the shear modulus of cement mortar, G'_{m+} ,⁷⁸

$$G'_{m+} = V'_h G'_h + \frac{V'_s G'_s}{1 + \frac{2.5 G'_s t_r}{K'_i + 3.33 G'_i}} \quad (3.5)$$

where, V'_s is volume fraction of sand; and V'_h is volume fraction of hcp.

The next step was to determine all the parameters involved in the above equations.

The bulk modulus and shear modulus of any material are related to its modulus of elasticity through Eqns. 3.6 and 3.7, respectively:⁷⁸

$$K' = \frac{E}{3(1 - 2\nu)} \quad (3.6)$$

$$G' = \frac{E}{2(1 + \nu)} \quad (3.7)$$

where, ν is the poisson's ratio of cement mortar.

From the above relationships, the bulk modulus and shear modulus of hydrated cement paste and fine aggregates were calculated as follows (considering $\nu = 0.2$ for both the hydrated cement paste⁷⁹ and fine aggregates⁸⁰):

The bulk modulus of hydrated cement paste, K'_h ,

$$K'_h = \frac{E_h}{3(1 - 2\nu)} = \frac{E_h}{3(1 - 2(0.2))} = 0.56E_h \quad (3.8)$$

The bulk modulus of sand (fine aggregate), K'_s ,

$$K'_s = \frac{E_s}{3(1 - 2\nu)} = \frac{E_s}{3(1 - 2(0.2))} = 0.56E_s \quad (3.9)$$

The shear modulus of hydrated cement paste, G'_h ,

$$G'_h = \frac{E_h}{2(1 + \nu)} = \frac{E_h}{2(1 + 0.2)} = 0.42 E_h \quad (3.10)$$

The shear modulus of sand (fine aggregate), G'_s ,

$$G'_s = \frac{E_s}{2(1 + \nu)} = \frac{E_s}{2(1 + 0.2)} = 0.42 E_s \quad (3.11)$$

Based on the above relationships, the bulk modulus and the shear modulus of the interfacial transition zone of cement mortar could also be determined as follows:

$$K'_i = 0.56 E_i \quad (3.12)$$

$$G'_i = 0.42 E_i \quad (3.13)$$

For the value of the modulus of elasticity of sand (E_s) ranging from 70 to 90 GPa, the corresponding values of K'_s and G'_s range from 39.2 to 50.4 and 29.4 to 37.8, respectively. A parametric study conducted to assess the significance of these ranges in determining the mechanical properties of mortar is presented below. The modulus of

elasticity of the interfacial transition zone (E_i) is a function of the modulus of elasticity (E_h) and capillary porosity (P_h) of the hydrated cement paste in cement mortar. The ratio of the thickness of the interfacial transition zone to a radius of a sphere equivalent to fine aggregate, t_r ,⁷⁸ can be expressed as follows:

$$t_r = \frac{t_i}{r_s} \quad (3.14)$$

where, t_i is thickness of the interfacial transition zone, and is a function of aggregate size;⁸¹ and r_s is the radius of an equivalent spherical aggregate. Thickness of interfacial transition zone (t_i) is proportional to the size of the aggregate it envelops.⁸¹

No information could be found in the literatures on the approximate thickness of the interfacial transition zone in mortar. Therefore, it was approximated, based on the maximum interfacial transition zone thickness in concrete. A linear relationship between the aggregate size and the thickness of the interfacial transition zone was assumed as shown in Fig. 3.1. The aggregates size was considered to range from 0.1 to 4 mm and from 4 to 25 mm, for fine and coarse aggregates, respectively. The maximum thickness of the interfacial transition zone in concrete is about 50 μm .^{82, 72} This size was considered to occur for the 25 mm aggregate size. No interfacial transition zone was assumed to occur for an aggregate size lower than 0.1 mm. This assumption is based on the fact that no interfacial transition zone has been detected so far around CH crystals of the same size. Based on this relationship, the value of t_i ranged from 0 to 3.9 μm for aggregate size

ranging from 0.1 to 4 mm. A parametric study was conducted to investigate the significance of this range on the mechanical properties of mortar, and the results are presented in the next section..

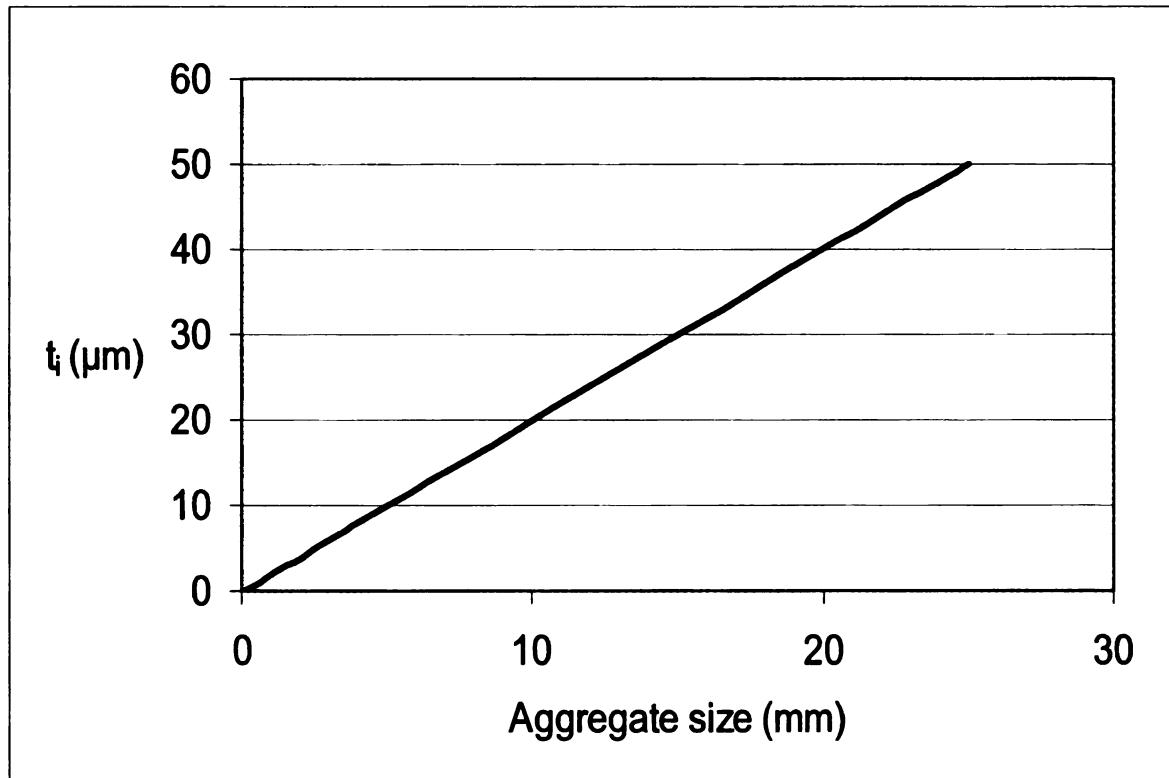


Fig. 3.1 - Variation of the interfacial transition zone thickness with aggregate size.

The significance of the three phases (hydrated cement paste, fine aggregates and interfacial transition zone) in determining the mechanical properties of cement mortar also depends upon their respective volume proportions in the mortar. The calculation of the volume fractions of hydrated cement paste (V'_h), fine aggregate (V'_s) and interfacial transition zone (V'_i) in cement mortar is discussed below.

Porosity of interfacial transition zone (P_i) is about two to three times that of hydrated cement paste, and 25% of the volume of interfacial transition zone is filled with CH crystals.⁸³ P_i was assumed to be about twice the porosity of hydrated cement paste.

The pore volume of mortar (V_{pm}) was expressed as the sum of the pore volumes of hydrated cement paste and the interfacial transition zones, as follows:

$$V_{pm} = V_{ph} + V_{pi} \quad (3.15)$$

where, V_{ph} and V_{pi} are the pore volumes of the hydrated cement paste and the interfacial transition zone, respectively.

Porosity of mortar (P_m) can also be expressed as the ratio of the pore volume of mortar to its total volume, as follows:

$$P_m = \frac{V_{pm}}{V_m} = \frac{V_{ph} + V_{pi}}{V_m} \quad (3.16)$$

where, V_m is the total volume of mortar, which is the sum of the volumes of fine aggregates and the bulk hydrated cement paste (the term bulk is used to refer to the hydrated cement paste and the interfacial transition zone as one entity). V_m can be expressed as follows:

$$V_m = V_s + V_h \quad (3.17)$$

When very large volume fractions of sand are used in cement mortar, the workability of the fresh mix tends to deteriorate. This damage to workability results in the formation of large voids and micro-defects, which would undermine the performance of the mortar. A reasonable range for the volume fraction of sand considered in this research is from 0.5 to 0.6. A mortar mix proportion, where sand and bulk hydrated cement paste constitute 55% and 45%, respectively, of the mortar volume was considered to represent conventional mortar mixtures. The volume of the interfacial transition zone surrounding a single sand particle in cement mortar (V_{it}) was calculated using Eqn. 3.18 based on the relationship between aggregate size and the interfacial transition zone thickness, as shown in Fig. 3.1. A circular cylinder with aspect (height-to-diameter) ratio equal to 1 was considered as a geometric model of sand (Fig. 3.2).

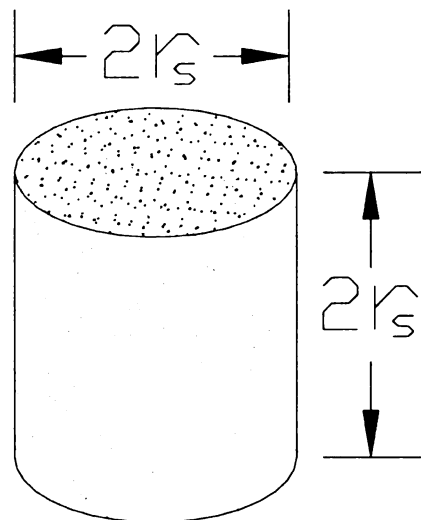


Fig 3.2 - Schematic presentation of the geometric model of a sand particle.

This geometric model implies that:

$$V_{1i} = 2\pi \left((r_s + t_i)^3 - r_s^3 \right) \quad (3.18)$$

Assuming a uniform aggregate size, the number of sand particles per unit volume of cement mortar (N_s) was calculated as follows:

$$N_s = \frac{V_s}{V_{1s}} = \frac{V_s}{2\pi r_s^3} \quad (3.19)$$

where, V_{1s} is the volume of a single cylindrical sand particle of radius r_s and height $2r_s$, as shown in Fig. 3.2.

The total volume of the interfacial transition zone (V_i) was then calculated as the product of N_s and V_{1i} , as follows:

$$V_i = V_{1i} \times N_s \quad (3.20)$$

Since the thickness of the interfacial transition zone is proportional to the size of fine aggregate, for a constant aggregate volume, the volume fraction of the interfacial

transition zone and the hydrated cement paste remain constant with a change in aggregate size (at constant aggregate volume), as shown in Table 3.1.

Table 3.1 - Volume fractions of the interfacial transition zone and the hydrated cement paste for different aggregate sizes (at constant aggregate volume) in cement mortar.

r_s (m)	t_i (m)	t_r	V_{ii} m^3	N_s	V_i	V_h
3.00E-04	1.20E-06	4.00E-03	2.04E-12	3.24E+09	0.007	0.443
1.20E-03	4.80E-06	4.00E-03	1.31E-10	5.07E+07	0.007	0.443
2.00E-03	8.00E-06	4.00E-03	6.06E-10	1.09E+07	0.007	0.443

3.2.2 Parametric Study of the Effect of the Fine Aggregate Elastic Modulus on the Modulus of Elasticity of Cement Mortar

Since the modulus of elasticity of fine aggregates used in cement mortar ranges from 70 to 90 MPa, an extensive parametric study was conducted to assess the significance of this range of aggregate elastic modulus in determining the modulus of elasticity of cement mortar. It could be observed from the results of the study presented below that the cement mortar elastic modulus does not change significantly as the aggregate elastic modulus varies within the applicable range. In this parametric study, all parameters related to hydrated cement paste were obtained from the results presented in preceding chapters (for example, $E_o = 38$ GPa, and capillary pore aspect ratio, a/b , equal to 2). Based on the results presented in Table 3.1, $V'_h = 0.443$, $V'_i = 0.007$ and $V'_s = 0.55$ were considered for determining the modulus of elasticity of cement mortar. The elastic modulus of hydrated

cement paste was calculated by substituting the above values into Eqn. 2.29, and simplifying it to obtain:

$$E_h = 5.852(1 - p_h) \frac{(\pi - 4p_h)^{0.37}}{p_h^{0.37}} \quad (3.21)$$

The modulus of elasticity of the interfacial transition zone was calculated by modifying Eqn. 3.21 assuming that the porosity of the interfacial transition zone is twice that of the hydrated cement paste.⁷⁶ The value of the modulus of elasticity of the interfacial transition zone was multiplied by a factor of 0.75 to account for the 25% volume fraction of the directionally oriented CH crystals in the transition zone.

$$E_i = 3.4(1 - 2p_h) \frac{(\pi - 8p_h)^{0.37}}{p_h^{0.37}} \quad (3.22)$$

E_h and E_i were calculated using Eqns. 3.21 and 3.22, for a reasonable range of capillary porosity in cement mortar. The results are presented in Table 3.3.

Table 3.3 - The E_h and E_i values calculated for different values of capillary porosity in hydrated cement paste

P_h	E_h (Pa)	E_i (Pa)
0.01	4.84E+10	2.77E+10
0.06	2.31E+10	1.22E+10
0.11	1.70E+10	8.12E+09
0.16	1.36E+10	5.73E+09
0.21	1.12E+10	4.04E+09
0.26	9.39E+09	2.75E+09
0.31	7.91E+09	1.71E+09
0.36	6.66E+09	8.44E+08

The next step was to find a relationship between E_h and E_i . This relationship was obtained by plotting the corresponding values of E_h and E_i from Table 3.3, and fitting a curve as shown in Fig. 3.3. The resulting equation relating E_h and E_i is shown below.

$$E_i = 0.642 E_h - 3.15 \quad (3.23)$$

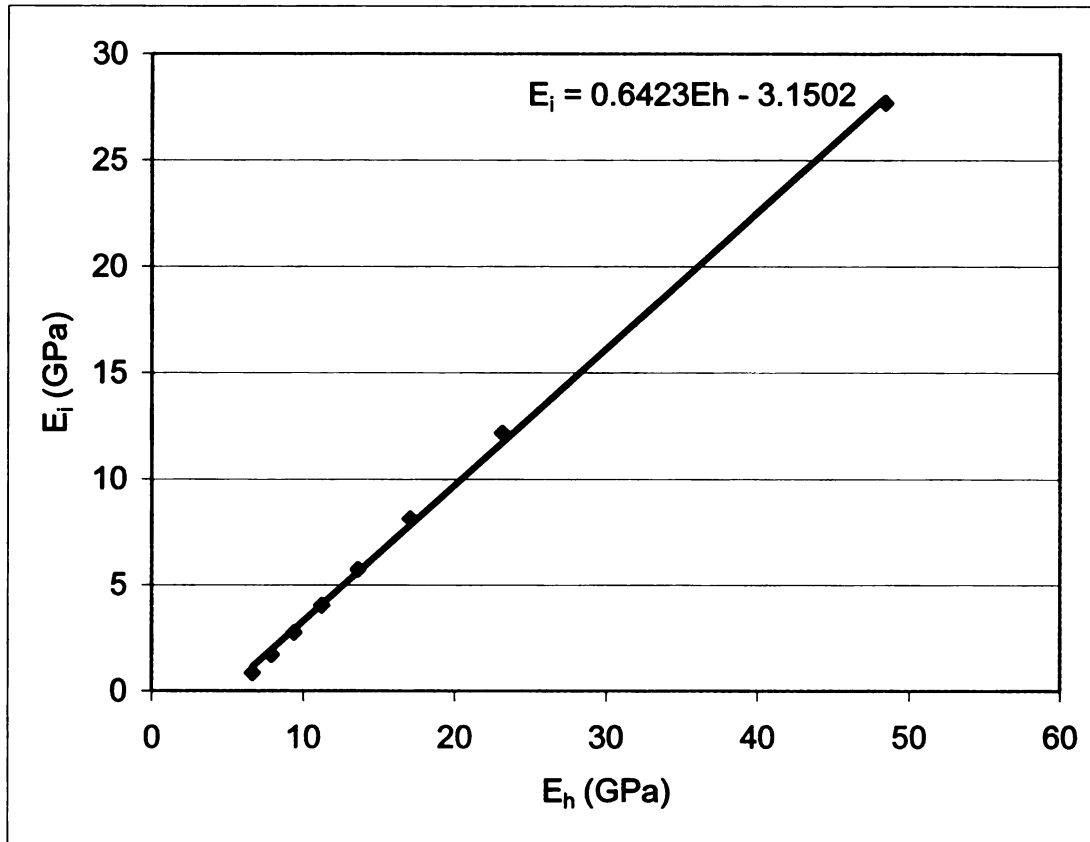


Fig. 3.3 - The relationship between the moduli of elasticity of the hydrated cement paste and the interfacial transition zone in cement mortar.

The values of K'_s and G'_s for sand were calculated using Eqns. 3.9 and 3.11, for various values of the modulus of elasticity of fine aggregates. The resulting values are shown in Table 3.4.

Table 3.4 - The bulk and shear moduli of fine aggregate (sand) in mortar.

E_s (GPa)	K'_s (GPa)	G'_s (GPa)
70	39.2	29.4
80	44.8	33.6
90	50.4	37.8

Tables 3.5, 3.6 and 3.7 present the results of the parametric studies concerned with determining the effects of the variations in E_s . From these tables, one can also conclude that the variation in aggregate size does not have a considerable effect on the modulus of elasticity of cement mortar. Three aggregate sizes (0.6 mm, 2.3 mm and 4 mm) were compared, and the results suggest that the upper and lower bounds of the shear modulus and the bulk modulus did not change considerably with aggregate sizes. The reason for this is that the bulk modulus and the shear modulus of a material, as shown in corresponding equations, depend on volume fractions and elastic moduli of the individual phases in the composite material and not on aggregate size. In the case of the third phase in cement mortar, the interfacial transition zone, though its volume depends on aggregate size, its volume fraction remains constant because its thickness changes linearly with aggregate size as discussed previously.

Table 3.5 - The upper and lower bounds of bulk modulus and shear modulus of cement mortar with fine aggregate having modulus of elasticity of 70 GPa.

	K' (Gpa)			K'_{m*} (Gpa)			G'_{m*} (Gpa)			G'_{m*} (Gpa)		
	0.6 (mm)	2.3 (mm)	4 (mm)	0.6 (mm)	2.3 (mm)	4 (mm)	0.6 (mm)	2.3 (mm)	4 (mm)	0.6 (mm)	2.3 (mm)	4 (mm)
d _s												
P _h												
0.01	32.83	32.83	32.83	33.18	33.18	33.18	24.48	24.48	24.48	25.01	25.01	25.01
0.06	20.62	20.62	20.62	26.54	26.54	26.54	15.34	15.34	15.34	20.19	20.19	20.19
0.11	16.43	16.43	16.43	24.70	24.70	24.70	12.21	12.21	12.21	18.95	18.95	18.95
0.16	13.74	13.74	13.74	23.44	23.44	23.44	10.19	10.19	10.19	18.16	18.16	18.16
0.21	11.69	11.69	11.69	22.29	22.29	22.29	8.65	8.65	8.65	17.51	17.51	17.51
0.26	10.02	10.02	10.02	21.01	21.01	21.01	7.38	7.38	7.38	16.85	16.85	16.85
0.31	8.56	8.56	8.56	19.25	19.25	19.25	6.27	6.27	6.27	16.01	16.01	16.01
0.36	7.19	7.19	7.19	16.03	16.03	16.03	5.19	5.19	5.19	14.42	14.42	14.42

Table 3.6 - The upper and lower bounds of bulk modulus and shear modulus of cement mortar with fine aggregate having modulus of elasticity of 80 GPa.

	K _m (Gpa)			K _{m*} (Gpa)			G _m (Gpa)			G _{m*} (Gpa)			
	d _s	0.6 (mm)	2.3 (mm)	4 (mm)	0.6 (mm)	2.3 (mm)	4 (mm)	0.6 (mm)	2.3 (mm)	4 (mm)	0.6 (mm)	2.3 (mm)	4 (mm)
P _h													
0.01	34.83	34.83	34.83	34.83	36.16	36.16	36.16	25.97	25.97	25.97	27.29	27.29	27.29
0.06	21.40	21.40	21.40	21.40	29.40	29.40	29.40	15.92	15.92	15.92	22.43	22.43	22.43
0.11	16.92	16.92	16.92	16.92	27.46	27.46	27.46	12.56	12.56	12.56	21.15	21.15	21.15
0.16	14.08	14.08	14.08	14.08	26.09	26.09	26.09	10.44	10.44	10.44	20.32	20.32	20.32
0.21	11.94	11.94	11.94	11.94	24.79	24.79	24.79	8.83	8.83	8.83	19.61	19.61	19.61
0.26	10.19	10.19	10.19	10.19	23.28	23.28	23.28	7.51	7.51	7.51	18.85	18.85	18.85
0.31	8.69	8.69	8.69	8.69	21.18	21.18	21.18	6.36	6.36	6.36	17.85	17.85	17.85
0.36	7.29	7.29	7.29	7.29	17.34	17.34	17.34	5.25	5.25	5.25	15.91	15.91	15.91

Table 3.7 - The upper and lower bounds of bulk modulus and shear modulus of cement mortar with fine aggregate having modulus of elasticity of 90 GPa.

d_s	K'_{m+} (Gpa)			K'_{m-} (Gpa)			G'_{m+} (Gpa)			G'_{m-} (Gpa)		
	0.6 (mm)	2.3 (mm)	4 (mm)									
0.01	36.57	36.57	36.57	39.13	39.13	39.13	27.26	27.26	27.26	29.56	29.56	29.56
0.06	22.04	22.04	22.04	32.24	32.24	32.24	16.39	16.39	16.39	24.65	24.65	24.65
0.11	17.32	17.32	17.32	30.19	30.19	30.19	12.86	12.86	12.86	23.33	23.33	23.33
0.16	14.35	14.35	14.35	28.68	28.68	28.68	10.64	10.64	10.64	22.45	22.45	22.45
0.21	12.14	12.14	12.14	27.21	27.21	27.21	8.98	8.98	8.98	21.67	21.67	21.67
0.26	10.34	10.34	10.34	25.47	25.47	25.47	7.62	7.62	7.62	20.82	20.82	20.82
0.31	8.79	8.79	8.79	23.01	23.01	23.01	6.44	6.44	6.44	19.64	19.64	19.64
0.36	7.36	7.36	7.36	18.54	18.54	18.54	5.30	5.30	5.30	17.33	17.33	17.33

The upper and lower bounds of the modulus of elasticity of cement mortar (E_{m+} & E_{m-}) for different elastic moduli of fine aggregates were calculated using Eqn. 3.1. The results (as shown in Table 3.8) were plotted (Fig. 3.4) in order to assess the influence of the variation in fine aggregate elastic modulus (E_s) on the modulus of elasticity of mortar (E_m).

Table 3.8 - The upper and lower bounds of the elastic moduli of three cement mortars each containing a fine aggregate with a specific modulus of elasticity.

Ea	E _{m-}			E _{m+}		
	70	80	90	70	80	90
P _h	GPa	GPa	GPa	GPa	GPa	GPa
0.01	58.83	62.40	65.50	59.97	65.41	70.84
0.06	36.88	38.26	39.40	48.33	53.65	58.94
0.11	29.35	30.21	30.92	45.27	50.48	55.65
0.16	24.50	25.10	25.59	43.31	48.39	53.42
0.21	20.82	21.25	21.60	41.64	46.55	51.38
0.26	17.78	18.10	18.35	39.89	44.54	49.08
0.31	15.12	15.34	15.52	37.60	41.80	45.87
0.36	12.55	12.70	12.82	33.27	36.56	39.65

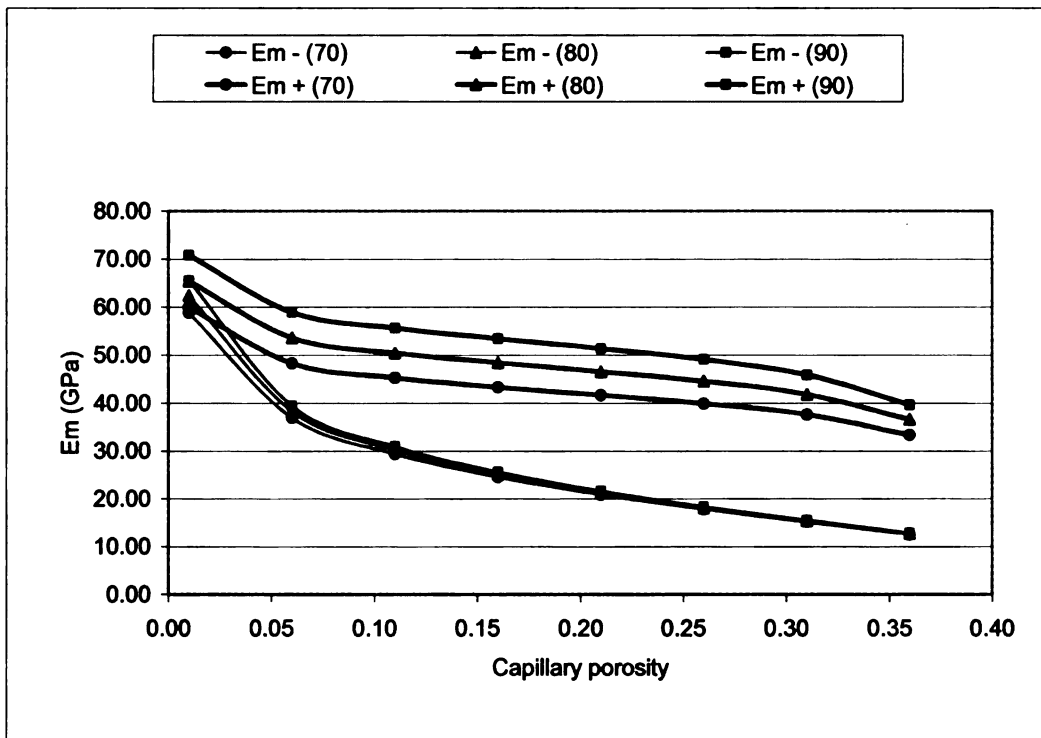


Fig. 3.4 - The upper and lower bounds of the elastic moduli of three cement mortars each containing fine aggregates with different elastic moduli.

It can be observed in Fig. 3.4 that the variations in the upper bounds for E_m tend to be more pronounced relative to those in the lower bounds. However, it could generally be concluded that the effect of the variation in the fine aggregate elastic modulus, within the given range, on the modulus of elasticity of cement mortar is not of great significance. Based on this observation, an average value for the modulus of elasticity of fine aggregate, 80 GPa, was considered as a representative value in development of the model.

3.2.3 Comparing the Predictions of Mechanistic Model of the Elastic Modulus of Cement Mortar with those of Empirical Models

Once the upper and lower bounds of the elastic modulus of cement mortar were established, the next step was to narrow down these bounds and develop a reasonable model for the modulus of elasticity of cement mortar that can also be applied toward development of the corresponding strength model. For this purpose, the predictions of an empirical⁸⁴ model for elastic modulus (based on substantial experimental data) were introduced into Fig. 3.4, with the results shown in Fig. 3.5. This figure suggests that the predictions of the empirical model fall within the upper and lower bounds of the theoretical model, leaning more toward the lower bounds.

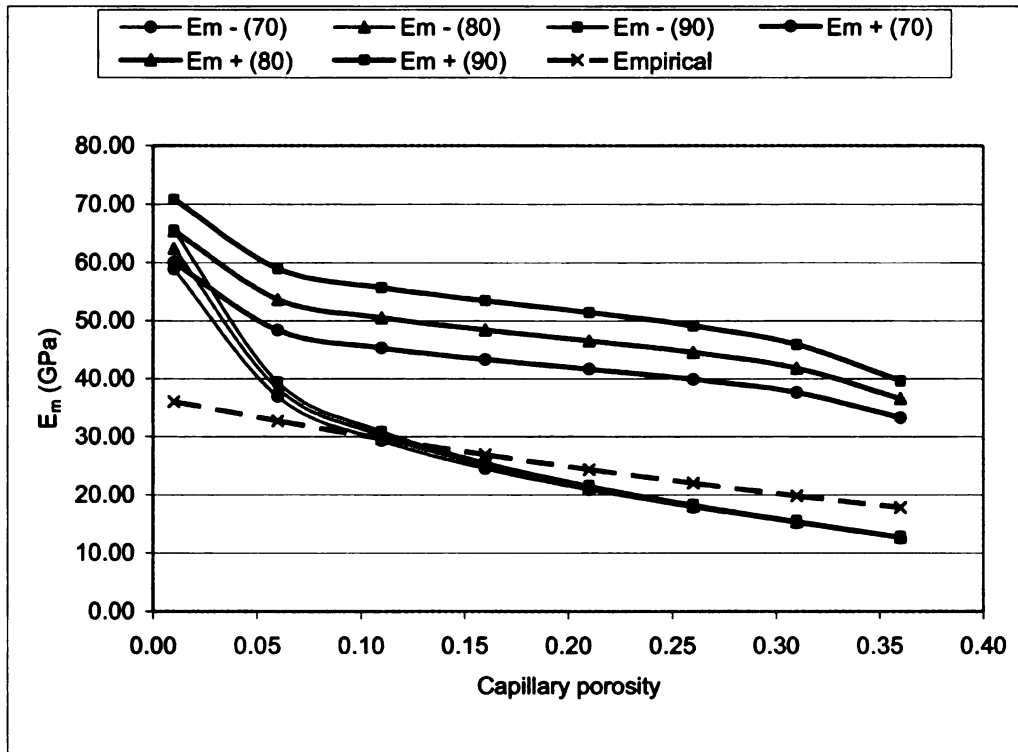


Fig. 3.5 – Comparing the predictions of theoretical model for the elastic modulus of cement mortar with those of empirical model based on substantial test data

Based on the trends observed in Fig. 3.5, it was concluded that the lower-bound model of elastic modulus reasonably represents the trends observed in experimentally obtained elastic modulus of cement mortar. The modulus of elasticity of cement mortar was then represented as follows:

$$E_m \approx \frac{9K'_{m-} G'_{m-}}{3K'_{m-} + G'_{m-}} \quad (3.24)$$

With aggregate elastic modulus (E_s) of 80 GPa, Eqn. 4.35 yields the following expression for the modulus of elasticity of cement mortar in terms of the elastic modulus of hydrated cement paste.

$$E_m \approx \frac{5.78E_h^2 - 28.35E_h}{0.04E_h^2 + 2.43E_h - 12.46} \quad (3.25)$$

where, E_h is the modulus of elasticity of hydrated cement paste, given by Eqn. 3.21.

3.2.4 Mechanistic Model for the Fracture Toughness of Cement Mortar

It was noted earlier that the key source of fracture toughness in hydrated cement paste is the pull-out of CH crystals. In the case of cement mortar, one should add the contributions of sand (fine aggregate) pull-out to fracture toughness. This phenomenon is

expected to make major contributions to fracture toughness by increasing the surface area involved in frictional pull-out. Sand particles are assumed to have rough surfaces, with the hydrated cement paste interacting with sand particles as shown in Fig. 3.6.

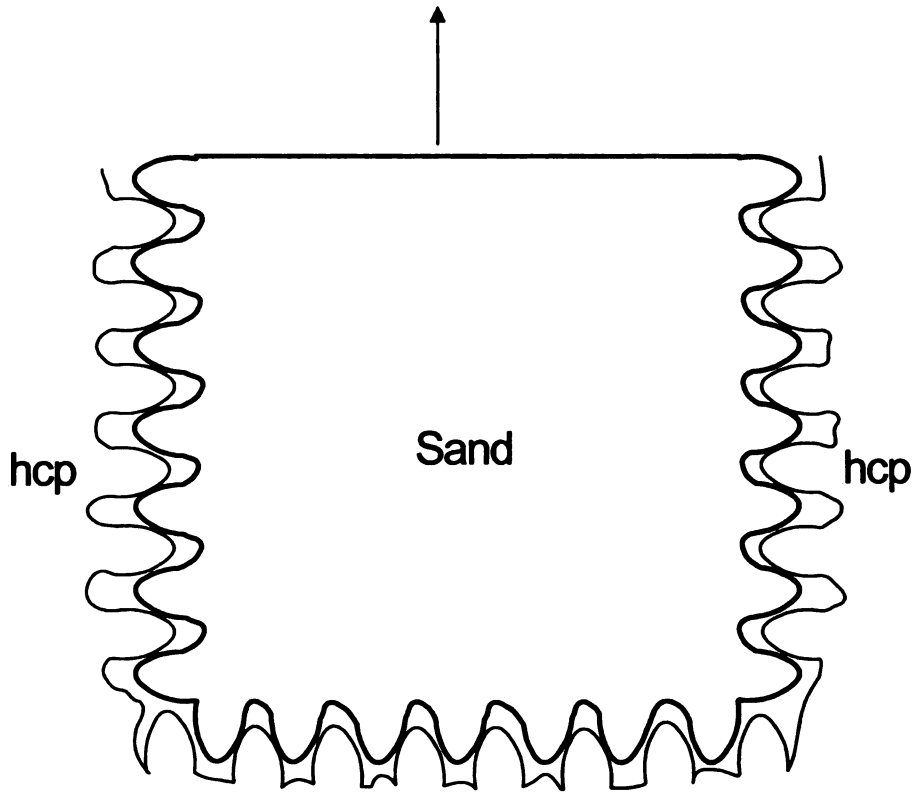


Fig. 3.6 - Surface roughness of fine aggregate, and interaction of the hydrated cement paste (hcp) at the interfacial transition zone

The computation of the fracture toughness of cement mortar was based upon the energy dissipated during the pull-out of sand particles, which involves phononic friction as the dendrites of hydrated cement paste bonding to the sand surface shear off (Fig. 3.6). Further, the crack-shielding effect associated with sand particles contributes to fracture toughness by enhancing formation of process zones in front of the crack tip. Actually, it is assumed that each dendrite of hydrated cement paste is subjected to shearing force

from the sand surfaced dendrites, acting at the median contact surface. This causes a diagonal tension stress on the hydrated cement paste dendrites, generating a 45 degree diagonal crack as shown in Fig. 3.7. When sand particle pulls out, its rough surface exerts a stress on the dendrites of the hydrated cement paste causing them to shear off. The surface area of the hydrated cement paste subjected to this type of stress was approximated to be about half of the pulled-out surface area of the sand.

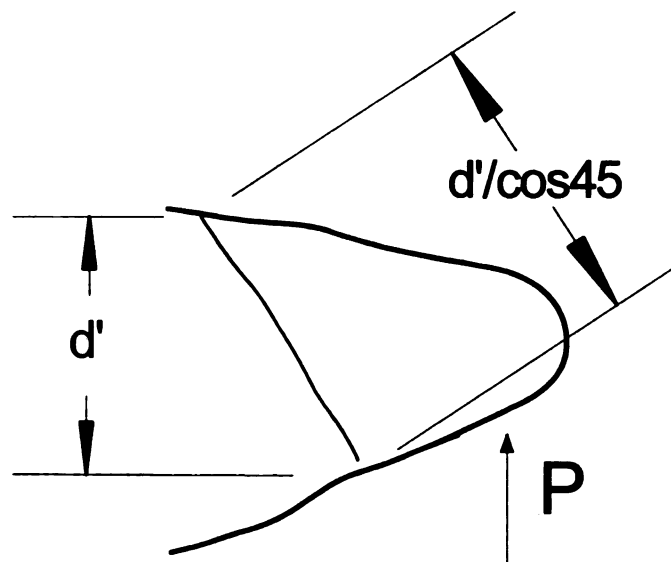


Fig 3.7 - The cracking pattern of the hydrated cement paste dendrite due to force P generated by sand pull-out.

The surface area of sand subjected to pull-out and debonding was computed by considering a circular cylinder sand particle model as shown in Fig. 3.8. The shaded region in Fig. 3.8 is the mean surface area of sand which would be subjected to friction during pull-out. This region is assumed to occur, on the average, at the lower quarter of the cylinder height.

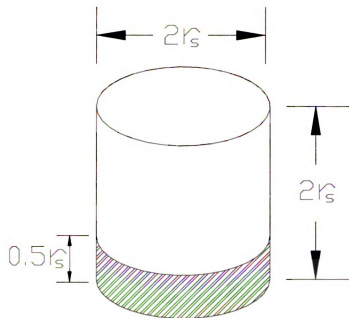


Fig. 3.8 - Surface of sand particle subjected to frictional pull-out

3.2.4.1 Energy Released During Debonding of Sand Particles from Hydrated Cement Paste

The interfacial surface area of sand that is subjected to debonding (followed by pull-out), A_{sd} , can be expressed as follows:

$$A_{sd} = 2\pi r_s^2 \quad (3.26)$$

In order to account for the porosity of the interfacial transition zone (estimated at twice that of hydrated cement paste, P_h), equation 3.26 was further modified as follows:

$$A'_{sd} = 2\pi r_s^2 (1 - 2P_h) \quad (3.27)$$

Debonding of sand occurs essentially through cracking of the interface zone, and involves debonding of C-S-H globules. The energy lost due to debonding of C-S-H globules, calculated earlier, is about 1.56 J/m². Therefore, the energy (in Joule) released (U_{sd}) due to the debonding of sand from hydrated cement paste (i.e., due to debonding of C-S-H globules in the interfacial transition zone) can thus be calculated as follows:

$$U_{sd} = 1.56 A'_{sd} \quad (3.28)$$

$$\Rightarrow U_{sd} = 3.12\pi r_s^2 (1 - 2P_h) \quad (3.29)$$

The fracture energy released per unit area of mortar (G_{sd} , in J/m²), due to C-S-H/C-S-H debonding, can be calculated as the total debonding energy released due to one sand particle divided by the projected area of the sand on a plane perpendicular to the pull-out direction (see equations 3.30 and 3.31).

$$G_{sd} = \frac{3.12\pi r_s^2}{\pi r_s^2} (1 - 2P_h) \quad (3.30)$$

$$\Rightarrow G_{sd} = 3.12 (1 - 2P_h) \quad (3.31)$$

3.2.4.2 Energy Released During Pull-out of Sand Particles from Hydrated Cement Paste

The surface area of sand subjected to frictional pull-out (A'_{sp}) is the shaded area of the cube in Fig. 3.8 excluding the bottom surface.

$$A'_{sp} = \pi r_s^2 (1 - 2P_h) \quad (3.32)$$

When the dendrites of hydrated cement paste shear off due to sand pull-out, the fractured diameter of the dendrites is about $1.414 d'$ (due to diagonal shear effect), as shown in Fig. 3.7. Due to the assumption that the dendrites of both hydrated cement paste and sand are interlocked (Fig 3.6), the total surface area of hydrated cement paste subjected to shear stress (A'_{sph}) is about 1.414 times A'_{sp} . Therefore,

$$A'_{sph} = 1.414 \pi r_s^2 (1 - 2P_h) \quad (3.33)$$

The energy (U_{chspi}) released due to CH pull-out upon fracture over A'_{sph} can be calculated as the product of G_p and A'_{sph} (see equation 3.34). G_p is the energy released per unit

fractured surface area (due to CH pull-out in hydrated cement past), and is considered to be equal to 27.88 J/m^2 , as discussed in Chapter 2.

$$U_{chsp1} = 27.88 A'_{sph} \quad (3.34)$$

$$\Rightarrow U_{chsp1} = 39.42 \pi r_s^2 (1 - 2P_h) \quad (3.35)$$

Let U_{chsp2} represent the energy released due to CH pull-out at the bottom surface of sand particle. It can be calculated as the product of G_p and the base area of sand particle:

$$U_{chsp2} = 27.88 \pi r_s^2 (1 - 2P_h) \quad (3.36)$$

The total energy released due to CH pull-out during the pull-out of sand from hydrated cement paste in mortar (U_{chsp}) is, therefore, the sum of U_{chsp1} and U_{chsp2} , and is given as:

$$U_{chsp} = U_{chsp1} + U_{chsp2} \quad (3.37)$$

$$U_{chsp} = 67.3 \pi r_s^2 (1 - 2P_h) \quad (3.38)$$

The energy released per unit fractured area of interfacial transition zone (G_{chsp} , in J/m²), due to CH pull-out, can be calculated as the total energy released as one sand particle pulls out divided by the projected area of the sand on a plane perpendicular to the pull-out direction (see equations 3.39 and 3.40).

$$G_{chsp} = \frac{67.3\pi r_s^2 (1 - 2P_h)}{\pi r_s^2} \quad (3.39)$$

$$\Rightarrow G_{chsp} = 67.3(1 - 2P_h) \quad (3.40)$$

The total energy released rate per unit fractured area of the interfacial transition zone in mortar (G_{im}) can now be calculated as the sum of G_{chsp} and G_{sd} :

$$G_{im} = G_{chsp} + G_{sd} \quad (3.41)$$

$$\Rightarrow G_{im} = 70.4(1 - 2P_h) \quad (3.42)$$

The other factor which contributes to the fracture toughness of cement mortar is the crack growth shielding effect of sand particles. This crack shielding effect results from bridging of the two crack surfaces by sand particles near the crack tip. This phenomenon promotes multiple microcracking ahead of the crack tip in hydrated cement paste. The region where

these microcracks form is called crack process zone. For typical volume fractions of sand used in mortar, formation of the process zone further increases the fracture toughness of hydrated cement paste by about 65%. The total fracture toughness of hydrated cement paste (G_o) was calculated in Chapter 2 at about 29.44 J/m². Therefore, the modified fracture toughness of hydrated cement paste in mortar will be about 1.65 x 29.44 = 48.58 J/m².

Fracture toughness of mortar (G_m) was calculated as the sum of the fracture toughness of the interfacial transition zone and that of hydrated cement paste, proportional to their respective volume fractions in cement mortar:

$$G_m = G_{im} V'_s + G_h V'_h \quad (3.43)$$

where, V'_s is the sand (and the small interfacial transition zone) volume fractions in mortar; and V'_h is the hydrated cement paste volume fraction in mortar. As noted in previous sections, $V'_s = 0.557$ and $V'_h = 0.443$ are used as reasonable examples. It was also shown in Chapter 2 that $G_h = G_o(1-P_h)$ and $G_o = 48.58$ J/m². Substituting these values into equation 3.43 yields:

$$G_m = 70.4(1 - 2P_h) + 21.38(1 - P_h) \quad (3.44)$$

$$\Rightarrow G_m = 91.78(1 - 1.75P_h) \quad (3.45)$$

The fracture toughness from this model for a reasonable capillary porosity ranges from 44 to 76 J/m², which is in conformance with the experimental values of the fracture toughness of cement mortar which ranges from 55 to 75 J/m².⁸⁵

The resulting values of G_m are plotted as shown in Fig. 3.9 versus the capillary porosity of hydrated cement paste.

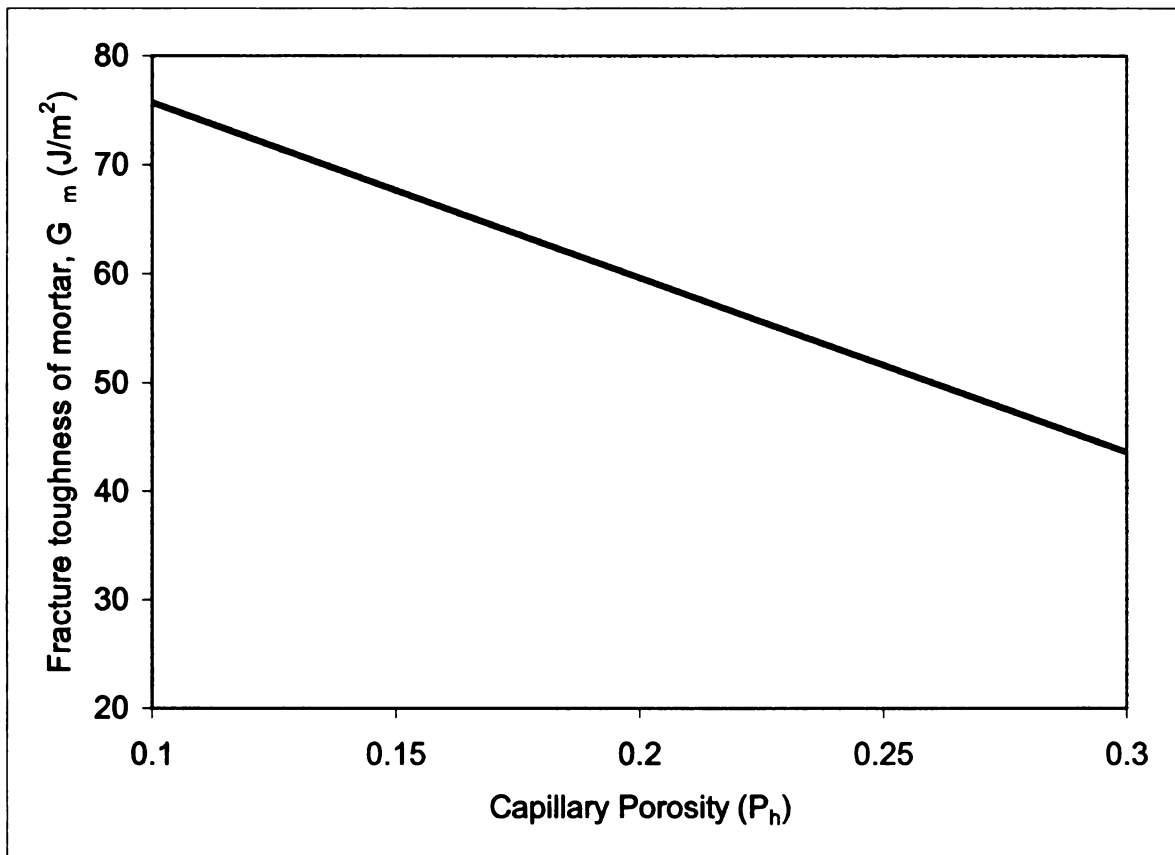


Fig. 3.9 - Fracture toughness of mortar as a function of the capillary porosity of hydrated cement paste

A parametric study was conducted to investigate the significance of sand volume fraction in determining the fracture toughness of cement mortar. The relationships between the fracture toughness of cement mortar (G_m) and the volume fraction of sand (V'_s) for capillary porosities (P_h) of 0.3, 0.05 and 0 are plotted as shown in Figs. 3.10, 3.11 and 3.12, respectively (for the typical conditions considered earlier). The addition of sand is observed to yield marked improvements in fracture toughness; however, the increase in sand volume fraction have relatively small effects on the fracture toughness of cement mortar.

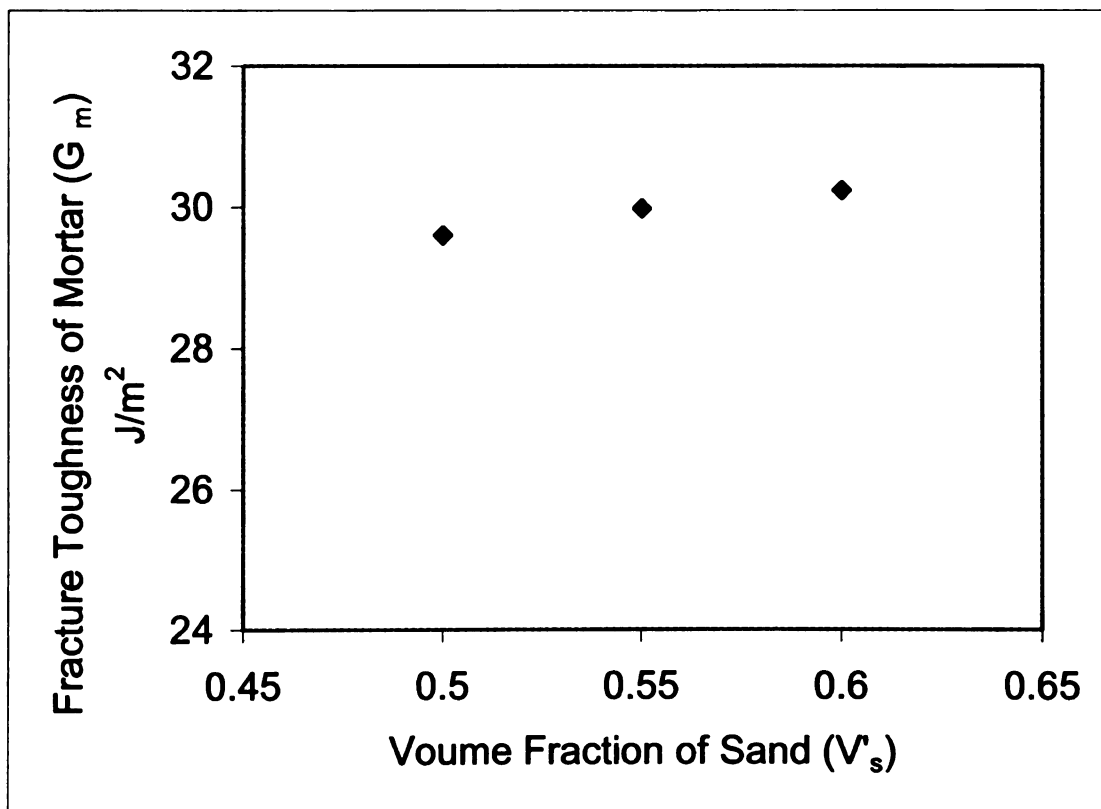


Fig. 3.10 - Fracture toughness of mortar as a function of the volume fraction of sand for a capillary porosity of 0.3

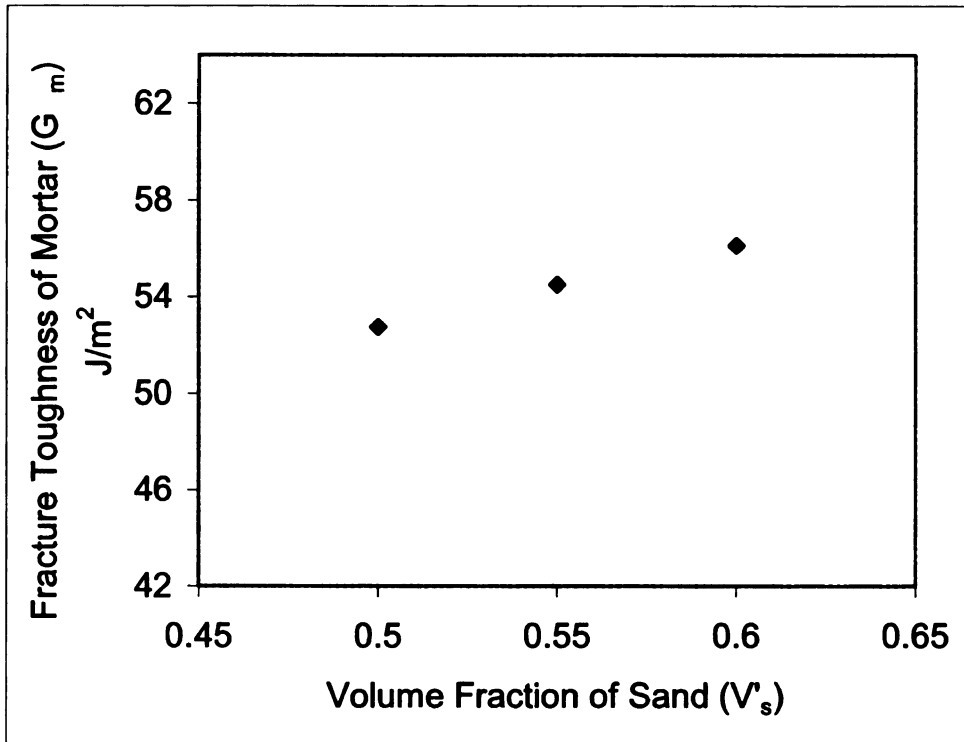


Fig. 3.11 Fracture toughness of mortar as a function of the volume fraction of sand for a capillary porosity of 0.05.

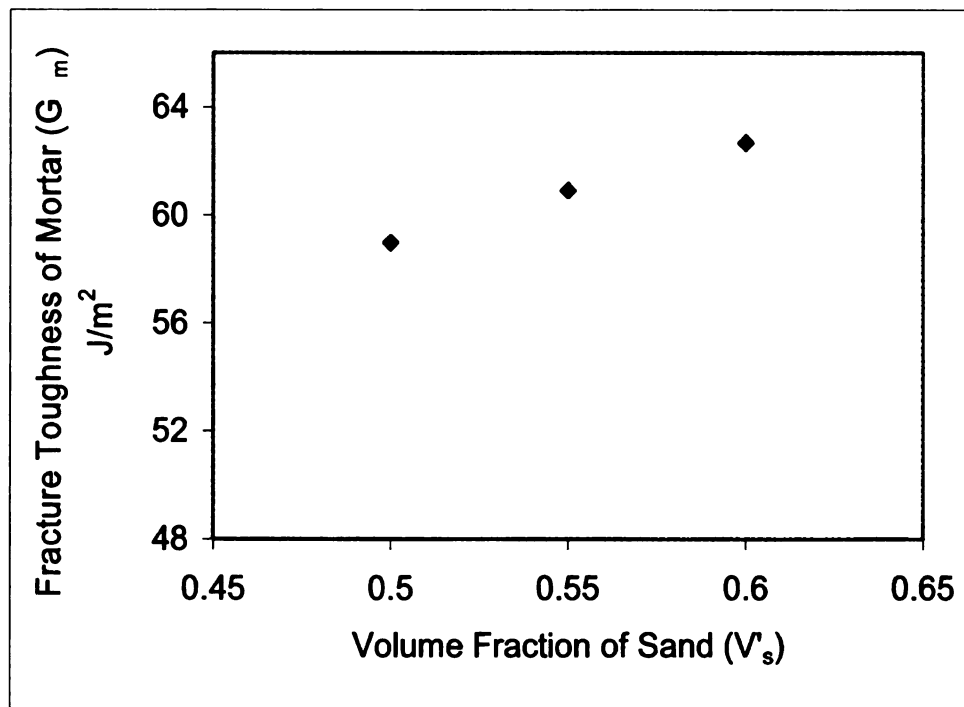


Fig. 3.12 Fracture toughness of mortar as a function of the volume fraction of sand for a capillary porosity of 0.

3.2.5 Tensile Strength Model of Cement Mortar

The tensile strength model of cement mortar was developed in the same manner as that for hydrated cement paste. The Griffith equation is applied to develop the strength-porosity relationship of cement mortar as follows:

$$\sigma_{mt} = \sqrt{\frac{E_m G_m}{\pi l_m}} \quad (3.46)$$

where, E_m is the modulus of elasticity of cement mortar; G_m is the fracture toughness of cement mortar; and l_m is half the critical crack length at which unstable crack propagation occurs in mortar. Many microcracks form in cement mortar prior to any loading due to restrained shrinkage effects. The restraint of drying shrinkage partly results from the presence of the dimensionally stable and high-modulus aggregates within the cement paste. Microcracks tend to initiate at the interfacial transition zone, and then propagate towards the hydrated cement paste. These cracks may extend over and bridge between two adjacent sand particles.^{73,86} In this research, the critical crack length in cement mortar is considered to extend between two sand particles, as shown in Fig. 3.13.

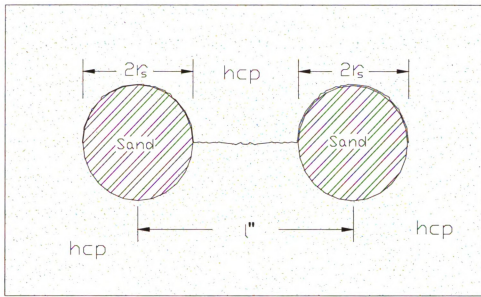


Fig. 3.13 - The critical shrinkage crack in cement mortar bridging between two adjacent sand particles

The interfacial transition zone is the weakest region where restrained shrinkage cracks initiate. Therefore, from Fig. 3.13, initial crack length in mortar was determined as the sum of the center-to-center distance between two sand particles (l'') and the size of sand (a) (Eqn. 3.47).

$$l_m = 0.5(l'' + 2r_s) \quad (3.47)$$

Shrinkage cracks are more likely to occur around larger aggregates due to the fact that their interfaces are weaker (due to attraction of greater quantities of bleeding water) and also because restrained shrinkage stresses tend to be greater in their vicinity. For this reason, the aggregate size in mortar where crack is likely to initiate was considered to be 4 mm (i.e., close to the upper bound of fine aggregate particle size). If we assume a

uniform sand particle size in cement mortar, the center-to-center spacing of sand particles (l'') can be calculated for the case with sand volume fraction of 0.55 as follows:

$$\Rightarrow 2\pi r_s^3 = 0.55 l''^3 \quad (3.48)$$

For a 4 mm diameter sand,

$$\Rightarrow l'' = \left(\frac{2\pi(2)^3}{0.55} \right)^{1/3} = 4.50 \text{ mm} \quad (3.49)$$

Substituting the result of Eqn. 3.51 into Eqn. 3.49 yields $l_m = 4.24$ mm.

The tensile strength model of cement mortar was then obtained by substituting Eqns. 3.25, 3.47 and 3.49, for E_m , G_m and l_m , respectively, into Eqn. 3.48. The resulting model is shown below.

$$\sigma_{mt} = 28.9 \left[\frac{(1 - 1.75 P_h) [1.2 \beta^2 - \beta]}{\beta^2 + 10.4 \beta - 9.23} \right]^{1/2} \quad (3.50)$$

where, P_h is porosity of hydrated cement paste; and β is defined as:

$$\beta = \alpha (1 - P_h) \quad (3.51)$$

and α is defined as:

$$\alpha = \left(\frac{\pi - 4P_h}{P_h} \right)^{0.37} \quad (3.52)$$

The relationship between the tensile strength of cement mortar (σ_{mt}) and the porosity of hydrated cement paste (P_h) (Eqn. 3.50) is plotted in Fig. 3.14.

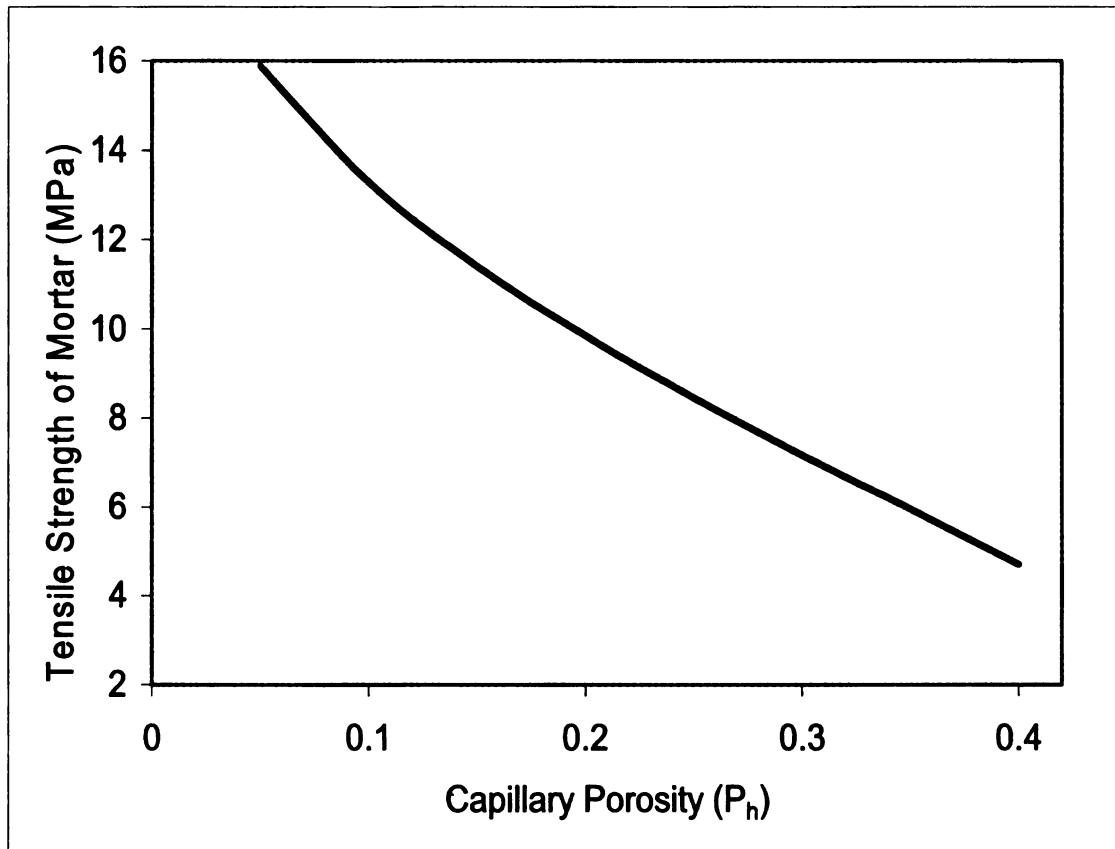


Fig. 3.14 - Tensile strength of cement mortar as a function of the capillary porosity of hydrated cement paste.

A parametric study was conducted to investigate the effect of sand volume fraction on the tensile strength of cement mortar. Figs. 3.15 shows the relationships between the tensile strength of cement mortar (σ_{mi}) and the volume fraction of sand (\bar{V}_s) for a capillary porosities (P_h) of 0.3 (covering a typical range of sand volume fraction). Theoretical predications indicate a slight increase in tensile strength with increasing sand volume fraction within the range considered here. It should be noted that excess quantities of sand can compromise workability (at constant water/cement ratios), thereby complicating production of cement mortar and potentially introducing large defects which are damaging to tensile strength.

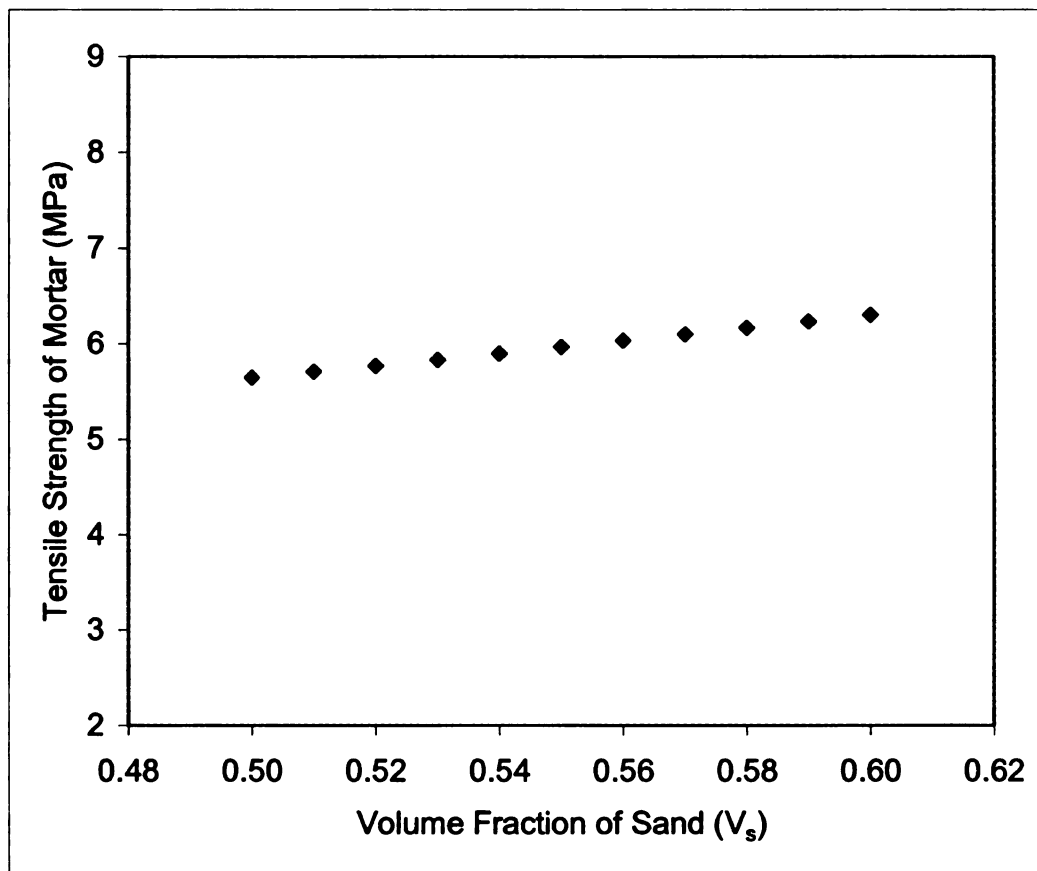


Fig. 3.15 - Tensile strength of mortar as a function of the volume fraction of sand for a capillary porosity of 0.3

CHAPTER 4

MODELING THE MECHANICAL PROPERTIES OF CONCRETE BASED ON MECHANISTIC APPROACH

4.1 Introduction

Well-compacted concrete prepared with dense aggregates may be considered as a multiphase ceramic material consisting of coarse aggregates embedded in mortar matrix. The mortar matrix consists of fine aggregates, the hydrated cement paste, and the pore system.⁸⁷ Hydration of cement produces a product consisting of solid and a pore phases.⁸⁸ Pores are thus inherent to cement-based materials; inadequate compaction further increases the pore content (and pore size) of cement-based materials. The pore system influences most important properties of concrete, including strength and stiffness.^{89,90} The pore system present in the mortar of concrete, however, is different from the pores of cement mortar prepared independently using identical proportions of various ingredients. This difference is due to the presence of the interfacial transition zone at the mortar-aggregate interfaces.^{91,92,93} The capillary porosity of hardened cement paste depends upon water-to-cement ratio, curing time and methods, and other factors. Similar parameters partly determine the porosity of the interfacial transition zone in concrete where the accumulation of bleeding water and the geometric constraints against full development of hydration products lead to increased porosity.⁸⁷

There are several strength versus water–cement ratio relationships, which indirectly relate the strength of concrete to its pore system characteristics.^{87, 94, 95} These relationships serve their purpose very well in the design of concrete mixes. However, such indirect relationships cannot consider the effects of various factors (curing conditions, aggregate size, etc.) on pore system characteristics and thus strength and other mechanical properties of concrete.

The most important characteristics of pore system are porosity and pore size distribution, which can be determined through mercury intrusion porosimetry (MIP). However, MIP results are affected by a number of factors.^{96, 97, 98, 99, 100} For example, the smallest size of pores, in which mercury can intrude, depends upon the maximum intrusion pressure applied. Consequently, the extent of porosity that can be determined by the porosimetry test depends upon the nature of the pores, the size of the smallest pores likely to be encountered in the material, and the maximum intrusion pressure applied. While developing an empirical strength–porosity relationship for concrete, the contributions of gel pores to the overall porosity and pore size distribution of concrete can be neglected without introducing significant errors.¹⁰¹ Hence, to determine the pore system characteristics influencing strength, the maximum pressure in the porosimetry test must be sufficient to cause intrusion of mercury into the smallest capillary pores. In mercury porosimetry, a major part of gel pores remains non-intruded. Further, the closed pores also remain non-intruded. One other limitation of mercury porosimetry is that it measures the entry sizes rather than the true pore size. Thus, the porosity determined using the mercury porosimetry test represents an apparent (but not actual) porosity.¹⁰¹

A number of relationships relating the strength of cement-based materials to their pore system characteristics are available in the literature. In this research, a theoretical strength-capillary porosity relationship model is developed for concrete. This model was evaluated by comparing its predictions with those of empirical models. Some minor discrepancies are found between the theoretical and empirical models, which may be attributed to the differences in estimation of porosity.

4.2 Modeling

The mechanical models of cement were developed by expanding upon the models of cement mortar. While cement mortar contains only fine aggregates, concrete incorporates both fine and coarse aggregates. The presence of coarse aggregates benefits the stiffness of concrete but negatively affects its strength. Concrete is a three-phase composite material at macro-level, comprising hydrated cement paste, fine aggregates and coarse aggregates. At micro-level, concrete can also be treated as a four-phased composite material, with the interfacial transition zone constituting the fourth phase.

Our approach involved modeling of hydrated cement paste, and then mortar as a three-phase material comprising the hydrated cement paste, fine aggregates and interfacial transition zone. Concrete is considered here to comprise three phases: mortar, coarse aggregate and the interfacial zone, noting that mortar itself is a three-phase material. The interfacial transition zone in concrete is the region at the interface between cement mortar

and surfaces of the coarse aggregates. The introduction of coarse aggregates improves the modulus of elasticity of concrete because coarse aggregates have relatively large elastic moduli and occupy a relatively large volume of concrete. However, the strength of concrete is lower than either hydrated cement paste or mortar. This could be attributed to the presence of larger intrinsic cracks at the interface and also the introduction of the interfacial transition zone which is highly porous with oriented CH crystals and low C-S-H gel packing.

4.2.1 Modulus of Elasticity of Concrete

To develop the modulus of elasticity model of concrete, it was necessary to determine the modulus of elasticity, bulk modulus and shear modulus of every constituent phase of the composite material. For cement mortar, the modulus of elasticity model developed in the preceding chapter (Eqn. 3.25) was applied. A model for the elastic modulus of the interfacial transition zone of concrete (E_{ic}) was developed in a way similar to that of cement mortar with some modifications. The porosity of the interfacial transition zone was considered to be about twice that of hydrated cement paste.⁷⁶ This rise in porosity was accounted for in modeling the elastic modulus of the interfacial transition zone (E_{ic}) using that of hydrated cement paste (E_h), as was the case for cement mortar.

As for the fine aggregates, the modulus of elasticity of coarse aggregates (E_{ca}) ranges from 70 GPa to 90 GPa, depending upon the type of aggregate.⁷⁷ A parametric study was

conducted to evaluate the significance of this range in determining the modulus of elasticity of concrete.

The upper and lower bounds of the modulus of elasticity of concrete were calculated from an equation relating the modulus of elasticity of a composite material to its shear modulus (G'_c) and bulk modulus (K'_c) (Eqn. 4.1).⁷⁸ The upper and lower bounds of the shear modulus and bulk modulus were calculated using Hashin's modulus of elasticity model for three-phase composite materials (Eqns. 4.2 – 4.5).⁷⁸ The steps followed in the computation of the upper and lower bounds of the modulus of elasticity of concrete are presented below.

The upper and lower bounds of the elastic modulus of concrete (E_c) was approximated as follows:⁷⁸

$$\frac{9K'_{c-}G'_{c-}}{3K'_{c-} + G'_{c-}} \leq E_c \leq \frac{9K'_{c+}G'_{c+}}{3K'_{c+} + G'_{c+}} \quad (4.1)$$

where K'_{c+} and K'_{c-} are the upper and lower bounds of the bulk modulus of concrete, respectively; and G'_{c+} and G'_{c-} are the upper and lower bounds of the shear modulus of concrete, respectively.⁷⁸ These parameters were calculated as follows:

Lower bound of the bulk modulus of concrete, K'_{c-} ,⁷⁸

$$\frac{1}{K'_{c-}} = \frac{V'_m}{K'_m} + \frac{V'_{ca}}{K'_{ca}} + \frac{3V'_{ca}t_{rc}}{K'_{ic} + 1.33G'_{ic}} \quad (4.2)$$

Upper bound of the bulk modulus of concrete, K'_{c+} ,⁷⁸

$$K'_{c+} = V'_m K'_m + \frac{V'_{ca} K'_{ca}}{1 + \frac{3K'_{ca}t_{rc}}{K'_{ic} + 1.33G'_{ic}}} \quad (4.3)$$

Lower bound of the shear modulus of concrete, G'_{c-} ,⁷⁸

$$\frac{1}{G'_{c-}} = \frac{V'_m}{G'_m} + \frac{V'_{ca}}{G'_{ca}} + 0.4V'_{ca}t_{rc} \left(\frac{2}{K'_{ic} + 1.33G'_{ic}} + \frac{6}{G'_{ic}} \right) \quad (4.4)$$

Upper bound of the shear modulus of concrete, G'_{c+} ,⁷⁸

$$G'_{c+} = V'_m G'_m + \frac{V'_{ca} G'_{ca}}{1 + \frac{2.5G'_{ca}t_{rc}}{K'_{ic} + 3.33G'_{ic}}} \quad (4.5)$$

The next step was to determine all the parameters included in the above equations. The bulk modulus and shear modulus of any material are related to its modulus of elasticity through an Eqns. 4.6 and 4.7, respectively.⁷⁸

$$K' = \frac{E}{3(1 - 2\nu)} \quad (4.6)$$

$$G' = \frac{E}{2(1 + \nu)} \quad (4.7)$$

where, ν is the poison's ratio of cement mortar for the model of concrete.

From the above relationships, the bulk modulus and shear modulus of cement mortar and coarse aggregates were calculated as follows ($\nu = 0.2$ was considered for both cement mortar and coarse aggregates⁸⁰):

The bulk modulus of cement mortar, K'_m ,

$$K'_m = \frac{E_m}{3(1 - 2\nu)} = \frac{E_m}{3(1 - 2(0.2))} = 0.56E_m \quad (4.8)$$

The bulk modulus of coarse aggregate, K'_{ca} ,

$$K'_{ca} = \frac{E_{ca}}{3(1-2\nu)} = \frac{E_{ca}}{3(1-2(0.2))} = 0.56E_{ca} \quad (4.9)$$

The shear modulus of cement mortar, G'_m ,

$$G'_m = \frac{E_m}{2(1+\nu)} = \frac{E_m}{2(1+0.2)} = 0.42E_m \quad (4.10)$$

The shear modulus of coarse aggregate, G'_{ca} ,

$$G'_{ca} = \frac{E_{ca}}{2(1+\nu)} = \frac{E_{ca}}{2(1+0.2)} = 0.42E_{ca} \quad (4.11)$$

Based on the above relationships, the bulk modulus and the shear modulus of the interfacial transition zone of concrete could be determined as follows:

$$K'_{ic} = 0.56E_{ic} \quad (4.12)$$

$$G'_{ic} = 0.42E_{ic} \quad (4.13)$$

For the elastic modulus of coarse aggregate (E_{ca}) ranging from 70 to 90 GPa, the corresponding values of K'_{ca} and G'_{ca} range from 39.2 to 50.4 GPa and 29.4 to 37.8 GPa, respectively. A parametric study conducted to evaluate the significance of these ranges on the mechanical properties of concrete. The modulus of elasticity of the interfacial transition zone in concrete (E_{ic}) is a function of the modulus of elasticity of cement mortar (E_m) and capillary porosity. t_{rc} is the ratio of the thickness of the interfacial transition zone in concrete to the radius of an equivalent sphere representing coarse aggregates,⁷⁸ and was calculated as follows:

$$t_{rc} = \frac{t_{ic}}{r_{ca}} \quad (4.14)$$

where, t_{ic} is thickness of the interfacial transition zone in concrete, which is a function of the coarse aggregate size,⁸¹ and r_{ca} is the radius of an equivalent spherical coarse aggregate. Thickness of the interfacial transition zone in concrete (t_{ic}) is proportional to the size of the coarse aggregate it envelops.⁸¹

The next step was to determine the relationship between the interfacial transition zone thickness and aggregate size in concrete. This relationship was approximated based on a linear relationship developed in the preceding chapter. The linear relationship between aggregate size and thickness of the interfacial transition zone, shown in Fig. 3.1, was adapted for concrete. The size of coarse aggregates considered in this analysis ranges from 4 to 25 mm. The maximum thickness of the interfacial transition zone is about 50

μm .^{72,82} This thickness was considered to occur around 25-mm aggregates which represent a common maximum coarse aggregate size in concrete. No interfacial transition zone was assumed to occur for aggregates that are smaller than 0.1 mm in size. This assumption is based on the fact that no interfacial transition zone has been detected so far around CH crystals of the same size. From this relationship, it was calculated that the value of t_r ranges from 3.9 to 50 μm for aggregate size ranging from 4 to 25 mm. A parametric study conducted to investigate the significance of this range in deciding the mechanical properties of concrete is presented in the next sections.

The significance of the three phases (cement mortar, coarse aggregates and interfacial transition zone) in determining the mechanical properties of concrete also depends on their respective volume proportions in concrete. Calculations of the volume fractions of cement mortar (V'_m), coarse aggregate (V'_{ca}) and interfacial transition zone (V'_{ic}) in concrete are discussed below.

Porosity of the interfacial transition zone in concrete (P_{ic}) is about two times that of hydrated cement paste, and 25% of the volume of interfacial transition zone is filled with CH crystals.⁸³

The pore volume of concrete (V_{pc}) could be expressed as the sum of the pore volumes of cement mortar and the interfacial transition zones, as follows:

$$V_{pc} = V_{pm} + V_{pic} \quad (4.15)$$

where, V_{pm} and V_{pic} are the pore volumes of cement mortar and the interfacial transition zone in concrete, respectively.

The porosity of concrete (P_c) can also be expressed as the ratio of the pore volume of concrete to its total volume, as follows:

$$P_c = \frac{V_{pc}}{V_c} = \frac{V_{pm} + V_{pic}}{V_c} \quad (4.16)$$

where, V_c is the total volume of concrete, which is the sum of the volumes of coarse aggregate and cement mortar. In this statement, the volume of the interfacial transition zone is included in the volume of cement mortar. V_c can be expressed as follows:

$$V_c = V_{ca} + V_m \quad (4.17)$$

In a normal concrete mix, the volume of aggregates comprises about 75% of the total volume of concrete. Since the fine-to-coarse aggregate volumetric ratio in concrete is about 2:3, fine and coarse aggregates typically comprise about 30% and 45%, respectively, of the total volume of concrete. Therefore, a typical volume of fraction of cement mortar in concrete (including the interfacial transition zone), calculated as the sum of the volume fractions of the hydrated cement paste (0.25) and the fine aggregate

(0.3), can be estimated at about 0.55. The volume of interfacial transition zone surrounding a single coarse aggregate in concrete (V_{lic}) can be calculated using Eqn. 4.18 based on the relationship between the aggregate size and the thickness of interfacial transition zone, as discussed in the preceding chapter (Fig. 3.1). The shape of coarse aggregate has been modeled as spherical, cylindrical or cubic in the literature. Evaluation of the geometry of a random sample of concrete coarse aggregates has indicated that a cylindrical shape with aspect ratio (height-to-diameter ratio) of about 1.25 would reasonably represent the concrete coarse aggregate. The assumed shape of the coarse aggregate is shown in Fig. 4.1.

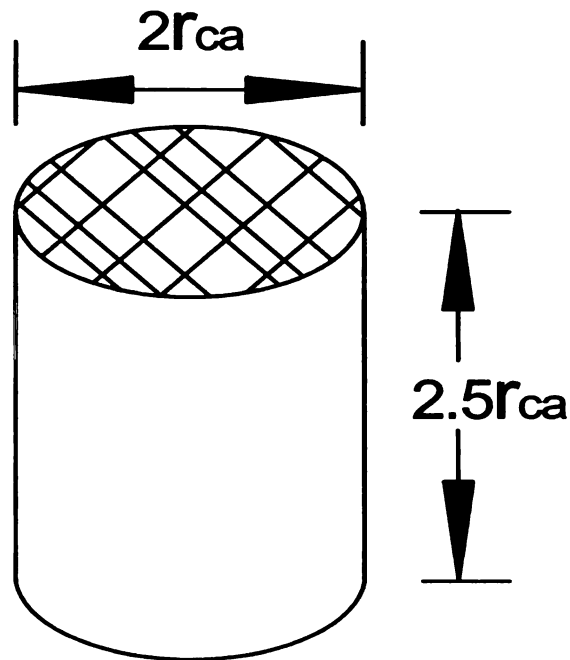


Fig 4.1 - The coarse aggregate shape model

The volume of the interfacial transition zone of thickness t_{ic} surrounding a single coarse aggregate with a shape shown in Fig. 4.1 can be calculated as follows:

$$V_{1ic} = \pi t_{ic} (7r_{ca}^2 + 6.5r_a t_{ic} + 2t_{ic}^2) \quad (4.18)$$

Assuming a uniform coarse aggregate size, the number of coarse aggregates per unit volume of concrete (N_{ca}) can be calculated as follows:

$$N_{ca} = \frac{V_{ca}}{V_{1ca}} = \frac{V_{ca}}{2.5\pi r_{ca}^3} \quad (4.19)$$

where, V_{1ca} is the volume of a single cylindrical coarse aggregate of radius r_{ca} and height $2.5r_{ca}$.

The total volume of the interfacial transition zone (V_{ic}) can then be calculated as the product of N_{ca} and V_{1ic} :

$$V_{ic} = V_{1ic} \times N_{ca} \quad (4.20)$$

Since the thickness of the interfacial transition zone is proportional to the size of the coarse aggregates in concrete, the volume fractions of the interfacial transition zone and the cement mortar remain constant as the aggregate size changes, as shown in Table 4.1.

Table 4.1 - Volume fractions of the interfacial transition zone and the cement mortar for different sizes of coarse aggregates in concrete

r_{ca}	t_{ic}	t_{rc}	V_{1ic}	N_{ca}	\bar{V}_{ic}	\bar{V}_m
(m)	(m)		m^3			
2.00E-03	8.00E-06	4.00E-03	7.06E-10	7.16E+06	0.005	0.545
7.00E-03	2.80E-05	4.00E-03	3.03E-08	1.67E+05	0.005	0.545
1.20E-02	4.80E-05	4.00E-03	1.53E-07	3.32E+04	0.005	0.545

4.2.1.1 Parametric Study on the Influence of the Modulus of Elasticity of Coarse Aggregates on the Concrete Elastic Modulus

Since the elastic modulus of the coarse aggregate used in concrete ranges from 70 to 90 MPa, a parametric study was conducted to assess the sensitivity of concrete elastic modulus to that of coarse aggregate over this range. In this parametric study, all the parameters related to hydrated cement paste and cement mortar were taken constant at typical levels established in the preceding chapters (for example, E_o equal to 38 GPa, and the aspect ratio of capillary pores, a/b , equal to 2). From Table 4.1, we considered $V'_m=0.545$, $V'_{ic}=0.005$ and $V'_{ca}=0.45$ for determining the modulus of elasticity of concrete. The elastic modulus model of cement mortar developed in the preceding chapter (Eqn. 3.25) was used for evaluation of the elastic modulus of concrete. The equation for the elastic modulus of the interfacial transition zone in concrete (E_{ic}) was based on the similar equation developed for the interfacial transition zone in mortar (E_i):

$$E_{ic} = 3.4(1 - 2 p_h) \frac{(\pi - 8 p_h)^{0.37}}{p_h^{0.37}} \quad (4.21)$$

E_m and E_{ic} were calculated, using Eqns. 3.25 (from the preceding chapter) and 4.21, for a reasonable range of capillary porosity in concrete. The result is shown in Table 4.2.

Table 4.2 - E_m and E_{ic} values calculated for different values of hydrated cement paste capillary porosity

P_h	E_m (GPa)	E_{ic} (GPa)
0.05	40.25	13.46
0.10	31.14	8.73
0.15	25.70	6.14
0.20	21.71	4.34
0.25	18.50	2.98
0.30	15.76	1.90
0.35	13.29	1.01
0.36	12.81	0.84
0.37	12.33	0.68
0.38	11.83	0.50
0.39	11.32	0.25

The next step was to find a relationship between E_m and E_{ic} . This relationship was developed by plotting the corresponding values of E_m versus E_{ic} from Table 4.2, and fitting a curve as shown in Fig. 4.2. The resulting equation, relating E_m and E_{ic} , is shown below.

$$E_{ic} = 0.447 E_m - 5.01 \quad (4.22)$$

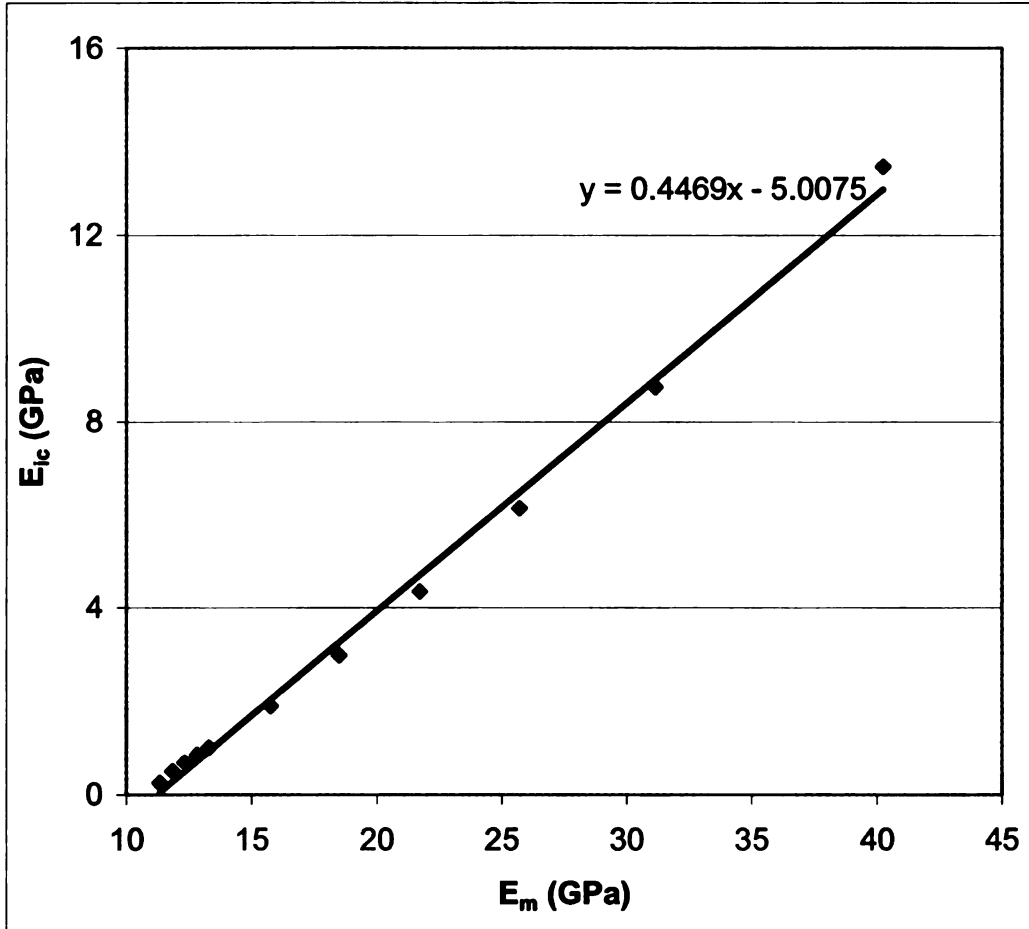


Fig. 4.2 - Relationship between the elastic moduli of cement mortar and interfacial transition zone in concrete

The bulk and shear modulus (K'_{ca} and G'_{ca}) values for coarse aggregates were calculated using Eqns. 4.9 and 4.11, respectively, for various values of the fine aggregate elastic modulus. The resulting values are shown in Table 4.3.

Table 4.3 - Bulk and shear moduli of coarse aggregates in concrete.

E_{ca} (GPa)	K_{ca} (GPa)	G_{ca} (GPa)
70	39.2	29.4
80	44.8	33.6
90	50.4	37.8

Tables 4.4, 4.5 and 4.6 show the outcomes of a parametric study for determining the significance of the coarse aggregate elastic modulus, E_{ca} , and size (varying within typical ranges) in determining the concrete elastic modulus. The data presented in these tables indicate that variation of the coarse aggregate size within a typical range does not significantly alter the elastic modulus of concrete. Three aggregate sizes (8 mm, 16 mm and 20 mm) were considered, and the results showed that the upper and lower bounds of concrete shear and bulk moduli did not change considerably with aggregate sizes. The reason for this is that the bulk and shear moduli of a material, as shown in their corresponding equations, depend upon the volume fractions and elastic modulus of the individual phases in the composite material, and not on aggregate size. The volume of the third phase in cement mortar, the interfacial transition zone, remains constant because of the opposite effects of coarse aggregate size on its thickness and surface area.

Table 4.4 - Upper and lower bounds of the bulk and shear moduli of concrete for different sizes of coarse aggregates having an elastic modulus of 70 GPa.

	K _c (Gpa)			K _{ct} (Gpa)			G _c (Gpa)			G _{ct} (Gpa)		
	8 (mm)	16 (mm)	20 (mm)	8 (mm)	16 (mm)	20 (mm)	8 (mm)	16 (mm)	20 (mm)	8 (mm)	16 (mm)	20 (mm)
d _{ca}												
P _h												
0.05	27.70	27.70	27.70	29.44	29.44	29.44	20.61	20.61	20.61	22.29	22.29	22.29
0.10	23.04	23.04	23.04	26.37	26.37	26.37	17.11	17.11	17.11	20.10	20.10	20.10
0.15	19.89	19.89	19.89	24.38	24.38	24.38	14.73	14.73	14.73	18.74	18.74	18.74
0.20	17.37	17.37	17.37	22.73	22.73	22.73	12.83	12.83	12.83	17.66	17.66	17.66
0.25	15.18	15.18	15.18	21.13	21.13	21.13	11.16	11.16	11.16	16.68	16.68	16.68
0.30	13.16	13.16	13.16	19.27	19.27	19.27	9.61	9.61	9.61	15.64	15.64	15.64
0.35	11.14	11.14	11.14	16.52	16.52	16.52	8.02	8.02	8.02	14.18	14.18	14.18
0.36	10.70	10.70	10.70	15.70	15.70	15.70	7.65	7.65	7.65	13.73	13.73	13.73
0.37	10.22	10.22	10.22	14.66	14.66	14.66	7.24	7.24	7.24	13.15	13.15	13.15
0.38	9.64	9.64	9.64	13.19	13.19	13.19	6.73	6.73	6.73	12.28	12.28	12.28
0.39	8.54	8.54	8.54	10.03	10.03	10.03	5.66	5.66	5.66	10.09	10.09	10.09

Table 4.5 - Upper and lower bounds of the bulk shear moduli of concrete with coarse aggregates of different size having elastic modulus of 80 GPa.

	K'_{c+} (Gpa)				K'_{c+} (Gpa)				G'_{c+} (Gpa)				G'_{c+} (Gpa)			
	d_{ca} P_h	8 (mm)	16 (mm)	20 (mm)	8 (mm)	16 (mm)	20 (mm)	8 (mm)	16 (mm)	20 (mm)	8 (mm)	16 (mm)	20 (mm)	8 (mm)	16 (mm)	20 (mm)
0.05	28.84	28.84	28.84	28.84	31.80	31.80	31.80	31.80	31.80	31.80	21.45	21.45	21.45	24.13	24.13	24.13
0.10	23.83	23.83	23.83	23.83	28.65	28.65	28.65	28.65	28.65	28.65	17.69	17.69	17.69	21.91	21.91	21.91
0.15	20.48	20.48	20.48	20.48	26.57	26.57	26.57	26.57	26.57	26.57	15.16	15.16	15.16	20.51	20.51	20.51
0.20	17.81	17.81	17.81	17.81	24.80	24.80	24.80	24.80	24.80	24.80	13.15	13.15	13.15	19.38	19.38	19.38
0.25	15.51	15.51	15.51	15.51	23.03	23.03	23.03	23.03	23.03	23.03	11.41	11.41	11.41	18.34	18.34	18.34
0.30	13.41	13.41	13.41	13.41	20.92	20.92	20.92	20.92	20.92	20.92	9.79	9.79	9.79	17.18	17.18	17.18
0.35	11.32	11.32	11.32	11.32	17.73	17.73	17.73	17.73	17.73	17.73	8.14	8.14	8.14	15.48	15.48	15.48
0.36	10.87	10.87	10.87	10.87	16.77	16.77	16.77	16.77	16.77	16.77	7.77	7.77	7.77	14.96	14.96	14.96
0.37	10.37	10.37	10.37	10.37	15.57	15.57	15.57	15.57	15.57	15.57	7.34	7.34	7.34	14.26	14.26	14.26
0.38	9.78	9.78	9.78	9.78	13.88	13.88	13.88	13.88	13.88	13.88	6.82	6.82	6.82	13.23	13.23	13.23
0.39	8.64	8.64	8.64	8.64	10.35	10.35	10.35	10.35	10.35	10.35	5.72	5.72	5.72	10.66	10.66	10.66

Table 4.6 - Upper and lower bounds of the bulk and shear moduli of concrete with coarse aggregates of different size having elastic modulus of 90 GPa.

d_{ca}	K'_{c*} (Gpa)			K'_{c*} (Gpa)			G'_{c*} (Gpa)			G'_{c*} (Gpa)		
	8 (mm)	16 (mm)	20 (mm)	8 (mm)	16 (mm)	20 (mm)	8 (mm)	16 (mm)	20 (mm)	8 (mm)	16 (mm)	20 (mm)
P_n												
0.05	29.80	29.80	29.80	34.13	34.13	34.13	22.16	22.16	22.16	25.95	25.95	25.95
0.10	24.48	24.48	24.48	30.90	30.90	30.90	18.16	18.16	18.16	23.70	23.70	23.70
0.15	20.95	20.95	20.95	28.72	28.72	28.72	15.51	15.51	15.51	22.26	22.26	22.26
0.20	18.17	18.17	18.17	26.82	26.82	26.82	13.41	13.41	13.41	21.09	21.09	21.09
0.25	15.79	15.79	15.79	24.87	24.87	24.87	11.60	11.60	11.60	19.97	19.97	19.97
0.30	13.62	13.62	13.62	22.48	22.48	22.48	9.94	9.94	9.94	18.68	18.68	18.68
0.35	11.47	11.47	11.47	18.84	18.84	18.84	8.24	8.24	8.24	16.73	16.73	16.73
0.36	11.00	11.00	11.00	17.75	17.75	17.75	7.86	7.86	7.86	16.12	16.12	16.12
0.37	10.49	10.49	10.49	16.39	16.39	16.39	7.43	7.43	7.43	15.31	15.31	15.31
0.38	9.88	9.88	9.88	14.50	14.50	14.50	6.89	6.89	6.89	14.11	14.11	14.11
0.39	8.73	8.73	8.73	10.62	10.62	10.62	5.77	5.77	5.77	11.17	11.17	11.17

The upper and lower bounds of the elastic modulus of concrete (E_{c+} & E_{c-}) for different coarse aggregate elastic moduli were calculated using Eqn. 4.1. The results (shown in Table 4.7) are plotted in Fig. 4.3 to determine the influence of the variation in coarse aggregate elastic modulus (E_{ca}) on the concrete elastic modulus (E_c).

It can be observed from Fig. 4.3 that the variations in the upper bounds for E_c with changes in coarse aggregate elastic modulus seem to be more pronounced with compared with those in lower bounds. However, the overall variations in concrete elastic modulus with changes in coarse aggregate elastic modulus are small enough to justify selection of an average value of 80 GPa for the coarse aggregate elastic modulus.

Table 4.7 - Upper and lower bounds of the modulus of elasticity of three concretes with coarse aggregates of different elastic moduli.

E_a	E_{c-}			E_{c+}		
	70 GPa	80 GPa	90 GPa	70 GPa	80 GPa	90 GPa
0.05	49.54	51.58	53.28	53.40	57.77	62.12
0.10	41.14	42.53	43.69	48.08	52.37	56.62
0.15	35.45	36.48	37.33	44.75	48.93	53.07
0.20	30.88	31.66	32.30	42.09	46.13	50.13
0.25	26.89	27.48	27.96	39.62	43.48	47.25
0.30	23.19	23.63	23.98	36.93	40.47	43.89
0.35	19.40	19.70	19.94	33.07	35.98	38.73
0.36	18.54	18.82	19.04	31.89	34.59	37.12
0.37	17.58	17.83	18.03	30.37	32.78	35.03

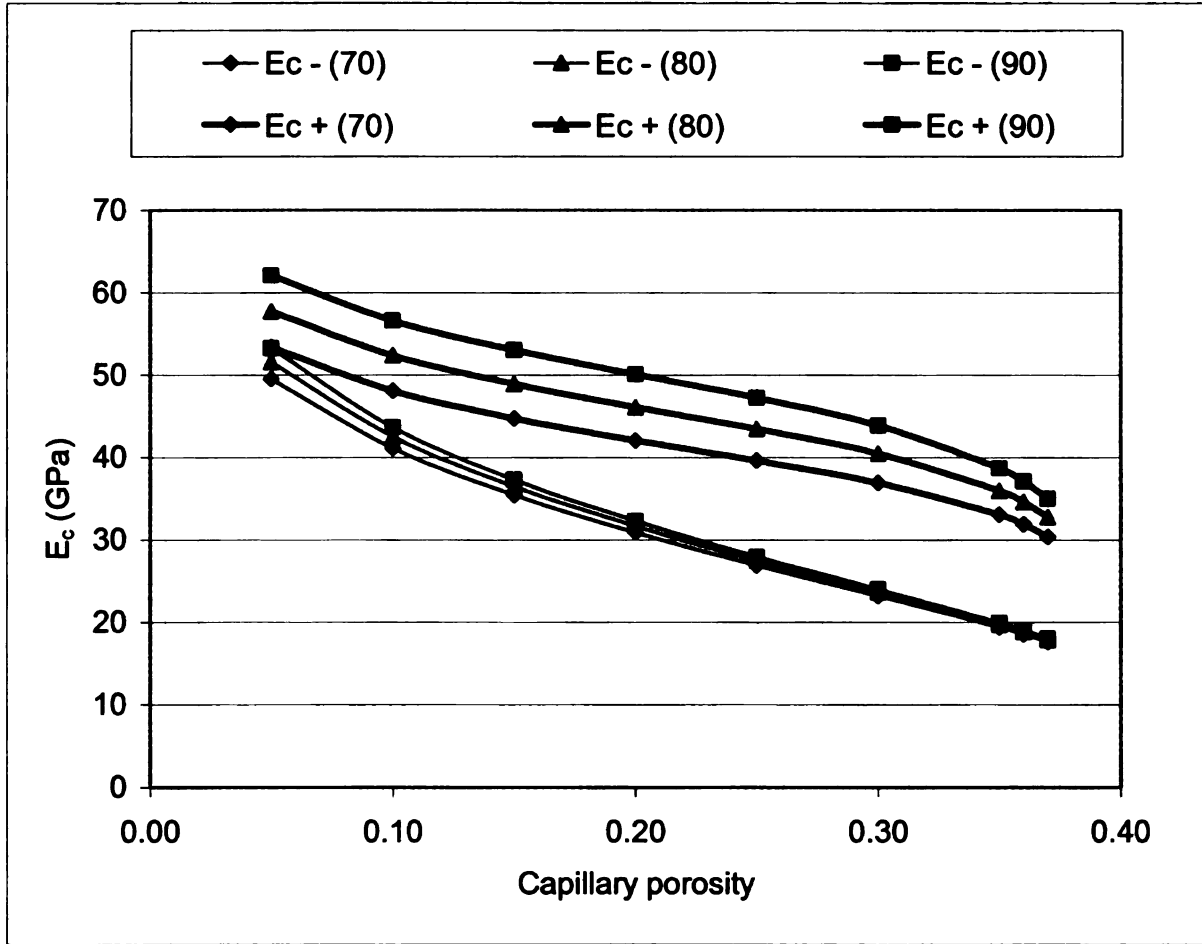


Fig. 4.3 - Upper and lower bounds of the modulus of elasticity of three concretes with coarse aggregates of different elastic moduli.

4.2.1.2 Comparing the Predictions of the Mechanistic Model of Concrete Elastic Modulus with those of Empirical Models

After establishing the upper and lower bounds of the elastic modulus of concrete, the next step was to narrow down these bounds and develop a reasonable model of concrete elastic modulus for use toward development the concrete strength model. This was performed by introducing the values of concrete elastic modulus obtained from an empirical model based on comprehensive experimental results⁸⁴ into Fig. 4.3, as shown in

Fig. 4.4, where the experimental results (represented by the empirical model) are observed to lean towards the lower-bound values of the theoretically predicted elastic moduli.

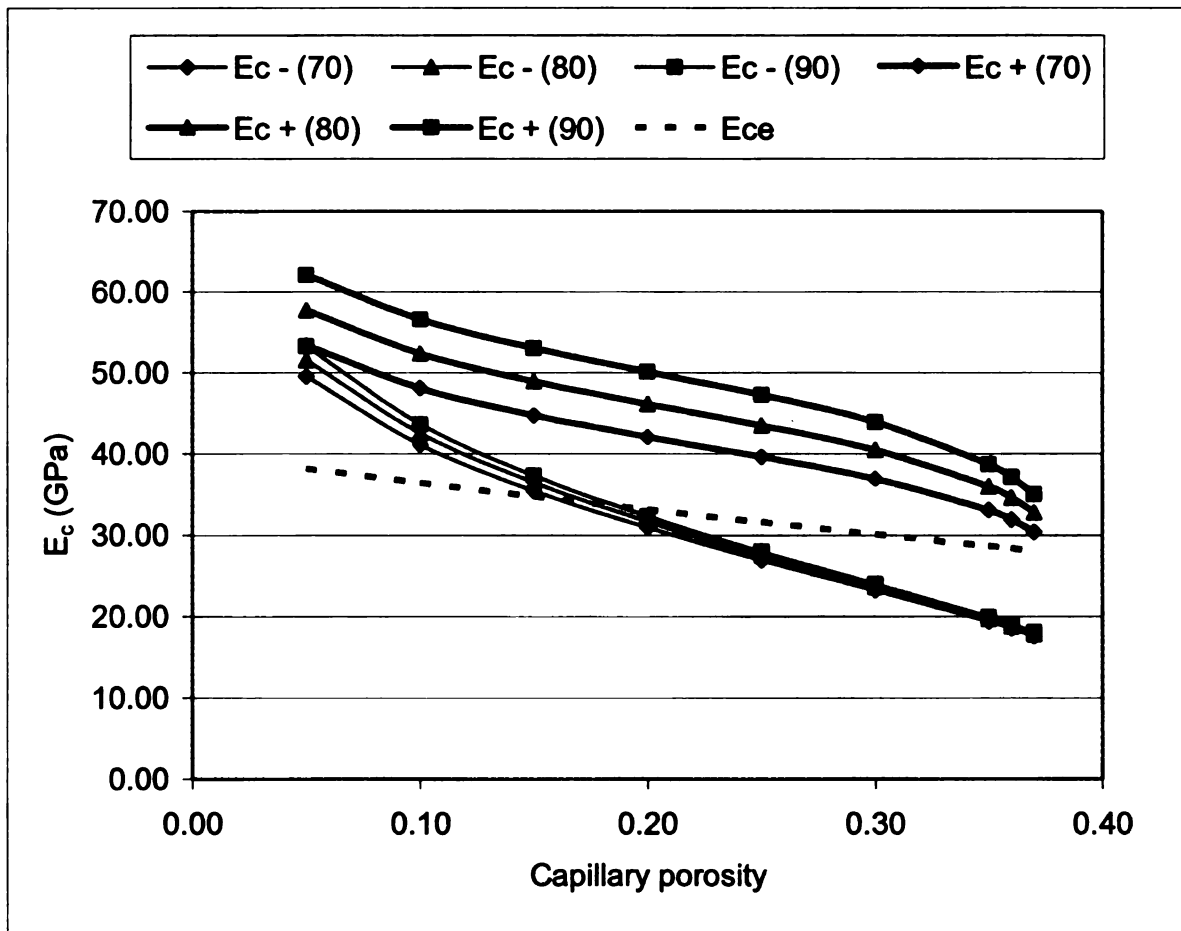


Fig. 4.4 - Comparing the predictions of theoretical model for the elastic modulus of concrete with those of empirical model based on substantial test data

Based on the data presented in Fig. 4.4, the lower-bound theoretical model was chosen to represent the elastic modulus of concrete. The modulus of elasticity of concrete was thus approximated as follows:

$$E_c \approx \frac{9K'_{c-}G'_{c-}}{3K'_{c-} + G'_{c-}} \quad (4.23)$$

With the aggregate elastic modulus (E_{ca}) estimated at 80 GPa, substituting the parameters in Eqn. 4.23 with their relevant equations expressed earlier yields the following expression for the concrete elastic modulus as a function of the cement mortar elastic modulus.

$$E_c \approx \frac{4.02E_m^2 - 45.09E_m}{0.023E_m^2 + 1.96E_m - 24.38} \quad (4.24)$$

where, E_m is the elastic modulus of cement mortar, given by Eqn. 3.25 in the preceding chapter.

4.2.2 Mechanistic Model for the Fracture Toughness of Concrete

It was shown in the previous chapters that the major contributor to the fracture toughness of hydrated cement paste and cement mortar is the frictional pull-out of CH crystals. In the case of cement mortar, CH pull-out accompanies sand-pull out. Following the same approach, in concrete also the CH pull-out is considered to be associated with coarse aggregate pull-out. The latter phenomenon makes major contributions to fracture toughness by increasing the surface area involved in frictional pull-out. Coarse

aggregates have rough surfaces where cement mortar develops bonds through the interfacial transition zone as shown in Fig. 4.5.

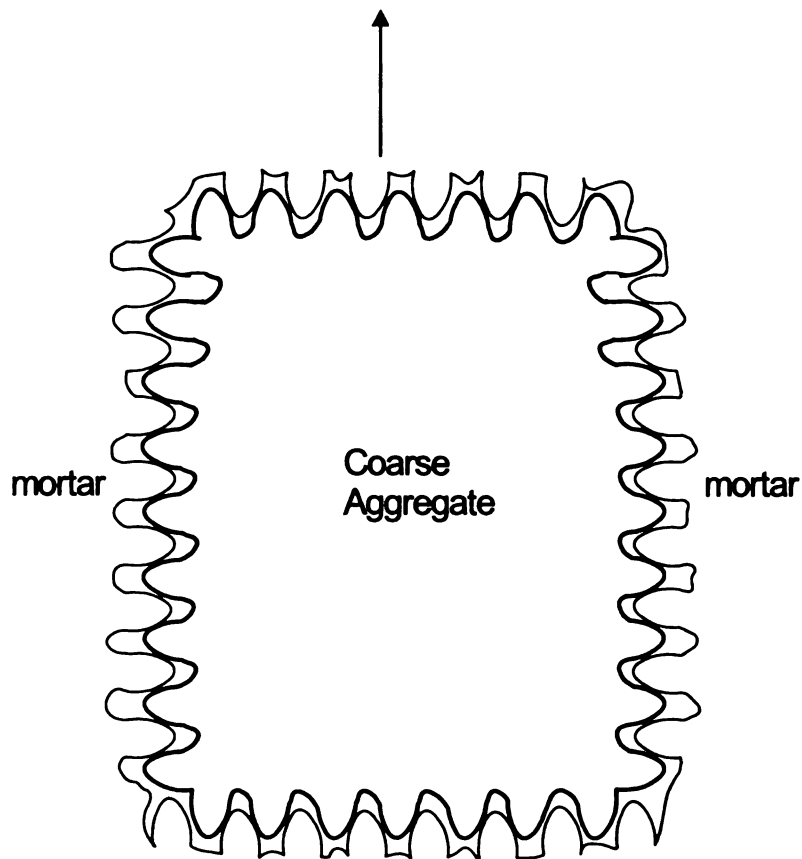


Fig. 4.5 - Surface roughness of the coarse aggregate, and bonding of cement mortar at the interfacial transition zone

The computation of the fracture toughness of concrete was based upon the energy dissipated during the pull-out of coarse aggregates. This process involves phononic friction as the dendrites of the hydrated cement paste bonding to the coarse aggregate surface shear off (Fig. 4.5). Further, the crack shielding effect associated with coarse aggregates contributes to the fracture toughness by enhancing the formation of the

process zone in front of a crack tip. It was assumed that each dendrite of hydrated cement paste is subjected to a shearing force from the dendrites defining the coarse aggregate rough surface, acting at the centers of their contact surfaces. This produces a diagonal tensile stress within the dendrites of cement mortar, generating 45-degree diagonal cracks as shown in Fig. 4.6. When the coarse aggregate pulls out from the cement mortar, its rough surface exerts a stress on the dendrites of the mortar and shears them off. The surface area of the cement mortar subjected to this type of stress was approximated to be about half the pulled-out surface area of the coarse aggregate.

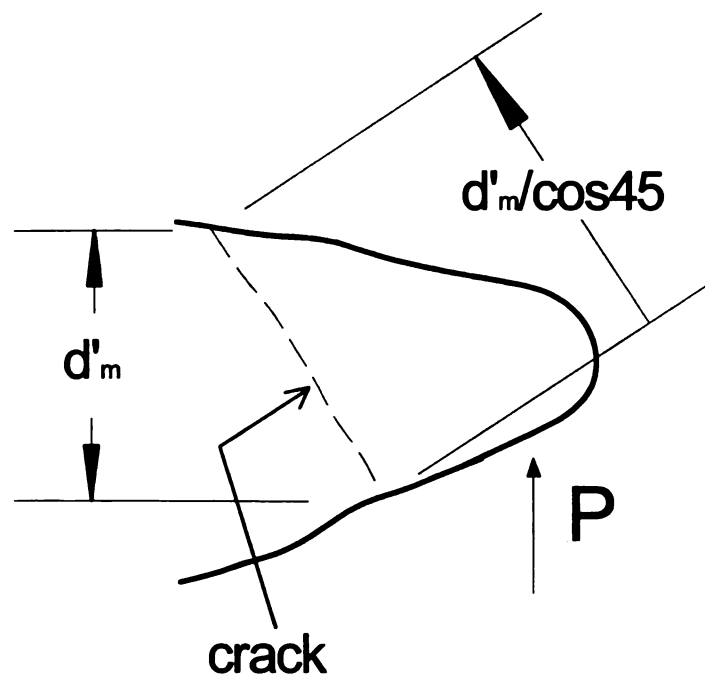


Fig 4.6 - The cracking pattern of the cement mortar dendrite due to the force P associated with the coarse aggregate pull-out stress

The surface area of the coarse aggregate subjected to pull-out and debonding was computed by considering a cylindrical coarse aggregate model shown in Fig. 4.7. The shaded region in Fig. 4.7 is the mean surface area of the coarse aggregate which could be subjected to friction as the aggregate pulls out of the mortar. This region is reasonably estimated to be at the lower quarter of the cylinder height, representing take an average pull-out depth.

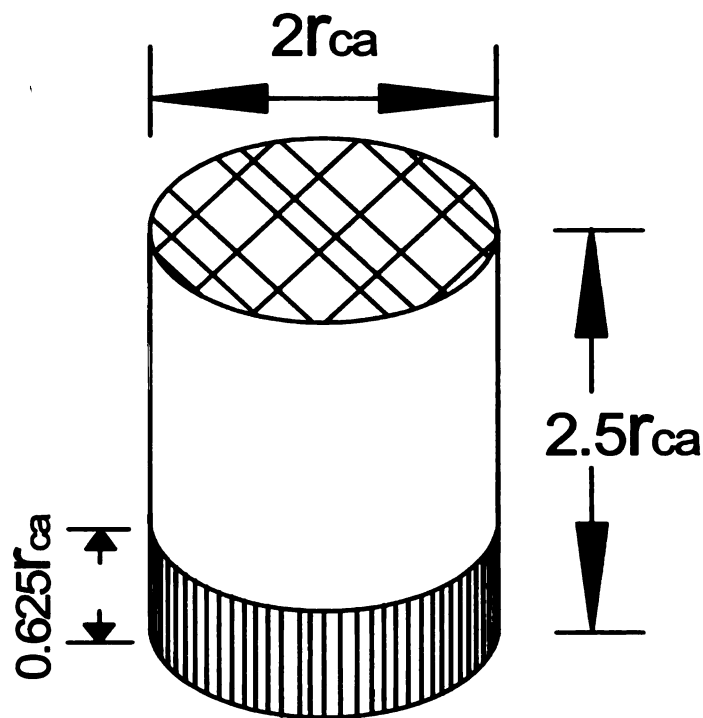


Fig. 4.7 - Average surface area of the aggregate particle subjected to frictional pull-out

4.2.2.1 Energy Released During Debonding of Coarse Aggregate from Hydrated Cement Paste in the Interfacial Transition Zone of Concrete

The surface area of a coarse aggregate subjected to debonding and pull-out, A_{cad} , is:

$$A_{cad} = 2.25 \pi r_{ca}^2 \quad (4.25)$$

The calcium hydroxide (CH) crystals are oriented to make planes of weakness around the aggregate surface. To account for this effect and also the porosity of the interfacial transition zone (which is about twice that of the bulk hydrated cement paste), equation 4.25 is modified as follows:

$$\Rightarrow A'_{cad} = 2.25 \pi r_{ca}^2 (1 - 2P_h) \quad (4.26)$$

The total energy dissipated during concrete cracking is the sum total of the energy dissipated by the cracking of mortar and the debonding/pull-out phenomena in the interfacial transition zone of concrete. The contribution of mortar cracking to fracture toughness was calculated in the previous chapter. The energy lost due to the debonding of C-S-H globules, which is equal to 1.56 J/m^2 , and the fracture toughness of cement mortar (determined in chapter 3), which is 91.78 J/m^2 , are used here towards calculation of the fracture toughness of concrete. The additional energy released (U_{cad} Joules) due to the

debonding of coarse aggregate from the hydrated cement paste (in the interfacial transition zone) is calculated using the above relationship as follows:

$$U_{cad} = 1.56 A'_{cad} \quad (4.27)$$

$$\Rightarrow U_{cad} = 3.51 \pi r_{ca}^2 (1 - 2P_h) \quad (4.28)$$

The energy released per unit fractured area of the interfacial transition zone (G_{cad} , in J/m^2) due to C-S-H/C-S-H debonding can be calculated as the total debonding energy of one coarse aggregate divided by the projected area of the aggregate on a plane perpendicular to the pull-out direction (see equations 4.29 and 4.30).

$$G_{cad} = \frac{3.51 \pi r_{ca}^2}{\pi r_{ca}^2} (1 - 2P_h) \quad (4.29)$$

$$\Rightarrow G_{cad} = 3.51 (1 - 2P_h) \quad (4.30)$$

4.2.2.2 Energy Released During Pull-out of Coarse Aggregates from Cement Mortar in the Interfacial Transition Zone of Concrete

The surface area of coarse aggregate subjected to frictional pull-out (A'_{cap}) is the shaded area of the cylinder in Fig. 4.7, excluding the bottom surface.

$$A'_{cap} = 1.25 \pi r_{ca}^2 (1 - 2P_h) \quad (4.31)$$

When the dendrites of the cement mortar shear off due to aggregate pull-out, the fractured diameter of the dendrites is about $1.414 d'_m$ (due to the diagonal shear effect), as shown in Fig. 4.6. Due to the assumption that the dendrites of both cement mortar and coarse aggregate are interlocked (Fig 4.5), the total surface area of the cement mortar subjected to shear stress (A'_{capm}) is about 1.414 times A'_{cap} . Therefore,

$$A'_{capm} = 1.414 \times 1.25 \pi r_{ca}^2 (1 - 2P_h) \quad (4.32)$$

$$\Rightarrow A'_{capm} = 1.77 \pi r_{ca}^2 (1 - 2P_h) \quad (4.33)$$

The energy released due to CH pull-out when A'_{capm} fractures (U_{chcap1}) can be calculated as the product of the modified G_{pm} and A'_{capm} (see equation 4.34). G_{pm} is the energy per unit surface area released due to CH pull-out in a compact cement mortar paste. It is calculated in the previous chapter, and is equal to 91.78 J/m^2 .

$$U_{chcap1} = 91.78 A'_{capm} \quad (4.34)$$

$$\Rightarrow U_{chcap1} = 162.22 \pi r_{ca}^2 (1 - 2P_h) \quad (4.35)$$

Let U_{chcap2} represent the energy released due to CH pull-out at the bottom surface of the aggregate particle. It can be calculated as the product of the modified G_p and the base area of the coarse aggregate:

$$U_{chcap2} = 91.78 \pi r_{ca}^2 (1 - 2P_h) \quad (4.36)$$

The total energy released due to CH pull-out during the pull-out of the aggregate particle from the cement mortar (U_{chcap}) is, therefore, the sum of U_{chcap1} and U_{chcap2} , that is:

$$U_{chcap} = U_{chcap1} + U_{chcap2} \quad (4.37)$$

$$\Rightarrow U_{chcap} = 254 \pi r_{ca}^2 (1 - 2P_h) \quad (4.38)$$

The energy released per unit fractured area of the interfacial transition zone (G_{chcap} , in J/m^2), due to CH pull-out, is the total energy released as one coarse aggregate pulls out divided by the projected area of the aggregate on a plane perpendicular to the pull-out direction (see equations 4.39 and 4.40).

$$G_{chcap} = \frac{254 \pi r_{ca}^2 (1 - 2P_h)}{\pi r_{ca}^2} \quad (4.39)$$

$$\Rightarrow G_{chcap} = 254 (1 - 2P_h) \quad (4.40)$$

The total energy release rate per unit fractured area of the interfacial transition zone in concrete (G_{ic}) can be calculated as the sum of G_{chcap} and G_{cad} , as shown below:

$$G_{ic} = G_{chcap} + G_{cad} \quad (4.41)$$

$$\Rightarrow G_{ic} = 257.5 (1 - 2P_h) \quad (4.42)$$

As was discussed for cement mortar, the other factor which enhances the fracture toughness of concrete is the shielding of crack growth. Coarse aggregates render crack shielding or arresting effect by bridging between the two crack surfaces near a crack tip. This phenomenon causes multiple microcracking ahead of the crack tip (in the so-called process zone) within the cement mortar. For the volume fractions of coarse aggregate commonly used in concrete, formation of the process zone increases the fracture toughness of cement mortar by about 50%. Therefore, the modified fracture toughness of mortar is: $1.5 \times 91.78 = 137.67 \text{ J/m}^2$.³⁻¹⁵

The fracture toughness of concrete (G_c) can be calculated as the sum of the fracture toughness associated with the debonding/pull-out at the interfacial transition zone and that of the cement mortar, accounting for the coarse aggregate and mortar volume fractions. Therefore, G_c can be expressed as follows:

$$G_c = G_{ic} V'_{ca} + G_m V'_m \quad (4.43)$$

where, V'_{ca} is the volume fraction of coarse aggregates (including interfacial transition zone) in concrete; and V'_m is volume fraction of the cement mortar in concrete. Using the example (typical) values of $V'_{ca} = 0.455$ and $V'_m = 0.545$, as explained in the previous sections, and substituting for G_{ic} and G_m , in equation 4.43 yield:

$$G_c = 0.455 \times 257.5(1 - 2P_h) + 0.545 \times 137.7(1 - P_h) \quad (4.44)$$

$$G_c = 117.21(1 - 2P_h) + 75.05(1 - P_h) \quad (4.45)$$

$$\Rightarrow G_c = 192.2(1 - 1.61P_h) \quad (4.46)$$

The resulting values of G_c are plotted in Fig. 4.8 versus the capillary porosity of the hydrated cement paste.

The fracture toughness from this model for reasonable levels of capillary porosity ranges from 105 to 161 J/m², which is in conformance with the experimental values of the fracture toughness of concrete, which range from 100 to 200 J/m².⁸⁵

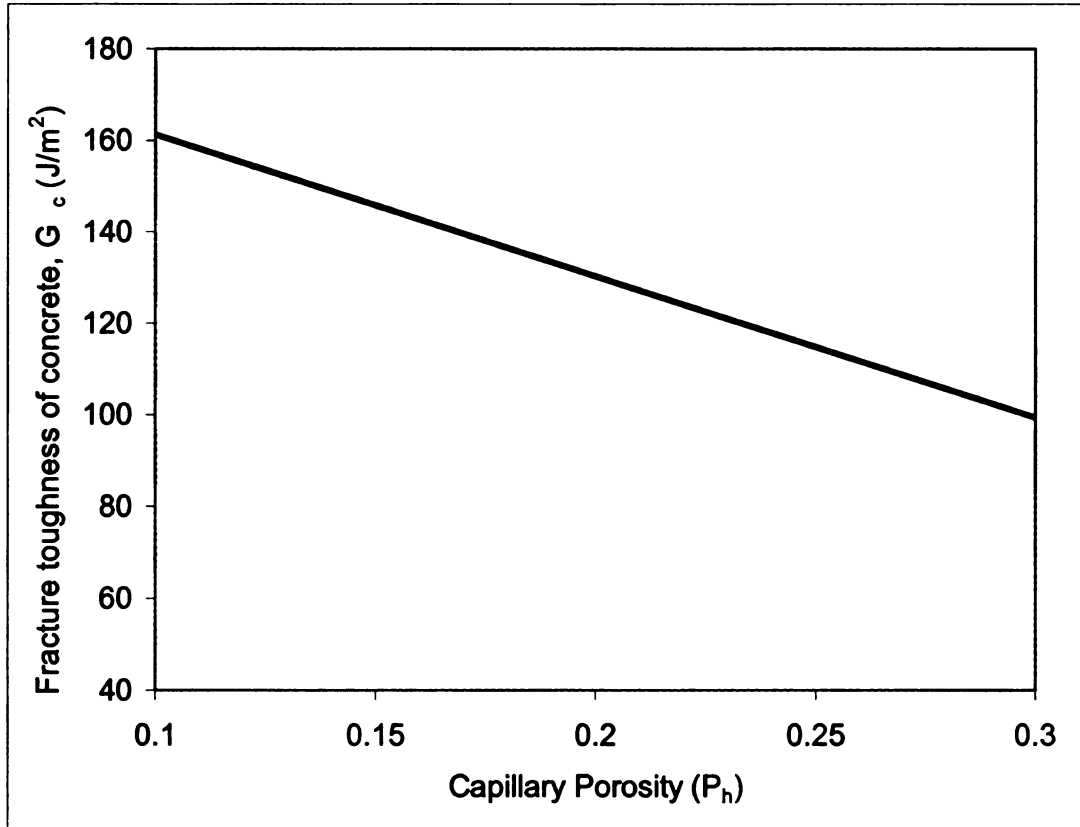


Fig. 4.8 - Fracture toughness of concrete as a function of the capillary porosity of hydrated cement paste

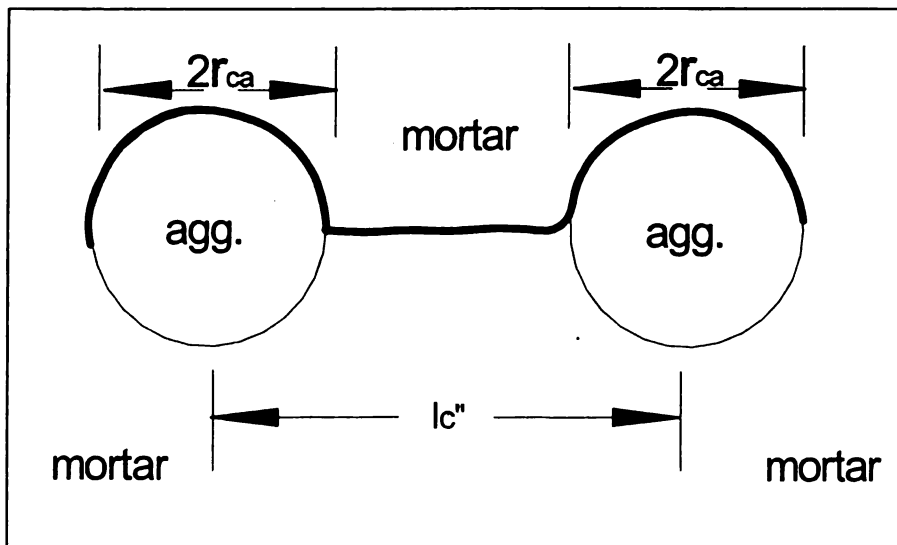
4.2.3 Mechanistic Model for the Tensile Strength of Concrete

The tensile strength model of concrete was developed using the Griffith equation, as was done in the case of cement mortar and hydrated cement paste. Since the tensile behavior of concrete is nearly linearly elastic at lower porosities, Griffith's equation was employed to develop the strength-porosity relationship for concrete:

$$\sigma_{ct} = \sqrt{\frac{E_c G_c}{\pi l_c}} \quad (4.47)$$

where, E_c is the modulus of elasticity of concrete; G_c is fracture toughness of concrete; and l_c is half the critical crack length at which an unstable crack propagates in concrete under tension. Several microcracks form in concrete during its hardening due to differential shrinkage stresses prior to application of any external loads. Microcracks are expected to initiate at the interfacial transition zones and propagate into the cement mortar. The size of these cracks may vary depending on several factors, including the homogeneity of the distribution of coarse aggregates in mortar. It was assumed here, as done in the case of mortar, that the largest existing microcrack bridges between two coarse aggregates¹⁰ as shown in Fig. 4.9.

Fig. 4.9 - The largest inherent shrinkage crack in cement mortar between two coarse aggregate particles



From Fig. 4.9, the initial crack length in concrete was determined as the sum of the center-to-center distance between two coarse aggregates (l_c'') and size of coarse aggregate ($2r_{ca}$):

$$l_c = 0.5(l_c'' + 2r_{ca}) \quad (4.48)$$

Shrinkage cracks are more likely to occur around larger aggregates due to the fact that they block more of the bleeding water and also generate larger differential shrinkage stresses in their vicinity. For this reason, the maximum aggregate size in concrete was considered in computation of the critical crack length. If we assume a uniform distribution of coarse aggregates in cement mortar, the center-to-center spacing between two aggregates (l_c'') using the following procedures for the typical (example) case with coarse aggregates comprising 45% of the concrete volume:

$$V_{ca} = 0.45V_c \quad (4.49)$$

where, V_{ca} is the volume of a (cylindrical) coarse aggregate; and V_c is volume of concrete.

Substituting their approximate values (refer to Fig. 4.9) yields:

$$\Rightarrow 2.5\pi r_{ca}^3 = 0.45l_c''^3 \quad (4.50)$$

$$\Rightarrow l_c^n = \left(\frac{2.5\pi(r_{ca}^3)}{0.45} \right)^{\frac{1}{3}} = 2.6r_{ca} \quad (4.51)$$

Substituting equation 4.51 into equation 4.48 yields $l_c = 2.3r_{ca}$. This means that the critical crack length is about 2.3 times the maximum aggregate size.

The tensile strength model of concrete can then be derived by substituting equations 4.24, 4.46 and 4.48, for E_c , G_c and l_c , respectively, into equation 4.47. The resulting model is:

$$\sigma_{ct} = 96.4 \left[\frac{(1 - 1.61P_h)(E_m^2 - 11.2E_m)}{d_{ca}(E_m^2 + 85.2E_m - 1060)} \right]^{\frac{1}{2}} \quad (4.52)$$

where, P_h is capillary porosity of the hydrated cement paste; d_{ca} is the maximum aggregate size ($2r_{ca}$); and E_m is modulus of elasticity of cement mortar that is expressed as follows:

$$E_m \approx \frac{5.78E_h^2 - 28.35E_h}{0.04E_h^2 + 2.4E_h - 12.46} \quad (4.53)$$

where, E_h , the modulus of elasticity of hydrated cement paste is given below as :

$$E_h = \frac{5.852}{p_h^{0.37}} (1 - p_h)(\pi - 4p_h)^{0.37} \quad (4.54)$$

Table 4.8 shows the tensile strength of concrete computed for different maximum aggregate sizes. The maximum aggregate sizes considered are, 20, 16 and 10 mm.

Table 4.8 - Tensile strength of concrete with different maximum aggregate sizes

P_h	E_h	E_m	E_c	G_c	σ_{tc}	σ_{tc}	σ_{tc}
	(GPa)	(GPa)	(GPa)	(J/M ²)	(MAS = 20 mm) (Mpa)	(MAS = 16 mm) (Mpa)	(MAS = 10 mm) (Mpa)
0.05	25.11	40.15	51.10	176.73	11.18	12.50	15.81
0.10	17.93	31.08	42.24	161.26	9.71	10.86	13.73
0.15	14.17	25.66	36.29	145.78	8.56	9.57	12.10
0.20	11.63	21.68	31.52	130.31	7.54	8.43	10.66
0.25	9.72	18.46	27.37	114.84	6.60	7.37	9.33
0.30	8.17	15.71	23.48	99.37	5.68	6.35	8.04
0.35	6.89	13.23	19.20	83.90	4.72	5.28	6.68
0.37	6.43	12.25	16.51	77.71	4.21	4.71	5.96

The relationship between tensile strength (σ_{ct}) and capillary porosity (P_h) of concrete (equation 4.52) is shown in Fig. 4.10.

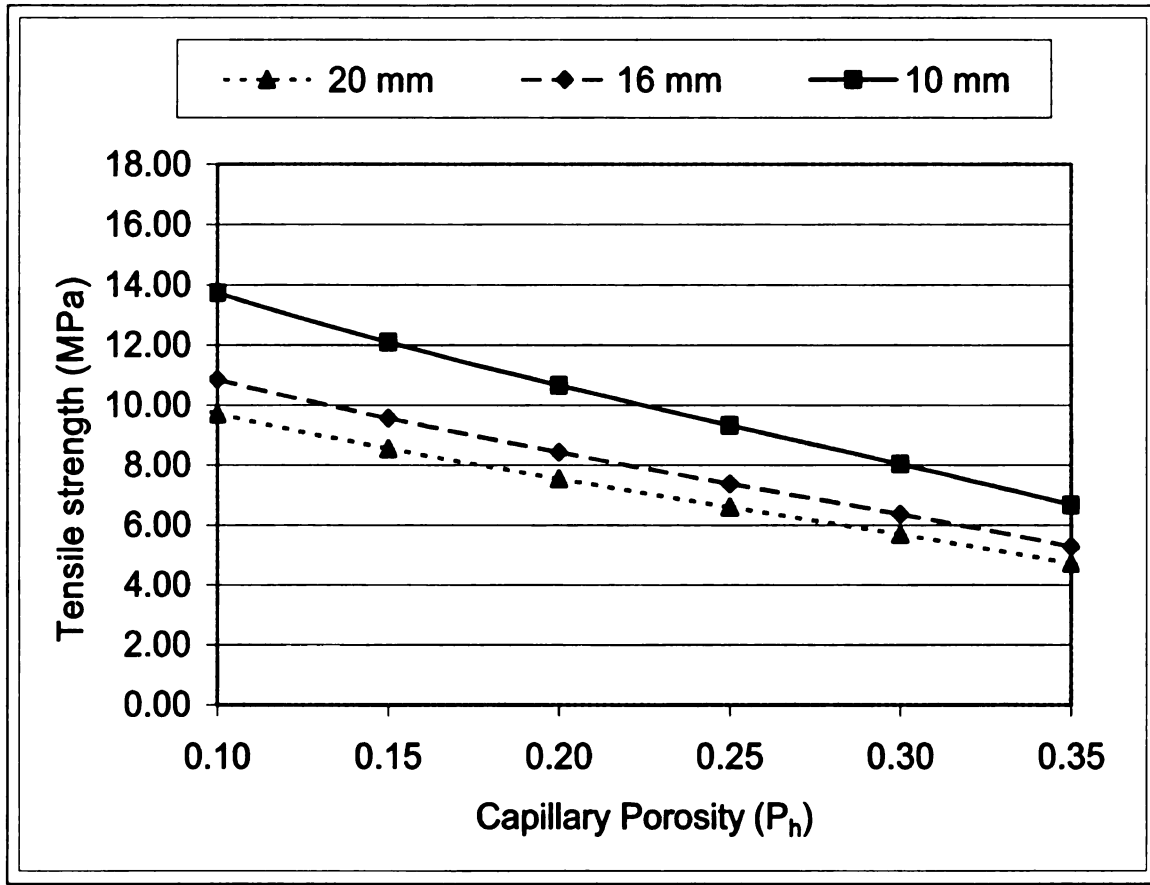


Fig. 4.10 - Tensile strength-capillary porosity relationship for concretes with different maximum aggregates sizes

The measured values of tensile strength for concrete materials with the typical fracture toughness range of the model (105-161 J/m²) are from 4.9 to 7.6 MPa, for a maximum aggregate size of 20 mm.⁸⁵ The theoretical range of tensile strength derived here is from 4.5 to 9.5 MPa for a maximum aggregate size of 20 mm (Fig. 4.10), which is comparable to the experimental range.

4.2.4 Compressive Strength Model of Concrete

The mechanism of failure of concrete under compression is different from that of hydrated cement paste and cement mortar. Failure of hydrated cement paste and cement mortar under compression involves formation of straight cracks parallel to the direction of the applied compressive stress. Therefore, the compressive strengths of hydrated cement paste or cement mortar could be estimated by comparing the lateral tensile strains caused by the Poisson's effect under compression against the cracking strain. In the case of concrete, the lateral tensile stress resulting from the Poisson's effect under compression produces cracks at the interfacial transition zones around the coarse aggregates, and the combined effects of compressive stresses and lateral strains extend these cracks in such a way that they form conical shaped hats on opposite sides of the aggregates (Fig. 4.11). The schematic and dimensions of Fig. 4.11, representing the cones formed on opposite sides of coarse aggregates, are based on experimental observations.⁴⁹ The conical hats act as wedges to further crack the concrete as the compressive stress increases toward the peak (failure) stress. Therefore, determination of the compressive strength of concrete involves computation of the frictional energy loss at conical surfaces associated with the wedging effect that leads to failure of concrete.

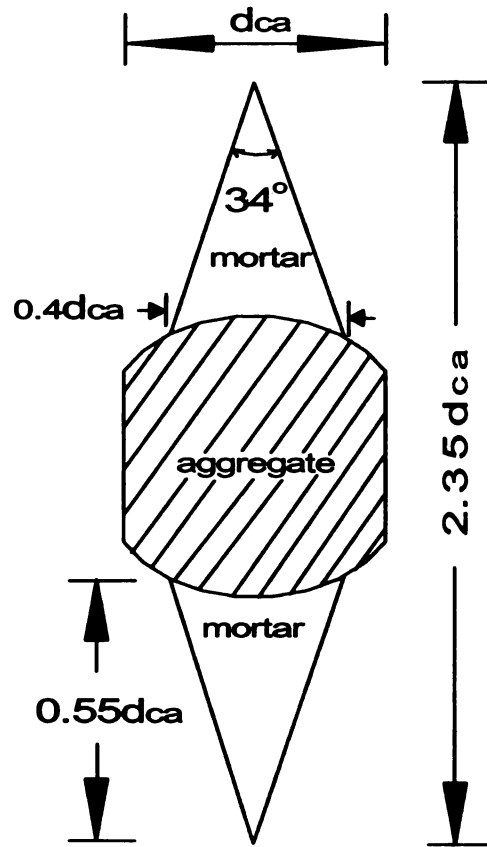


Fig. 4.11 Schematic of conical wedges forming above and below coarse aggregates as concrete fails under compression

The surface area of one of the mortar conical wedges covering the coarse aggregate was calculated as follows:

$$S_c = \pi(0.2d_{ca})\sqrt{(0.55d_{ca})^2 + (0.2d_{ca})^2} \quad (4.55)$$

$$\Rightarrow S_c = 0.36d_{ca}^2 \quad (4.56)$$

The energy dissipated as the mortar surrounding a coarse aggregate shears along the surfaces of conical wedges was considered as an addition to the fracture toughness of concrete (calculated originally under tension). Since this energy dissipation is totally related to the mortar phase of concrete, the additional energy is calculated as the product of the fracture toughness of mortar and the ratio of the surface area of the wedge to the projected area of aggregate:

$$G_{add} = \frac{S_c}{0.25\pi d_{ca}^2} (G_m) \quad (4.57)$$

$$\Rightarrow G_{add} = \frac{0.36d_{ca}^2}{0.25\pi d_{ca}^2} 91.8(1 - 1.75P_h) \quad (4.58)$$

$$\Rightarrow G_{add} = 42.08(1 - 1.75P_h) \quad (4.59)$$

The fracture toughness of concrete under compression (G_{cc}) was calculated by adding the contribution to fracture toughness of the conical mortar wedges (G_{add}) to the fracture toughness of concrete under tension (G_c):

$$G_{cc} = G_{add} + G_c \quad (4.59)$$

$$\Rightarrow G_{cc} = 234(1 - 1.64P_h) \quad (4.60)$$

The compressive strength of concrete was then calculated using the Griffith's equation based on the tensile implications of compression associated with the Poisson's effect:

$$\sigma_{cc} = \sqrt{\frac{E_c G_{cc}}{\pi l_c \nu^2}} \quad (4.61)$$

where, σ_{cc} is the compressive strength of concrete; E_c is the modulus of elasticity of concrete; G_{cc} is the fracture toughness of concrete; l_c is half the critical crack length in concrete; and ν is the Poisson's ratio of concrete.

Expressions for the parameters of equation 4.61 have been determined in the previous section, and their substitution into equation 4.61 yields the following expression for the compressive strength of concrete:

$$\sigma_{cc} = 532 \left[\frac{(1 - 1.64 P_h)(E_m^2 - 11.22 E_m)}{d_{ca}(E_m^2 + 85.22 E_m - 1060)} \right]^{1/2} \quad (4.62)$$

where, E_m and E_h are the elastic modulus of mortar and hydrated cement paste as given by equations 4.53 and 4.54, respectively.

Table 4.9 shows the computed values of the compressive strength of concrete for different maximum aggregate sizes (10, 16 and 20 mm).

Table 4.9 - Computed values of the compressive strength of concrete materials with different maximum aggregate sizes

P_h	E_h (GPa)	E_m (GPa)	E_c (GPa)	G_{cc} (J/M ²)	σ_{cc} (MAS = 20 mm) (Mpa)	σ_{cc} (MAS = 16 mm) (Mpa)	σ_{cc} (MAS = 10 mm) (Mpa)
0.05	25.11	40.15	51.10	214.81	61.63	68.90	87.16
0.10	17.93	31.08	42.24	195.62	53.47	59.78	75.62
0.15	14.17	25.66	36.29	176.44	47.06	52.62	66.56
0.20	11.63	21.68	31.52	157.25	41.41	46.30	58.57
0.25	9.72	18.46	27.37	138.06	36.16	40.43	51.14
0.30	8.17	15.71	23.48	118.87	31.08	34.75	43.95
0.35	6.89	13.23	19.20	99.68	25.73	28.77	36.39
0.37	6.43	12.25	16.51	92.01	22.92	25.63	32.42

The theoretically derived relationship between the compressive strength (σ_{cc}) and capillary porosity (P_h) of concrete (equation 4.62) is plotted in **Fig. 4.12**.

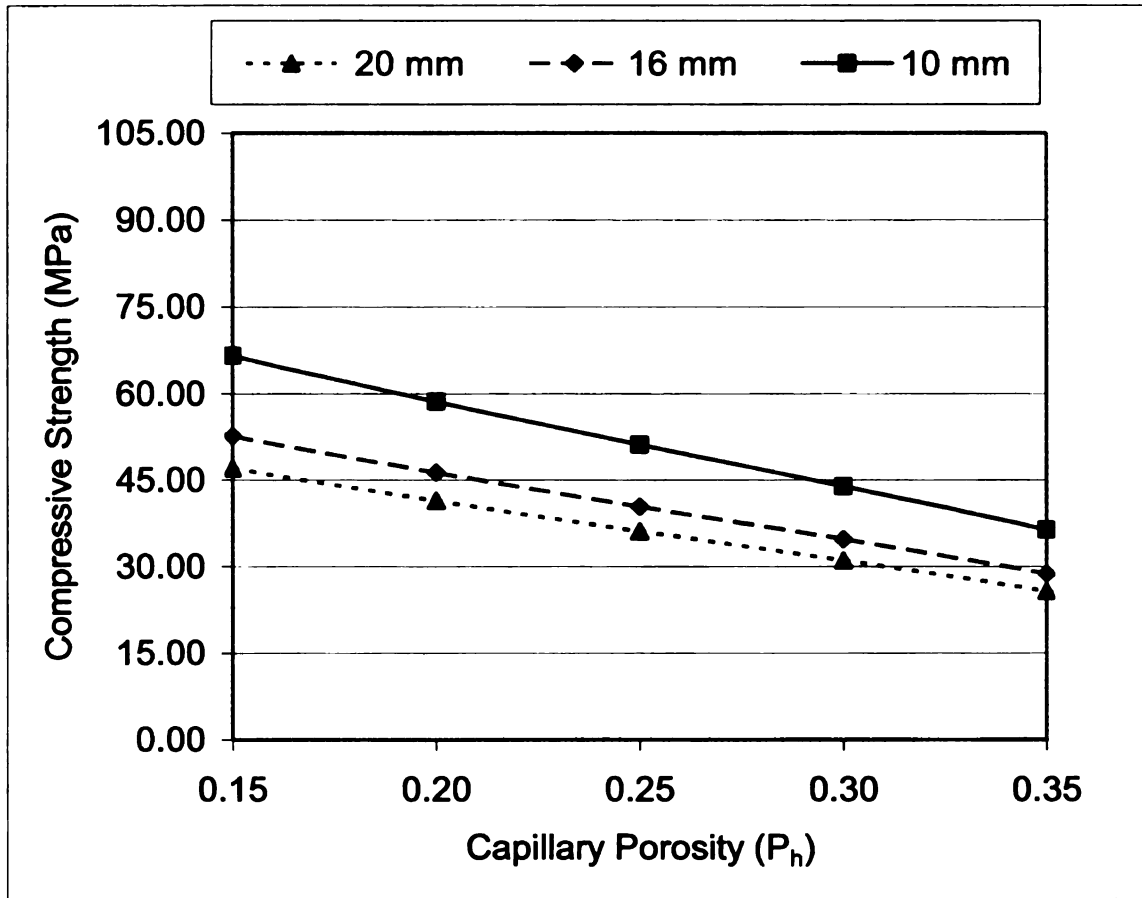


Fig. 4.12 Theoretically derived compressive strength-capillary porosity relationships for concretes with different maximum aggregates sizes

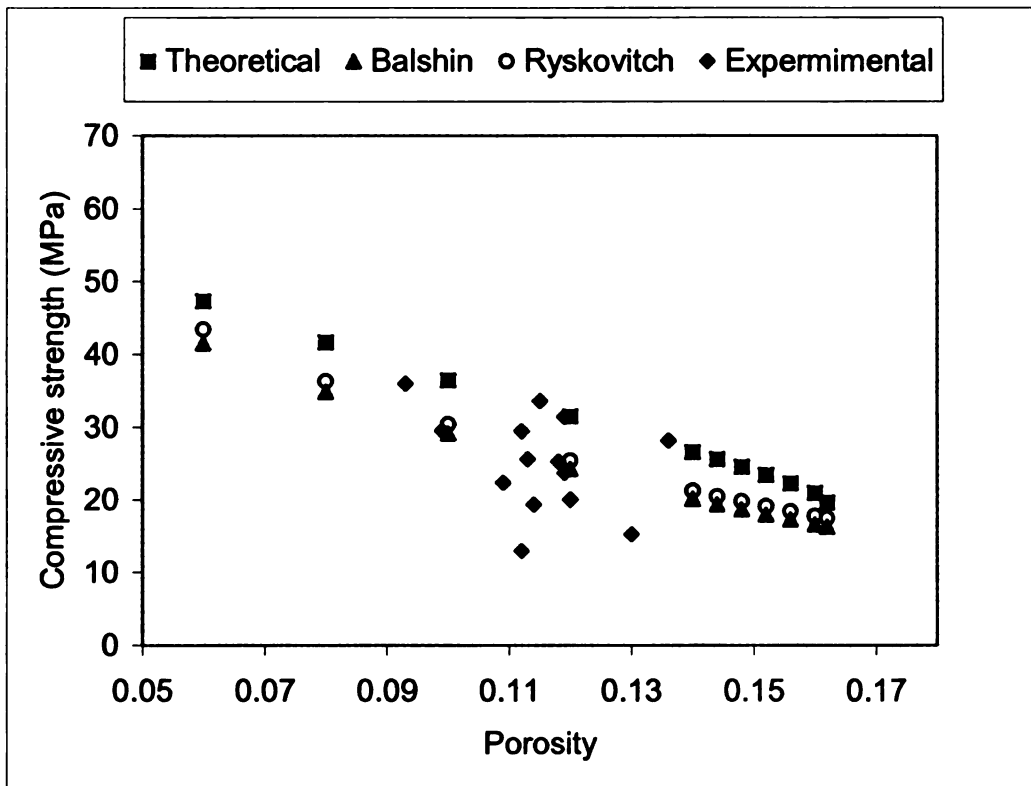
4.2.5 Comparing the Predictions of the Compressive Strength Model of Concrete with those of Empirical Models

The compressive strength model of concrete presented above was evaluated by comparing its predictions with the experimental results reported in the literatures and also with empirical models. The empirical models developed by Balshin⁴ (Eqn. 4.63) and Ryshkevitch⁵ (Eqn. 4.64) were used for evaluating the predictions of the theoretical model for the compressive strength of concrete.

$$\sigma_{cc} = 68.74(1 - p)^{8.15} \quad (4.63)$$

$$\sigma_{cc} = 74.4e^{-8.96 p} \quad (4.64)$$

The comparisons between theoretical predictions of compressive strength, experimental results and empirical models is presented in Fig. 4.13. It can be observed in Fig. 4.13 that the predictions of the mechanistic compressive strength model compare favorably with experimental values and predictions of the empirical models, though the theoretical predictions are slightly on the higher side.



CHAPTER 5

MECHANICAL MODELS OF HIGH-VOLUME FLY ASH CONCRETE

5.1 Introduction

Fly ash is the most commonly used mineral admixture in concrete. The use of coal fly ash as a pozzolanic admixture partially replacing cement in concrete started in late 1940s.¹⁰² Coal fly ash is commonly used to replace about 25% (by weight) of Portland cement in concrete. Recent research has demonstrated the potential to further improve the performance, cost, environmental and energy benefits of fly ash use in concrete by increasing the replacement level of cement with fly ash up to 50% (or more). In order to make optimum use of fly ash in concrete, one needs models which relate the structure of fly ash concrete to its properties. So far, various empirical formulas relating fly ash concrete strength to fly ash content have been developed by simply fitting curves to experimental data. These formulas, however, apply to limited ranges of material types and proportions, and do not provide a comprehensive basis to optimize the use of coal fly ash in concrete. In this chapter, an attempt has been made to model the mechanical properties of high-volume fly ash concrete. In this investigation, 50% replacement of cement with fly ash is considered to represent high-volume fly ash concrete.

The mechanistic model developed here is based on the microstructure of hydrated cement paste, cement mortar, and concrete. The main influence of fly ash results from its reaction with the hydration product CH (calcium hydroxide) at later ages, and involves refinement of the capillary pore system. This affects the size and shape of capillary pores, which in turn alter the strength and other mechanical properties of cementitious materials. During pozzolanic reaction, there is a reduction of CH crystals, which alters the fracture toughness of cementitious materials.

5.2 Development of a Strength Model for High-Volume Fly Ash Concrete

High-volume fly ash concrete generally incorporates more than about 30% fly ash by weight of cement. As explained in previous chapters, parameters influencing the strength of concrete include: capillary porosity, pore size distribution, intrinsic crack length, and CH size. The approach to development of the model for high-volume fly ash concrete was based on the influence of fly ash on these parameters. The major effect of fly ash on the strength of concrete is due to the capillary pore-size refinement and the reduction of CH content and size. In this research, the effect of 50% replacement of Portland cement with fly ash was analyzed. The 50% fly ash content is a practical level targeted for commercial use in the United States.

5.3 Concrete Containing 50% Replacement of Cement with Fly Ash

As the concentration of CH in the hydration solution reaches the critical mass for pozzolanic reaction to occur (which tends to take longer with increasing fly ash content), new C-S-H gels start to form due to the reaction between the CH and the silicates from fly ash. This pozzolanic reaction reduces the amount and size of CH over time.

In developing the mechanical model of high-volume fly ash concrete, the relatively slow rate of pozzolanic reactions make it important to consider the factor of time. This requires a model for the rate of pozzolanic reactions in cementitious materials. The percent reduction with time of fly ash during pozzolanic reaction for concrete containing 50% fly ash as replacement for cement was obtained from literatures as:¹⁰³

$$R_{FA} = 13.177(\log t) + 5.07 \quad (5.1)$$

where, R_{FA} is percent reduction of fly ash after t day of hydration.

Since the fly ash content is expressed as the percent by weight replacing cement, an equivalent percent by volume was calculated by taking the specific gravities of fly ash and Portland cement to be 2.3 and 3.15, respectively.¹⁰³ For a given water-to-binder ratio of w/b and 50% fly ash replacement of cement, the volume of hydration products that could be obtained from 1 gram of cementitious binder can be calculated as follows:

$$V_h = w/b + \frac{0.5}{SG_{FA}} + \frac{0.5}{SG_{PC}} \quad (5.2)$$

where, V_h is the total volume of mixture; w/b is water-to-binder ratio; SG_{FA} is the specific gravity of fly ash ($SG_{FA}=2.3$); and SG_{PC} is the specific gravity of Portland cement ($SG_{PC}=3.15$).

Substituting the values of SG_{FA} and SG_{PC} (2.3 and 3.15, respectively) into Equation 5.2 yields an expression for the volume of hcp that can be obtained from 1 gram of binder:

$$V_h = w/b + \frac{0.5}{2.3} + \frac{0.5}{3.15} = w/b + 0.376 \quad (5.3)$$

The volume fraction of fly ash in hydrated cement paste was then determined as the ratio of the volume of fly ash to the total volume of hydrated cement paste for a given w/b ratio:

$$V'_{fa} = \frac{0.5/2.3}{w/b + 0.376} \quad (5.4)$$

where, V'_{fa} is the volume fraction of fly ash in hydrated cement paste.

The volume fractions of fly ash (V'_{fa}) in hydrated cement paste for w/b ratios of 0.3 and 0.4 were calculated (for 50 wt.% replacement level of cement with coal fly ash) using Equation 5.4, and the corresponding values were 0.32 and 0.28, respectively.

5.3.1 Fracture Toughness of Concrete Containing 50% Fly Ash as Replacement for Cement

The unreacted fly ash particles were treated as spherical micro-aggregates in hydrated cement paste. Cracks in hydrated cement paste are expected to deflect and pass around these particles. This implies that fly ash particles pull out upon fracture of hydrated cement paste. The same logic applies to unreacted cement grains, which are irregular in shape and are expected to dissipate more energy during pull-out. The first task in development of a time-dependent model for high-volume fly ash concrete was to determine the significance of unreacted fly ash particles and cement grains in determining the fracture toughness of hydrated cement paste, and thereby that of concrete.

The contribution of unreacted fly ash particles to the fracture toughness of hydrated cement paste can be approximated by estimating the average additional surface area created as the crack deflects around fly ash particles. The maximum possible pull-out distance is half the particle diameter, and the minimum is zero. Therefore, half of the radius was assumed as a reasonable average pull-out distance, as was the case with CH pull-out. The contribution of fly ash pull-out to fracture toughness can be estimated by

considering the ratio of the fractured surface area of the spherical cap (Fig. 5.1) to its projected plane area:

$$S_{fa} = \pi r_{fa}^2 \quad (5.5)$$

$$A_{fa} = 0.75\pi r_{fa}^2 \quad (5.6)$$

where, S_{fa} is the pulled-out surface area of fly ash, which is the shaded surface in Fig. 5.1 (spherical cap); A_{fa} is the projected plane area of the shaded region; and r_{fa} is the radius of the fly ash particle.

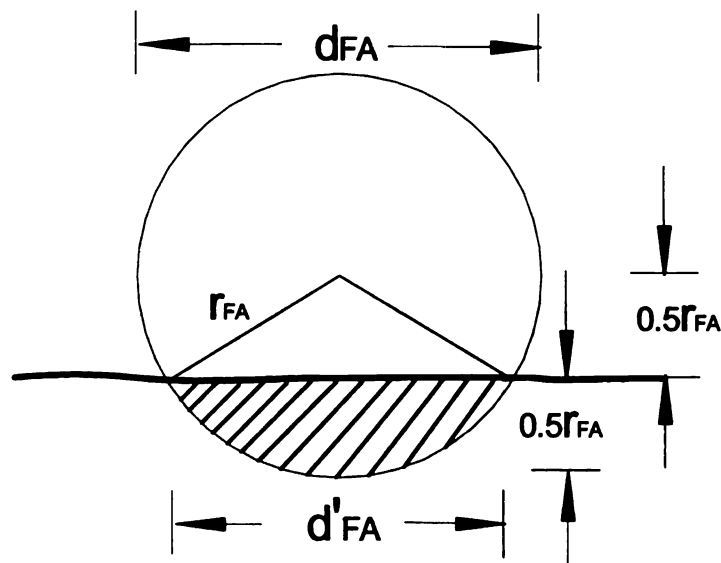


Fig. 5.1 - Schematic presentation of the average surface area of fly ash particle subjected to pull-out upon cracking of the hydrated cement paste

Therefore, the influence of the pull-out of fly ash particles on the fracture toughness of hydrated cement paste can be estimated by considering the additional fractured area due to the pull-out of fly ash particles along the crack path which tends to be smooth in the case of plain cement paste. Because fly ash particles are spherical in shape, their effect on the fracture toughness results from the debonding of C-S-H globules, and not from frictional pull-out. Hence, the contribution of the pull-out of unreacted fly ash particles to the fracture toughness of hcp was determined as follows:

$$G_{fa} = \left(\frac{S_{fa}}{A_{fa}} \right) G_d \quad (5.7)$$

where, G_{fa} is the contribution to fracture toughness of a single fly ash particle; and G_d is fracture toughness of hydrated cement paste associated with the debonding of C-S-H globules, as discussed in Chapter 2. Substituting the values of S_{FA} and A_{FA} into Equation 5.4 and simplifying it yields the following relationship between G_{fa} and G_d :

$$G_{fa} = \left(\frac{\pi r_{fa}^2}{0.75 \pi r_{fa}^2} \right) G_d = 1.33 G_d \quad (5.8)$$

Since G_d is the minor contributor to the fracture toughness of hcp (it constitutes only about 5% of the hcp fracture toughness), the effect of unreacted fly ash particles on the fracture toughness of hcp is not significant, and could be reasonably ignored.

The other major contributor to fracture toughness of hydrated cement paste is the pull-out of unreacted cement grains. These grains are irregular in shape and have rough surfaces. To simplify the model, they were assumed to have a flat surface. Since their mean size is almost the same as that of CH, their effect on fracture toughness was almost similar to that of CH.

To determine the amount of fly and cement grains reacted at a given age of hydration, it was necessary to develop a relationship between the degree of hydration of hcp and its age. The degree of hydration of hcp for a given w/b ratio can be estimated from the empirical relationship given below: ¹⁰⁴

$$\alpha_{t=28} = 96 e^{\frac{-0.135}{w/b}} \quad (5.9)$$

where, $\alpha_{t=28}$ is degree of hydration at the age of 28-days.

The above equation was further refined for estimating the degree of hydration at any hydration time:

$$\alpha_{t=28} = 96 e^{\frac{-0.135}{w/b}} (t^{0.16}) \quad (5.10)$$

It was necessary to express the effect of the unreacted cement particles and CH on the fracture toughness of hcp in an equation format so that it could be incorporated into the concrete model. The procedure followed was to determine the relevant parameters shown in Tables 5.1 and 5.2. The values of R_{FA} and α were computed from Equations 5.1 and 5.10, respectively. The amount CH produced (CH_p) at a given time, as a percentage of hcp, was calculated as the product of the degree of hydration and the total amount of CH as a percentage of hcp (which is 22% upon full hydration).¹⁰⁵ The value of CH_p (in grams) was obtained by multiplying the percent CH_p by the volume of hcp (V_h from Equation 5.3) and the unit weight of CH (which is 2.21). During pozzolanic reaction, 0.85 grams of CH is needed to react with one gram of fly ash.¹⁰⁶ Therefore, the amount of CH in grams reacted (CH_r) at a given time was computed using this relationship, with the results presented in Table 5.1.

Table 5.1 - Reduction of CH and fly ash in hcp during pozzolanic reactions

t (day)	R_{FA} %FA	α	CH_p %hcp	CH_p (g)	CH_r (g)
28	24.19	0.630	0.139	0.223	0.103
90	30.85	0.760	0.167	0.268	0.131
180	34.80	0.849	0.187	0.300	0.148
270	37.12	0.906	0.199	0.320	0.158
360	38.76	0.949	0.209	0.335	0.165

After determining the amount of reacted fly ash, cement and CH, the amounts of unreacted cement grains (U_{CG}) and unreacted CH crystals (U_{CH}) were computed. These are the two major contributors to the fracture toughness of hcp, which affect G_o . The value of G_{ot} at a given time was determined by varying the amounts of unhydrated particles (cement and CH) with time, as shown in Table 5.2. The maximum G_o that can be obtained under full hydration is about 29.44 J/m^2 , when CH is 22% of hcp. The effect of unhydrated particles on the fracture toughness of hcp at different hydration times is shown as a ratio of the G_o to the maximum value of 29.44 J/m^2 . It can be observed from Table 5.2 that fly ash reduces the fracture toughness of concrete over time.

Table 5.2 - Effect of unreacted fly ash and cement particles on fracture toughness of hydrated cement paste

t (day)	U_{CG} %hcp	U_{CH} %hcp	$U_{CG}+U_{CH}$ %hcp	G_{ot} J/m^2	G_{ot}/G_o
28	8.079	7.464	15.543	23.93	0.813
90	5.248	8.548	13.796	23.72	0.806
180	3.300	9.461	12.761	23.65	0.803
270	2.056	10.100	12.156	23.56	0.800
360	1.123	10.604	11.728	23.49	0.798

A graph shown in Fig. 5.2 was plotted using the data presented in Table 5.2 in order to show the trends in development of the fracture toughness of cementitious paste with high fly ash volume over time. The following relationship expresses this trend:

$$G_{of} = 1.0274 G_o t^{-0.0069} \quad (5.11)$$

where, G_{of} is intrinsic fracture toughness of high-volume fly ash concrete.

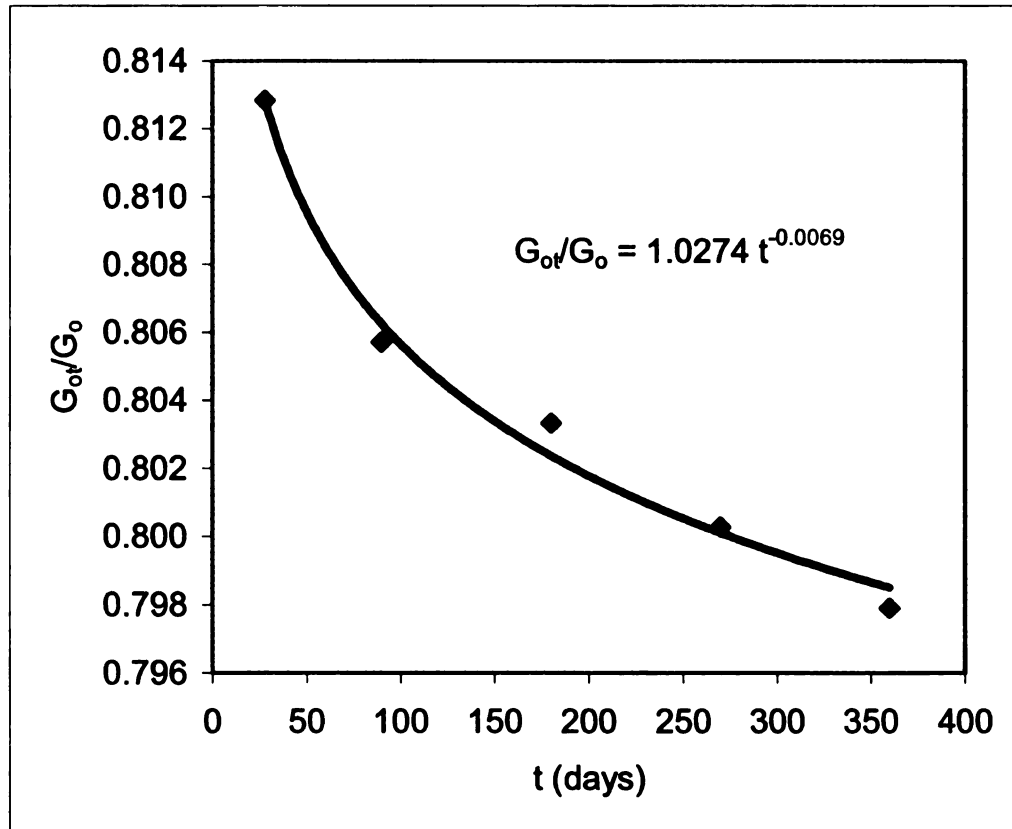


Fig. 5.2 - Effect of age on fracture toughness of high-volume fly ash hcp

Since the G_o has a direct relation with fracture toughness of hcp (G_h), the fracture toughness of hcp containing high-volumes of fly ash (G_{hf}) can be determined based on Equation 5.11 as follows:

$$G_{hf} = 1.0274 G_h t^{-0.0069} \quad (5.12)$$

The above relationship indicates that the effect of fly ash on the fracture toughness of hydrated cement paste is relatively small (Fig. 5.3). The reason for this could be that the pozzolanic reaction consumes relatively small amounts of CH to produce new C-S-H particles; therefore, much of the CH crystals remain unreacted to almost preserve the original fracture toughness of the hydrated cement paste.

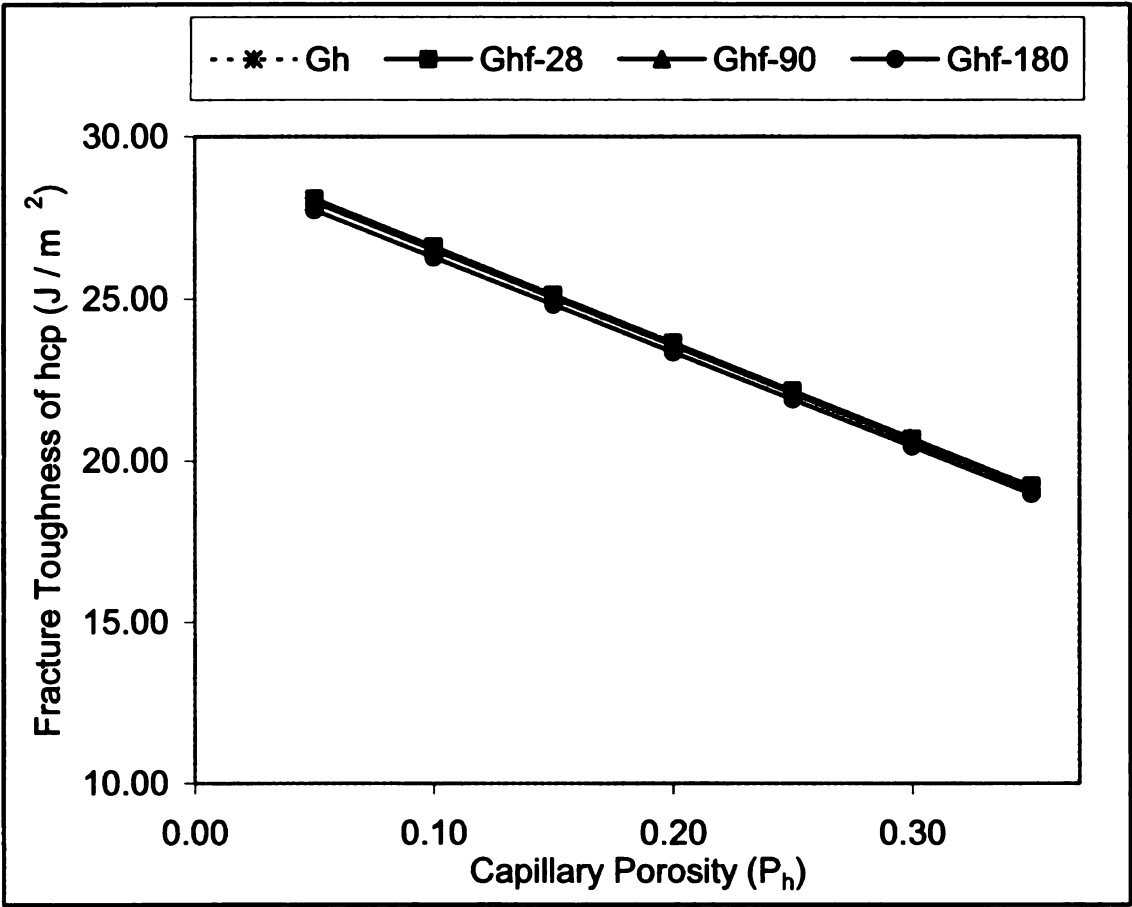


Fig 5.3 – Comparison between the fracture toughness of normal hcp with that of high-volume fly ash cement pastes at the ages of 28, 90 and 180 days.

5.3.2 Modulus of Elasticity of Concrete Containing 50% Fly Ash As Replacement for Cement

In determining the effect of fly ash on the elastic modulus of concrete, it was necessary to evaluate the change in the structure of concrete phases resulting from pozzolanic reaction. During pozzolanic reaction, the newly produced C-S-H gels grow in capillary pores and thus refine the pore sizes. The reduction in capillary pore sizes is considered to be proportional to the reduction in the aspect ratios (a/b) of capillary pores. An important task is to determine the reduction in capillary pore size with time. A relationship was drawn by plotting experimental results collected from the literatures addressing the effect of time on capillary pore size in high-volume fly ash concrete. This relationship was as follows:¹⁰⁷

$$\frac{a}{b} = 8.4t^{-0.38} \quad (5.13)$$

Substituting the above equation into Equation 2.29 (from Chapter 2) yields an expression for the elastic modulus of hydrated cement paste at time t :

$$E_{hf} = \frac{0.77E_o(1-p)(\pi - 4p_h)^{0.37}}{(1 + 2(8.4t^{-0.38}))p_h^{0.37}} \quad (5.14)$$

where, E_{hf} is the modulus of elasticity at time t of hcp containing high-volume of fly ash.

Stating E_{hf} as a function of the modulus of elasticity of normal hcp (E_h) yields:

$$E_{hf} = \frac{5E_h}{1 + 16.8t^{-0.38}} \quad (5.15)$$

Fly ash refines the capillary pore size, and lowers the aspect ratio of the elliptical capillary pores which undermine the modulus of elasticity. As can be observed from Fig. 5.4, high-volume fly ash paste offers improved elastic moduli when compared with normal Portland cement paste at later ages due to the relatively slow pace of pozzolanic reactions.

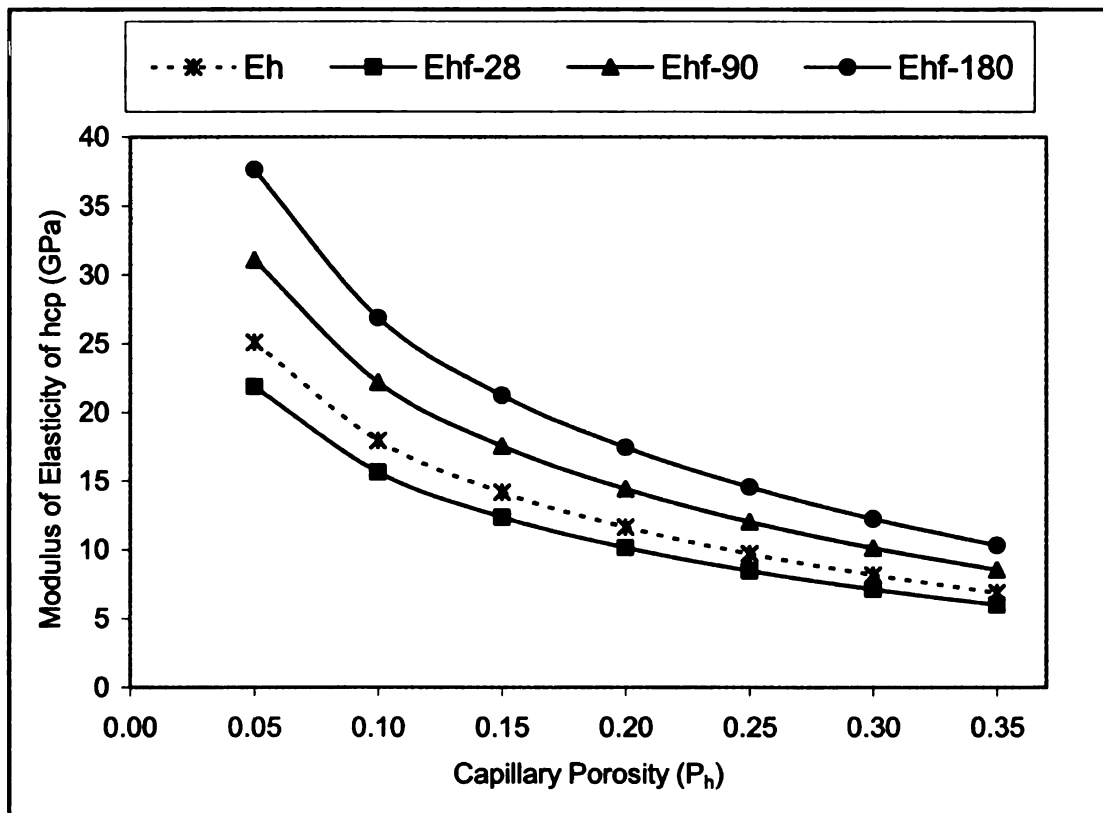


Fig 5.4 – Comparison of the modulus of elasticity model of normal hcp with that of high-volume fly ash cement pastes at 28, 90 and 180 days.

In the same manner, the modulus of elasticity of mortar (E_{mt}) was determined by substituting E_{ht} in Equation 3.25 (from Chapter 3) for E_h to get an expression for E_{mt} as follows:

$$E_{mf} = \frac{5.78E_{hf}^2 - 28.35E_{hf}}{0.04E_{hf}^2 + 2.4E_{hf} - 12.46} \quad (5.16)$$

The effect of fly ash on the elastic modulus of cement mortar is results from the corresponding effects of fly ash on cement paste. As shown in Fig. 5.4, the elastic modulus of high-volume fly ash mortar exceeds that of cement paste at later ages. At 28 days of age, however, the elastic modulus of cement mortar is still higher than that of the high-volume fly ash mortar, which is due to the slow pace of pozzolanic reactions.

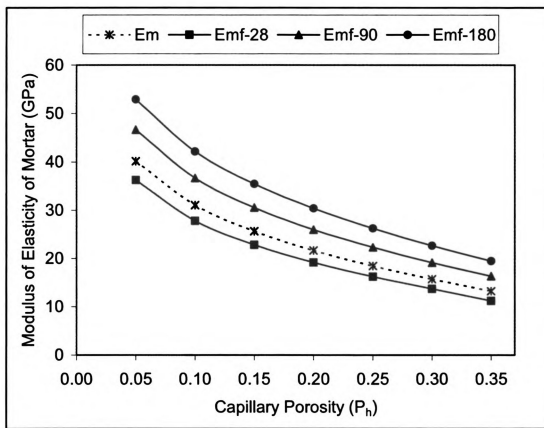


Fig 5.4 – Comparison of the modulus of elasticity of cement mortar with that of high-volume fly ash mortar at the ages of 28, 90 and 180 days.

The elastic modulus of concrete containing high fly ash volume (E_{ctf}) was also determined by substituting E_{mf} for E_m in Equation 4.24:

$$E_{ctf} = \frac{4.02E_{mf}^2 - 45.09E_{mf}}{0.023E_{mf}^2 + 1.96E_{mf} - 24.38} \quad (5.17)$$

The comparison between the elastic modulus of normal concrete and high-volume fly ash concrete depicted in Fig. 5.5 indicates that, at later ages, high-volume fly ash concrete

offers higher elastic moduli when compared with normal concrete. At 28 days of age, however, normal concrete still provides a higher elastic modulus than high-volume fly ash concrete, which is due to the relatively slow pace of pozzolanic reactions.

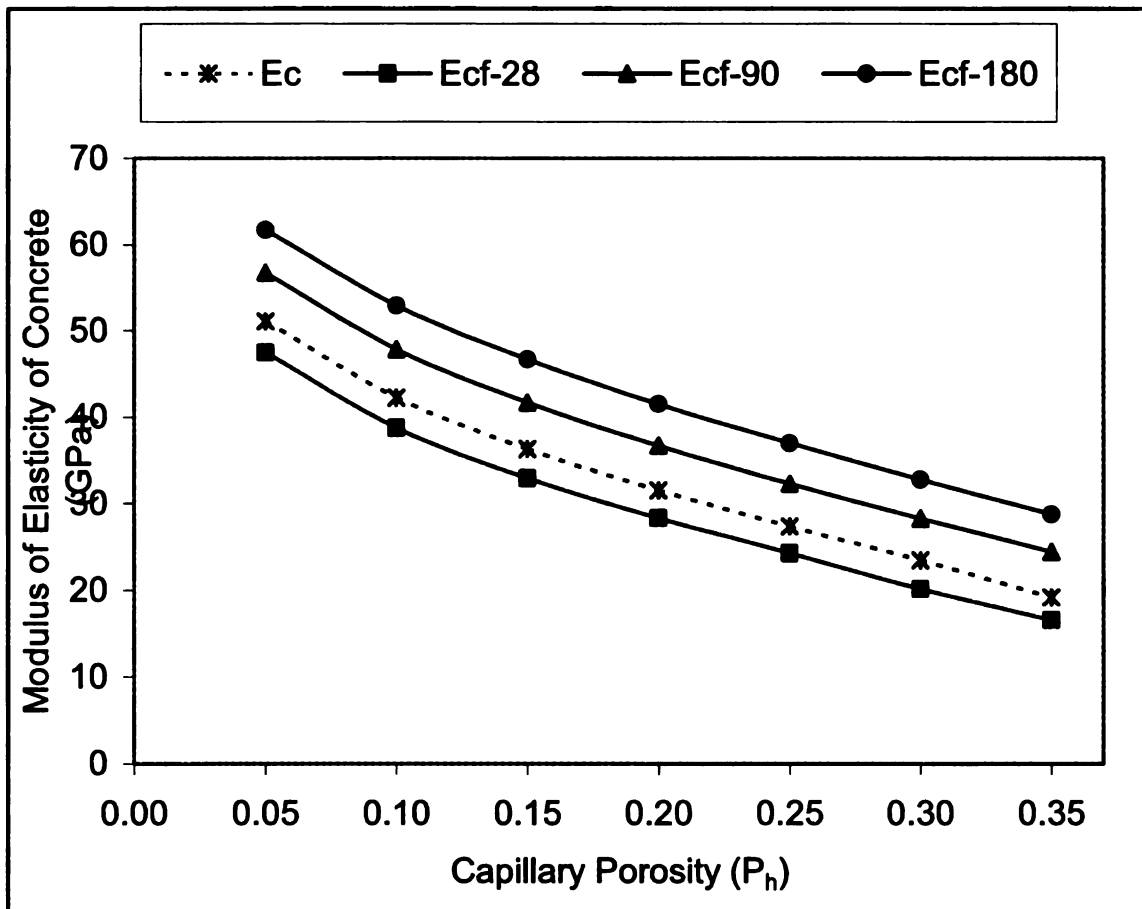


Fig 5.5 – Comparison of the modulus of elasticity model of normal concrete with that of high-volume fly ash concrete at the ages of 28, 90 and 180 days.

5.3.3. Tensile Strength of Concrete Containing 50% Fly Ash

The tensile strength model of concrete containing 50% replacement of cement with fly ash was determined by upgrading the tensile strength model for Portland cement concrete developed in Chapter 4. In this process, the effect of fly ash on the properties of hydrated cement paste, cement mortar and concrete were considered. The hypothesis is that the major effect of fly ash on cementitious materials involves their fracture toughness and capillary porosity, and thus the tensile strength model of concrete was developed by modifying Equation 4.52 (from Chapter 4) as follows:

$$\sigma_{ctf} = \sqrt{\frac{E_{cf} G_{ctf}}{\pi l_c}} \quad (5.18)$$

Substituting equation 5.12 and 5.17 for G_{FA} and E_{ct} , respectively, into equation 5.18 yields:

$$\sigma_{ctf} = 96.4 \left[\frac{(1 - 1.61P_h)(E_{mf}^2 - 11.22E_{mf})t^{-0.007}}{d_{ca}(E_{mf}^2 + 85.22E_{mf} - 1060)} \right]^{\frac{1}{2}} \quad (5.19)$$

where, σ_{ct} is the tensile strength of concrete with 50% replacement of cement with fly ash; E_{mt} is the modulus of elasticity of mortar as defined in equation 5.15; t is (hydration) age of concrete in days; and d_{ca} is the maximum aggregate size.

The changes in elastic modulus of high-volume fly ash hcp, cement mortar and concrete, also tensile strength of concrete (50% fly ash) with time, at the age of 28, 90 and 180 days, is shown in Tables 5.3, 5.4 and 5.5, respectively, for maximum aggregate size of 20 mm.

Table 5.3 - Modulus of elasticity of hcp, mortar and concrete and fracture toughness and tensile strength of concrete, containing 50% fly ash, in 28-days.

P_h	E_h (GPa)	E_{hf} (GPa)	E_{mf} (GPa)	E_{cf} (GPa)	G_{ctf} J/m ²	σ_{ctf} MPa
0.05	25.11	21.89	36.27	47.46	48.11	6.30
0.10	17.93	15.63	27.83	38.73	44.35	5.47
0.15	14.17	12.35	22.84	32.95	40.59	4.82
0.20	11.63	10.14	19.19	28.35	36.83	4.26
0.25	9.72	8.47	16.25	24.29	33.07	3.74
0.30	8.17	7.13	13.71	20.17	29.31	3.20
0.34	7.13	6.21	11.76	13.89	26.30	2.51

Table 5.4 - Modulus of elasticity of hcp, mortar and concrete and fracture toughness and tensile strength of concrete, containing 50% fly ash, in 90-days.

P_h	E_h (GPa)	E_{hf} (GPa)	E_{mf} (GPa)	E_{cf} (GPa)	G_{ctf} J/m ²	σ_{ctf} MPa
0.05	25.11	31.08	46.66	56.75	44.40	6.89
0.10	17.93	22.20	36.66	47.84	40.93	6.08
0.15	14.17	17.55	30.55	41.68	37.46	5.43
0.20	11.63	14.40	26.01	36.69	33.99	4.85
0.25	9.72	12.03	22.31	32.31	30.52	4.31
0.30	8.17	10.12	19.16	28.30	27.05	3.80
0.35	6.89	8.53	16.36	24.44	23.58	3.30

Table 5.5 - Modulus of elasticity of hcp, mortar and concrete and fracture toughness and tensile strength of concrete, containing 50% fly ash, in 180-days.

P_h	E_h (GPa)	E_{hf} (GPa)	E_{mf} (GPa)	E_{cf} (GPa)	G_{ctf} J/m ²	σ_{ctf} MPa
0.05	25.11	37.64	52.93	61.72	42.33	7.19
0.1	17.93	26.88	42.18	52.92	39.02	6.39
0.15	14.17	21.25	35.47	46.68	35.71	5.74
0.2	11.63	17.44	30.40	41.53	32.40	5.16
0.25	9.72	14.57	26.25	36.97	29.10	4.61
0.3	8.17	12.26	22.68	32.76	25.79	4.09
0.35	6.89	10.33	19.51	28.76	22.48	3.58

The effect of fly ash on the tensile strength of normal concrete is related to the corresponding effects of fly ash on the fracture toughness and modulus of elasticity of concrete. The gain in the the strength of concrete with high-volumes introduction of fly ash becomes evident at later ages, which is due to the relatively slow pace of pozzolanic reactions. A comparisons between the tensile strength of normal concrete and that of high-volume fly ash concrete at 28, 90 and 180 days of age is shown in Fig. 5.6. At the age of 28 days, the strength of normal concrete is higher than that of high-volume fly ash concrete. With time, the strengths of high-volume fly ash concrete increases beyond that of normal concrete.

The relationship between tensile strength (σ_{cf}) and capillary porosity (P_h) of concrete containing 50% replacement of cement with fly ash (Equation 5.19) is shown in Fig. 5.6.

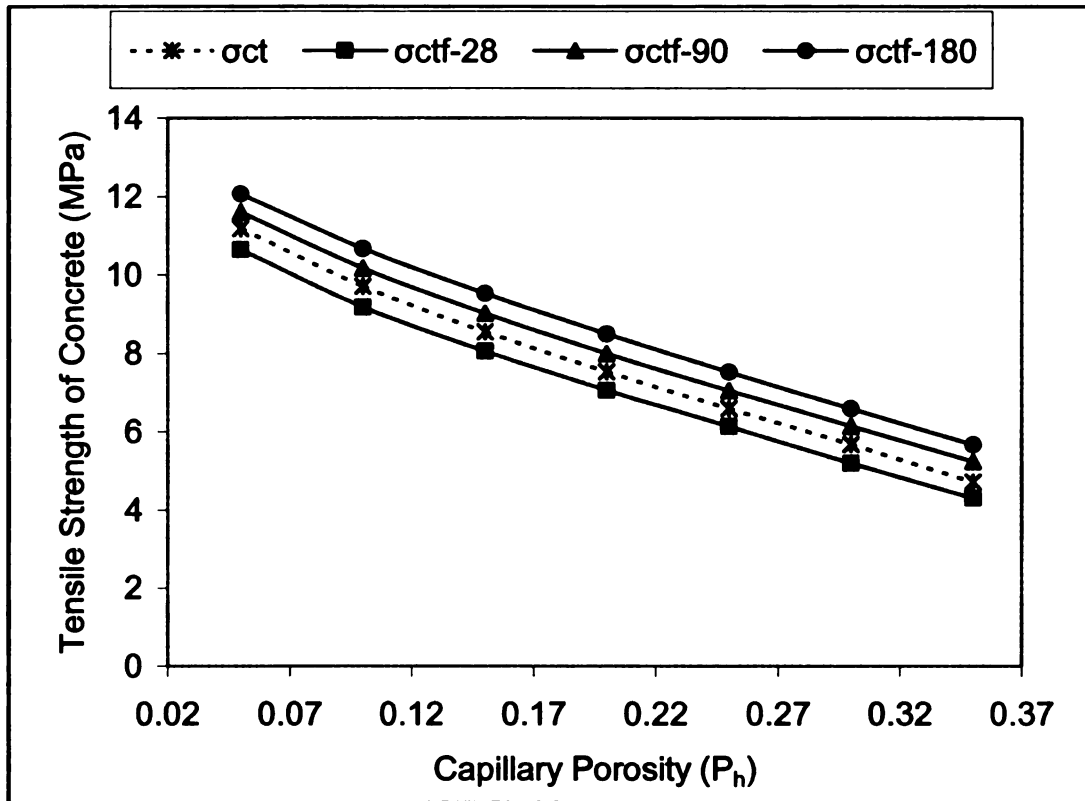


Fig 5.6 – Comparison of the tensile strength of normal concrete with that of high-volume fly ash concrete at the ages of 28, 90 and 180 days.

5.3.4 Compressive Strength of Concrete Containing 50% Fly Ash

After determining the modulus of elasticity and fracture toughness of concrete, the next step was to develop a model for the compressive strength of concrete. The same concept and approach as in the case of normal concrete (Chapter 4) was applied for modeling the compressive strength of high-volume fly ash concrete. For this purpose, the elastic modulus and fracture toughness models of normal concrete were replaced with the

corresponding models of high-volume fly ash concrete introduced above. The resulting model for the compressive strength of high-volume fly ash concrete is presented below:

$$\sigma_{ccf} = 532 \left[\frac{(1 - 1.64 P_h) (E_{mf}^2 - 11.22 E_{mf}) t^{-0.0069}}{d_{ca} (E_{mf}^2 + 85.22 E_{mf} - 1060)} \right]^{1/2} \quad (5.20)$$

Tables 5.6, 5.7 and 5.8 show the calculated modulus of elasticity and fracture toughness at various ages of concrete. The resulting compressive strength of concrete, as computed from Equation 5.20, is shown in the tables and also plotted in Fig. 5.4. It can be observed from the graph that the strength of high-volume fly ash concrete gains strength slowly with time, as stated in several literatures.

Table 5.6 - Modulus of elasticity of hcp, mortar and concrete and fracture toughness and compressive strength of concrete, containing 50% fly ash, in 28-days.

P_h	E_h (GPa)	E_{hf} (GPa)	E_{mf} (GPa)	E_{cf} (GPa)	G_{ccf} J/m ²	σ_{ccf} MPa
0.05	25.11	21.89	36.27	47.46	143.20	57.35
0.10	17.93	15.63	27.83	38.73	132.01	49.74
0.15	14.17	12.35	22.84	32.95	120.82	43.89
0.20	11.63	10.14	19.19	28.35	109.62	38.77
0.25	9.72	8.47	16.25	24.29	98.43	34.00
0.30	8.17	7.13	13.71	20.17	87.23	29.16
0.34	7.13	6.21	11.76	13.89	78.28	22.86

Table 5.7 - Modulus of elasticity of hcp, mortar and concrete and fracture toughness and compressive strength of concrete, containing 50% fly ash, in 90-days.

P_h	E_h (GPa)	E_{hf} (GPa)	E_{mf} (GPa)	E_{cf} (GPa)	G_{ccf} J/m ²	σ_{ccf} MPa
0.05	25.11	31.08	46.66	56.75	132.15	62.70
0.10	17.93	22.20	36.66	47.84	121.82	55.27
0.15	14.17	17.55	30.55	41.68	111.49	49.35
0.20	11.63	14.40	26.01	36.69	101.16	44.10
0.25	9.72	12.03	22.31	32.31	90.83	39.22
0.30	8.17	10.12	19.16	28.30	80.50	34.55
0.35	6.89	8.53	16.36	24.44	70.17	29.97

Table 5.8 - Modulus of elasticity of hcp, mortar and concrete and fracture toughness and compressive strength of concrete, containing 50% fly ash, in 180-days.

P_h	E_h (GPa)	E_{hf} (GPa)	E_{mf} (GPa)	E_{cf} (GPa)	G_{ccf} J/m ²	σ_{ccf} MPa
0.05	25.11	37.64	52.93	61.72	125.99	65.40
0.1	17.93	26.88	42.18	52.92	116.15	58.14
0.15	14.17	21.25	35.47	46.68	106.30	52.24
0.2	11.63	17.44	30.40	41.53	96.45	46.93
0.25	9.72	14.57	26.25	36.97	86.60	41.96
0.3	8.17	12.26	22.68	32.76	76.75	37.18
0.35	6.89	10.33	19.51	28.76	66.90	32.53

Fig. 5.7 compares the compressive strength of normal concrete versus those of high-volume fly ash concrete at different ages. While normal concrete provides a higher compressive strength at 28 days of age, the 90- and 180-day compressive strengths of high-volume fly ash concrete exceed the compressive strength of normal concrete. The relatively slow pace of pozzolanic reactions explain why high-volume fly ash concrete exhibits improved performance at later ages.

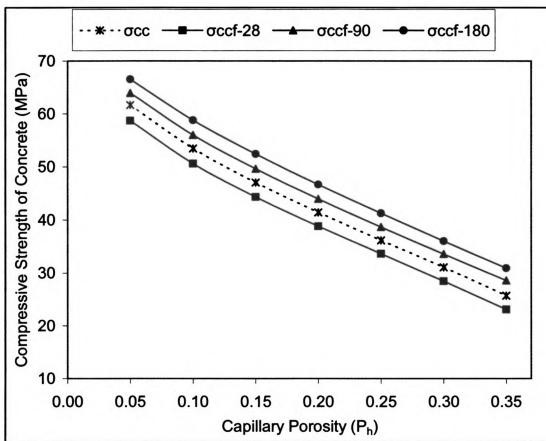


Fig 5.7 – Comparison of the compressive strength model of normal concrete with that of high-volume fly ash concrete at the ages of 28, 90 and 180 days.

5.3.5 Comparing the Predictions of the Mechanistic Model of the Strength of Concrete Containing 50% Fly Ash Cement with Experimental Results

Verification of the mechanistic models involves comparison of their predictions with the corresponding experimental results. Noting that the experimental data on high-volume fly ash concrete are relatively limited, an attempt was made to verify the mechanistic models of high-volume fly ash concrete using the available experimental data.¹⁰⁸ Fig. 5.8 presents a comparison of the mechanistic model predictions of the 28-days compressive strength of concrete containing 50% fly ash versus experimental results. The experimental data are observed to cover a narrow range of porosity, which could be the reasonable porosity of high-volume fly ash concrete concrete at 28 days of age. The mechanistic model predictions appears to compare reasonable with experimental results, especially at the lower capillary porosities measured in this experimental study. The mercury intrusion technique used here to measure capillary porosity tends to overestimate the actual porosity. Removal of this effect could improve the comparison between the predictions of the mechanistic model and the experimental results.

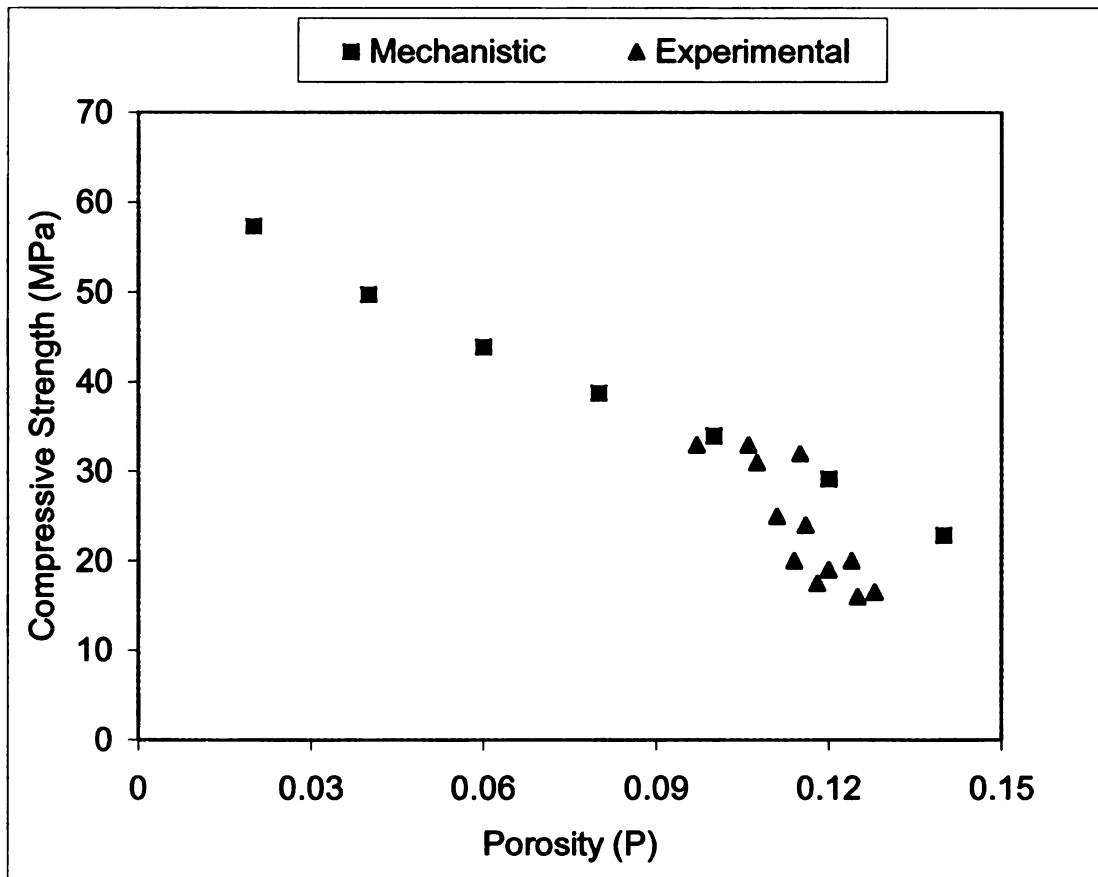


Fig. 5.8 - Comparison of the predictions of the mechanistic model for the 28-day compressive strength of concrete containing 50% fly ash versus experimental results

Fig. 5.9 shows a comparison of the 90-day compressive strength of high-volume fly ash concrete versus experimental results. The mechanistic model is observed to predict experimental results with reasonable accuracy. The general over-estimation of the experimental results could be partly attributed to the over-estimation of capillary porosity measurements by the mercury intrusion technique.

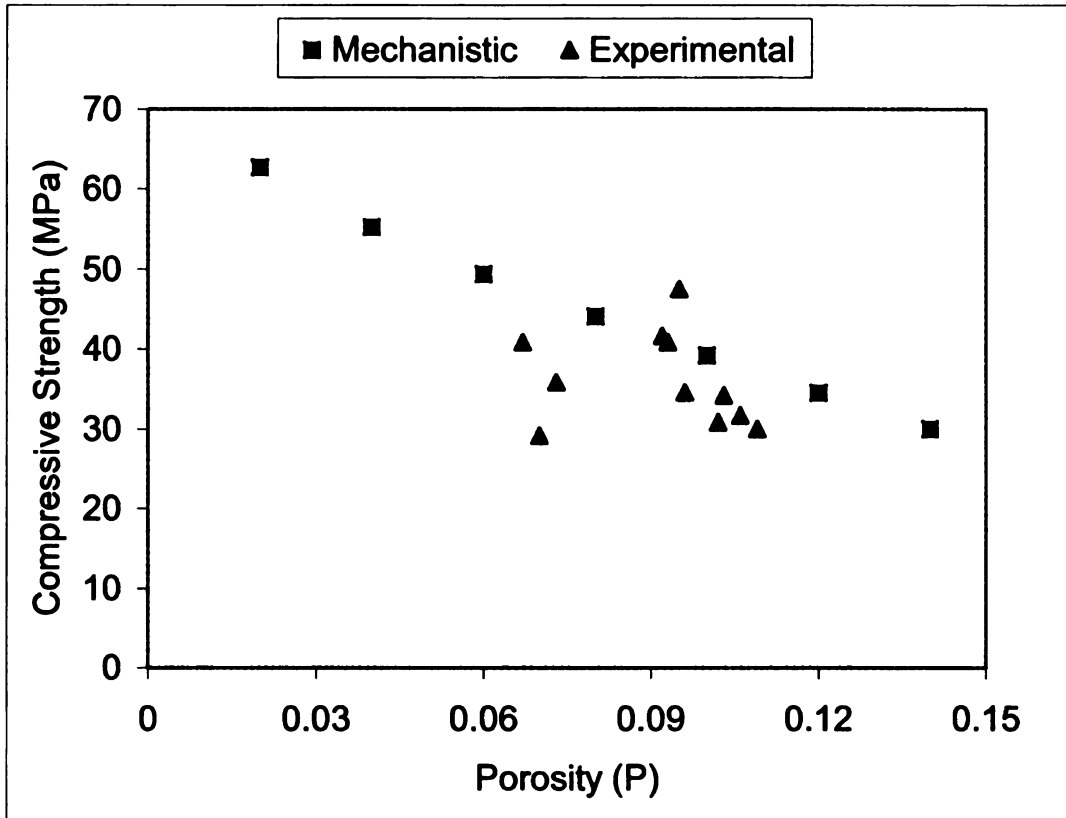


Fig. 5.9 - Comparison of the predictions of the mechanistic model for the 90-day compressive strength of concrete containing 50% fly ash versus experimental results

SUMMARY AND CONCLUSIONS

Theoretical models, based on structure-property relationships, were developed sequentially for prediction of the mechanical properties of hydrated cement paste, mortar and concrete. Experimental results and empirical models were used to verify the mechanistic models. The models were used to predict the effects of high-volume replacement of Portland cement with coal fly ash on mechanical properties of concrete.

For the purpose of mechanistic modeling, hydrated cement paste was treated as a multi-phase material with calcium silicate hydrate (C-S-H) particles acting as the binder (glue) rendering cementing effects. The model starts with simulation of the structure of C-S-H at nano-scale. The nano-scale C-S-H particles offer effective adhesive qualities capable of developing physical bonds (based on van der Waals interactions) between themselves and also with other hydration products as well as aggregates. This adhesive force provided the fundamental basis for the development of the mechanistic models. The intrinsic elastic modulus was modeled based on the energy buildup associated with bond deformations. The energy required to break van der Waals bonds was accounted for in development of the intrinsic fracture toughness model of hydrated cement paste; the energy associated with pullout of calcium hydroxide (CH) crystals was also considered in development of the fracture toughness model of hydrated cement paste. The phononic frictional pullout of CH crystals from the C-S-H matrix was found to be the major

contributor to the intrinsic fracture toughness of hydrated cement paste. The elastic modulus and fracture toughness models of hydrated cement paste were developed based on the above intrinsic models by introducing the effects of capillary pores and microcracks. The strength model of hydrated cement paste was developed using fracture mechanics concepts considering the effects of restrained shrinkage microcracks. Experimental data and empirical models were used to verify the mechanistic models at different stages of development.

The mechanistic models of cement mortar were developed using the corresponding models of hydrated cement paste, accounting for the effects of fine aggregates and their interfacial transition zone. The elastic modulus of cement mortar was modeled by simulating mortar as a three-phase solid comprising the hydrated cement paste, fine aggregates, and the interfacial transition zone. While the high-modulus fine aggregates positively affected the elastic modulus of mortar, the corresponding effects of the transition zone were negative. The fracture toughness model of cement mortar was developed by introducing the energy dissipation associated with pullout of fine aggregates to the fracture toughness model of hydrated cement paste, and also by considering the positive effects of multiple crack formation in cement mortar in the presence of aggregates. The tensile strength model of cement mortar was developed using fracture mechanics concepts, with due consideration given to the effect of fine aggregates on the restrained shrinkage microcrack size in mortar. Experimental results and empirical models were used to verify the mechanistic models developed for the mechanical properties of cement mortar.

The mechanistic models of concrete were developed based on the corresponding models of mortar by considering the effects of coarse aggregates and their interfacial transition zone. Concrete was analyzed as a three-phase material comprising cement mortar, coarse aggregates, and the interfacial transition zone. The presence of the interfacial zone negatively affected the elastic modulus and strength of concrete. The relatively high-modulus coarse aggregates, on the other hand, made positive contributions to the elastic modulus of concrete. The fracture toughness model of concrete was developed by accounting for the energy dissipation associated with the pullout of coarse aggregates with rough surfaces from cement mortar, and also the crack diverging effects of coarse aggregates. The tensile strength model of concrete was developed based on fracture mechanics principles, using procedures similar to those used for mortar, considering the effect of coarse aggregates on restrained shrinkage microcrack size in concrete. A compressive strength model was also developed for concrete considering the tensile stress development in concrete under compression and also the shear friction effects associated with the peculiar failure modes of concrete under compression. Experimental results and empirical models were used to verify the mechanistic models developed for various aspects of the mechanical performance of concrete.

The mechanistic models developed for concrete were refined for application to high-volume fly ash concrete with 50% replacement of Portland cement with coal fly ash. Given the slow rate of hydration of high-volume fly ash concrete, the models were developed as a function of time. The effect of fly ash on conversion of CH to C-S-H and

on refinement of the capillary pore size provided a basis to develop the mechanistic models of high-volume fly ash concrete. Further, the effects of unhydrated cement grains and unreacted fly ash particles were considered in development of time-dependent mechanistic models. The predictions of mechanistic models were compared with the limited test data available for high-volume fly ash concrete.

The following conclusions can be drawn from the research conducted on mechanistic modeling of hydrated cement paste, mortar and concrete:

1. The physical interatomic bonds between calcium silicate hydrate (C-S-H) globules together with the phononic frictional pullout of calcium hydroxide (CH) crystals govern the intrinsic mechanical properties of hydrated cement paste. The predicted intrinsic strength, elastic modulus and fracture toughness of the compact hydrated cement paste were in conformance with the corresponding experimentally measured values.
2. The introduction of defects (capillary pores and microcracks) significantly alters the engineering properties of hydrated cement paste when compared with the corresponding intrinsic properties. The geometry and volume fraction of capillary pores and the size of microcracks are important factors governing the mechanical performance of hydrated cement paste and also cement mortar and concrete.

3. The fracture toughness of hydrated cement paste receives contributions from debonding of the C-S-H globules and frictional pullout of CH crystals, with the latter mechanism playing the dominant role. The fracture toughness of cement mortar and concrete exceed that of hydrated cement paste due to the energy dissipation associated with the frictional pullout of fine and coarse aggregates as well as the crack arresting and diverting effects of aggregates. Predictions of the fracture toughness models compared well with experimental results.
4. The elastic modulus model of hydrated cement paste was developed to account for the effect of the elliptical geometry of capillary pores on local stress rises that undermine the stiffness of the hydrated cement paste. Predictions of the elastic modulus model compared well with experimental results.
5. The tensile strength model of hydrated cement paste was developed based on fracture principles using the elastic modulus and fracture toughness models, and compared favorably with experimental results when considering the presence of intrinsic restrained shrinkage microcracks.
6. The energy absorption capacity of concrete in compression benefits from the wedging action of conical cement mortar attached to the coarse aggregates in the direction of loading. The corresponding energy dissipation is due to the shear friction effects on surfaces of these conical wedges.

7. The elastic modulus model of cement mortar was developed based on the corresponding model of hydrated cement paste and considering the effects of the elastic modulus of fine aggregates as well as the negative effects of the interfacial transition zone. The predictions of the model were evaluated by comparing them with experimental results.
8. The fracture toughness models of cement mortar and concrete reflect the significance of the contributions made by fine and coarse aggregates through frictional pullout, crack arresting and diverting effects, and its predictions compare favorably with experimental results.
9. The strength models of cement mortar and concrete are based on the corresponding elastic modulus and fracture toughness models, considering the effects of aggregates on restrained shrinkage microcracking of concrete. The predictions of these models occur within the range of experimental results.
10. In high-volume fly ash concrete, the slow pace of pozzolanic reactions necessitate development of time-dependent models. Pozzolanic reactions consume calcium hydroxide to generate the calcium silicate hydrate binder and thus refine the capillary pore system of hydrated cement paste. Given the slow pace of pozzolanic reactions, one should also account for the effects of unhydrated cement grains and fly ash particles on the mechanical performance of high-volume fly ash paste, mortar and concrete. The theoretical models developed for normal cement,

mortar and concrete were refined to account for the above time-dependent effects of fly ash (when 50% of cement is replaced with fly ash). The models indicated that high-volume fly ash concrete can surpass normal concrete in terms of elastic modulus, and tensile and compressive strengths over longer time periods; the fracture toughness of high-volume fly ash concrete is comparable to that of normal concrete. At the age of 28 days normal concrete still offers better elastic modulus and tensile and compressive strengths, and comparable fracture toughness when compared with high-volume fly ash concrete; the advantages of high-volume fly ash concrete are apparent at 90 (or more) days of age.

11. The mechanistic models developed in this research provide insight into the mechanical performance and failure mechanisms of cement-based materials. The fundamental nature of these models makes them of value in guiding development efforts toward further improvement of the mechanical performance of cement-based materials and/or use of new ingredients in cementitious mixtures. The favorable comparisons of the predictions of these models with experimental results suggest that the complex structure of cement-based materials should not be viewed as an unsurmountable obstacle against development of fundamental models and structure-property relationships for concrete. The mechanistic models developed in this project provide a basis for development of more refined structure-property relationships for hydrated cement paste, mortar and concrete.

12. The models developed in this research express concrete properties in terms of interatomic interactions and the concrete structure at nano-, micro- and macro-scales. These models highlight the key aspects of concrete structure which critically influence its mechanical performance, and reveal the sensitivity of various mechanical attributes of concrete to its structure at different scales. The models can guide new developments in concrete technology aimed at achieving enhanced mechanical properties through refinement of concrete structure.

Future research needs:

13. The research reported herein has highlighted some key aspects of the structure of cement-based materials which govern their mechanical performance. These structural attributes, however, are largely unexplored. Development of fundamental models for cement-based material thus requires making assumptions on some basic aspects of their structure. The models developed in this research could be further improved (and verified) through efforts devoted to better understanding of the structure of calcium silicate hydrate at nano-scale, and calcium silicate hydrate, capillary pores and microcracks (at micro-scale). More detailed information is also needed on the structure, composition and failure mechanisms of the interface zone. Finally, the interaction of calcium hydroxide crystals with cracks is a topic which requires further investigation.

14. Certain aspects of the models developed in this research also require improvement. In particular, the complex interactions of aggregates with the crack

propagation process have been considered in this research in a simplified way. More refined modeling procedures are needed to capture the effects of aggregates on the tortuosity of cracks and also on multiple cracking.

15. The models developed in this research express the mechanical properties of cementitious materials in terms of capillary porosity. These models could be developed into more practical models which predict properties in terms of mix proportions and curing conditions/time. For this purpose, relationships are needed for predicting capillary porosity in terms of the mix proportions and curing conditions/time. The models can be even more beneficial towards new developments in the field if predictive models could be developed to predict the effects of (chemical, mineral and polymeric) admixture on the structure of cementitious materials (e.g., the nano-structure of calcium silicate hydrate or the micro-structure of capillary pores). Such predictive models would complement the models developed in this research to predict the effects of various admixtures on the mechanical properties of cementitious materials.

16. Finally, efforts to further validate the developed models require availability of experimental results on the mechanical properties and structure (at least capillary porosity) of cementitious materials. The available test results on mechanical properties generally do not accompany measurements of capillary porosity (or other structural aspects).

REFERENCES

1. Scott, H. Y. D. and Redgrave, G. R., "The manufacture and Testing of Portland Cement," Paper No. 1649 in Portland Cement, Edited by James Forrest, The Institution of Civil Engineers, London, 1880.
2. Klemm, W. A., "Cementitious Materials: Historical Notes, Material Science of Concrete-I," The American Ceramic Society, 1989.
3. Ramezani-pour, A. A. and Malhotra, V. M., "Effect of Curing on the Compressive Strength, Resistance to Chloride-Ion Penetration and Porosity of Concretes Incorporating Slag, Fly Ash Or Silica Fume," Cement and Concrete Composites, V. 17, 1995, pp. 125-133.
4. M. Y. Balshin; Dokl. Akad. Nauk. SSSR, V. 67, 1949, pp. 831-834.
5. R. Ryshkewitch, "Compression Strength of Porous Sintered Alumina and Zirconia," Journal of American Ceramic Society, V. 36, No. 2, 1953, pp.65-68.
6. L.F., Nielson, "Strength Development in Hardened Cement Paste: Examination of Some Empirical Equations," Materials and Structures, V. 26, 1993, pp. 255-260.
7. K. K. Schiller, "Strength of Porous Materials," Cement and Concrete Research, V.1, No. 4, 1971, pp. 419-422.
8. Ortiz, M., Popov, E.P, Plain Concrete as a Composite Material, Mechanics of Materials, V. 1, No. 2, May, 1982, p 139-150.
9. Brunaver, S., Skalny, J., Odler, I. and Yudenfreund, M., "Hardened Portland Cement Paste of low Porosity," Cement and Concrete Research, V. 3, No. 3, pp. 279-294.
10. Taylor, H. F. W., Cement Chemistry, 1990.
11. Mehta, P. K. and Monteiro, P. J. M., Concrete Structure, Properties, and Materials, Prentice Hall, 2nd ed. 1993.
12. Taylor, H.F.W. and Turner, A.B., Cement Concrete Research V. 17, 1987, pp. 613.

13. Copeland, L. E. and Schulz, E. G., "Electron Optical Investigation of the Hydration Products of Calcium Silicates and Portland Cement," *Journal of the PCA Research and Development Laboratories*, V. 4, No. 1, 1962.
14. Diamond, S., "In Hydraulic Cement Pastes: Their Structure and Properties," *Cement and Concrete association*, Slugh, UK, 1976, pp. 2.
15. Powers, T. C. and Brownyard, T. L., "Studies of the Physical Properties of Hardened Portland Cement Paste," (Bull. 22), pp992, Portland Cement Association, Chicago(1984); reprinted from *J. Am. Concr. Inst. (Proc.)*43, 101,249,469,549,669,845,993 (1947).
16. Young, J. F. and Hansen, W., *Master. Res. Soc. Symp. Proc.*, V. 85, 1987, pp. 313.
17. Hadley, D. W., Dolch, W. L. and Diamond, S., "On the Occurrence of Hollow-Shell Hydration Grains in Hydrated Cement Paste," *Cement and Concrete Research*, V. 30, 2000, pp. 1-6.
18. Feldman, R. F. and Ramachandran, V. S., "A study of The State of Water and Stoichiometry of Bottle-Hydrated Ca_3SiO_5 ," *Cement and Concrete Research*, V. 4, No. 2, 1974, pp. 155-166.
19. Neville, A. M. "Properties of Concrete," 1996, 4th ed.
20. Brown, P.W. and Shi, D., "Porosity/Permeability Relationships, Material Science of Concrete-II," *The American Ceramic Society*, 1989.
21. Powers, T. C. and Brownyard, T. L., "Studies of the Physical Properties of Hardened Portland Cement Paste (Nine parts)," *Journal American Concrete Institute*, V. 43, Oct. 1946 to April 1947.
22. Powers, T. C., "The Physical Structure and Engineering Properties of Concrete," *Portland Cement Association Res. Dept. Bul.*, July 1958, pp. 39.
23. Torii, K. and Kawamura, M., "Chloride Permeability of Concrete Containing a Fly Ash and a Blastfurnace Slag", *Proc. of Material Research Society Symposium*, V. 137, 1989, pp. 411-416.
24. Verbeck, G. J., "Hardened Concrete-Pore Structure," *ASTM Sp. Tech. Publ. No. 169*, 1955, pp. 136-42.
25. Odler, I. and Dorr, H., *Cement Concrete Research*, v.11, 1977, pp. 239.
26. Odler, I. and Rossler, M., *Cement Concrete Research*, V. 15, 1985, pp. 401.

27. Helmut, R. A. and Turk, D. A., In Symposium on "Structure of Portland Cement Paste and Concrete" (Sp. Rpt 90), Highway Research Board, Washington, 1996, pp. 135.
28. Ortiz, M., "Constitutive Theory for the Inelastic Behavior of Concrete," *Mechanics of Materials*, V. 4, No. 1, Mar, 1985, p 67-93.
29. Resende, L., "Damage Mechanics Constitutive Theory for the Inelastic Behavior of Concrete," *Computer Methods in Applied Mechanics and Engineering*, v 60, No. 1, Jan. 1987, pp 57-93.
30. J. Mattei, N.J, Mehrabadi M.M., Zhu, H., "A micromechanical Constitutive Model for the Behavior of Concrete," *Mechanics of Materials*, V. 39, 2007, pp. 357-379.
31. Vandewalle, L. and Mortelmans, F, "The Effect of Curing on the Strength Development of Mortar Containing High-Volumes of Fly Ash," *Fly Ash, Silica Fume, Slag, and Natural Pozzolans in Concrete*, Proceedings of the Fourth International Conference, V. 1, May 1992, pp. 53-63.
32. Lam, L., Wong, Y. L. and Poon, C. S., "Degree of Hydration and Gel/Space Ratio of High-Volume Fly Ash/Cement Systems," *Cement Concrete Research*, V. 30, 2000, pp. 747-756.
33. Mehta, P. K., "Pozzolanic and Cementitious by-Products in Concrete- Another Look," Proceedings of the 3rd International Conference on the Use of fly Ash, Silica Fume, Slag, and Natural Pozzolans in Concrete, V.M. Malhotra (Ed), ACI, 1989, pp. 1-43 (ACI SP-114, Trondheim).
34. Odler, I., Final Report of Task Group 1, 68-MMH Technical Committee on Strength of Cement, Materials and Structures, V. 24, No. 140, 1991, pp. 143-157.
35. Mehta, P. K. and Monteiro, P. J. M., *Concrete Structure, Properties, and Materials*, Prentice Hall, 2nd ed. 1993.
36. Alasali, M., Sivasundaram, V. and Malhotra, V. M., *Compilation of Abstracts of Papers from Intl. Conferences and Symposia on Fly Ash in Concrete: 1987-1992*.
37. Aitcin, P.C., Sarkar, S.L., Ranc, C. and Levy, C., "A High Silica Modulus Cement for High-Performance Concrete"; Proceedings of the Conference on Advances on Cementitious Materials, Gaithersburg, USA., 1990, American Ceramic Society, 1991, S. Mindess, ed., pp. 103-121.
38. Torii, K. and Kawamura, M., "Pore Structures and Chloride Permeability of Concretes Containing Fly Ash, Blast-Furnace Slag and Silica Fume" *Fly Ash*,

Silica Fume, Slag, and Natural Pozzolans in Concrete, Proceedings of the Fourth International Conference, V. 1, May 1992, pp. 135-150.

39. Ukita, K., Shigematsu, S. and Ishii, M. "Quality Improvement of Concrete Utilizing 'Classified Fly Ash' "; Proceedings of the 3rd International Conference on Fly Ash, Silica Fume, Slag, and Natural Pozzolans in Concrete, Threndheim, Norway, June 1989.
40. Malhotra, V. M., *Supplementary Cementing Materials for Concrete*, 1987.
41. Gebler, S. and Klieger, P., "Effect of Fly Ash on the Air-Void Stability of Concrete," Proceedings, First International Conference on the Use of Fly Ash, Silica Fume Slag and Other Mineral By-Products in Concrete, Montebello, Canada, Editor, V. M. Malhotra; ACI Special Publication SP-79, July 31-August 5 1983, pp. 103-42.
42. Burnes, J. S., Guarnaschelli, C. and McAskill, N., "Controlling the Effect of Carbon in Fly Ash on Air Entrainment," Proceedings, Sixth International Symposium on Fly Ash Utilization, Reno, Nevada, March 1982, pp. 294-313.
43. Yuan, R. L. and Cook, J. E., "Study of a Class C Fly Ash Concrete," Proceedings, First International Conference on the Use of Fly Ash, Silica Fume Slag and Other Mineral By-Products in Concrete; Montebello, Canada, Editor, V. M. Malhotra, ACI Special Publication SP-79, July 31-August 5, 1983, pp. 307-319.
44. Virtanen, J., "Freez-Thaw Resistance of Concrete Containing Blast-Furnace Slag, Fly Ash or Condensed Silica Fume," Proceedings, First International Conference on the Use of Fly Ash, Silica Fume Slag and Other Mineral By-Products in Concrete; Montebello, Canada; Editor, V. M. Malhotra; ACI Special Publication SP-79; July 31-August 5, 1983, pp. 923-42.
45. Brown, P. W., Clifton, J. R., Frohnsdorff, G. and Berger, R. L., "Limitations to Fly Ash Use in Blended Cements," Proceedings, Fourth International Symposium on Fly Ash Utilization; St. Louis; March 1976; pp. 518-529.
46. Malhotra, V. M., "Superplasticized Fly Ash Concrete for Structural Applications," *American Concrete Institute*, V. 8, 1986, pp. 28-31.
47. Xu, A., Sarkar, S. and Nilsson, L. O., "Effect of Fly Ash on the Microstructure of Cement Mortar," *Materials Structures*, V. 26, 1993, pp. 414-424.
48. Neville, A. M., *Properties of Concrete*, 3rd ed., 1981, pp. 257-279.

49. Poon, C. S., Lam, L. and Wong, Y. L., "A Study on High Strength Concrete Prepared with Large Volumes of Low Calcium Fly Ash," *Cement Concrete Research*, accepted for publication.
50. Berry, E. E., Hemmings, R. T., Zhang, M. H., Cornelius, B. J. and Golden, D. M., "Hydration in High-Volume Fly Ash Binders," *ACI Materials Journal*, V. 91, 1994, pp. 178-187.
51. Zhang, M. H., "Microstructure, Crack Propagation, and Mechanical Properties of Cement Pastes Containing High-Volumes of Fly Ashes," *Cement Concrete Research*, V. 25, 1995, pp. 1165-78.
52. Feldman, F. F., Carette, G. G. and Malhotra, V. M., "Studies on the Development of Physical and Mechanical Properties of High-Volume Fly Ash Cement Pastes," *Cement Concrete Composites*, V. 12, 1990, pp. 245-51.
53. Diamond, S., "Cement Paste Microstructure - An Overview at Several Levels," *Hydraulic Cement Pastes: Their Structure and Properties*, Conference Proceedings, University of Sheffield, Slough, Cement and Concrete Associations, V. 8, April 1976, pp. 2-30.
54. B. Jonsson, H. Wennerstrom, A. Nonat, B. Cabane, "Onset of Cohesion in Cement Paste," *Langmuir Journal*, V. 20, 2004, pp. 6702-6709.
55. C. Plassard, E. Lesniewska, I. Pochard, A. Nonat, "Nanoscale Experimental Investigation of Particle Interactions at the Origin of the Cohesion of Cement," *Langmuir Journal*, V. 21, 2005, pp. 7263-7270.
56. I.G., Richardson, "Tobermorite/Jennite- and Tobermorite/Calcium Hydroxide-Based Models for The Structure of C-S-H: Applicability to Hardened Pastes of Tricalcium Silicate, B-Dicalcium Silicate, Portland Cement, and Blends of Portland Cement With Blast-Furnace Slag, Metakaolin, or Silica Fume," *Cement and Concrete Research*, V. 34, 2004, pp. 1733-1777.
57. H.M, Jennings, "A Model for the Microstructure of Calcium Silicate Hydrate in Cement Paste," *Cement and Concrete Research*, V. 30, 2000, pp. 101-116.
58. J.J, Thomas, H.M., Jennings, " A Colloidal Interpretation of Chemical Aging of the C-S-H Gel and its Effects on The Properties of Cement Paste," *Cement and Concrete Research*, V. 36, 2006, pp. 3-038.
59. B.N.J., Persson, "Sliding Friction: Physical Principles and Applications," Springer (Nanoscience and Technology), Germany, 1998, pp. 54-59.
60. D.K. Felbeck, A.G. Atkins, "Strength and Fracture of Engineering Solids," Prentice-Hall, Inc., Englewood Cliffs, NJ, 1984, pp. 330-331.

61. V.S., Harutyunyan, E.S., Abovyan, P.J.M., Monterio, V.P., Mkrtchyan, M.K., Balyan, "Microstrain Distribution in Calcium Hydroxide Present in the Interfacial Tranzision Zone," *Cement and Concrete Research*, V. 30, 2000, pp. 709-713.
62. A. P. Barker, "Structural and Mechanical Characterization of Calcium Hydroxide in Set Cement and the Influence of Various Additives," *World Cement*, V. 15 January/February 1984, pp. 25-28.
63. S. Mindess, J.F. Young, D. Darwin, "Concrete," 2nd ed., Prentice Hall, Pearson Education, Inc., NJ, 2003, pp. 64-66 & 73.
64. S. Diamond, D. Bonen, "Microstructure of Hardened Cement Paste - A New Interpretation," *Journal of American Ceramic Society*, V. 76, 1993, pp. 2993-2999.
65. V.L. Popov, "Electronic and phononic friction of solids at low temperatures," *Tribology International*, V. 34, 2001, pp. 277-286.
66. E. Meyer, R.M. Overney, K. Dransfeld, T. Gyalog , "Nanoscience: Friction and Rheology on the Nanometer Scale," World Scientific, Eurasia Press, Singapore, 1998, pp. 176-179.
67. N.M. Alford, G.W. Groves, D.D. Double, Physical properties of high strength cement pastes, *Cem. Concr. Res.* 12 (1982) 349-358.
68. A. Ammouche, D. Breysse, H. Hornain, O. Didry, J. Marchand, "A New Image Analysis Technique for the Quantitative Assessment of Microcracks in Cement-Based Materials," *Cement and Concrete Research*, V. 30, 2000, pp. 25-35.
69. I. Tsukrov, M. Kachanov, "Stress Concentrations and Microfracturing Patterns in A Brittle-Elastic Solid with Interacting Pores of Diverse Shapes," *International Journal of Solid Structures*, V. 34, 1997, pp. 2887-2904.
70. S. Mindess, J.F. Young, D. Darwin, "Concrete," 2nd ed., Prentice Hall, Pearson Education, Inc., NJ, 2003, pp. 421.
71. S. Mindess, J.F. Young, D. Darwin, "Concrete," 2nd ed., Prentice Hall, Pearson Education, Inc., NJ, 2003, pp. 318.
72. R.K, Dhir, "Key Features in View of Modeling the Permeability of Concrete," *Cement Combinations for Durable Concrete Proceedings of the International conference Held at the University of Dundee, Scotland UK on 5-7 July 2005*, pp. 591-600.

73. J. Bisschop, J.G.M. van Mier, "Quantification of shrinkage microcracking in young mortar with fluorescence light microscopy and ESEM," *Heron*, V. 44, No. 4, 1999, pp. 245-255.
74. K.L. Scrivener, "Materials Science of Concrete I," Skalny, J.P., Ed.; American Ceramic Society: Westerville OH, 1989, pp. 127-161.
75. D.P. Bentz, E. Schlangen, E.J. Garboczi, "Materials Science of Concrete IV," Skalny, J.P.; Mindess, S. Eds.; American Ceramic Society: Westerville OH, 1995.
76. <http://www.glossary.oilfield.slb.com/Display.cfm?Term=poisson's%20ratio>
77. T.T.C. Hsu, F.O. Slate, G.M. Sturman, G. Winter, "Microcracking of Plain Concrete and the Shape of the Stress-Strain Curve," *ACI Journal, Proceedings* V. 60, No. 2, Feb. 1963, pp. 209-224.
78. S. Mindess, J.F. Young, D. Darwin, "Concrete," 2nd ed., Prentice Hall, Pearson Education, Inc., NJ, 2003, pp. 308-311.
79. C.S. Poon, L. Lam, Y.L. Wong, "Effects of Fly Ash and Silica Fume on Interfacial Porosity of Concrete," *Journal of Materials in Civil Engineering*, August 1999, pp. 197-205.
80. Mehta, P.K. and P.J.M. Monteiro, *Concrete: Microstructure, Properties, and Materials*, 2nd ed., McGraw-Hill Com. Inc., 1993.
81. S. Mindess, J.F. Young, D. Darwin, "Concrete," 2nd ed., Prentice Hall, Pearson Education, Inc., NJ, 2003, pp. 308-311.
82. K.L. Scrivener, A.K. Crumbie, P. Laugesen, "The Interfacial Transition Zone between Cement Paste and Aggregate in Concrete," *Interface Science*, V. 12, 2004, pp. 411-421.
83. A. Kliszczewicz, A. Ajdukiewicz, "Differences in Instantaneous Deformability of HS/HPC According to the Kind of Coarse Aggregate," *Cement and Concrete Research*, V. 24, No. 2, 2002, pp. 263-267.
84. N. Ramakrishnan, V.S. Arunachalam, "Effective Elastic Modulus of Porous Solids," *Journal of Materials Science*, V. 25, 1990, pp. 3930-3937.
85. G. Giaccio, R. Zerbino, "Failure Mechanism of Concrete: Combined Effect of Coarse Aggregates and Strength Level," *Advanced Cement Based Materials*, Vol. 31, 1998, pp. 41-48.
86. J. Liu, A.K. Mukhopadhyay, D.G. Zollinger, "Contribution of Aggregates to the Bonding Performance of Concrete," paper submitted to the Transportation

Research Board for presentation and publication at the 2006 annual meeting in Washington, D.C.

87. I. Soroka, "Portland Cement Paste and Concrete," Macmillan, London, UK, 1979.
88. T.S. Nagraj, B. Zahida, "Generalization of Abrams' Laws," *Cement and Concrete Research*, V. 26, No. 6, 1996, pp. 933– 942.
89. G.M. Darr, U. Ludwing, "Determination of Permeable Porosity," *Material Structures*, V. 6, No. 2, 1973, pp. 185– 190.
90. F.S. Rostasy, R. Weib, G. Wiedemann, "Changes of Pore Structure of Cement Mortar Due to Temperature, *Cement and Concrete Research*, V.10, No. 2, 1980, pp. 157– 164.
91. D. Winslow, D. Liu, "Pore Structure of Paste in Concrete," *Cement and Concrete Research*, V. 20, No. 2, 1990, pp. 227– 235.
92. H.W. Reinhardt, in: A. Aguado, R. Gettu, S.P. Shah (Eds.), "Concrete Technology: New Trends Industrial Applications," E & FN Spon, UK, 1995, pp. 19–32.
93. P.K. Mehta, "Concrete: Structure, Properties and Materials," Prentice-Hall, New York, 1986.
94. S. Popovics, "New Formulas for the Prediction of the Effects of Porosity on Concrete Strength," *ACI Materials Journal*, V. 78, No. 2, 1981, pp. 127–129.
95. S. Popovics, "Generalization of Abrams' Law," *ACI Materials Journal*, V. 82, No. 2, 1985, pp. 136– 146.
96. A.I. Laskar, R. Kumar, B. Bhattacharjee, "Some Aspects of Evaluation of Concrete Through Mercury Intrusion Porosimetry, *Cement and Concrete Research*, V. 27, No. 1, 1997, pp. 93– 105.
97. R. Kumar, "Strength and Permeation Quality of Concrete Through Mercury Intrusion Porosimetry, PhD Thesis, Department of Civil Engineering, Indian Institute of Technology Delhi, New Delhi, India, 1997.
98. R. Kumar, B. Bhattacharjee, "Study on Some Factors Affecting the Results in the Use of MIP Method in Concrete Research," *Cement and Concrete Research*, USA (submitted for publication).
99. D.N. Winslow, S. Diamond, "A Mercury Porosimetry Study of the Evaluation of Porosity in Portland Cement," *ACI Materials Journal*, V.5, No. 3, 1970, pp. 564– 585.

100. S. Diamond, "A Critical Comparison of Mercury Intrusion Porosimetry and Capillary Condensation Pore Size Distribution of Portland Cement Pastes," *Cement and Concrete Research*, V. 1, No. 5, 1971, pp. 531– 545.
101. S. Diamond, "Mercury Porosimetry; An Inappropriate Method for the Measurement of Pore Size Distributions in Cement-Based Materials," *Cement and Concrete Research*, V. 30, No. 10, 2000, pp.1517–1525.
102. T.R. Naik, B.W. Ramme, J.H. Tews, "Use of High Volumes of Class C and Class F Fly Ash in Concrete," *American Society of Testing and Materials*, 1994, pp. 12-20.
103. Y.M. Zhang, W. Sun, H.D. Yan, "Hydration of High-Volume Fly Ash Cement Pastes", *Cement & Concrete Composites*, Vo. 22, 2000, pp. 445-452.
104. L. Lam, Y.L. Wong, C.S. Poon, "Degree of Hydration and Gel/Space Ratio of High-Volume Fly Ash/Cement Systems," *Cement and Concrete Research*, V. 30, 2000, pp. 747-756
105. S. Mindess, J.F. Young, D. Darwin, "Concrete," Prentice Hall, NJ, 2nd Ed., 2003, pp. 73.
106. S. Mindess, J.F. Young, D. Darwin, "Concrete," Prentice Hall, NJ, 2nd Ed., 2003, pp. 97.
107. G. Carrete, V.M. Malhotra, "Studies on Mechanism of Development of Physical and Mechanical Properties of High-Volume Fly Ash Cement Pastes," *Cement and Concrete Composite*, V. 12, 1990, pp. 245-251.
108. C.D. Atis, "Carbonation-Porosity-Strength Model of Fly Ash Concrete", *Journal of Materials in Civil Engineering*, ASCE, Jan. 2004, pp. 91-94.

MICHIGAN STATE UNIVERSITY LIBRARIES



3 1293 02956 6134